(This page was intentionally left blank)

University of Southampton

Faculty of Engineering and Physical Sciences

Engineering Materials

Advanced 3D Characterisation of Failure Mechanisms in Fibre-Reinforced Composites

by

Erich Schöberl

A thesis presented for the degree of Doctor of Philosophy

December 2020

(This page was intentionally left blank)

In the loving memory of my father,

Horst Schöberl

Supervisors:

Professor S. Mark Spearing

Professor Ian Sinclair

Dr. Mark N. Mavrogordato

Engineering Materials

Faculty of Engineering and Physical Science

University of Southampton

Abstract

Faculty of Engineering and Physical Sciences
Engineering Materials
Doctor of Philosophy

Advanced 3D Characterisation of Failure Mechanisms in Fibre-Reinforced Composites

by
Erich Schöberl

This thesis focuses on developing the understanding of fibre fracture processes in unidirectional (UD) Carbon-Fibre Reinforced Polymers (CFRPs), by delineating aspects of the load shedding phenomenon. In this context, Digital Volume Correlation (DVC) has been applied, in concert with *in situ* Synchrotron Radiation Computed Tomography (SRCT) to representative double-edge notched cross-ply specimens subject to quasi-static loading, which allow observation of fibre fracture in the 0° plies. Analogous to surface-based Digital Image Correlation (DIC), DVC is a relatively novel volumetric method that can utilize Computed Tomography (CT) data to quantify internal three-dimensional (3D) displacements and implicit strain fields. The highly anisotropic and somewhat regular/self-similar microstructures found in well-aligned UD materials at high fibre volume fractions are shown to be intrinsically challenging for DVC, especially along the fibre direction. To permit the application of DVC to displacement and/or strain measurements parallel to the fibre orientation, a novel CFRP was developed, specifically tailored for the application of DVC and CT to experimental mechanics analyses of these materials. The strategy chosen was to dope the matrix with a sparse population of sub-micrometre particles to act as displacement trackers (*i.e.* fiducial markers). Barium titanate particles (400 nm, ~1.44 vol. %) were found to offer the most favourable compromise between contrast in CT images and the ability to obtain a homogeneous distribution in 3D space with sufficient particle compactness for local DVC analyses. By comparing the micromechanical behaviour of the particle-adapted material alongside its particle-free counterpart, it was determined through the application of *in situ* SRCT that the macroscopic and micromechanical responses of the newly developed CFRP are consistent with standard production materials indicating its suitability as a model system for mechanistic investigations. Following an experimental demonstration and validation of high-resolution 3D experimental strain measurement using DVC on CFRPs, via through-thickness strain analysis under a state of pure bending, this study has shown that the distance (~50-100 μm) over which strain is recovered in the broken fibres was consistent with previous estimates and model predictions from the literature. New evidence was also highlighted, whereby the recovery lengths were shown not only to increase with the applied force, but also with the number of broken fibres in a cluster.

Table of Contents

Abstract i

Table of Contents ii

Table of Figures vii

Table of Tables xv

Research Thesis: Declaration of Authorship xvi

Acknowledgements xviii

List of acronyms xx

Chapter 1 Introduction 22

1.1 General introduction 22

1.2 Project motivation and objectives 24

1.3 Thesis structure 25

1.4 List of publications 26

1.4.1 Journal papers 26

1.4.2 Conference papers 26

1.5 References 27

Chapter 2 Literature review 30

2.1 Introduction 31

2.2 Failure of continuous fibre-reinforced composites in tension 31

2.2.1 Fibre strength statistics 31

2.2.2 The fibre-matrix interface 36

2.2.2.1 The matrix phase and interfacial properties 36

2.2.2.2 The fibre break interaction 43

2.2.3 Damage assessment methods 46

2.2.4 Micromechanical representation of axial fibre failure 47

2.2.4.1 Stress redistribution around fibre breaks 47

2.2.4.2 The unidirectional strength model benchmarking exercise 51

2.2.4.3 State-of-the-art SRCT characterization of tensile failure in CFRPs 58

2.3 Computed Tomography 66
2.3.1 X-ray generation and interaction with matter 66
2.3.2 Principles of operation 69
2.3.3 Micro-focus Computed Tomography 69
2.3.4 Synchrotron Radiation Computed Tomography 72
2.3.5 Advantages of Synchrotron Radiation Computed Tomography 75
2.3.6 Artefacts 76
2.4 Digital Volume Correlation 79
2.4.1 Bulk deformation and strain measurement methods 79
2.4.2 Technique description 81
2.4.3 Effect of sub-set size 85
2.4.4 Effect of sub-set overlap 86
2.4.5 Previous uses of Digital Volume Correlation on fibre-reinforced polymers 87
2.5 Summary and conclusions 88
2.6 References 90

Chapter 3 Materials and methods 107

3.1 Material development and manufacturing 108
3.2 Specimen geometry and loading 108
3.2.1 Microstructural analysis 108
3.2.2 Double-edge notched tensile tests 109
3.2.3 Four-point bending test 109
3.3 Imaging methods 109
3.3.1 Micro-focus Computed Tomography 109
3.3.2 Synchrotron Radiation Computed Tomography 110
3.4 Digital Volume Correlation 110
3.5 Image processing 111
3.6 References 111

Chapter 4 A novel particle-filled Carbon-Fibre Reinforced Polymer model composite tailored for the application of Digital Volume Correlation and Computed Tomography 112

4.1 Introduction 113
4.2 Materials and methods 116
4.2.1 Material development 116
4.2.1.1 Carbon-fibre and resin system 116
4.2.1.2 Particle systems 116
4.2.1.3 Material manufacturing 118
4.2.2 Specimen geometry 119
4.2.2.1 Microstructural analysis 119
4.2.2.2 Tensile testing 119
4.2.3 Micro-focus Computed Tomography 121
4.2.4 Synchrotron Radiation Computed Tomography 122
4.2.5 Image processing 122
4.3 Results and discussion 123
4.3.1 Microstructural analysis 123
4.3.2 Fibre break behaviour 127
4.3.3 Cluster behaviour 133
4.4 Summary and conclusions 137
4.5 Appendix A – Micro-focus Computed Tomography 138
4.6 Appendix B – Microstructural analysis 144
4.7 References 147

Chapter 5 Fibre-direction strain measurement in a composite ply under pure bending using Digital Volume Correlation and Micro-focus Computed Tomography 153

5.1 Introduction 154
5.2 Materials and methods 156
5.2.1 Material manufacturing 156
5.2.2 Specimen geometry and loading 157
5.2.3 Computed Tomography 159
5.2.4 Digital Volume Correlation 160
5.2.5 Image processing 165

5.3 Results and discussion 167
5.3.1 Noise and sensitivity 167
5.3.1.1 Static noise test 167
5.3.1.2 Rigid body displacement 170
5.3.2 Evaluation of radius of curvature 173
5.3.3 Beam strain profiles 174
5.3.3.1 Volumetric sub-set averaging 176
5.3.3.2 Planar sub-set averaging 179
5.3.4 Summary and conclusions 184
5.3.5 References 185

Chapter 6 Fibre-direction strain measurement in a composite ply under quasi-static tensile loading using Digital Volume Correlation and *in situ* Synchrotron Radiation Computed Tomography 189

6.1 Introduction 190
6.2 Materials and methods 193
6.2.1 Material manufacturing 193
6.2.2 Specimen geometry and loading 194
6.2.3 Synchrotron Radiation Computed Tomography 195
6.2.4 Digital Volume Correlation 195
6.3 Results and discussion 200
6.3.1 Noise and sensitivity 200
6.3.2 Strain field assessment at single fibre breaks 200
6.3.2.1 Strain transfer lengths 201
6.3.2.2 Effect of applied load on strain transfer lengths 205
6.3.3 Strain field assessment at clusters of breaks 208
6.3.3.1 Evolution of clusters of breaks 208
6.3.3.2 Effect of clusters of breaks on strain transfer lengths 210
6.4 Summary and conclusions 212

6.5 Appendix A – Static noise test 214
6.6 Appendix B – Rigid body displacement 217
6.7 Appendix C – Effect of strain window size 220
6.8 Appendix D – Assessment against conventional microstructures 222
6.9 Appendix E – Assessment against Micro-focus Computed Tomography 225
6.10 References 227

Chapter 7 Summary, conclusions and further work 235

7.1 Summary 235
7.2 Conclusions 238
7.3 Further work 239
7.3.1 Experimental 239
7.3.2 Imaging 240
7.3.3 Digital Volume Correlation 241

Table of Figures

Figure 2-1 – Three-dimensional schematic model: (a) representative of a high modulus PAN-based carbon-fibre structure, (b) orientation of aromatic planes with respect to the fibre direction 32

Figure 2-2 – Scanning electron microscopy image illustrating the tensile fracture surface of a T800G carbon-fibre, which failed due to natural flaws 32

Figure 2-3 – Schematic representation of the 'Chain of links' model 33

Figure 2-4 – Histogram illustrating the natural flaw size representative of a T800G carbon-fibre at various gauge lengths (between 5 mm and 50 mm) 33

Figure 2-5 – Weibull distribution example, illustrating the decrease in fibre strength scatter with increasing Weibull modulus 35

Figure 2-6 – The four methods typically used to measure the interfacial shear strength 38

Figure 2-7 – Schematic representation of the fragmentation process in a single fibre composite subjected to uniaxial tension 39

Figure 2-8 – Schematic representation of the closely spaced/planar fractures sites in a microcomposite containing seven equally-spaced carbon-fibres 40

Figure 2-9 – Schematic representation illustrating the different interface bonding mechanisms in a fibre-bridged composite (interface frictional sliding and physical/chemical bonding) 41

Figure 2-10 – Schematic representation of the 'ineffective length' in the broken fibre and the 'positively affected length' or 'overload length' in the nearest neighbouring fibre, respectively 44

Figure 2-11 – Schematic illustration of interacting breaks in two-dimensions: (a) two single breaks, (b) one double and one single break, respectively 45

Figure 2-12 – Stress redistribution around a fibre break in a UD composite: (a) axial stress recovery (i.e. ineffective length), (b) SCF and overload length, respectively 47

Figure 2-13 – Normalized ineffective length for the different: (a) fibre packings, (b) fibre volume fractions, (c) fibre stiffnesses 48

Figure 2-14 – The effect of modulus ratio, volume fraction and applied strain on the ineffective length in a UD composite 50

Figure 2-15 – Model predictions for the real material case: (a) 0° ply strength, (b) composite failure strain, (c) fibre break accumulation as a function of applied strain, (d) evolution of the largest cluster, with the size expressed in number of broken encompassing fibres. Results represent a minimum of ten simulations per output 55

Figure 2-16 – Tomographic reconstruction showing segmented 90° ply transverse cracks and 0° ply splits, respectively, in a $[90/0]_s$ double-edge notched CFRP specimen at 40 % UTS 59

Figure 2-17 – Tomographic reconstruction showing segmented multi-scale damage in a [90/45/-45/0]s 'matchstick' CFRP specimen at 80 % UTS 60

Figure 2-18 – Tomographic reconstruction showing the interaction of various damage mechanisms across different slices: (a) reference plane, (b) 200 µm ahead of the notch, (c) 350 µm ahead of the notch 60

Figure 2-19 – Schematic illustration of the in situ loading rig: (a) semi-transparent view, (b) annotated cross-section 61

Figure 2-20 – Tomographic reconstruction showing segmented damage in a $[90/0]_s$ double-edge notched CFRP specimen at 94 % UTS 62

Figure 2-21 – Tomographic reconstruction showing a cluster encompassing 14 breaks across the different planes at 94 % UTS 62

Figure 2-22 – Estimate of the ineffective length based on the closest separation of fibre breaks along the longitudinal axis of the same fibre 63

Figure 2-23 – Total number of fibre breaks as a function of applied stress in the load bearing reduced cross-section of 0.45 mm^2 for the two specimens subjected to in situ continuous tensile testing 64

Figure 2-24 – Distribution of fibre breaks at different UTS levels: (a) and (b) total number of breaks, (c) and (d) proportion of breaks occurring as clusters of breaks 65

Figure 2-25 – Electromagnetic spectrum 66

Figure 2-26 – Schematic illustration of the X-ray CT acquisition and reconstruction process 69

Figure 2-27 – Schematic illustration of an X-ray (cathode) tube and its main constituents 70

Figure 2-28 – Schematic illustration of the target system of an X-ray tube: (a) reflection, (b) transmission 71

Figure 2-29 – Schematic illustration of the different data acquisition configurations and radiation flux geometries: (a) planar fan beam, (b) cone beam, (c) parallel beam 72

Figure 2-30 – Overview of a synchrotron facility (courtesy of ESRF) 73

Figure 2-31 – Main components of a storage ring 74

Figure 2-32 – Schematic illustration of a bending magnet 74

Figure 2-33 – Insertion device and it's schematic illustration 75

Figure 2-34 – Image matrix showing the in-plane domain (pixels) and volumetric domain (voxels).....81

Figure 2-35 – Schematic diagram of the DVC process. For a given measurement point 'p', the displacement is given by the vector 't', which connects the centroids of the reference sub-set 'k_0' and deformed sub-set 'k', respectively.....82

Figure 2-36 – An example of a simple 1D cross-correlation. The reference pattern 'A' is shifted through the space of the displaced pattern 'B' by integer increments of 'dx'. For each shift 'dx' the product of the height of pairs of overlapping bars from A and B is calculated, and the sum of these products returns the corresponding correlation coefficient (right-hand side of the figure). The correlation coefficient reaches its maximum at 'dx = 6', when the patterns exhibits an optimized match. Increasing the shift 'dx' even further causes the correlation coefficient to decrease. As a result, the best match is given by the maximum of the correlation peak 84

Figure 2-37 – Schematic illustration showing different sub-set overlapping percentages. Spatial density of sub-sets is increased, without reducing the actual size.....86

Figure 4-1 – Attenuation profiles for elemental media and compounds, representative of the different phases: matrix, carbon-fibres and fiducial markers. The attenuation of the matrix was estimated using bisphenol A diglycidyl ether (DGEBA), $C_{21}H_{24}O_4$. Based on NIST data.....117

Figure 4-2 – Schematic illustration of the cure cycle used as part of the autoclave process.....119

Figure 4-3 – Tensile specimens: (a) key specimen dimensions and field of view (FOV), (b) tabbed assembly (CFRP plus aluminium tabs), (c) SRCT slice showing a cross-section of the notch region doped with high contrast fiducial markers ($BaTiO_3$, 400 nm ~1.44 vol. %), including the region of interest (ROI), which encompasses the 0° plies.....121

Figure 4-4 – SRCT experimental setup illustrating the key components (ID19 beamline, ESRF) 122

Figure 4-5 – Representative µCT slices showing the doping of the CFRP with aluminium and barium titanate, respectively (0° plies shown).....126

Figure 4-6 – Fibre break accumulation as a function of applied stress for the three specimens subjected to in situ SRCT tensile testing. Data shown for an equivalent ROI volume of ~0.34 mm^3 for each specimen.....130

Figure 4-7 – Fibre break accumulation as a function of % UTS for the two specimens loaded to fracture. Based on in situ SRCT data. Data shown for an equivalent ROI volume of ~0.34 mm^3 for each specimen.....131

Figure 4-8 – Number of singlets as a function of applied stress for the three specimens subjected to in situ SRCT tensile testing. Data shown for an equivalent ROI volume of ~0.34 mm^3 for each specimen.....132

Figure 4-9 – Fraction of singlets to N-plets as a function of applied stress for the three specimens subjected to in situ SRCT tensile testing. Data shown for an equivalent ROI volume of ~0.34 mm^3 for each specimen. Nomenclature example: three 7-plets are counted as 21 breaks in total) 132

Table of Figures

Figure 4-10 – Distribution of N-plets as a function of applied stress for the three specimens subjected to in situ SRCT tensile testing: (a) doped specimen, (b) undoped specimen 'A', (c) undoped specimen 'B'. Data shown for an equivalent ROI volume of ~0.34 mm³ for each specimen 135

Figure 4-11 – Distribution of N-plets in 3D space at the maximum stress recorded prior to fracture: (a) doped specimen – 2267 MPa, (b) undoped specimen 'A' – 3486 MPa, (c) undoped specimen 'B' – 3082 MPa. Visualizations reconstructed from break centroid coordinates. Each volume corresponds to ~0.34 mm³ 136

Figure 5-1 – Schematic illustration of the prepreg manufacturing (drum winding) process 157

Figure 5-2 – (a) Specimen geometry (thickness as measured via CT), and (b) direction of loading relative to the composite layup (orthogonal to the 0° plies – XZ-plane shown). The ROI shown schematically corresponds to that of the cropped CT volume for DVC analysis 157

Figure 5-3 – (a) Reaction tube with relevant dimensions, (b) wedges designed to maintain optimum alignment of the specimen, (c) complete assembly – showing both a bent and unbent geometry to illustrate the operating principle 158

Figure 5-4 – Experimental setup illustrating the loading device in acquisition position 160

Figure 5-5 – Generalized workflow of the correlation process (for simplicity, the illustration is shown in 2D). Strain post-processing strategies employed in the present work are highlighted 162

Figure 5-6 – Schematic diagram of the DVC process: inclusion of fiducials and presence of a user-specific search region when using the 'DC' method 163

Figure 5-7 – Example stack comprised of 4 DVC slices in the Z-direction ('Z=0' to 'Z=3'), applicable to a sub-set size of 120 voxels with 50 % overlap. In turn, each DVC slice (i.e. plane of sub-sets, one volumetric sub-set thick) is representative for 60 raw CT data slices. Raw data volumes cropped from the 0° plies: 795 × 885 × 230 voxels. Y-axis indicates the fibre direction. X-axis is in-plane orthogonal to the fibre direction, while the Z-axis corresponds to the out-of-plane direction 164

Figure 5-8 – Workflow illustrating the evaluation of radius of curvature of the bent specimen using GOM Inspect 2018 and validating the metrologically obtained results in SOLIDWORKS 2015 166

Figure 5-9 – Influence of sub-set size on the strain resolution during SNT scanning (expressed as the standard deviation of the measured strain values), illustrating the compromise between strain and spatial resolution. The 'ε_{yy}' component of the strain tensor denotes the longitudinal (fibre) strain, 'ε_{xx}' the in-plane transverse strain, while the out-of-plane strain component is given by 'ε_{zz}' 168

Figure 5-10 – 3D isometric CT view of an isotropic sub-set with a characteristic length of 100 voxels, containing segmented $BaTiO_3$ particles 169

Figure 5-11 – Number of particles as function of sub-set size, using a grey-level threshold of 100/255 169

Figure 5-12 – Illustration of VSG and sub-set size, in conjunction with spatial resolution vs. strain resolution (ε_{yy}). Voxel size corresponds to ~0.64 µm.....170

Figure 5-13 – DVC slice 'Z=2' illustrating the 'ε_{yy}' strain map (noise) overlaid with the microstructure following RBD correction. Masking applied (795 × 16 × 230 voxels) to remove edge artefacts for the Y-displaced scans. Map range: -0.065 to 0.065 % 171

Figure 5-14 – (a) Strain resolution (ε_{yy}), and (b) strain mean (ε_{yy}) for the SNT and RBD corrected scans for various sub-set sizes with 50 % overlap. Masking applied (795 × 16 × 230 voxels) to remove edge artefacts for the Y-displaced scans. Voxel size corresponds to ~0.64 µm.....172

Figure 5-15 – Metrologically fitted circle with a radius of 65.38 mm on the specimen bent geometry (~1 mm × ~4 mm) captured within the FOV of the 4 × scan.....173

*Figure 5-16 – Schematic diagram illustrating the 3D grid of DVC sub-sets, applicable to matching volumes of 795 × 885 × 230 voxels, correlated with an isotropic sub-set size of 120 voxels and 50 % overlap. For simplicity, only overlapping windows (steps) are shown as opposed to the grid comprised of overlapped sub-sets. Displacement vectors, and implicit strain values are computed for each step (i.e. a distance of 60 voxels or ~38.4 µm). The sub-set averaging schemes are indicated as follows in decreasing stages (applicable to each permutation along the X-direction: **yellow** – volumetric across four slices (planes) of sub-sets, **orange** – planar, across a single slice of sub-sets, **blue** – planar, single median block of five sub-sets '2/3', **pink**, **cyan** and **green** – planar, three central blocks each consisting of three sub-sets '2/5', '3/5', '4/5' and **red** – planar, standalone sub-sets (rows) through the beam thickness compared with the analytical solution* 175

Figure 5-17 – Strain mapping illustration overlapped with the microstructure (795 × 885 voxels, ~0.64 µm voxel size), showing the through-thickness strain distribution. Fibres in tension on the left-hand side and in compression on the right-hand side. Sub-set size: 120 voxels with 50 % overlap. DVC slice number 'Z=2'. Interpolation/smoothing not applied to the strain map.....176

Figure 5-18 – Strain gradient obtained through the application of DVC vs. classical beam theory prediction. Sub-set size: (a) 120 voxels, (b) 100 voxels, (c) 80 voxels with 50 % overlap. Volumetric sub-set averaging through all DVC slices: (a) 'Z=0' to 'Z=3', (b) 'Z=0' to 'Z=4', (c) 'Z=0' to 'Z=5'. Number of averaged sub-sets per column: (a) 60 (15 × 4), (b) 72 (18 × 4), (c) 88 (22 × 4). Number of data points: (a) 13 columns, (b) 16 columns, (c) 20 columns. Indicated RDB corrected error of (a) 0.0211 %, (b) 0.0293 %, (c) 0.0415 % 178

Figure 5-19 – Strain gradient obtained through the application of DVC vs. classical beam theory prediction. Sub-set size: 120 voxels with 50 % overlap. Planar sub-set averaging performed independently in both DVC slices 'Z=1' and 'Z=2'. Number of averaged sub-sets per column: 15 (15 × 1). Edge-artefacts located at the perimeter truncated (XY-plane), yielding 14 data points (7 columns × 2 DVC slices). Indicated RDB corrected error of 0.0211 %.....179

Figure 5-20 – Strain gradient obtained through the application of DVC vs. classical beam theory prediction. Sub-set size: 120 voxels with 50 % overlap. DVC slice number 'Z=2'. Planar averaging scheme: (a) single median block '2/3' containing 5 averaged sub-sets per column on the grid (block contains 33.33 % of the total number of sub-sets per column), and (b)

central blocks '2/5', '3/5', '4/5' each containing 3 averaged sub-sets per column on the grid (one block contains 20 % of the total number of sub-sets per column). Edge-artefacts located at the perimeter and ends of the stack truncated (XY and Z-plane), resulting in: (a) 7 data points (1 block of averaged sub-sets × 7 columns), and (b) 21 data points (3 blocks of averaged sub-sets × 7 columns). Indicated RDB corrected error of 0.0211 %.....181

Figure 5-21 – Strain gradient obtained through the application of DVC vs. classical beam theory prediction. Sub-set size: 120 voxels with 50 % overlap. Sub-set averaging scheme removed (i.e. each data point corresponds to strain value of a standalone sub-set). Rows of sub-sets (Y-direction) plotted: 4/15, 5/15, 7/15, 11/15, resulting in 28 data points (7 sub-sets × 4 rows). Edge-artefacts located at the perimeter and ends of the stack truncated (XY and Z-plane). Indicated RDB corrected error of 0.0211 %.....182

Figure 5-22 – Raw CT data slices showcasing changes in material microstructure, potentially accountable for an uneven strain distribution at fibre-level. Each slice has a FOV of 795 × 885 voxels (~0.64 µm voxel size): (a) illustrating tow-level misalignment, (b) large resin-rich channel coupled with fibre direction errors, (c) multiple, parallel resin-rich channels and fibre misalignment, (d) large resin-rich channel and fibre misalignment. The spatial distribution of particles is uniformly random, providing this is considered in 3D space.....183

Figure 6-1 – Workflow diagram of the DVC process.....196

Figure 6-2 – Example stack comprised of 33 DVC slices in the Z-direction ('Z=0' to 'Z=32'), applicable to a sub-set size of 72 voxels with 75 % overlap, loaded to 950 N. In turn, each DVC slice (i.e. plane of sub-sets, one volumetric sub-set thick) is representative for 18 raw CT data slices. Raw data volumes cropped from the 0° plies: 600 × 600 × 600 voxels. Y-axis indicates the fibre direction. X-axis is in-plane orthogonal to the fibre direction, while the Z-axis corresponds to the out-of-plane direction.....198

Figure 6-3 – Schematic illustration of different VSGs , depending on the strain window size (L_{SW}) used: (a) anisotropic – L_{SW} of 1 × 3 × 1 vectors, (b) anisotropic – L_{SW} of 3 × 3 × 1 vectors, and (c) isotropic – L_{SW} of 3 × 3 × 3 vectors. Each cube represents a sub-set and its associated centroid, with a grid spacing of one step. Sub-sets are not overlapped here for simplicity reasons. Strain window size of 1 × 3 × 1 emphasises smoothing along the fibre direction, 3 × 3 × 1 in the fibre layup plane, and 3 × 3 × 3 smooths isotopically. Higher-order strain window sizes are possible, but this can lead to an over-smoothing of the strains computed (i.e. reduction in signal-to-noise ratio).....199

Figure 6-4 – DVC slice 'Z=23' illustrating the 'ε_{yy}' strain field surrounding singlet 'C'. Following correlation with a sub-set size of 32 voxels (75 % overlap) and strain post-processing with a strain window size of 1 × 3 × 1 vectors, the DVC output yields two near-symmetrical and distinct strain regions longitudinally from the break plane: (1) an 'elevated strain length' measuring ~16 µm, and (2) a 'lower strain length' of ~21 µm, after which the far-field strain level of ~1.5 % is attained. Microstructure subjected to in situ tensile loading of 950 N (98 % UTS), with acquisition performed at 855 N. FOV amounts to ~100 µm × ~100 µm. The measurement error corresponds to ~0.093 % (see Appendices).....203

Figure 6-5 – Half of the 'full-recovery length' split into the two distinct strain regions, measured longitudinally from the bottom side of singlet 'C'. The measurement error corresponds to ~0.093 %.....203

Figure 6-6 – Strain gradients (ε_{yy}) measured longitudinally from eight distinct singlets (both sides of the break plane). Microstructure subjected to in situ tensile loading of 950 N (98 % UTS), with acquisition performed at 855 N. The measurement error corresponds to ~0.093 %.....204

Figure 6-7 – Strain gradient (ε_{yy}) measured longitudinally from singlet 'F' (both sides of the break plane) and repeated stepwise in the transverse direction (X). The far-field strain level of ~1.5 % is attained beyond a radial distance of ~26 µm. Strain distribution indicated in red follows a longitudinal axis from the break plane. Results applicable to DVC slice 'Z=35' Microstructure subjected to in situ tensile loading of 950 N (98 % UTS), with acquisition performed at 855 N. The measurement error corresponds to ~0.093 %.....204

Figure 6-8 – Strain gradients (ε_{yy}) indicating 90 % strain recovery for the different applied load steps: (a) average of eight distinct singlets ('A' to 'H'), and (b) singlet ('A'). Measurements performed on both sides of the break plane. The measurement error corresponds to ~0.093 %.....207

Figure 6-9 – Illustrating the evolution of a cluster of breaks: (a) 'proto-break' site at the 850 N load step – DVC slice 'Z=36', (b) one singe break at the 900 N load step – DVC slice 'Z=36', (c) duplet 'IJ' at the 950 N load step – DVC slice 'Z=36', (d) duplet 'KL' at the 950 load step – DVC slice 'Z=38'. Note the interacting 'ε_{yy}' strain fields surrounding duplets 'IJ' and 'KL', respectively. Correlation performed with a sub-set size of 32 voxels (75 % overlap), while strains were post-processed with a strain window size of 1 × 3 × 1 vectors. FOV amounts to ~100 µm × ~100 µm. The measurement error corresponds to ~0.093 %.....209

Figure 6-10 – Strain gradients (ε_{yy}) measured longitudinally from breaks 'I' and 'K' of the two duplets (both sides of the break plane). Note the longitudinal (visible), transverse and out-of-plane separation distances of ~21 µm, ~16 µm and ~10 µm, respectively. Microstructure subjected to in situ tensile loading of 950 N (98 % UTS), with acquisition performed at 855 N. The measurement error corresponds to ~0.093 %.....212

Figure 6-11 – The influence of sub-set size on the strain resolution during SNT scanning (expressed as the standard deviation of the measured strain values), illustrating the compromise between strain and spatial resolution. The 'ε_{yy}' component of the strain tensor denotes the longitudinal (fibre) strain, 'ε_{xx}' the in-plane transverse strain, while the out-of-plane strain component is given by 'ε_{zz}'.....215

Figure 6-12 – Illustration of VSG and sub-set size, in conjunction with spatial resolution vs. strain resolution (ε_{yy}). Voxel size corresponds to 0.65 µm.....216

Figure 6-13 – DVC slice 'Z=16' illustrating the 'ε_{yy}' strain map (noise) overlaid with the microstructure following RBD correction. Masking applied (600 × 8 × 600 voxels) to remove edge artefacts for the Y-displaced scans. Map range: -0.060 to 0.060 %. Applicable for a correlation performed with a sub-set size of 72 voxels and 75 % overlap.....218

Figure 6-14 – (a) Strain resolution (ε_{yy}), and (b) strain mean (ε_{yy}) for the SNT and RBD corrected scans for various sub-set sizes with 75 % overlap. Masking applied (600 × 8 × 600 voxels) to remove edge artefacts for the Y-displaced scans...219

Figure 6-15 – Strain resolution (ε_{yy}) for the SNT and RBD corrected scans for various strain window sizes (L_{sw}), computed with a sub-set size of 32 voxels and 75 % overlap 221

Figure 6-16 – Influence of sub-set size on the strain resolution during SNT scanning, illustrating the compromise between strain and spatial resolution using the different materials (i.e. 'undoped material' vs. 'doped material' with 400 nm, 7.5 wt. % $BaTiO_3$). Results presented for the 'ε_{yy}' component of the strain tensor and applicable to SRCT data. Computed via 'DC' 223

Figure 6-17 – DVC slice 'Z=40' illustrating correlation maps overlaid with the microstructure following SNT scanning: (a) 'doped material' and (b) 'undoped material'. Both materials exhibit very similar correlation coefficients, indicating the need for SNT and RBD tests. Map range: 0.995 to 1.0. Correlation performed with a sub-set size of 32 voxels and 75 % overlap via 'DC' 224

Figure 6-18 – The influence of sub-set size on the strain resolution during SNT scanning, illustrating the compromise between strain and spatial resolution using different imaging acquisition methods (µCT vs. SRCT). Results presented for the 'ε_{yy}' component of the strain tensor 225

Figure 6-19 – (a) Strain resolution (ε_{yy}), and (b) strain mean (ε_{yy}) for the SNT and RBD corrected scans for various sub-set sizes with 75 % overlap. Masking applied (795 × 16 × 230 voxels) to remove edge artefacts for the Y-displaced scans. Applicable to µCT data (voxel size corresponds to ~0.64 µm) 226

Table of Tables

*Table 4-1 – Experimental matrix showing the particle compositions in conjunction with the concentrations used. *Approximate values based on element (or compound) density* 117

*Table 4-2 – Experimental matrix showing the particle compositions in conjunction with the nominal particle sizes used (*as specified by the manufacturer)* 118

Table 4-3 – Basic characteristics of the double-notched specimens subjected to SRCT-based tensile testing 120

Table 4-4 – ROI from the 0° plies used for fibre break data quantification (SRCT data, 1 voxel = 0.65 µm) 123

Table 4-5 – Ranking system highlighting the overall attributes of the different materials manufactured 125

Table 4-6 – Summary of fibre break behaviour as a function of applied load, stress and % UTS: (a) doped specimen, (b) undoped specimen 'A', (c) undoped specimen 'B'. Based on in situ SRCT tensile data 129

Table 4-7 – Detailed comments complementing the ranking system in Table 4-5 146

Table 5-1 – Summary of 'DC' settings used in the multi-step, multi-pass approach (50 % sub-set overlap). Weighted windows used in the last iteration step (dual-pass) 163

*Table 5-2 – Number of DVC slices (planes of sub-sets) for a given sub-set size with 50 % overlap, and the corresponding number of raw data slices per DVC slice. *Nomenclature: DVC slice numbering starts with 0* 164

Table 5-3 – Number of in-plane data points (X- and Y-direction) per DVC slice, applicable to a sub-set with 50 % overlap 165

Table 6-1 – Summary of 'DC' settings used in the multi-step, multi-pass approach (75 % sub-set overlap). Weighted windows used in the last iteration step (dual-pass) 197

*Table 6-2 – Number of DVC slices (planes of sub-sets) for a given sub-set size with 75 % overlap, and the corresponding number of raw data slices per DVC slice. *Nomenclature: DVC slice numbering starts with 0. Applicable to a cropped volume of 600 × 600 × 600 voxels* 198

*Table 6-3 – Far-field and recovery strain as a function of different load levels. *Strains computed at acquisition load and not compensated for existing preload in the specimen* 206

Table 6-4 – Equivalent VSG sizes in physical units (1 voxel = 0.65 µm) and fibre diameters (1 fibre diameter = 7 µm), respectively, based on different strain window sizes, applicable to a sub-set size of 32 voxels with 75 % overlap 221

Research Thesis: Declaration of Authorship

Print name: Erich Schöberl

Title of thesis: Advanced 3D Characterisation of Failure Mechanisms in Fibre-Reinforced Composites

I declare that this thesis and the work presented in it are my own and has been generated by me as the result of my own original research.

I confirm that:

1. This work was done wholly or mainly while in candidature for a research degree at this University;
2. Where any part of this thesis has previously been submitted for a degree or any other qualification at this University or any other institution, this has been clearly stated;
3. Where I have consulted the published work of others, this is always clearly attributed;
4. Where I have quoted from the work of others, the source is always given. With the exception of such quotations, this thesis is entirely my own work;
5. I have acknowledged all main sources of help;
6. Where the thesis is based on work done by myself jointly with others, I have made clear exactly what was done by others and what I have contributed myself;
7. Parts of this work have been published as:

E. Schöberl, C. Breite, S. Rosini, Y. Swolfs, M. N. Mavrogordato, I. Sinclair and S. M. Spearing, "A novel particle-filled carbon-fibre reinforced polymer model composite tailored for the application of digital volume correlation and computed tomography," *Journal of Composite Materials,* in press*,* 2020.

E. Schöberl, M. N. Mavrogordato, I. Sinclair and S. M. Spearing, “Fibre-direction strain measurement in a composite ply under pure bending using digital volume correlation and micro-focus computed tomography,” *Journal of Composite Materials,* vol. 54, no. 14, pp. 1889-1911, 2020.

E. Schöberl, C. Breite, A. Melnikov, Y. Swolfs, M. N. Mavrogordato, I. Sinclair and S. M. Spearing, “Fibre-direction strain measurement in a composite ply under quasi-static tensile loading using digital volume correlation and in situ synchrotron radiation computed tomography,” *Composites Part A,* vol. 137, no. 105935, 2020.

E. Schöberl, M. N. Mavrogordato, I. Sinclair and S. M. Spearing, “The mapping of damage behaviour in a unidirectional composite subjected to uniaxial loading using digital volume correlation,” in *The 12th International Conference on Composite Science and Technology*, Sorrento, Italy, 8-10 May 2019.

E. Schöberl, C. Breite, A. Melnikov, Y. Swolfs, M. N. Mavrogordato, I. Sinclair and S. M. Spearing, “Mapping strains and fibre fracture in carbon fibre composites using in situ digital volume correlation,” in *The 22nd International Conference on Composites Materials*, Melbourne, Australia, 11-16 August 2019.

Signature: Date: 14th of December 2020

Acknowledgements

I would like to acknowledge a number of individuals and groups who have made this work possible. First and foremost, I would like to thank my supervisors: Professor S. Mark Spearing, Professor Ian Sinclair and Dr. Mark N. Mavrogordato, for their extraordinary support, encouragement, effort and knowledge throughout the project. Many of the achievements presented in this PhD thesis would not have been possible without their constant mentoring. Likewise, my thanks are extended to Professor Yentl Swolfs and the entire Composite Materials Group at KU Leuven, Belgium, for providing scientific know-how, raw materials, as well as manufacturing facilities. In this context, I would also like to acknowledge Christian Breite, Arsen Melnikov and Yoran Geboes, without whom, composite manufacturing would have not been possible in a timely manner. The composite materials fabricated at KU Leuven are at the heart of the three papers published during the course of the programme.

I am grateful for the Marie Skłodowska-Curie ITN grant agreement No. 722626 and the µ-VIS X-Ray Imaging Centre at the University of Southampton, supported by EPSRC grant agreement No. EP/H01506X/1. I also recognize LaVision GmbH for the off-site software supply and technical support from Dr. David Hollis, Dr. Alex Nila and Dr. Manuel Grewer. Tomographic imaging has benefited from the expertise of Dr. Richard Boardman, Dr. Kathryn Rankin, Dr. Orestis Katsamenis, Dr. Daniel Bull and Mr. Nicholas Hale. I am grateful for all team members that consistently stepped up to the plate and helped to organize and run the many synchrotron sessions: Dr. Mark N. Mavrogordato, Dr. Sebastian Rosini and Stephen Wilby. I would also like to acknowledge the fact that experimental trials were performed during the beam time allocated for Stephen's work, while the core experimental campaign was included in Sebastian's beam time. While it is difficult to name everyone from all of the experimental sessions, I would like you to know that your help has been greatly appreciated.

Thanks to all my colleagues within the 'FiBreMoD' project. You are all amazing people, and I wish you the best of success in your future endeavours. Hats off to Carol and Martinus for organizing the best catering services and excluding sandwiches as a viable option. The meals in Berlin, Rehovot, Tel Aviv and Jerusalem will definitely be remembered. Thanks to the staff within the Faculty of Engineering and Physical Sciences, Sue Berger, Katherine Day and Fiona Haigh, as well as the graduate school office and finance office for all of their efforts behind the scenes. Credit is further extended to Mr. Simon Beever – University of Southampton Engineering Design and Manufacturing Centre (EDMC), Mr. Adrian Walker – Safire Associates UK for the short notice water-jet cutting of various components required for the experimental work, as well as Mr. Manuël Adams and Mr. Marc Peeters – KU Leuven for the short notice repairs on various laboratory equipment.

I am grateful to have had close friends providing moral support throughout the project: Bogdan Profir, David-Alexandru Serban, Guoqiang Yu, Edgar-Daniel Pacurariu, Filip Gaga, David-Alexandru Timis, Toni Barta, Daniel Berindeie, Bledian Leka, Alvaro Cordoba Gomez, Christian Breite and Martinus Widjaja, to name a few. Likewise, I would like to thank my roommates Mateo Salam Perez, Mahmoud Mohamed, Davide Bufalini and Tristan Madeleine for the “oven-free cooking lessons”, as well as fruitful scientific discussions during the 2020 pandemic lockdown period.

It goes without saying that my achievements to date would not have been possible without the support of my family from Romania and Portugal. In particular, I want to thank my parents Adrian and Cristina, and grandparents Ioan and Silvia, for always supporting me in pursuing my dreams, as well as my siblings for whose support and love I am so grateful. Razvan, I hope one day you will find this piece of work inspiring for your own thesis, should you decide to pursue a PhD. Finally, my sincerest appreciation goes to my girlfriend Anca. She corrected a vast number of presentations for linguistic errors and encouraged me to stay on track and successfully defend my thesis. Thank you for always being there with a smile, even though I know it was difficult being nearly 2000 miles away. You are truly a special person.

List of acronyms

1D	One-dimensional
2D	Two-dimensional
3D	Three-dimensional
AE	Acoustic Emission
C-scanning	Ultrasonic scanning
CFRP	Carbon-Fibre Reinforced Polymer
CM	Confocal Microscopy
CNR	Contrast-to-noise ratio
CT	Computed Tomography
DC	Direct Correlation (refers to DVC)
DIC	Digital Image Correlation
DGEBA	Bisphenol A diglycidyl ether (refers to epoxy constituent)
DVC	Digital Volume Correlation
ESRF	European Synchrotron Radiation Facility
FBP	Filtered Back Projection
FE	Finite Element
FFT	Fast Fourier Transform (refers to DVC)
FOV	Field of view
FRP	Fibre-Reinforced Polymer
GFRP	Glass-Fibre Reinforced Polymer
IFSS	Interfacial shear strength

IT	Infrared Thermography
MRI	Magnetic Resonance Imaging
NDT	Non-destructive testing
NIST	National Institute of Standards and Technology
OCT	Optical Coherence Tomography
PAL	Positively affected length (equivalent to overload length)
PAN	Polyacrylonitrile (refers to carbon-fibre precursor)
PLAW	Power-law accelerated Weibull distribution
PMMA	Poly(Methyl Methacrylate)
RBD	Rigid body displacement
ROI	Region of interest
RVE	Representative Volume Element
SAXS	Small-angle X-ray scattering
SCF	Stress (or strain) concentration factor
SNR	Signal-to-noise ratio
SNT	Static noise test
SRCT	Synchrotron Radiation Computed Tomography
UD	Unidirectional (refers to fibre orientation)
UTS	Ultimate tensile strength
VSG	Virtual Strain Gauge
WAXD	Wide-angle X-ray diffraction
WoW	Weibull of Weibulls
µCT	Micro-focus Computed Tomography

Chapter 1 Introduction

1.1 General introduction

Climate change continues to be a major societal challenge. In December 2015, nations across the world were brought together under the Paris Agreement [1] into a common cause of undertaking ambitious efforts to combat climate change. The main objective of the Paris Agreement is to limit any global temperature rise to well below 2°C within this century [1]. If the European Union (EU) member states are to achieve this set goal, the source of pollutants and associated greenhouse gases (*e.g.* CO_2, NO_x) are to be drastically reduced. For example, 27 % of the greenhouse gas emissions emitted by the EU-28 in 2017 were a by-product of the transport sector, with CO_2 emissions being 2.2 % higher compared to the previous year [2]. Since the transport sector is a significant contributor to an undesirable atmospheric chemistry, the EU has classified this segment as a key factor for its program, the 'Innovation Union' [3].

In recent years, progress has been made regarding engine efficiencies, as well as power output per capacity in a concept known in the automotive industry, as 'downsizing' [4]. Despite such innovations, it is well known that fuel consumption, and the implicit emission of greenhouse gases of a moving object is considerably influenced by its mass. Therefore, structural light-weighting is a key strategy for improving efficiency in transport systems. In this context, substituting half of the steel structural parts of a motor vehicle with carbon fibre-reinforced composites, could potentially lower the fuel consumption by as much as 0.38 l/100 km (corresponding to ~0.89 kg CO_2/100 km) in the use phase [5]. Adding to the fact that the average lifespan of a car is 200,000 km [6], and that almost 92 million cars were produced worldwide in 2019 [7], this would reduce the CO_2 emissions of the cars produced in a single year by more than 160 million tonnes. Notwithstanding this, polymer composites present an important opportunity for weight reductions not just for road-based transport, but across all other transport sectors (sea, rail, air) [8], having desirable properties such as: low density, good specific stiffness and strength, as well as reduced susceptibility to corrosion [9].

Alongside such potential advantages, composites exhibit complex failure mechanisms, attributed to: a multiphase makeup, anisotropy and heterogeneity. Failure of laminated composites, in tension for example, is the result of a series of complex events such as: fibre-matrix debonding, interfacial sliding, matrix cracking, delamination, fibre-fracture and fibre pull-out, followed by catastrophic material failure [10]. In conjunction with the coupling that may arise between each of these mechanisms, forecasting the failure processes, and hence implicit strength, is therefore difficult. As a result, many applications are over-engineered, thereby encompassing a weight penalty – which somewhat compromises the rationale for designing structures with lighter materials in the first place [11].

Since the beginning of the modern age of composites (~1960's), a phenomenological approach has commonly been used to model and predict the failure behaviour. Over the years, coupon-based experiments have led to a wide variety of failure models and theories, which only partly account for the mechanisms which may govern failure [12]. This inhibits the ability to develop new materials with superior performance and to guide the structural design process. At the heart of this is a lack of a sufficient mechanistic understanding of, and accompanying models for, the key damage and failure processes. A significant step forward has arguably been achieved in recent years by the use of X-ray Computed Tomography (CT) to identify detailed chronologies of damage events down to the fibre-level, in three dimensions (3D), within the bulk of real materials under load [13].

More specifically, Synchrotron Radiation Computed Tomography (SRCT) has emerged as a powerful tool in Materials Science in the endeavour to analyse failure processes in fibre-reinforced composites. Various studies have been published such as those performed by Wright, Scott, Moffat, Rosini and co-workers [10, 13-15], in which image acquisition was carried out *in situ*. Commonly, *in situ* SRCT setups have required the loading test to be interrupted for imaging purposes, a technique identifiable as 'hold-at-load'. This procedure may introduce undesired time-based artefacts that would not arise in a conventional continuous loading [16-19].

In parallel, two-dimensional (2D) Digital Image Correlation (DIC) has emerged as an important advance in experimental mechanics of both composite [20] and non-composite materials [21]. It is widely demonstrated that sensitive and robust correlation algorithms may be used track stochastic surface contrast patterns on samples such that high-resolution strain maps may be obtained under simple white light illumination of specimen/object surfaces [22]. The 3D extension of DIC is Digital Volume Correlation (DVC), applying the sample principle to 3D datasets.

A logical experimental advance is, therefore, the combination of CT with DVC. An appealing advantage of this technique is that the same volume that is subjected to detailed *in situ* damage visualisation, can also be strain mapped. To date however, no research has investigated bulk fibre-matrix strain responses along the filament direction in aligned Fibre-Reinforced Polymers (FRPs) via DVC, attributable to a simple lack of stochastic imaging contrast parallel to the fibres.

The current project takes advantage of the latest developments in CT techniques, in particular the use of setups capable of fast acquisition times by which the hold-at-load artefacts can be mitigated during *in situ* testing. Tracking internal displacements (and hence strain fields) with milistrain accuracy is addressed, where the matrix material has been doped with sparse populations sub-micrometre particles to act as displacement trackers (*i.e.* fiducial markers). As such, this project sets to establish a first-of-kind quantitative visualisation of fibre-dominated damage formation in FRP materials, and more specifically, the processes associated with incipient fibre breaks accumulation in Carbon-Fibre Reinforced Polymers (CFRPs) under tensile loading. A

compromise of using such modified materials, is of course, their departure from a standard (commercial) microstructure. Acknowledging this, the artificially introduced fiducials have been chosen such that any potential mechanical property detriment was minimized.

Whilst representing only one of the underlying FRP failure mechanisms, fibre breaks typically play a key role in limiting tensile strength and must, therefore, be characterised if a comprehensive understanding of composite failure is to be achieved and captured in performance simulations. Combined with the work of project collaborators within the Marie Skłodowska-Curie ITN 'FiBreMoD', this aims to contribute to the design and performance optimization of composite parts, as well as competitiveness with other material families in alignment with the Union's Horizon 2020 strategy [23].

1.2 Project motivation and objectives

The underlying objective of this project is to gain a unique quantitative understanding of the fibre break processes in unidirectional CFRPs subjected to uniaxial quasi-static tensile loading to enhance the predictive capability for these materials, and subsequently support the optimization of realiable engineering designs.

In greater detail, the specific objectives are as follows:

I. Develop novel carbon-fibre reinforced epoxy laminates, tailored for the application of Digital Volume Correlation and Computed Tomography to experimental mechanics analyses of these materials.
    - Establish a method for doping such materials with a range of possible particles as fiducial markers.
    - Identify the combination of particle composition, size and concentration that yields the most favourable compromise between contrast in CT images and the ability to obtain a homogeneous distribution over useful imaging volumes with a sufficiently fine particle distribution for local DVC analyses.
    - Demonstrate the extent to which the macro- and micromechanical tensile responses of the newly developed CFRP are consistent with standard production materials, and hence evidence suitability as a model system for the subsequent mechanistic investigations.

II. Demonstrate and validate high-resolution three-dimensional experimental strain measurement capabilities using Digital Volume Correlation on the doped CFRP, via through-thickness strain analysis under a state of pure bending.

- Design a novel experiment that permits CT data to be acquired from a simple standard specimen subjected to a four-point flexural test, which results in a linear strain distribution through the beam thickness.
- Conduct noise and sensitivity tests to establish if the measured specimen translation parallel to the fibre direction is in line with the applied displacements, obviating a key problem in applying DVC to such uniformly aligned microstructures.
- Parametrically explore the effect of DVC parameters (*e.g.* sub-set size) on the high-resolution, fibre-level strain distributions and compare the results against the classical beam theory to determine whether the DVC outputs agree with the analytical solution.

III. Perform fibre-direction strain measurements in a composite ply under quasi-static tensile loading using Digital Volume Correlation and *in situ* SRCT.
    - Obtain and compare measurements of the recovery length from multiple individual fibre breaks.
    - Investigate whether the recovery lengths from individual fibre breaks increase with increasing applied load.
    - Determine whether the recovery lengths increase with the number of breaks within a cluster, and compare these measurements with those obtained from individual fibre breaks.

1.3 Thesis structure

The content of this thesis is based on three first-author peer-reviewed journal papers, which were published during the course of the research programme. These papers are found here as **Chapters 4** to **6**. As papers, they are essentially self-contained, with some overlap in content, mainly within the introduction and methods sections of these chapters. The structure of the thesis is summarized as follows:

- **Chapters 1**, **2** and **3** are essentially conventional, providing general introduction to the work, literature review and overall materials/methods used.
- **Chapter 4** was published in the Journal of Composite Materials. It presents the development of novel Carbon-Fibre Reinforced Polymer laminates, tailored for the application of Digital Volume Correlation and Computed Tomography to experimental mechanics analyses of these materials.
- **Chapter 5** was also published in the Journal of Composite Materials, and exploits the material developed in **Chapter 4**. It presents an experimental demonstration and validation of high-resolution three-dimensional experimental strain measurement using Digital Volume Correlation on Carbon-Fibre Reinforced Polymers, via through-thickness strain analysis under a state of pure bending.

- **Chapter 6** was published in Composites Part A, and builds on **Chapters 4** and **5**. It presents the first application of Digital Volume Correlation, in concert with in situ Synchrotron Radiation Computed Tomography, to Carbon-Fibre Reinforced Polymers under quasi-static tensile loading, focusing on the longitudinal strain fields surrounding fibre break sites.
- **Chapter 7** provides an overall summary and conclusions of the thesis. It also suggests future work from an overall experimental perspective, and addresses refinements to the materials and main techniques used (*i.e.* Computed Tomography and Digital Volume Correlation).

1.4 List of publications

This project has resulted in a number of journal and international conference papers as listed in the following two sub-sections.

1.4.1 Journal papers

- E. Schöberl, C. Breite, S. Rosini, Y. Swolfs, M. N. Mavrogordato, I. Sinclair and S. M. Spearing, "A novel particle-filled carbon-fibre reinforced polymer model composite tailored for the application of digital volume correlation and computed tomography," *Journal of Composite Materials,* in press, 2020. (https://doi.org/10.1177/0021998320966388).
- E. Schöberl, M. N. Mavrogordato, I. Sinclair and S. M. Spearing, "Fibre-direction strain measurement in a composite ply under pure bending using digital volume correlation and micro-focus computed tomography," *Journal of Composite Materials,* vol. 54, no. 14, pp. 1889-1911, 2020. (https://doi.org/10.1177/0021998320918648).
- E. Schöberl, C. Breite, A. Melnikov, Y. Swolfs, M. N. Mavrogordato, I. Sinclair and S. M. Spearing, "Fibre-direction strain measurement in a composite ply under quasi-static tensile loading using digital volume correlation and in situ synchrotron radiation computed tomography," *Composites Part A,* vol. 137, no. 105935, 2020. (https://doi.org/10.1016/j.compositesa.2020.105935).

1.4.2 Conference papers

- E. Schöberl, M. N. Mavrogordato, I. Sinclair and S. M. Spearing, "The mapping of damage behaviour in a unidirectional composite subjected to uniaxial loading using digital volume correlation," in *The 12th International Conference on Composite Science and Technology*, Sorrento, Italy, 8-10 May 2019.
- E. Schöberl, C. Breite, A. Melnikov, Y. Swolfs, M. N. Mavrogordato, I. Sinclair and S. M. Spearing, "Mapping strains and fibre fracture in carbon fibre composites using in situ digital volume correlation,"

in *The 22nd International Conference on Composites Materials*, Melbourne, Australia, 11-16 August 2019.

1.5 References

[1] United Nations, “Paris Agreement,” New York City, NY, USA, 2015.

[2] European Environment Agency, “Greenhouse gas emissions from transport in Europe – Indicator assessment,” [Online]. Available: https://www.eea.europa.eu/data-and-maps/indicators/transport-emissions-of-greenhouse-gases/transport-emissions-of-greenhouse-gases-12. [Accessed 21 10 2020].

[3] European Commission, “Europe 2020 Flagship Initiative – Innovation Union,” Publications Office of the European Union, Luxembourg, Luxemburg, 2011.

[4] Automotive iQ, “Engine downsizing and the future,” [Online]. Available: https://www.automotive-iq.com/powertrain/articles/engine-downsizing-and-the-future. [Accessed 21 10 2020].

[5] K. Van Acker, I. Verpoest, J. De Moor, J.-R. Duflou and W. Dewulf, “Lightweight materials for the automotive: Environmental impact analysis of the use of composites,” in *The 3rd International Seminar on Society & Materials*, Freiberg, Germany, 2009.

[6] C. Dun, G. Horton and S. Kollamthodi, "Improvements to the definition of lifetime mileage of light duty vehicles," Ricardo-AEA, Harwell Oxford, Didcot, United Kingdom, 2015.

[7] Statista, "Estimated worldwide automobile production from 2000 to 2019," [Online]. Available: https://www.statista.com/statistics/262747/worldwide-automobile-production-since-2000/. [Accessed 21 10 2020].

[8] N. M. Aly, “A review on utilization of textile composites in transportation towards sustainability,” in *17th World Textile Conference*, Corfu, Greece, 2017.

[9] C. Zhang, D. Zheng, G.-L. Song, Y. Guo, M. Liu and H. Kia, “Influence of microstructure of carbon fibre reinforced polymer on the metal in contact,” *Journal of Materials Research and Technology,* vol. 9, no. 1, pp. 560-573, 2020.

[10] P. Wright, A. J. Moffat, I. Sinclair and S. M. Spearing, "High resolution tomographic imaging and modelling of notch tip damage in a laminated composite," *Composites Science and Technology,* vol. 70, no. 10, pp. 1444-1452, 2010.

[11] MachineDesign, "How to avoid overengineering composite parts," [Online]. Available: https://www.machinedesign.com/3d-printing-cad/article/21832899/how-to-avoid-overengineering-composite-parts. [Accessed 21 10 2020].

[12] A. S. Kaddour, M. J. Hinton, P. A. Smith and S. Li, "The background to the third world-wide failure exercise," *Journal of Composite Materials,* vol. 47, no. 20-21, pp. 2417-2426, 2013.

[13] A. E. Scott, M. N. Mavrogordato, P. Wright, I. Sinclair and S. M. Spearing, "In situ fibre fracture measurement in carbon-epoxy laminates using high resolution computed tomography," *Composites Science and Technology,* vol. 71, no. 12, pp. 1471-1477, 2011.

[14] A. J. Moffat, P. Wright, J.-Y. Buffiere, I. Sinclair and S. M. Spearing, "Micromechanisms of damage in 0° splits in a [90/0]s composite material using synchrotron radiation computed tomography," *Scripta Materialia,* vol. 59, no. 10, pp. 1043-1046, 2008.

[15] S. Rosini, M. N. Mavrogordato, O. Egorova, E. S. Matthews, S. E. Jackson, S. M. Spearing and I. Sinclair, "In situ statistical measurement of local morphology in carbon-epoxy composites using synchrotron X-ray computed tomography," *Composites Part A,* vol. 125, pp. 1-14, 2019.

[16] J. M. Lifshitz and A. Rotem, "Time-dependent longitudinal strength of unidirectional fibrous composites," *Fibre Science and Technology,* vol. 3, no. 1, pp. 1-20, 1970.

[17] S. Blassiau, A. R. Bunsell and A. Thionnet, "Damage accumulation processes and life prediction in unidirectional composites," *Proceedings of the Royal Society A,* vol. 463, no. 2080, pp. 1135-1152, 2007.

[18] A. R. Bunsell and A. Thionnet, "Life prediction for carbon fibre filament wound composite structures," *Philosophical Magazine,* vol. 90, no. 31-32, pp. 4129-4146, 2010.

[19] A. R. Bunsell and A. Thionnet, "Failure processes governing long term reliability of carbon fibre composites structures," *Composites and Nanostructures,* vol. 7, no. 4, pp. 216-224, 2015.

[20] L. P. Canal, C. González, J. M. Molina-Aldareguía, J. Segurado and J. LLorca, “Application of digital image correlation at the microscale in fiber-reinforced composites,” *Composites Part A,* vol. 43, no. 10, pp. 1630-1638, 2012.

[21] V.-T. Nguyen, S.-J. Kwon, O.-H. Kwon and Y.-S. Kim, “Mechanical properties identification of sheet metals by 2D-digital image correlation method,” *Procedia Engineering,* vol. 184, pp. 381-389, 2017.

[22] B. Pan, K. Qian, H. Xie and A. Asundi, “Two-dimensional digital image correlation for in-plane displacement and strain measurement: A review,” *Measurement Science and Technology,* vol. 20, no. 6, pp. 1-17, 2009.

[23] European Commission, “Horizon 2020 – Sections,” [Online]. Available: https://ec.europa.eu/programmes/horizon2020/h2020-sections. [Accessed 21 10 2020].

Chapter 2 Literature review

This chapter focuses on the fundamental background relevant to the research performed. The chapter first reviews the relevant literature regarding the failure of fibre-reinforced composites in tension, with an emphasis on the fibre break process. A review of previous studies employing Computed Tomography to study damage in tensile loaded CFRPs is provided, in conjunction with the gaps identified in the literature that this project aims to fill. Next, the basic principles of X-rays are introduced. The operating principles of computed tomography are then presented, together with the key differences between Micro-focus Computed Tomography and Synchrotron Radiation Computed Tomography. Finally, the chapter focuses on the principles of Digital Volume Correlation in the context of other optical methods for measuring deformation. The impact of various influential correlation parameters is also summarized, followed by relevant applications to fibre-reinforced polymers.

2.1 Introduction

Composite materials exhibit a myriad of complex failure mechanisms, occurring over multiple length scales and involving various interacting damage processes [1, 2]. The discrepancies between the properties of the constituent phases, the heterogeneous microstructure of the material, and the directionality of the reinforcement material not only introduces anisotropy in overall properties, but also complexities in geometrical features at the micromechanical level (*e.g.* clustering of fibre breaks in tension [3]). The presence of interfaces, between the reinforcing-fibres and the matrix as well as between the plies in a laminate, contribute to the stress/strain transfer and provide an environment for multiple damage mechanisms to occur [2, 4]. Subsequently, predicting damage and failure in composites is not easy, with any robust model relaying on the accuracy of capturing of these aspects [5]. Furthermore, despite the fact there has been a continuous stream of work since the ~1960's on the investigation of the failure of composite materials, research focusing on theoretical content outweighed that with a major experimental emphasis [6].

In recent years, high-resolution X-ray Computed Tomography has provided an opportunity to investigate the internal architecture of materials [1], with a view to understanding composite behaviour down to the level of individual fibres [3]. When the naturally occurring texture of some materials was introduced into context, further applications of the volumetric data became evident. Digital Volume Correlation is essentially an extension of the in-plane domain or Digital Image Correlation, thereby dealing with volumetric rather planar imaging. Correlation procedures are implemented in DVC to track the displacements of the sub-sets for an appropriate material texture, *i.e.* some form of speckle-like pattern. As such, 3D displacement and strain mapping may be possible for specimens between undeformed and deformed states [7].

2.2 Failure of continuous fibre-reinforced composites in tension

2.2.1 Fibre strength statistics

Carbon-fibres are generally assumed to exhibit a linear-elastic, brittle, stress-strain behaviour under tension [8-10]. While, to a certain degree, this is a valid approximation, it is not strictly true, as carbon-fibres have been shown to exhibit non-linear behaviour prior to the onset of failure. More specifically, studies of the tensile stress-strain behaviour have revealed a form of non-linear elasticity. This phenomenon, observed for the first time by Curtis *et al.* [11] in polyacrylonitrile-based (PAN) carbon-filaments, is known as 'strain stiffening'. It describes an increase in modulus with increasing strain [10, 12, 13], on the order of 20 % for every 1 % of strain increment [14]; nevertheless, the assumption of linear-elasticity is generally found to provide reasonable predictions for the constitutive response in the fibre direction.

Griffith *et al.* [15] suggested that the presence of discontinuities such as microstructural flaws, affects the strength of brittle materials. Furthermore, a size-dependency was reported, whereby specimens with small dimensions (*e.g.* wires or fibres) might be expected to exhibit greater strengths than their larger counterparts, as for the former a restriction exists, which essentially limits the size of the flaw itself. Given, however, that the structure of carbon-fibres is not entirely crystalline (**Figure 2-1**), but is rather composed of a combination of non-crystalline and graphite regions (the stable crystalline form of carbon at ambient conditions) [16], in addition to exhibiting natural surface flaws (**Figure 2-2**) [17], the strength of filaments cannot be reliably expressed as a single average value [14]. These flaws could have stemmed from the precursor material and/or have been introduced during the manufacturing process (*e.g.* carbonisation/graphitisation stages), implying the strength of a fibre is governed by distribution of such flaws, most likely the largest flaw along the length under load [18].

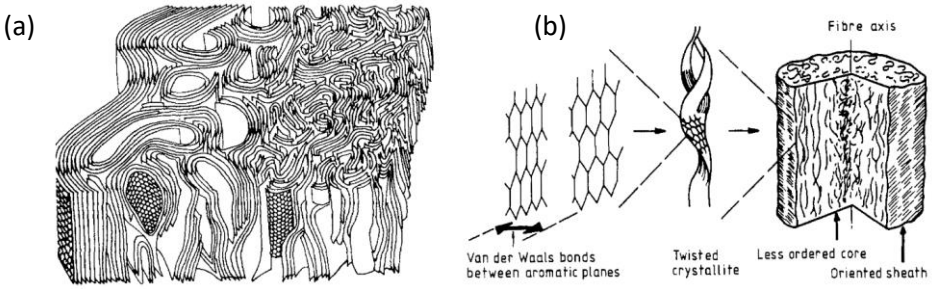

Figure 2-1 – Three-dimensional schematic model: (a) representative of a high modulus PAN-based carbon-fibre structure [16]*, (b) orientation of aromatic planes with respect to the fibre direction* [19]*.*

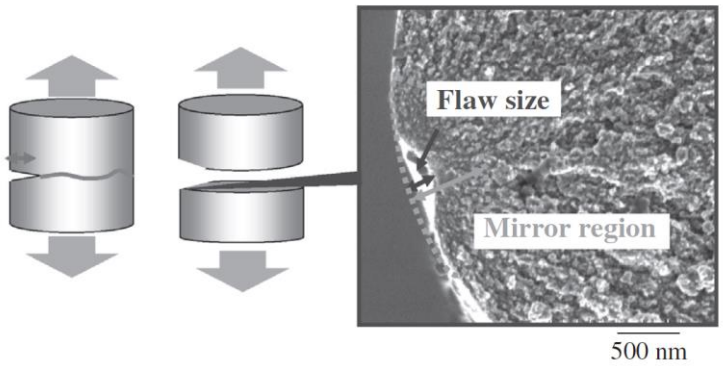

Figure 2-2 – Scanning electron microscopy image illustrating the tensile fracture surface of a T800G carbon-fibre, which failed due to natural flaws [17]*.*

This understanding of the strength-controlling flaw population leads to the modelling assumption that a fibre can be divided into multiple segments or 'links', each encompassing a flaw with a different effect on the local strength. As shown in **Figure 2-3**, the failure of one of these links, leads to the failure of the entire fibre. This model is referred to as the 'Chain of links' model [18], through which carbon-fibres (and glass-fibres) are

characterized by a 'weakest-link' behavior, implying that they fracture as soon as the weakest link experiences an overload above its local strength [14]. Therefore, the failure probability of the fibres is directly related to the presence of weak links (or flaws), whereby shorter fibres are expected to have a lower probability of containing such weak links, and are more likely to exhibit higher strength [14, 18]. Similarly, Tanaka *et al.* [17] have shown that the probability of finding flaws of a given critical size decreased as the gauge length decreases (**Figure 2-4**), whereby a higher fibre strength was reported in conjunction with smaller flaw sizes.

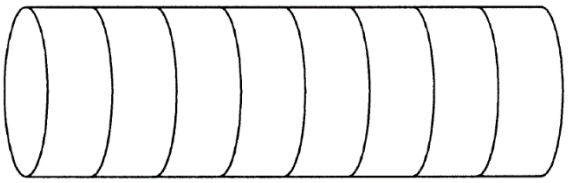

(a) Fibre exhibiting chain of links.

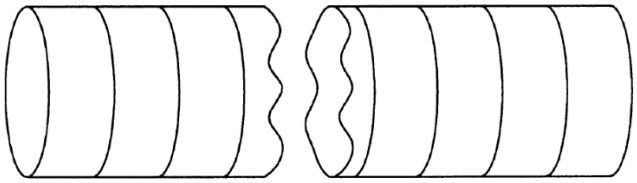

(b) Fibre with a failed link.

Figure 2-3 – Schematic representation of the 'Chain of links' model [18].

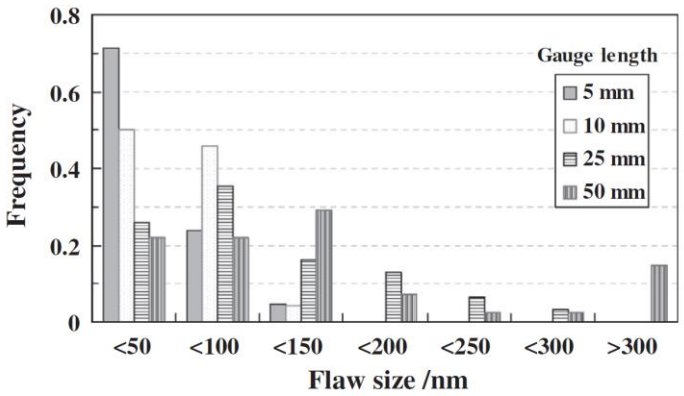

Figure 2-4 – Histogram illustrating the natural flaw size representative of a T800G carbon-fibre at various gauge lengths (between 5 mm and 50 mm) [17].

As such, for single fibres randomly sampled from a tow, and uniaxially loaded in tension, their strength is typically presumed to follow a Weibull distribution [20], which is a statistical function that describes the key

feature of their characteristic 'weakest-link' behaviour [14]. The standard, unimodal, Weibull probability distribution function *'P'* for fibre strength is given by [14]:

$$P(\sigma_f) = 1 - exp\left(-\left(\frac{L}{L_0}\right)\left(\frac{\sigma_f}{\sigma_0}\right)^m\right)$$

Equation 2-1

where *'L'* is the characteristic gauge length, *'L_0'* is the reference gauge length (generally, at which fibre tensile test results are available), *'σ_f'* is the fibre strength, *'σ_0'* is the characteristic strength (stress) at which 63.2 %, *i.e.* $(1 - e^{-1})$ %, of the fibres fail (also known as the scale parameter) and *'m'* is the Weibull modulus (or the shape parameter, describing the dispersion of fibre strengths across a tow) [20], [21]. For carbon-fibres, the Weibull modulus *'m'* typically ranges from 3 to 7, while the scale parameter *'σ_0'* ranges from 2500 to 6500 MPa [20], with these two parameters being typically calculated from single fibre tensile tests at gauge lengths *'L_0'* ranging between 10 mm and 50 mm [14]. For T700 carbon-fibres, such as the ones used in this project, Mesquita *et al.* [10] have reported a Weibull modulus *'m'* on the order of 3.94 and a scale parameter *'σ_0'* on the order of 4.71 GPa, at a gauge length *'L_0'* of 12 mm, across more than 200 single fibre tensile tests. The characteristic strength *'σ_0^*'* may be extrapolated from *'σ_0'* to different characteristic gauge lengths *'L'* through the following relationship [14]:

$$\sigma_0^* = \sigma_0\left(\frac{L_0}{L}\right)^{\frac{1}{m}}$$

Equation 2-2

As shown in **Figure 2-5**, the scatter around a mean value is given by the Weibull modulus, whereby small values of *'m'* indicate a wide distribution (or large variability in fibre strength) [14]. When embedded in a composite, this will lead to a certain number of particularly weak fibres, that will be distributed among the remaining stronger fibres. Subsequently, this may imply that more of the weaker fibres will break at a lower applied stress, while at the same time, the stronger fibres may prevent the catastrophic failure of the composite (*i.e.* composite will apparently sustain more damage) [10, 22].

Likewise, a small Weibull modulus may be expected to reduce the likelihood of cluster formation and growth, or at least stall the formation of closely-packed clusters, and instead promote the emergence of dispersed breaks, and/or diffuse clusters (*i.e.* fibres that break may be very much weaker than neighbours, therefore, neighbours less likely to break). At an early onset of damage, this diminishes the ability of any one cluster to grow in an unstable manner, subduing cluster-driven failure. That is because the presence of stronger fibres

within the bundle impedes cluster growth, making it less likely to propagate (*i.e.* a relatively weak fibre will break at low loads, but the general body of stronger fibres surrounding remains intact) [22]. Consequently, composite failure may result from the coalescence of small clusters and dispersed breaks, notwithstanding that after a certain threshold of initially dispersed fracture events, cluster growth can occur [22]. In contrast, a large Weibull modulus (or low variability in fibre strengths) may be expected to advance the formation of clusters, whereby one of these clusters can become large enough to propagate in an unstable manner, leading to the catastrophic failure of the composite [22].

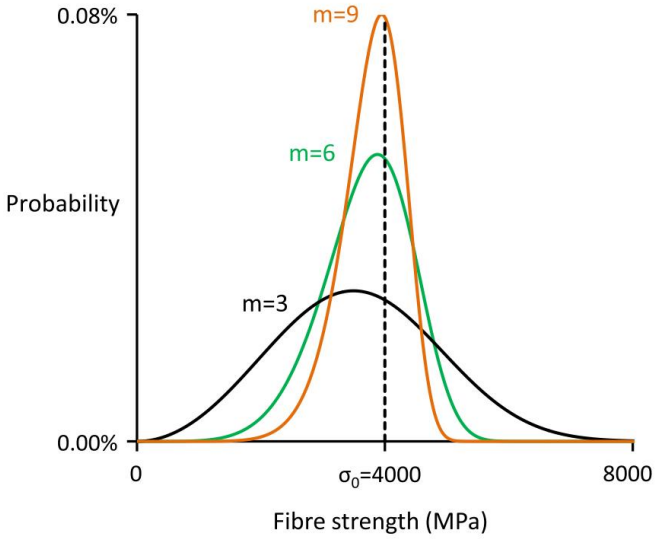

Figure 2-5 – Weibull distribution example, illustrating the decrease in fibre strength scatter with increasing Weibull modulus [14].

It should be noted that the Weibull distribution detailed above is a relatively simple model to describe the 'weakest-link' behaviour. As such it assumes the presence of a single flaw population [14]. This, however, may not be entirely accurate as experimental evidence of different flaw types within the same kind of fibre are reported in the literature [23], with the most frequently reported being sub-micrometre sized ferrous/mineral contaminant inclusions, surface pits and surface cracks [24, 25]. Due to variations in processing and handling (*e.g.* the occurrence of a temperature gradient and/or the outer fibres being subjected to more friction and abrasion during processing) these flaws might not be randomly distributed across the fibres in a given tow [14]. Therefore, to account for multiple strength-defining flaw populations, the bimodal Weibull distribution is sometimes implemented [14]. In this regard, Watanabe *et al.* [23] have reported the following: (a) the Weibull modulus parameter for short gauge lengths (high-strength range), on the order of 1 mm to 10 mm, was higher than that for long gauge lengths (low-strength range), suggesting that the tensile strength of carbon-fibres was governed by two different flaw populations, corresponding to the short and long gauge lengths, respectively, and (b) the composite tensile strength predicted on the basis of the bimodal Weibull

distribution was in better agreement with the experimental data, compared to that predicted by the unimodal Weibull distribution.

While beyond the scope of the present project, it is valuable to note the existence of other distributions as well. The power-law accelerated Weibull distribution (PLAW) adds an exponent *'α'* to the ratio $^{L}/_{L_0}$ in the original model described by **Equation 2.1** [14]. The exponent is a correction factor satisfying the condition $0 < \alpha \leq 1$, and is determined from single fibre tensile tests at various gauge lengths. The factor is typically unique to a given fibre type, and in conjunction with the Weibull modulus across the tow (higher variability), it reflects the fibre-to-fibre variations along a tow (lower variability) [20]. If *'α'* equals to unity, the power law-accelerated Weibull distribution reduces to the simple unimodal Weibull distribution [14].

Another distribution is the so-called Weibull of Weibulls (WoW), proposed by Curtin [26]. This model presumes that the strength along a given fibre is governed by the standard Weibull distribution, whereby a characteristic strength may be obtained for each fibre at a certain length *'L'*. Then, the characteristic strength of each fibre is assumed to be different, which in turn also follows a Weibull distribution. However, due to its intrinsic complexity, the WoW model has not been widely implemented in contemporary strength models [14].

2.2.2 The fibre-matrix interface

2.2.2.1 The matrix phase and interfacial properties

In fibre-reinforced polymers, the matrix (or continuous) phase performs several essential functions. First it acts as a binder, fastening the fibres together and preserving the overall desired orientation of the reinforcing phase. Secondly, it forms a barrier protecting the fibre surfaces from abrasion and/or environmental damage [27]. Thirdly, it separates the fibres and regulates crack initiation and propagation [28]. Additionally, in case of fibre fracture, it transfers the stress (or strain) back onto the broken fibre, as well as between it and the neighbouring intact fibres [14]. The fibre-matrix interface, *i.e.* the boundary between the continuous and reinforcing phase, plays a key role in the efficiency of this transfer mechanism, which occurs predominantly through shear [29-34]. As such, the mechanical behaviour of fibre-reinforced polymers depends to a large extent, not just on the properties of the fibres and matrix, but also on the properties of the interface [14, 35].

The interfacial shear strength (IFSS) is a quantitative parameter typically used to characterise the stress transfer from the matrix to the fibre. The IFSS is highest (typically at the expense of toughness) provided the bonding between the matrix and the fibre is good. In contrast, if adhesion is limited, the load-bearing capacity of the composite may be expected to be reduced [35-39]. In this context, carbon-fibres generally undergo a partial oxidation treatment [40] and fibre sizing [41] during manufacture. The former process removes a defect laden friable layer that is not well adhered to the fibre surface, in addition to providing organic reactive groups

on the fibre surface that promote bonding to the (organic) matrix [42, 43]. The latter process is essentially the application of a polymer coating, similar to, or at least compatible with the matrix to be used in the composite (*e.g.* thermosetting resins), onto the fibre surface. This coating primarily protects the fibre surface during subsequent processing, but also acts as coupling agent, promoting adhesion to the matrix, thereby creating an interface with enhanced mechanical properties [39, 41, 44].

Various methods can be employed to assess interfacial failure. As shown in **Figure 2-6**, common methods include pull-out, fragmentation, microcompression and droplet microtension (or microbond) tests [36]. The pull-out test typically consists of a partially embedded fibre in a clamped block of resin, which is drawn out through the application of an external force [45]. For a very small embedded length (< 1 mm [46]), the peak interfacial shear stress *'τ_p'* is may be computed through the following relationship (Pitkethly and Doble [47]):

$$\tau_p = \frac{F_p}{\pi d L}$$

Equation 2-3

where *'F_p'* is the peak external force applied, *'d'* is the fibre diameter and *'L'* is the embedded length of the fibre in the resin block. A particular issue with this test is that as the load transfer from the matrix to the fibre occurs primarily through shear over a certain transfer length, the shear strength calculated from a fibre-matrix system, in which the embedded length of the fibre is greater than the shear transfer length, would in fact be underestimated. This is because a certain length of the fibre is embedded in the matrix, over which little stress transfer occurs [45, 47]. In contrast, the microcompression test generally produces results which overestimate the interfacial shear strength, due to Poisson expansions and subsequently increased interfacial clamping pressure [36]. Finally, the droplet microtension test yields results with significant scatter due to the difficulty in controlling the positioning of the drop in the shearing vice (and the resultant variation of matrix microcracking), as well as uncertainty in the fibre perimeter measurement [46, 48].

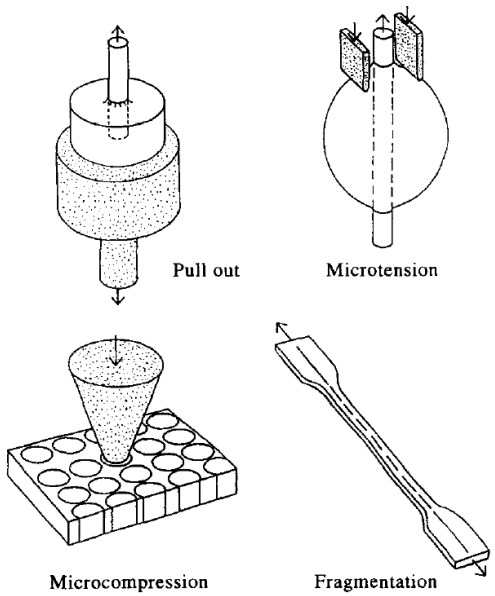

Figure 2-6 – The four methods typically used to measure the interfacial shear strength [36].

As noted above, an alternative method to assess the interfacial failure is the fragmentation test, which is shown schematically in **Figure 2-7**. This is arguably the most popular, due to the inherent simplicity in specimen preparation, relative ease of testing and ample amount of information gained in terms of microstructural damage processes [35, 36, 49]. Therefore, it is also commonly used for assessing the effect of various surface treatments on the interfacial shear strength of both glass- and carbon-fibres [37, 39, 42, 43, 49, 50]. In its most basic form, an external load is applied to a tensile dumbbell specimen (consisting of a single fibre embedded in a matrix), and in doing so, normal stress is transferred from the matrix onto the fibre through interfacial shear stress. After a certain threshold, the tensile stress will exceed the tensile strength of the fibre, causing it to fracture. As the load is further increased, the fibre continues to fracture into shorter fragments, until a saturation state is reached, dominated by matrix plastic yielding together with fibre-matrix interfacial debonding, whereby it becomes too short to break [35, 49].

At the fragment ends of a fibre, normal stress is absent, and stress transfer occurs through shear only (*i.e.* shear stress reaches its maximum). Away from the break plane in the longitudinal direction, the normal stress is recovered, while the shear stress reduces to zero [51]. The fragment with the shortest length, which cannot fracture further upon the application of increased load, is known as the 'critical length' or *'l_c'* [35, 49] – see **Figure 2-7**. The critical length may, therefore, be viewed as the length of fibre over which the shear stress transferred from the matrix to the fibre generates a normal stress equal to the tensile strength of the fibre, *i.e.* the minimum fibre length for which the ultimate strength of the fibre can be achieved [51].

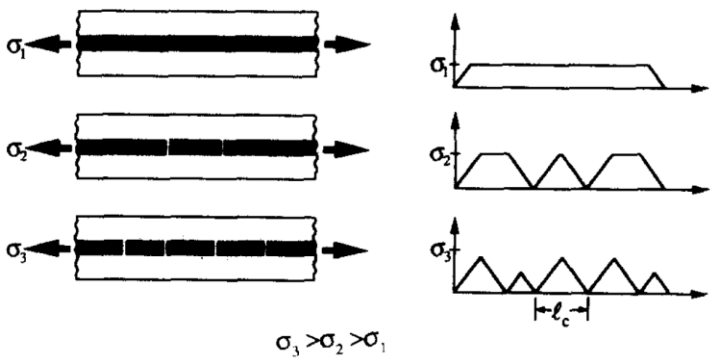

Figure 2-7 – Schematic representation of the fragmentation process in a single fibre composite subjected to uniaxial tension [35].

Due to the flaw-driven statistical nature of the fibre strength (see **Section 2.2.1**), the fibres will not break in fragments with equal lengths, but rather a wide range of fragment lengths is obtained [49]. The average interfacial shear strength *'τ_{ave}'* may be estimated through the Kelly-Tyson perfect-plasticity (or constant interfacial shear stress) model [52]:

$$\tau_{ave} = \frac{\sigma_f^* d}{2 l_c}$$

Equation 2-4

where *'σ_f^*'* is the tensile strength of the fibre at the critical length and *'d'* is the fibre diameter, respectively. In turn, the critical fibre length may be expressed as $l_c \approx {}^4/_3\, l_{ave}$, where *'$l_{ave}$'* is the average fragment length (Ohsawa *et al.* [53]).

A key limitation of this method is the fact that tests are conventionally performed on composites with single fibres [35, 49], or more rarely on multi-fibre composites, however, with a limited number of fibres positioned at predefined inter-fibre spacings [54, 55]. For example, Chohan *et al.* [55] used two different planar arrays, each consisting of seven equally-spaced carbon-fibres, which were aligned in parallel, in a dumbbell-type specimen. As such, key controlling parameters in predicting the tensile failure of practical unidirectional (UD) composites with realistic fibre volume fractions, such as the interfacial shear strength, and particularly the effects on neighbouring fibres (*i.e.* the stress/strain redistribution around fibre breaks, as well the length over which it occurs – see **Section 2.2.2.2**), may not be accurately represented. This has been attributed to large inter-fibre spacings (on the order of 50 μm, for a fibre diameter of ~7 μm), such that stress (or strain) concentration factors (SCFs) in the intact fibres adjacent to the fractured ones were not significant, causing a random distribution of breaks with applied load. Conversely, for very small inter-fibre spacings, whereby the

array of fibres are almost touching each other, SCFs on the order of 1.5 were reported experimentally through Raman spectroscopy, leading to the development of closely spaced/planar fibre fracture sites (**Figure 2-8**), noting that the distance over which fibres were overstressed, was comparable in size to the shear transfer length in the broken fibre [55].

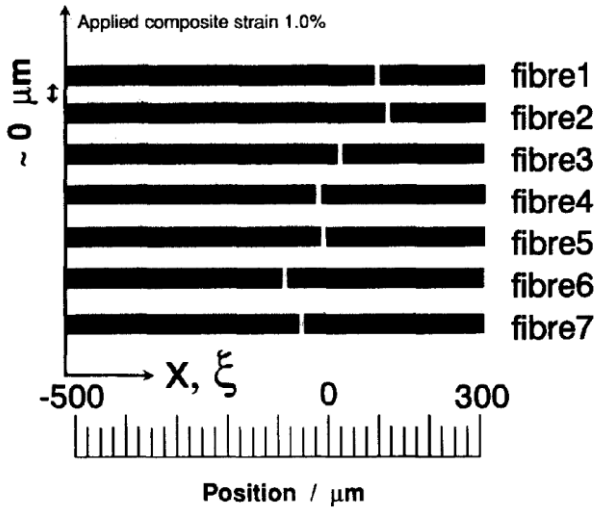

Figure 2-8 – Schematic representation of the closely spaced/planar fractures sites in a microcomposite containing seven equally-spaced carbon-fibres [55].

Notwithstanding their limited representation of realistic structural materials, these tests are useful for fundamental research, such as studying the effects of different surface treatments to rank various material configurations [41, 56, 57]. In this regard, Paipetis *et al.* [41], have shown that a sized system, was distinguished from its unsized counterpart by a consistently higher interfacial shear strength. Concurrently, the interfacial failure of the sized system was predominantly characterized by extensive matrix microcracking. This was reported to be undesirable, especially at very high levels of applied load, as there was no effective bridging mechanism to promote effective stress (or strain) transfer, causing a reduction in the effective shear transfer length, and thus, an ineffective utilization of fibre strength. On the other hand, the weaker interface associated with the unsized system exhibited fibre-matrix interfacial debonding, notwithstanding that the efficiency of the stress transfer was somewhat preserved through radial stresses at the interface, whereby surface roughness/friction acted as a bridging mechanism between the surfaces of the matrix and fibre (**Figure 2-9**).

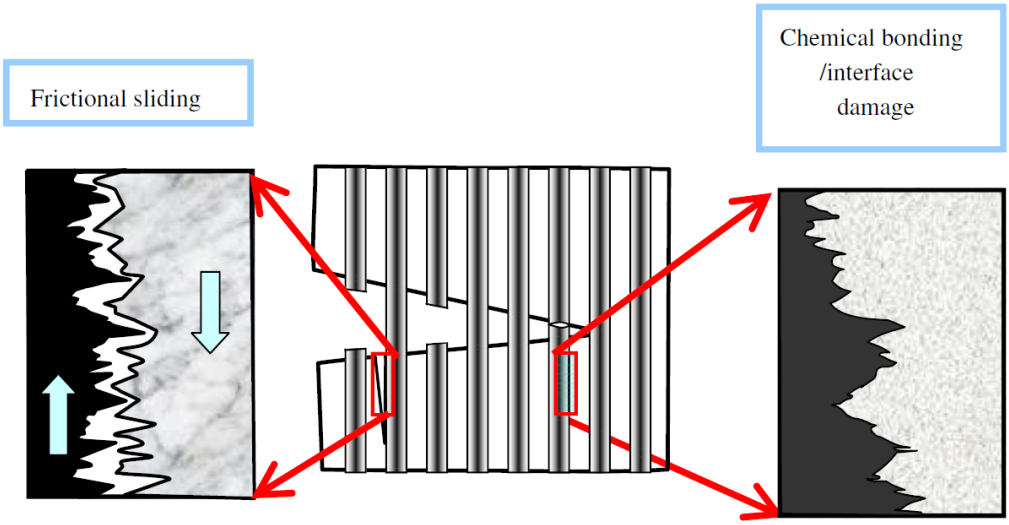

Figure 2-9 – Schematic representation illustrating the different interface bonding mechanisms in a fibre-bridged composite (interface frictional sliding and physical/chemical bonding) [58].

The findings of Paipetis *et al.* [41] agree with those reported by Zhao and co-workers [56, 57], in which a strong dependence of the critical length on the interfacial shear strength was also reported. More precisely, the system with the poorest interfacial adhesion, and implicitly the lowest IFSS, exhibited the longest critical lengths, with the stress concentrations being distributed over a larger gauge volume. The system with the highest interface shear strength was dominated by matrix microcracking in the vicinity of the break, the system with the average interface shear strength presented rough interface debonding accompanied by matrix microcracking, while the system with the lowest interface shear strength was characterized by smooth interface debonding at the ends of the broken fibre and discontinuous debonding at some distance away from the break plane (*i.e.* exhibiting stick-slip behaviour). Matrix microcracks can, however, also grow and extend along the interface if the fibre-matrix interface is weak. Otherwise, they may be expected to form and propagate into the matrix, with the corresponding stress concentration originating at the crack tip; taking note that if intact fibres still exist, which connect the crack faces behind the crack front, they may act as a bridging mechanism (**Figure 2-9**), reducing local stress concentrations [58].

Watanabe *et al.* [59] have indicated that the nano-scale mechanisms of crack initiation and propagation in carbon-fibre/epoxy specimens are governed by two competing mechanisms (fibre-matrix interface debonding and matrix plastic deformation), notwithstanding that the observations were conducted under opening load conditions, and as such it is unknown whether the behaviour may be reproduced in tension. When fibre-matrix interface debonding is dominant, for example in 'thin' resin regions (*i.e.* small inter-fibre spacing, with little or no epoxy between the carbon fibres), they have reported that cracks propagated along the interface, which resulted in cracks with a sharp geometry. The surrounding resin presented little or no deformation, suggesting

that the cracks in the 'thin' epoxy regions propagated in a brittle manner. This damage mode also occurred in locations where the fibre-matrix adhesion was weak, even if the epoxy thickness remained larger. In contrast, when matrix plastic deformation is dominant, for example in 'thick' resin regions, the mechanisms of crack initiation and propagation presented a ductile behaviour. Cracks were observed to initiate at the fibre-matrix interface, however, they did not only propagate along the interface, but also into the matrix with a blunted crack tip, leading to in-resin crack initiation, being accompanied by crazes and/or voids in front of the crack tip; which then merged with the propagating crack. Similarly, multiple cracks were observed to coalesce to form a single larger crack, increasing the local stress/strain concentration.

Overall, the formation of matrix microcracks next to a fibre break may lead to higher local stress concentrations in the surrounding intact fibres than would otherwise occur in the absence of such damage mechanisms (also noted by Swolfs *et al.* [60], see **Section 2.2.4.1**). These stress concentrations are expected to increase with increasing interface shear strength, which in turn may give rise to a higher fibre failure probability, reducing the overall strength of the composite [56, 57]. At the same time, it is worth recognizing that debonding may shift the stress concentration peak away from the fibre break plane, noting that the stress concentration will still be high (and more or less constant, provided the friction is low) over the entire debonded length. As this extends the gauge volume over which there are still significant stress concentrations, it may lead to the development of earlier and larger clusters of breaks. From an energy perspective, fibre-matrix interfacial debonding may act as a dissipating mechanism through which some of the strain energy associated with a fibre break (or matrix crack) is absorbed, arresting the propagating crack, and thereby, reducing the local stress concentrations within the debonded region in the intact fibres adjacent to a crack [56, 57, 61].

Consequently, for an effective utilization of fibre strength, the interfacial adhesion (and the interfacial shear strength) should be optimized rather than maximized – *i.e.* high enough to stimulate effective stress/strain transfer between the constituent phases, yet permitting some damage modes, such as matrix microcracking and interface debonding (to delocalize stress concentrations), and prevent the occurrence of an disproportionately large number of closely spaced/planar fracture sites. Excessive debonding is equally detrimental to the strength of the composite as stress/strain cannot be recovered effectively in the broken fibre, reducing the reinforcing effect of the fibres [41, 56, 57].

2.2.2.2 The fibre break interaction

The stress transfer mechanism reintroduces stress into the broken fibre, and the length over which this process occurs is commonly referred to as the 'ineffective length'. It is worth recognizing that both the 'critical length' and 'ineffective length' have a similar meaning – *i.e.* a region of fibre length that is characterized by an ineffective utilization of fibre strength. The first term is generally reserved for fragmentation tests, while the second refers to twice the fibre length over which 90 % of strain recovery occurs (Rosen [62]) – see **Figure 2-10**. It should be noted that while the definition of the ineffective length is somewhat arbitrary, the measure is critical as it is closely related to the distance over which stress concentrations are of significant magnitude in the surrounding intact fibres [14], as detailed below.

Following the failure of the weakest fibres, the loading on remaining intact fibres increases [58]. On this basis, a 'region of influence' exists, in which the stress/strain in immediately neighbouring filaments is increased [56]. This 'positively affected length' (commonly referred to as 'PAL', Chohan *et al.* [55], Marston *et al.* [63], van den Heuvel *et al.* [64]), or the 'overload length' (Swolfs *et al.* [65]), is given by twice the distance between the break plane and the plane at which the intact fibre has an SCF of 0 %. Therefore, as the broken fibre is not capable of carrying the full load, nearby intact fibres will be subjected to local stress concentrations, but the magnitude decreases with increasing distance from the fibre break (**Figure 2-10**) [65]. The SCFs, defined as the relative change in the average stress (or strain) over the cross-section of a neighbouring fibre (at a given distance from the break plane) due to the occurrence of a fibre break, are expected to increase the probability of fracture in these intact fibres, particularly within the positively affected gauge volume [32, 60, 65-67]. With ongoing loading, this increased failure probability may lead to the evolution of breaks, whereby the initially spatially distributed fibre fracture sites subsequently develop into interacting breaks in the form of clusters [3, 60, 68-72], which in turn impart even greater SCFs in the neighbouring intact fibres, creating a positive feedback and expediting their growth [22]. This then represents the damage state which evolves over a range of load prior to the onset of unstable failure in a quasi-static uniaxial tensile loading. Catastrophic failure of the composite is assumed to occur when sufficient neighbouring fibres are broken, and a cascade effect is eventually triggered – *i.e.* the formation of a 'critical cluster', which grows in an unstable, self-sustaining manner [14, 65, 70, 72].

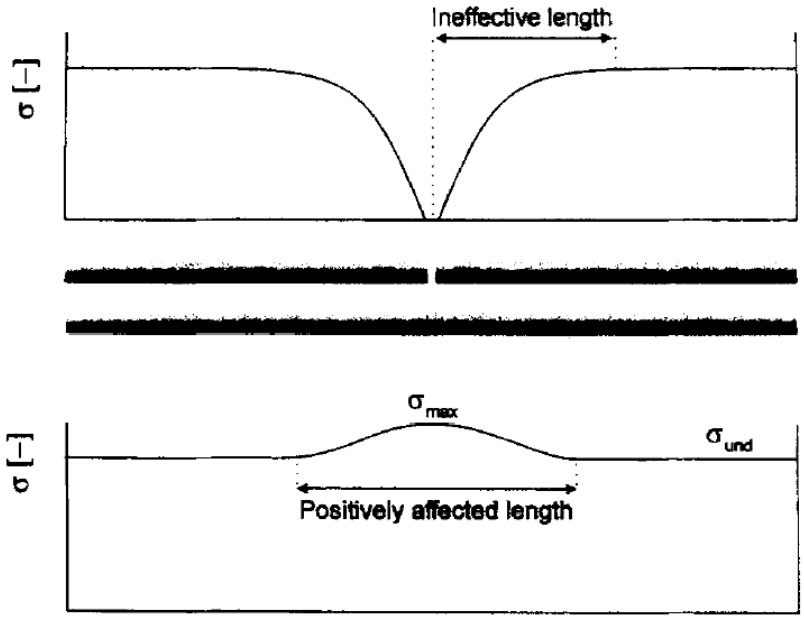

Figure 2-10 – Schematic representation of the 'ineffective length' in the broken fibre and the 'positively affected length' or 'overload length' in the nearest neighbouring fibre, respectively [64].

A two-dimensional fibre break interaction is shown schematically in **Figure 2-11**, with the interpretation performed by Wisnom and Green [73]. For one fibre break, two distinct damage containing regions are generally assumed to appear on each side of the break plane, in which stress/strain is recovered over a distance $l_c/_2$. As detailed in **Section 2.2.2.1**, these regions may be expected to contain damage modes such as matrix plastic yielding, fibre-matrix interfacial debonding and matrix microcracking. If a second fibre is broken, adjacent to the first, within a distance *'l_c'* on either side of the first break, then a cumulative damage region will form along the length of the two breaks, which can be presumed to coalesce. For simplicity, the two breaks can be considered to exist at the same location, and may be treated as a single entity (*i.e.* one cluster). With double the load to be transferred (two, rather than one fibre broken), the simplest approximation under a constant interfacial shear stress model suggests that the ineffective length be doubled, *i.e.* there will be an ineffective length *'l_c'* on each side of the double break. This can be further extended with a third adjacent break joining the cluster, if located within $3l_c/_2$ on either side of the double break, to form one cluster, which encompasses three breaks. This concept can be generalized in three-dimensions, whereby a group of *i* neighbouring fibre breaks with the same cross-section area may be regarded as a singular 'equivalent break', which is scaled by a *Vi* increase in effective cluster radius (or diameter). In reality, however, such interactions are of course more complex, as they are not only dependent on the material properties and local packing geometry, but also on the strain field interaction associated with each break [73]. In this context,

non-coplanar clusters may be characterized by shorter ineffective lengths, as the SCF peak of one break may triggered within the recovery length of the other [74].

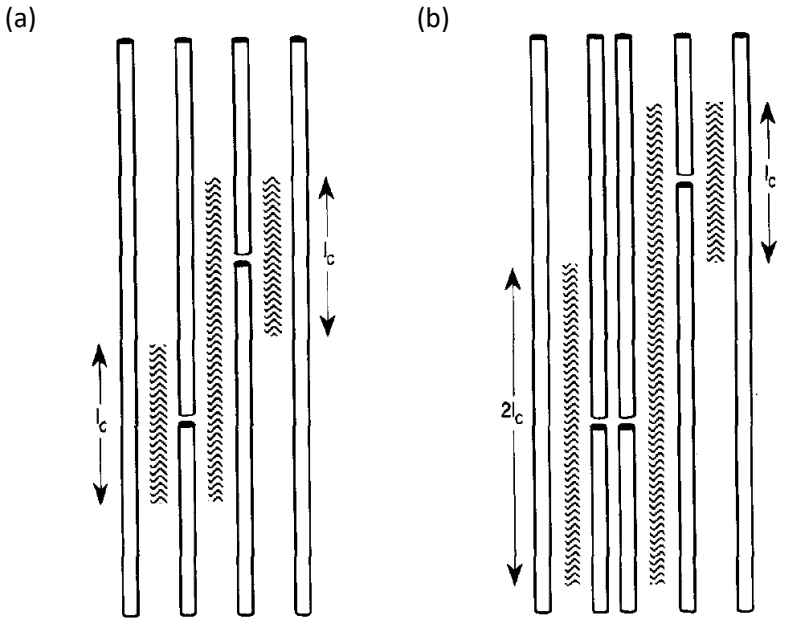

Figure 2-11 – Schematic illustration of interacting breaks in two-dimensions: (a) two single breaks, (b) one double and one single break, respectively [73].

It is worth highlighting that the concept of a 'critical cluster', or more precisely the nature of damage triggering final failure remains hypothetical. That is because even the latest generation SRCT instruments do not permit imaging acquisition to be made at a sufficiently high temporal resolution to capture the final state of the damage prior to the onset of catastrophic failure [71]. In fact, the largest cluster detected by Scott *et al.* [3] encompassed 14 breaks (see **Section 2.2.4.3**). However, as this was detected at the last load step, which corresponded to 94 % UTS, there was no evidence with respect to its further growth. In addition, the notion of a 'cluster' itself has no unified definition throughout the literature, implying that results from different studies must be evaluated carefully [71].

Notwithstanding the lack of an agreed definition for a cluster, a common feature of their discussion in the literature is that clusters are generally defined based on some geometrical (proximity) criterion [3, 60]. This, in turn, is assessed by an indirect measurement (*e.g.* through Raman spectroscopy [35, 54, 75, 76] or Finite Element (FE) models [4, 65]) of the gauge volume over which stress/strain is recovered in the broken fibre and SCFs are of significant magnitude in the intact fibres, respectively. Garcea *et al.* [71] presented a more conservative definition, whereby a cluster of breaks was only considered if it encompassed breaks that were immediately adjacent to one another. Compared to the definition used in [3] and [60], respectively, this potentially made an equivalent 'distance-based' cluster significantly larger.

2.2.3 Damage assessment methods

Unlike monolithic structural materials such metals, composites often exhibit extensive sub-surface damage, which in turn may lead to severe strength and stiffness degradation. As such, various techniques have been employed to assess three-dimensional damage in CFRPs, of which optical microscopy, scanning electron microscopy (SEM), ultrasonic scanning (C-scanning), infrared thermography (IT), acoustic emission (AE), and X-ray radiography are among the most widely used [77].

Optical microscopy can be used in conjunction with metallographic serial sectioning to obtain through-thickness information with respect to the specimen's microstructure, *i.e.* material characterization [78]. Nonetheless, in contrast to tomographic X-ray imaging methods, this approach is destructive and incomplete (*i.e.* quasi-3D). That is because through CT, microstructural information can be obtained non-invasively at any given point inside the material bulk (through quantitative mapping of the linear X-ray attenuation coefficient), provided this is located within the field of view [79]. Scanning electron microscopy provides high-resolution topographical imaging of surfaces [80, 81], however, as in the case of optical microscopy, specimen preparation can result in artefacts; as in order to assess the internal damage, traditional sectioning or other machining techniques to remove surface material are still required [82]. For fibre-reinforced polymers, common sectioning artefacts may include microcracks and induced matrix strains, while during the polishing/grinding stage, scratches, fibre pull-out, matrix smears, streaks, differential removal of different phases, as well as rounding of fibre/specimen edge can occur [78]. Moreover, as this is a destructive technique, the specimen is essentially lost, in addition to the fact that the sectioning is commonly restricted to two-dimensions on the exposed surface. Ultrasonic scanning [83-85] and infrared thermography [86] are commonly used as non-destructive testing (NDT) techniques, but lack the required sub-micrometre resolution, as well as the capacity to represent accurately the interaction of various damage modes within the composite. This limitation can be partially resolved by coupling different techniques (*e.g.* acoustic emission and infrared thermography [87]), notwithstanding that the internal damage cannot be directly visualized. Damage assessment of composites via X-ray radiography may involve the penetration of the cracked composite areas with a dye having a high attenuation coefficient (*e.g.* zinc iodide solution [88]), unless *in situ* experiments are carried out where cracks are kept open. Radiographic projections can potentially deliver the required resolution to evaluate many different damage modes, but produces an essentially 2D integrated image which does not allow for the different damage mechanisms to be differentiated through the thickness of the material [88].

In recent years, X-ray CT tomographic X-ray imaging methods using both laboratory sources and synchrotron radiation facilities, has been used to conduct multi-scale damage assessment of CFRPs, providing the opportunity to study the various internal damage modes in 3D, essentially being a non-destructive, non-

invasive, radiographic method capable of *in situ* imaging of planar and volumetric structures, respectively [89-91]. In this context is interesting to note that CT may be used not just for material characterization purposes, but is also a versatile NDT technique [92]. CT, therefore, has an even role in both contexts whilst other techniques typically have a distinct leaning in one direction or the other. Micro-focus computed tomography (µCT) presents an effective routine evaluation of composite damage at mesoscopic and macroscopic levels in engineering-scale test specimens, and at relatively high spatial resolution for micromechanistic investigations on small-scale coupons [90]. Synchrotron Radiation Computed Tomography renders scans with the highest image quality, thus allowing failure micromechanisms to be studied in even greater detail, and is particularly characterized by the shortest acquisition time [90, 91]. Further details with respect to the background and operational principles of the two CT techniques can be found in **Section 2.3**.

2.2.4 Micromechanical representation of axial fibre failure

2.2.4.1 Stress redistribution around fibre breaks

The stress redistribution around fibre breaks, and the subsequent influence of various parameters, was comprehensively investigated, for example, by Nedele and Wisnom [67], Swolfs *et al.* [4, 65] and Tavares *et al.* [93, 94], with debonding being considered in [67]. In [4] and [65], respectively, a series of FE analyses were performed to obtain the ineffective length, SCF and overload length, respectively (**Figure 2-12**). The results were based on a Representative Volume Element (RVE) model of cylindrical geometry, whereby a single fibre break (*i.e.* non-interacting) was surrounded by intact fibres in a specific packing arrangement. It encompassed up to 84 fibres (using a 3.5 µm fibre radius and 50 % fibre volume fraction *'V_f'*, respectively), and measured 40 fibre radii in length. In this first instance [65], the model was subjected to an applied strain of 0.1 %, while linear-elasticity and perfect bonding were assumed between the matrix and fibres. Unless otherwise stated, the key reference for the following interpretations is [65], noting that the trends are in agreement with those in [93, 94].

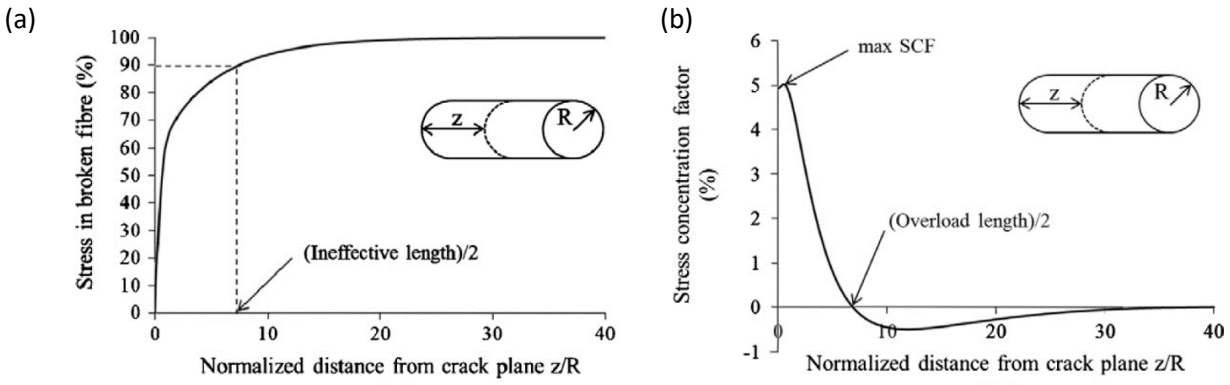

Figure 2-12 – Stress redistribution around a fibre break in a UD composite: (a) axial stress recovery (i.e. ineffective length), (b) SCF and overload length, respectively [65].

The effect of different fibre packings was investigated at a fibre volume fraction of 70 %. **Figure 2-13 (a)** shows single values representative for the ordered packings (square, hexagonal), and an average value with a standard deviation for the random packing model (corresponding to five simulation runs). The hexagonal packing indicated the longest ineffective length, while the random packing exhibited the shortest ineffective length. These variations were attributed to the differences in the shear stiffness in the immediate vicinity of a fibre break, as outlined below.

The shear stress responsible for stress recovery is primarily found in the material surrounding a fibre break, whereby a high contribution to stress recovery is given by the shear stiffness associated with this part of the material. As such, for a higher local shear stiffness, the stress recovery in a broken fibre was reported to take place over a smaller length. More specifically, in the hexagonal packing model, the nearest intact neighbouring fibres adjacent to a given fibre break are located at the same distance. In contrast, in the random packing model, some of the intact fibres will naturally be located in very close proximity to the same broken fibre (*i.e.* almost being in contact), while others will be located further apart. Around these closely-packed fibres, the matrix shear stress is expected to be higher than they would otherwise be if the fibres were loosely packed. In turn, this promoted stress recovery over a shorter distance from the fracture plane, and subsequently resulted in a shorter ineffective length. As the nearest neighbouring intact fibres in the square packing model were located closer to the broken fibre than that in the hexagonal counterpart, but not as close as in the random packing model, the ineffective length for the square packing model was situated between the ineffective length associated with the random and hexagonal packing model, respectively.

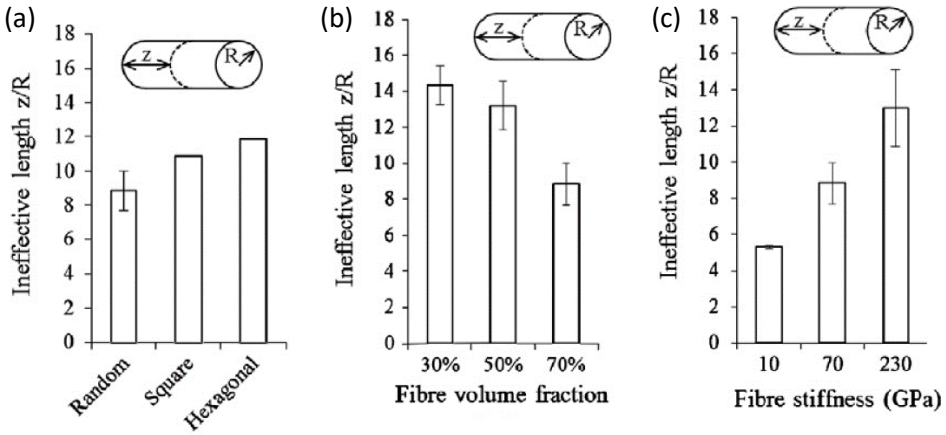

Figure 2-13 – Normalized ineffective length for the different: (a) fibre packings, (b) fibre volume fractions, (c) fibre stiffnesses [65].

In terms of stress concentration, a strong decreasing trend was reported as a function of radial distance for all packing types, to the point where, beyond two fibre diameters, the stress concentrations are somewhat negligible. This coincides with that reported in [67] for a hexagonal array. However, when the these were

compared at a fixed radial distance from a broken fibre, the hexagonal packing model predicted SCFs higher by up to 45 % compared to its random counterpart. This was associated with a so-called 'shielding effect', which essentially implies higher stresses at small radial distances and lower stresses at larger radial distances, respectively. In particular, the second nearest neighbouring intact fibres are shielded from high stresses by the first array encompassing the six nearest neighbours in the hexagonal packing model. Hence, the second neighbouring intact fibres exhibited significantly lower SCFs. This phenomenon was retained in the random packing model, however with a much stronger effect, due to the fact that the single nearest neighbouring intact fibre is located closer to the broken fibre, compared to the six nearest neighbours specific to the hexagonal packing model. In other words, a high SCF implies that a significant proportion of the total overload is already sustained by single nearest neighbouring intact fibre, thereby reducing the overload on the intact fibres situated further apart. The intact fibre located closest to the broken fibre in the random packing model, therefore, shields the fibres located further away, which in turn yielded a lower SCF for the same radial distance. Given the fact the SCFs are a consequence of the broken fibre not being capable of carrying the full load (see **Section 2.2.2.2**), the trends in overload lengths were comparable to those for the ineffective lengths.

The random packing model was also subjected to a fibre volume fraction investigation (30 %, 50 %, 70 %), whereby the number of simulation runs was increased to seven for the lowest fibre volume fraction case. As illustrated in **Figure 2-13 (b)**, the lowest fibre volume fraction indicated the longest ineffective length, while the highest volume fraction was associated with the shortest ineffective length, respectively. This trend was also confirmed by Landis and McMeeking, using a linear-elastic/perfect-plasticity matrix [95]. These variations were, again, attributed to the local matrix shear stress, which is expected to be higher, given the intrinsically smaller inter-fibre spacings for a material with a higher 'V_f'. As noted above, a higher shear stress in the vicinity of the broken fibre resulted in a higher stress recovery gradient adjacent to the fracture plane, which subsequently promoted a shorter ineffective length. Likewise, the shear stress transfer in the intact fibres, is also expected to be a contributing factor, due to the fact that the homogenised shear stiffness of the material surrounding a broken fibre is increased. This phenomenon was reported to particularly manifest at higher fibre volume fraction, where the homogenised shear stiffness is higher [14].

In the same context, a higher fibre volume fraction was also reported to promote a stronger 'shielding effect'. Indeed, a higher 'V_f' results, on average, in more intact fibres located closer to a fibre break, and therefore, higher 'V_f' materials experience higher SCFs. Nonetheless, when the SCFs were compared at a fixed radial distance from the fracture plane of a break, a higher fibre volume fraction was reported to produce lower SCFs. It is, however, valuable to note that this behaviour was noted to be distinctly relevant to random packings, in which no direct coupling occurred between the fibre volume fraction and the distance from a

given broken fibre to the nearest intact one. As such, for idealized two-dimensional, ordered packings (*e.g.* as in [34, 61, 66]), the SCFs were in fact reported to be consistently higher.

Another key aspect investigated by Swolfs *et al.* [65] was that of the fibre-to-matrix stiffness ratio, *'E_f/E_m'*. Three isotropic fibres were used (10 GPa, 70 GPa and 230 GPa), in conjunction with a Poisson's ratio of 0.22, and fibre volume fraction of 70 % for all cases. The epoxy matrix had a stiffness of 3 GPa and a Poisson's ratio of 0.4, respectively. Five runs were performed for each fibre stiffness case. As shown in **Figure 2-13 (c)**, the most compliant fibre indicated the shortest ineffective length, while the stiffest fibre was associated with the longest ineffective length, respectively. At first this may seem surprizing, as for a given Poisson's ratio, a higher fibre stiffness (or a higher stiffness mismatch between the constituents) is expected to produce a higher matrix shear stress, which in turn should lead to a shorter ineffective length. However, in parallel, it should also be noted that for a certain applied strain, a higher longitudinal shear fibre stiffness also implies a higher stress remote from the crack plane. This latter effect is reported to outweigh the increase in matrix shear stress, and as more stress requires to be transferred onto the broken fibre, this yielded a longer ineffective length. Here, it should be highlighted, that the increased fibre shear stiffness has a somewhat limited influence on the matrix shear stress, given the fact that it is primarily governed by the matrix shear stiffness, together with the distance from the broken fibre. Furthermore, as the matrix takes up most of the volume adjacent to a fibre break, the local shear stress will be dominated by the matrix shear stiffness. Given that the stress recovery for the stiffest fibre was spread out over the largest distance, the overload length was reported to follow the same trend as the ineffective length.

As shown in **Figure 2-14**, a decrease in *'E_f/E_m'* was also reported to produce a closer approximation of the perfect-plasticity behaviour, whereby the effect was attributed to an increase in the amount of plastic yielding. That is because for fixed *'E_f'*, a higher *'E_m'* implies that the yielding onset is reached earlier in strain terms [14, 95].

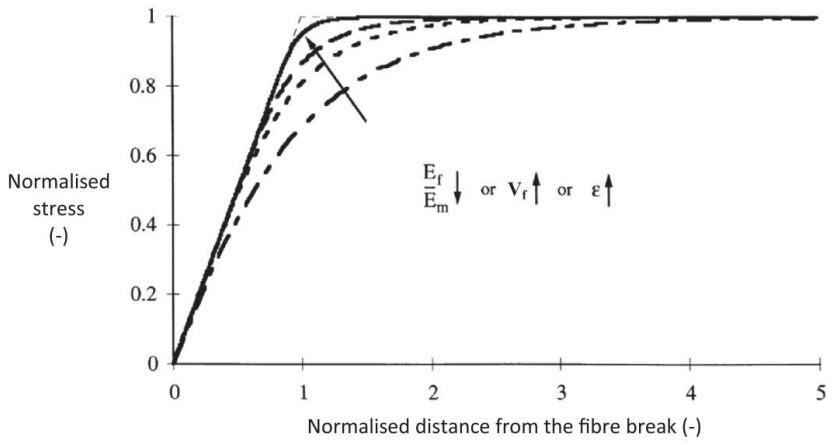

Figure 2-14 – The effect of modulus ratio, volume fraction and applied strain on the ineffective length in a UD composite [14].

In a subsequent RVE model, Swolfs *et al.* [4] employed an elasto-plastic matrix, while the applied strain was increased to 2 %. A matrix crack (covering an area between 100 μm^2 and 155 μm^2) was also implemented, which was assumed to be constrained by the nearby fibres. The resultant ineffective length measured (58 ± 4) and (57 ± 3) times the fibre radius for the models with, and without, a matrix crack, respectively. This also matches the order of magnitude reported elsewhere [66, 67]. The presence of matrix cracks was, therefore, found to have negligible influence on the ineffective length. With respect to SCFs, Swolfs *et al.* [60], reported a peak longitudinal stress equivalent to a 260 % very local SCF next to a broken fibre, notwithstanding the average SCF computed over the cross-section measured a significantly lower 23 %. In this context, whereby average fibre stresses were used rather than the peak stresses [65], matrix cracks were also reported to have a negligible impact on the SCFs [4].

The ineffective length has been reported to increase for large clusters, noting that this behaviour was not implemented in the corresponding strength model [4, 60]. This is due to the fact that for a random packing, an infinite number of possible cluster combinations exist, and calculating the underlying FE models for all of these is non-trivial (also valid for an ordered packing, though to a lesser extent). For the intact fibres, the interactions between fibre breaks were, therefore, taken into consideration (*i.e.* SCF), but not for the ineffective length associated with the broken fibres.

Other parameters, such as matrix plasticity and fibre-matrix interfacial debonding, were also reported to alter the stress redistribution around fibre breaks. Matrix plasticity resulted in a longer ineffective and overload length, together with delocalization of SCFs. A greater impact was, however, delineated in conjunction with debonding (stick-slip behaviour) – notwithstanding that a small coefficient of friction lead to a large ineffective length, and *vice versa*. As such, for a displacement equivalent to 1.5 % applied strain in the composite, the distance from the fibre break plane to where the influence of the break remained significant, was greater by a factor of ∼five compared to the linear-elastic case [67].

2.2.4.2 The unidirectional strength model benchmarking exercise

To predict the response of complex multidirectional composites subjected to 3D stress states, the World Wide Failure Exercises (WWFE) [5, 6, 96] relied on the basic mechanical properties of unidirectional plies as an input. In turn, predicting the underlying mechanical properties of unidirectional plies, and in particular the longitudinal tensile strength using the properties of the constituents (fibre, matrix, interface), is considered one of the essential elements for the reliable design of composite structures [97]. Bunsell and co-workers [97] have reported the benchmarking of different modelling strategies in a truly blind manner. While, undoubtedly, various unidirectional strength models have implemented the aforementioned concepts in fundamentally different ways since the ∼1960's, these have not been extensively compared to each other (*e.g.* as detailed in

the review [14]), nor against unseen test results. This latter aspect is particularly important as often model development and validation is performed alongside a series of small experiments known as *a priori*. Subsequently, this implies that models can be tailored to match a particular set of experiments, thereby introducing confirmation bias [97]. Furthermore, to obtain a reliable Weibull distribution with regards to the fibre strength, sufficient single fibre tests should be conducted (*i.e.* in the order of hundreds [70]). This is because using 25-100 fibres, which is the number that is generally considered, was reported to yield an uncertainty in the predicted strength of the composite of at least 10 %. Likewise, such single fibre tests should ideally be performed at the gauge length at which the Weibull distribution is required. Finally, different modelling assumptions and approaches are expected to result in predictions with varying levels of accuracy due to the simplifications used (*e.g.* perfectly straight and parallel fibres, homogenous matrix, amongst others) [97]. Consequently, to bridge the knowledge gap available in the literature with respect to the field of longitudinal tensile failure, an assessment similar to that performed in the WWFE was considered necessary to compare the different modelling strategies in terms of the relative importance of the various key features considered, their predictive capabilities, and computational cost [97].

Two different scenarios were considered in the context of the benchmarking exercise. The first relied on a hypothetical material, for which the model inputs had no factual experimental equivalence. Given that the absence of experimental results, and implicitly no data to compare with the modelling predictions, this scenario constituted a truly blind assessment between the participants. The second scenario relied on real T800/M21 composite specimens, with the required modelling inputs primarily collected from the literature, as detailed below. In terms of the experimental results from this material system, these were only made available after the modelling predictions were completed and collected, respectively.

The fibre geometry (5 µm diameter) and longitudinal modulus (294 GPa) were taken from the manufacturer's specifications (Toray Industries Inc., Tokyo, Japan [98]). Likewise, the matrix properties were taken from the manufacturer's data sheet (Hexcel Corp., Stamford, CT, USA [99]), while other elastic constants were extracted from [100] (assuming transverse isotropy). The fibre strength was assumed to follow a simple unimodal distribution, with the scale parameter of 3900 MPa and Weibull modulus of 4.8 (at gauge length of 100 mm, across a combination of 200 single fibre tests and 15 single fibre fragmentation tests) taken from [17]. The geometry of the one specimen tested was evaluated on the basis of SCRT scans, and had a gauge length of 1.54 mm, a fibre volume fraction of 55 %, and contained 5500 fibres (within a volume of 0.61 mm^3 encompassing the 0° plies).

An overview of the comparison of the three participating models is available in [97]. Given that a detailed analysis focusing on the construct of the different models is beyond the scope of this thesis, the framework of the 'Hierarchical scaling law', 'Direct numerical simulation' and 'Multi-scale FE model' is not repeated here.

Instead, emphasis is made on the accumulation of breaks and prediction of composite failure under uniform monotonic stress states in the context of real material, while at the same time, identifying drawbacks/benefits of the different modelling strategies and key assumptions used. Furthermore, open gaps in the literature are highlighted, that that require future attention on both the modelling and experimental side, respectively. Notwithstanding this, a key aspect of the 'Multi-scale FE model' is highlighted. More specifically, due to the intrinsic dimensions of the underlying RVE (which encompasses 32 fibres and has a length of 4 mm), the 'Multi-scale FE model' cannot be used with confidence for simulating specimens, or fields of view, with dimensions smaller than one RVE. As such, the modelling predictions were performed using longer 8 mm specimens, noting that this difference in the modelled gauge length was reported to have no significant influence on the results. Given the rigorous and comprehensive nature of its benchmarking exercise, unless otherwise stated, the key reference for the following explanations is [97].

From **Figures 2-15 (a)** and **(b)** it can be observed that the 'Hierarchical scaling law', and the 'Multi-scale FE model', predict a lower strength (and failure strain) compared to the 'Direct numerical simulation'. This was attributed to the implementation of the following assumptions:

- First, the 'Hierarchical scaling law', hypothesises a maximum stress concentration factor of 2 in the nearest neighbouring intact fibre, and at the same time, models clusters as co-planar fibre breaks. This is in contrast to the other two models, which employ lower stress concentration factors, that are estimated through FE. Also, contrary to the 'Direct numerical simulation' and the 'Multi-scale FE model', the 'Hierarchical scaling law' presumes that the ineffective length grows with both the applied stress and cluster size. Combined, these assumptions were reported to be responsible for the lower strength (and failure strain), predicted by the 'Hierarchical scaling law' (*cf.* the 'Direct numerical simulation').
- Secondly, the 'Multi-scale FE model' presumes that the stress concentrations affect the adjacent fibres along the entire length of the RVE in the longitudinal direction – which is 4 mm, as noted previously. In contrast, the 'Hierarchical scaling law' and 'Multi-scale FE model', assume that the stress concentrations only affect the neighbouring fibres along the corresponding ineffective length; noting that this results in a much more local effect (*i.e.* on the order of magnitude of 100 µm *cf.* 4 mm). This assumption, in conjunction with the largest specimen simulated (compared to the experiments and the other two modelling approaches), was reported to be responsible for the lowest strength predicted by the 'Multi-scale FE model'.

Progressing to the fibre break accumulation as a function of applied strain, it can be seen from **Figure 2-15 (c)** that the 'Hierarchical scaling law' and 'Direct numerical simulation' predict similar trends, while the results

from the 'Multi-scale FE model' are distinctly different. From a failure perspective, this was explained through the accumulation of breaks, which mostly encompasses single fibre breaks (*e.g.* as in [3, 71]), and in turn defined by the fibre strength statistics; whereby the latter is similar in the 'Hierarchical scaling law' and 'Direct numerical simulation', but different in the 'Multi-scale FE model' (accounting for different strength-defining flaw populations due to the different gauge-lengths, in conjunction with a significantly longer stress recovery length as detailed above).

Finally, **Figure 2-15 (d)** shows that the highest gradient in terms of fibre break clustering is predicted by the 'Multi-scale FE model', followed by the 'Hierarchical scaling law' and 'Direct numerical simulation', respectively. This discrepancy was again associated with size-scaling effects, and more specifically the single fibre strength considered by the 'Multi-scale FE model'. It is worth noting, however, that the evolution of the largest cluster size with applied strain matches the experimental results, and is relatively similar in the 'Hierarchical scaling law' and 'Direct numerical simulation' up to the development of 2-plets (*i.e.* clusters of breaks composed of two fibre breaks). Divergence occurs once 4-plets are observed experimentally or predicted by the 'Hierarchical scaling law'. This indicated that the formation of small clusters, such as 2-plets, is primarily associated with the distribution in fibre strength, while the different stress concentration implementations (and the corresponding gauge length over which they are relevant) predominantly affect the formation of larger clusters, at higher applied strains. At the onset of composite unstable failure, **Figure 2-15 (d)** also shows that from the three models investigated, the smallest cluster size is predicted by the 'Hierarchical scaling law'. This was reported to be consistent with the hypotheses considered, whereby clusters are modelled as co-planar fibre breaks with a stress concentration factor of 2 in the nearest neighbouring intact fibre to a broken fibre (or cluster of broken fibres), and considers a growing ineffective length with cluster size.

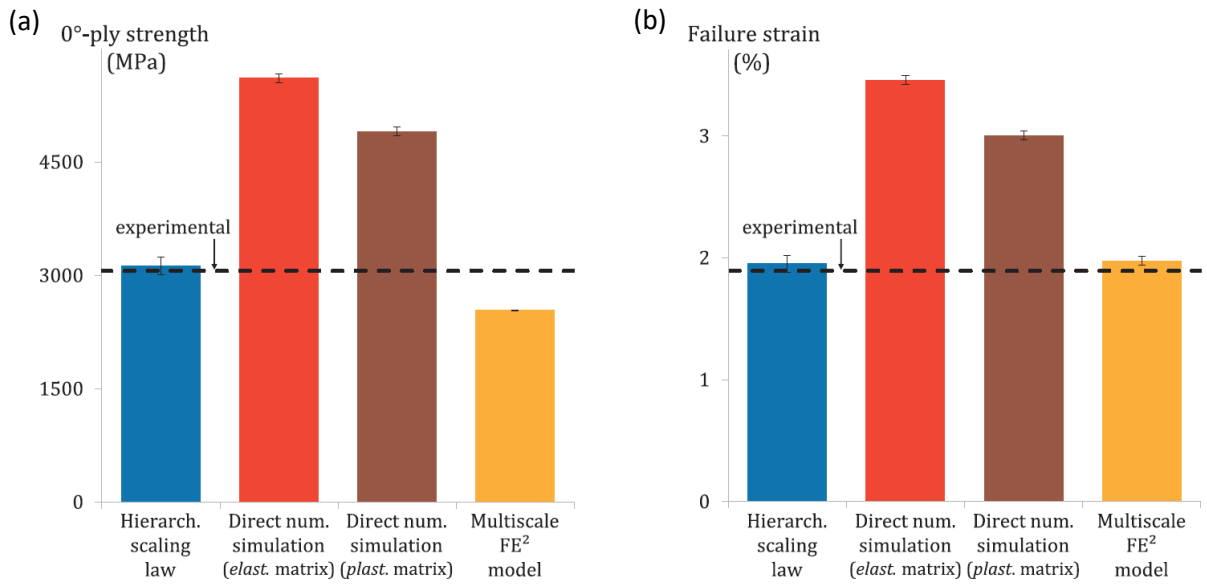

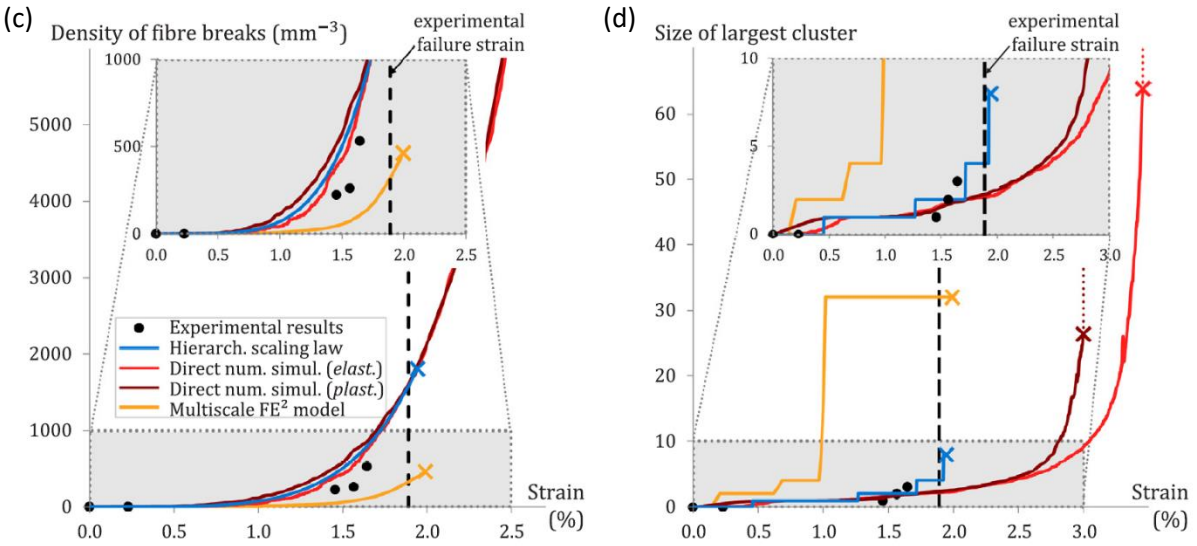

Figure 2-15 – Model predictions for the real material case: (a) 0° ply strength, (b) composite failure strain, (c) fibre break accumulation as a function of applied strain, (d) evolution of the largest cluster, with the size expressed in number of broken encompassing fibres. Results represent a minimum of ten simulations per output [97].

Taken together, the best agreement in terms of composite strength (and failure strain) prediction was observed between the 'Hierarchical scaling law' and 'Multi-scale FE model', while the best prediction with regards to the accumulation of breaks and cluster development as a function of applied strain was seen between the 'Hierarchical scaling law' and 'Direct numerical simulation'. This reveals that the damage predictions preceding the final failure (*i.e.* progressive accumulation of fibre breaks/development of clusters) and the final failure of the composite may not be necessarily linked directly. Furthermore, it also highlights the fact that while a specific modelling approach can lead to the ability of simulating a certain aspect of damage accurately (*e.g.* the accumulation of fibre breaks), it does not necessarily imply that the same model is capable of predicting the failure in line with the experimental results.

Matrix plasticity (applicable to the 'Hierarchical scaling law' and in one instance to the 'Direct numerical simulation') was seen to affect the clustering prediction significantly – **Figure 2-15 (d)**. In this regard, the 'Direct numerical simulation' predictions that considered such a matrix behaviour, were, generally, in better agreement with those obtained from the 'Hierarchical scaling law', compared to the results obtained by the 'Direct numerical simulation' with an elastic matrix. In contrast, if an elastic matrix was considered (*e.g.* as in the 'Direct numerical simulation' model), significantly larger clusters of breaks were predicted, compared to those reported experimentally. This is despite the fact that the 'Hierarchical scaling law' and 'Direct numerical simulation' employ dissimilar underlying modelling hypotheses (*e.g.* such as those related to the stress concentrations and clustering of fibre breaks). In turn, this highlights the fact that while the aforementioned

hypotheses undoubtedly affect the modelling predictions, the response assumed for the matrix may have even a greater effect on the results, and hence is essential for the accuracy of the simulations.

While the analysis performed in this benchmarking exercise is useful, Bunsell and co-workers [97] have also highlighted the following key open gaps in the literature that require further attention:

I. Improved experimental data for a more comprehensive review of the predictive capabilities.
   - Results for fibre breaks from a greater number of nominally identical specimens (*cf.* a single specimen) will usefully increase the statistical power of the studies and the data they are based on (*e.g.* fibre strength, fibre break and cluster behaviour, respectively).
   - Microstructural variations (*e.g.* matrix elastic properties, interfacial properties and/or fibre volume fraction) should be assessed for in composite with a specific fibre type. This will help understand the effects of these on the respective simulations, and to establish whether the reliability of the predictions is maintained for a range of different materials.
   - The fibre break and cluster behaviour should be captured along the entire loading history, rather than at specific load steps (*i.e.* stepwise). However, it is worth noting that the key experimental data is expected to be found closer to the onset of unstable failure, where the model predictions are also divergent.
   - CT acquisition time should be minimized (ideally continuous) to reduce the effect of hold-at-load artefacts. That is because scan interruptions (*e.g.* longer than two minutes) can promote the formation of additional breaks (and clusters) due to the viscoelastic effects (*i.e.* relaxation of the matrix) and subsequent overloading of the nearest neighbouring intact fibres next to a broken one.

II. More precise input parameters with regards to material properties, recognizing that agreement between experimental results and modelling predictions is of course conditioned by the accuracy of input measurements, and that performing accurate experimental measurements at a constituent level is generally difficult.
   - There is no agreed standard with respects to the methods and tools required to measure the fibre strength statistics accurately. For example, single fibre tensile tests have the disadvantage of being affected by stress concentration at the grips, while fragmentation tests require the assumption of fibre-matrix stress transfer (as detailed in **Section 2.2.2.1**).
   - A unimodal distribution (such as the one employed across this benchmarking exercise) might not be the appropriate model used to describe the fibre strength statistics, particularly at very small gauge volumes, encompassing a limited number of fibres.

- Matrix properties may also be modified by incorporation into a composite or exhibit size dependence [101, 102], and as such, the bulk mechanical properties (in particularly the strength) are unlikely to be representative of the actual *in situ* response in practical engineering composites with realistic fibre volume fractions. Furthermore, capturing the correct (and full) matrix behaviour is essential, as highlighted in the context of the 'Direct numerical simulation', whereby matrix plasticity was predicted to have a considerable effect on the failure strength (and strain), as well as fibre (and cluster) behaviour.

III. More detail with respect to the interaction of fibre breaks, cluster behaviour, and their definition.

- A clear and objective definition of what constitutes a cluster is not available, noting, that as mentioned previously (see **Section 2.2.2.2**), there is some consensus amongst researchers, that it should include a geometrical (proximity) criterion. This, however, is an indirect quantification of the gauge volume given by the ineffective and overload length, respectively, notwithstanding that comprehensive studies defining these underlying measurements, have yet to be performed with sufficient rigorousness to inform models. While the lack of such studies is certainly valid for non-interacting fibre breaks, it particularly applies to multiple interacting fibre breaks (*i.e.* located adjacent to each other) due to the increased micromechanical complexity. Equally, the evolution of the ineffective length/overload length with increasing load, in the bulk of practical specimens with realistic fibre volume fractions, and accurate fibre-matrix interfacial constitutive laws (*i.e*. matrix non-linearity, progressive matrix failure and fibre-matrix interface debonding) have not been thoroughly quantified. As a result, different definitions are used to describe fibre break interactions, which makes experiment-to-model and/or model-to-model comparison challenging. This uncertainty may be expected to be eliminated through detailed *in situ* stress/strain mapping at fibre break sites (both single fibre breaks and clusters of breaks), through state-of-the-art experimental approaches.
- Obtain detailed micromechanical information with respect to the dynamics of fibre failure. Presently, even by exploiting the latest advances in CT techniques (with temporal resolution on the order of one tomograph per second, as noted in **Section 2.3.5**), fibre breaks, and the majority of clusters, still appear 'instantaneously'. To revolve this experimental limitation, complementary damage-sensing techniques should be used. One possibility to achieve this aim is the use of acoustic emission capable of capturing the transient stress wave that that propagates along the broken fibre, as well as in the surrounding intact ones. This might be able to discern the sequence of single fibre break events that precedes cluster formation, and

is a key aspect, particularly highlighted in the 'Direct numerical simulation'; whereby this model predicted a shallower trend with regards to the accumulation of clusters, compared to what was observed experimentally (*e.g.* as in [60]). This discrepancy between models and experiments may, in turn, be associated with dynamic effects being disregarded, whereby the dynamic stress fields associated with the fibre fracture process may be considerably different from those considered under quasi-static conditions [103].

IV. Realistic microstructures are ought to be included. While some models such as the 'Direct numerical simulation', in conjunction with its underlying RVE [65], can capture the effects of a random packing and/or changes in the local fibre volume fraction (see **Section 2.2.4.1**), the effect of other key microstructural features should also be modelled, *e.g.* voids, large resin rich regions (tow gaps) and fibre misalignment.

2.2.4.3 State-of-the-art SRCT characterization of tensile failure in CFRPs

Moffat *et al.* [104] employed Synchrotron Radiation Computed Tomography to investigate multi-scale damage initiation and progression in CFRPs subjected to *in situ* tensile loading. A 2048 × 2048-pixel detector and microscope optics were used to yield a voxel size of 1.4 µm, in conjunction with a beam energy of 20 keV, 1,500 projections and 100 ms exposure time. To permit the damage micromechanisms to be captured within the narrow field of view, the study relied on 4 mm wide specimens, with 1 mm edge notches and 250 mm ply thickness, respectively. These were manufactured from a unidirectional commercial (aerospace-grade) prepreg in a $[90/0]_s$ cross-ply layup, and were machined via water-jet cutting. Examination of the resin-rich regions revealed the presence of thermoplastic toughening particles. They have shown that intralaminar damage, such as 90° ply transverse cracks, initiated at ∼30 % UTS, while 0° ply splits occurred at ∼40 % UTS (**Figure 2-16**). Individual fibre breaks were not reported to be common below ∼60 % UTS. Finally, toughening mechanisms such as crack pinning/retardation and bridging were observed in the resin-rich regions, while in areas with closely-packed fibres, the splits appeared to be less constrained, and thus, were reported to advance more freely.

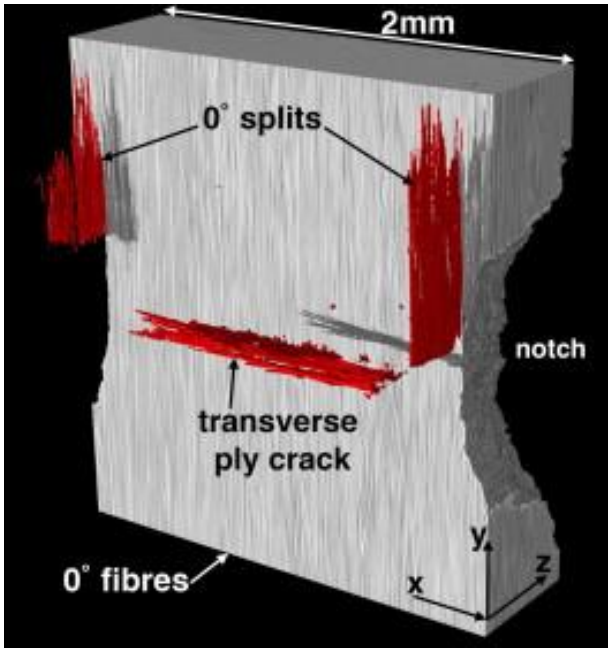

Figure 2-16 – Tomographic reconstruction showing segmented 90° ply transverse cracks and 0° ply splits, respectively, in a $[90/0]_s$ double-edge notched CFRP specimen at 40 % UTS [104].

Wright *et al.* [2, 105] performed both *ex situ* and *in situ* tensile tests, respectively, in conjunction with Synchrotron Radiation Computed Tomography. For the *ex situ* tests, slot cut plates were fabricated from untoughened T300/914C laminates, with a [90/45/-45/$\overline{0}$]s layup (125 µm ply thickness, 60 % fibre volume fraction, 7 µm nominal fibre diameter). These were loaded in quasi-static uniaxial tension to 80 % UTS. Afterwards, a low-speed diamond saw was used to cut single-notched 'matchsticks' specimens, with a width of 1 mm and height of 20 mm, respectively. SRCT was carried out at a voxel size of 0.7 µm, 1500 projections and 50 ms exposure time, respectively. They showed that damage occurred in each ply, and at their interfaces – **Figures 2-17** and **2-18**. More precisely, delamination was observed between the +45° and -45° plies, where the difference in lamina angle was twice that encountered at other interfaces. Fibre breaks were predominant in the 0° plies, whereas at the -45°/0° ply-interface, a cluster of breaks aligned with a split in the -45° lamina was detected. These fibre breaks were also noted to be accompanied by matrix microcracking, which interlinked the different break sites. Matrix cracks were observed to follow the direction of the fibre orientation and were predominant in the non-zero plies. Consequently, a strong relation between intralaminar cracks and fibre breaks was shown. However, as the *ex situ* experimental work only provided a post-mortem evaluation, no insight with respect to damage progression was gained.

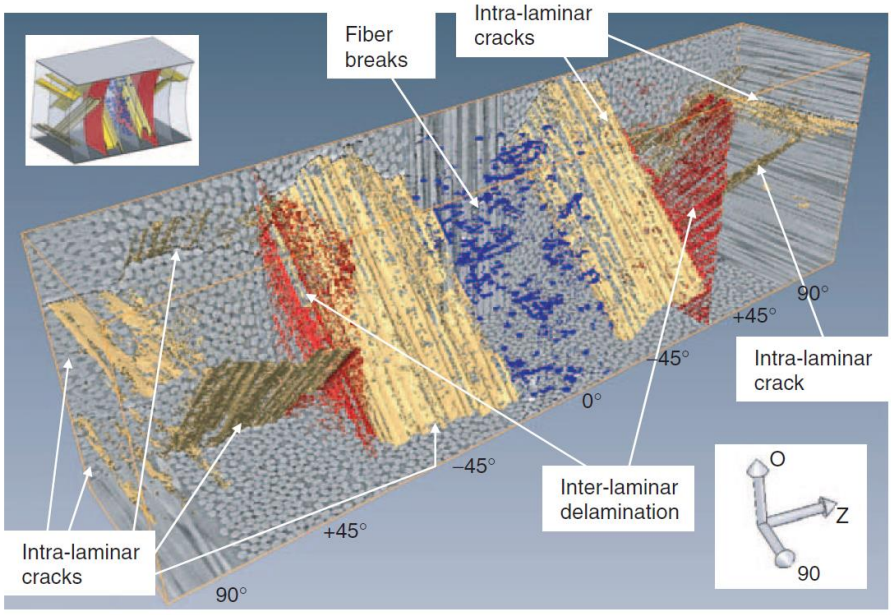

Figure 2-17 – Tomographic reconstruction showing segmented multi-scale damage in a [90/45/-45/$\overline{0}$]s 'matchstick' CFRP specimen at 80 % UTS [105].

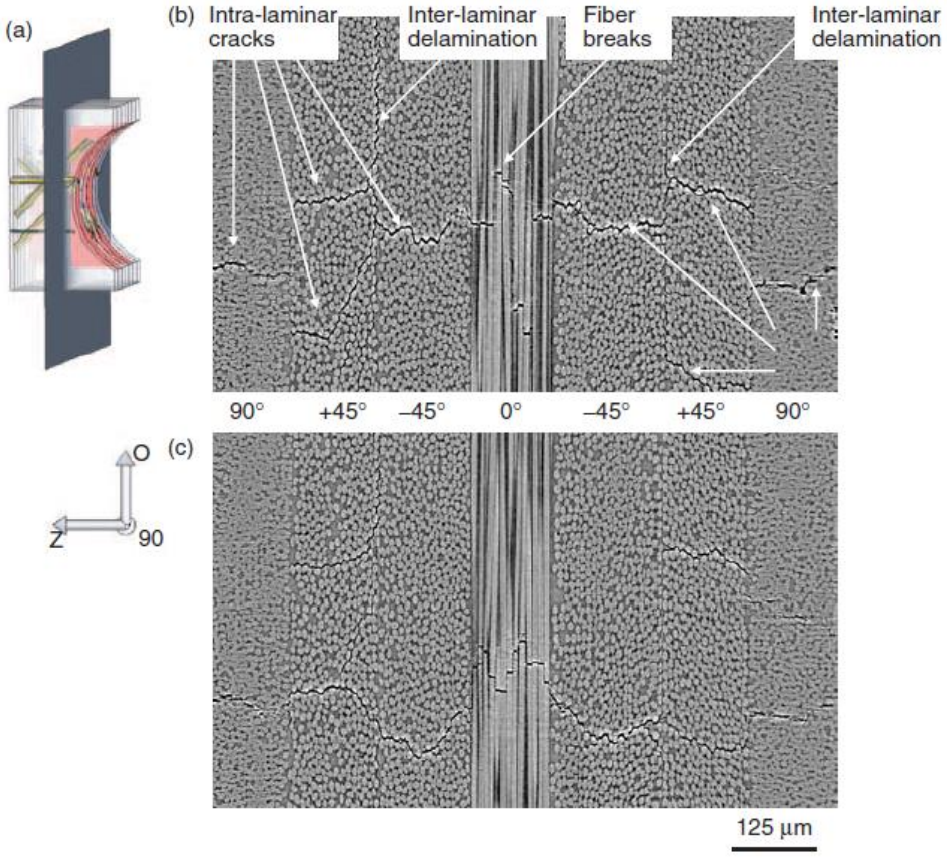

Figure 2-18 – Tomographic reconstruction showing the interaction of various damage mechanisms across different slices: (a) reference plane, (b) 200 µm ahead of the notch, (c) 350 µm ahead of the notch [105].

For the *in situ* tests, double-edge notched specimens were used. These were manufactured from a T700/M21 composite, containing thermoplastic toughening particles, and had a $[90/0]_s$ cross-ply configuration as in [104]. SRCT was conducted at a voxel size of 1.4 µm, whereas the number of projections and exposure time remained unchanged. Tension was applied using the loading rig shown in **Figure 2-19**, with stress increments ranging from 30 % to 90 % UTS. Three key interacting damage mechanisms were observed: 0° ply splits, 90° ply transverse cracks and 90°/0° ply-interface delaminations, with the latter occurring above 70 % UTS. The work focused on the global accumulation and interaction of *in situ* damage in concert with modelling at different length-scales, rather than a comprehensive analysis of fibre break behaviour.

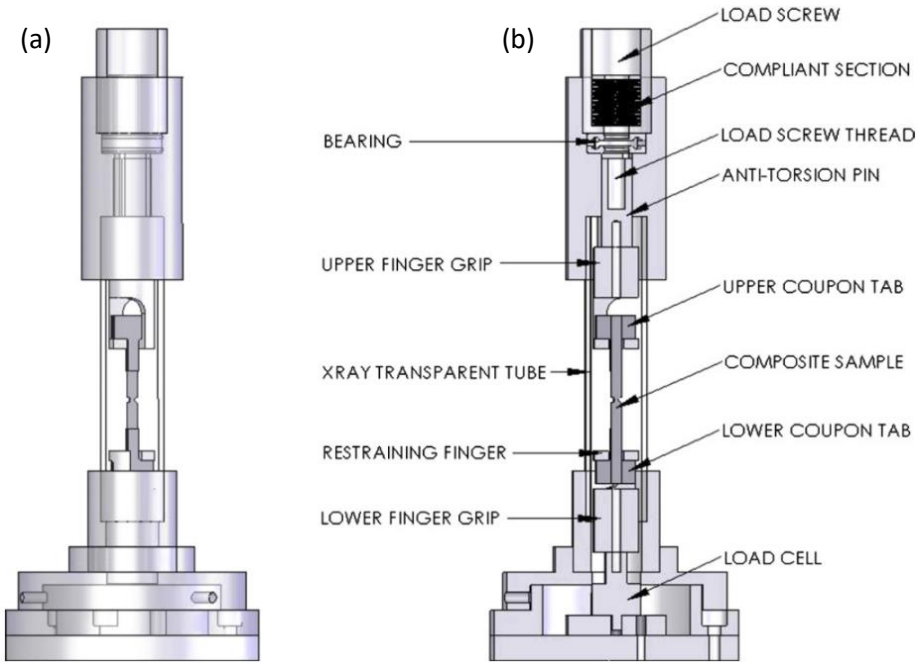

Figure 2-19 – Schematic illustration of the in situ loading rig: (a) semi-transparent view, (b) annotated cross-section [2].

Scott *et al.* [3, 68] subsequently investigated the final stage of failure, *i.e.* the accumulation and interaction of fibre breaks within the 0° plies. The materials and methods used were the same as those employed in [2], apart from the *in situ* loading, which was performed to 94 % of specimen UTS; with **Figure 2-20** presenting the multiple damage mechanisms at this load level. They showed that breaks accumulate exponentially with applied stress, with the majority of breaks occurring above ~90 % UTS. The total number of fibre breaks found within the load bearing reduced volume of 0.7 mm^3 was 290, with the largest cluster reported encompassing 14 breaks – **Figure 2-21**.

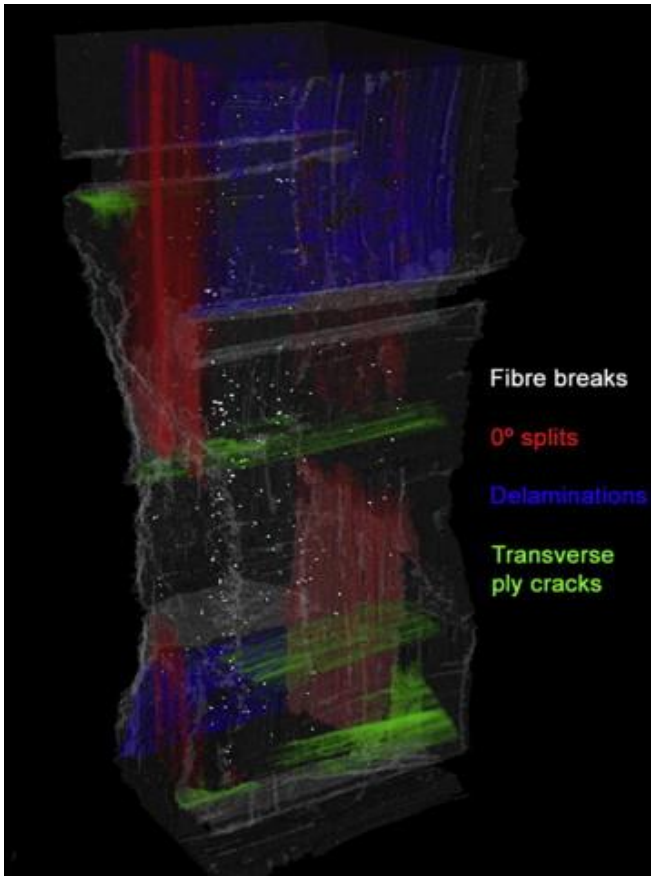

Figure 2-20 – Tomographic reconstruction showing segmented damage in a $[90/0]_s$ double-edge notched CFRP specimen at 94 % UTS [3].

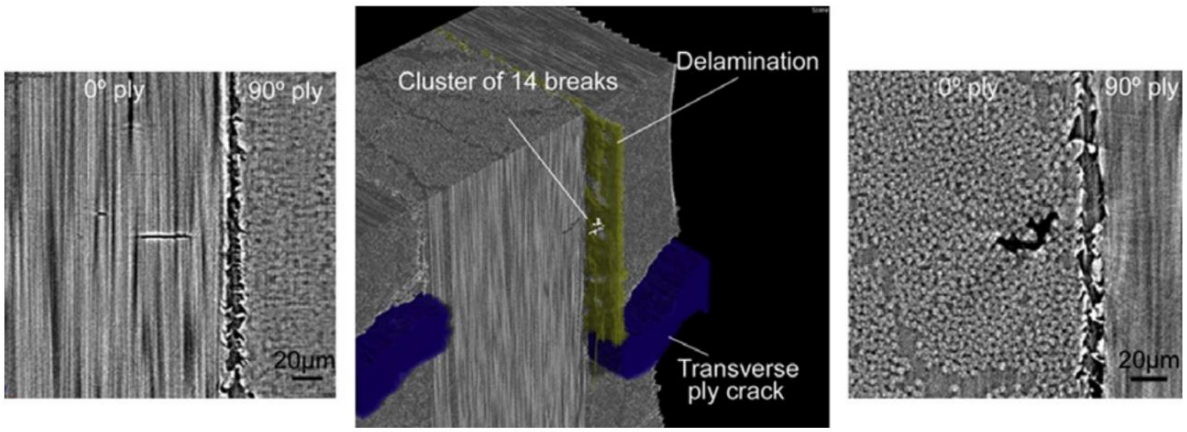

Figure 2-21 – Tomographic reconstruction showing a cluster encompassing 14 breaks across the different planes at 94 % UTS [3].

Large clusters of breaks were reported to form generally without a reduction in the number of smaller clusters. Furthermore, a 'break-by-break' accumulation with applied stress was not observed for the larger clusters, with a significant proportion forming in a single increment or 'burst', and without exhibiting any further growth. Contrary to the previous findings of Wright *et al.* [105], in which a cluster of breaks aligned with a split in the -45° lamina was detected at the -45°/0° ply-interface, no correlation was reported between the location of fibre breaks in the 0° plies and that of matrix cracks in the 90° plies, indicating that in this case the two damage mechanisms were decoupled between the plies. As such, the fact that the fibres were in a cross-ply appeared to have had no local effect on the fibre-scale break process.

Overall, these results are consistent with those reported by Swolfs *et al.* [60]. Scott [106] and Morton [107] have also shown that the total number of breaks is strongly dependant on the properties of constituent phases, as well as the fabrication route used. For example, they reported an excess of 1500 breaks/mm^3 in a CFRP based on T700-series fibres in conjunction with an Epon 826 epoxy-based resin (T403 hardener), and manufactured via filament winding. This is significantly higher than the total number of breaks reported in the aerospace-grade materials, noting that these filament wound materials were not subjected to autoclave curing as they originated from pressure vessels. In these materials, the presence of voids was shown to have a clear influence on fibre break location, as a significant proportion of fibre breaks occurred within half a fibre diameter of a void. Nevertheless, a distinct relationship between the total number of fibre breaks and the volume of the voids was not reported. This implies that a clear correlation between fibre breaks and voids, which affect the onset of composite failure, was not established [108]. A further analysis was carried out which provided an estimate of the ineffective length, by measuring the distance between fibre breaks that occurred along the axis of the same fibre (**Figure 2-22**). The observed closest separation of 70 µm was then used as a geometrical criterion in the quantification/classification of interacting breaks within a cluster [3].

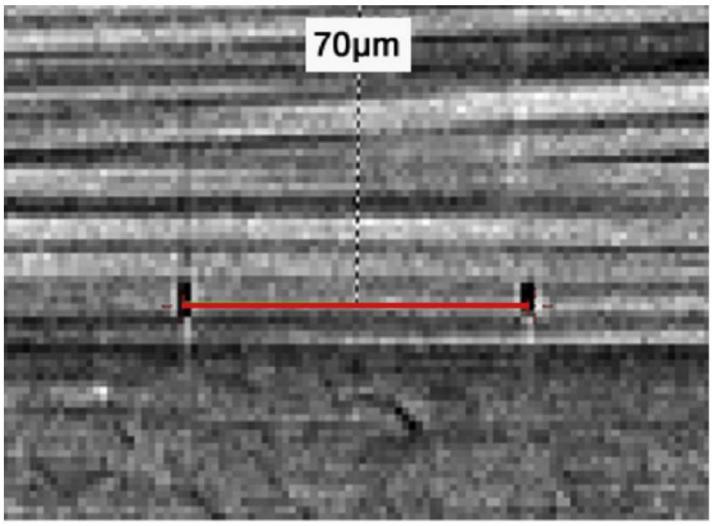

Figure 2-22 – Estimate of the ineffective length based on the closest separation of fibre breaks along the longitudinal axis of the same fibre [3].

Garcea *et al.* [71] also focused on the fibre break behaviour using Synchrotron Radiation Computed Tomography. However, unlike the previous studies [2, 3, 60, 104] *in situ* tensile testing was coupled with continuous, rather than stepwise scanning. This was enabled by improved imaging hardware on the synchrotron tomography beamlines, which permitted continuous scanning, while load was increased. The cross-ply configuration was retained, together with the materials (*i.e.* a T700/M21 composite) and specimen geometry, respectively. SRCT was carried out at voxel size of 1.1 µm. The number of projections was 500, and in conjunction with 2 ms exposure time, this resulted in 1 tomograph per second. Fibre break accumulation was studied in two identical specimens (labelled coupon 'A' and 'B', respectively), up to 99.9 % specimen UTS, as opposed to 94 % specimen UTS in Scott *et al.* [3]. This was showed to follow similar exponential trends, until the very last moment preceding macroscopic failure. It was confirmed that the majority of breaks occurred at new locations, rather than at pre-existing damaged sites. This agrees with the previous findings in [3]. Within the load bearing reduced cross-section of 0.45 mm^2 the specimens exhibited significant variability not just in terms of the total number of breaks (**Figure 2-23**), but also in terms of the largest clusters reported (**Figure 2-24**), highlighting the statistical nature of fibre behaviour. The continuous scans allowed the sequence and location of successive fibre fracture sites to be captured at much finer load steps than previously reported in [3, 60]. However, from an imaging perspective, the continuous scans in [71] represented a compromise between acquisition speed and quality, recognizing that for DVC analyses the latter should outweigh the former, as it is critical to reduce the measurement uncertainty.

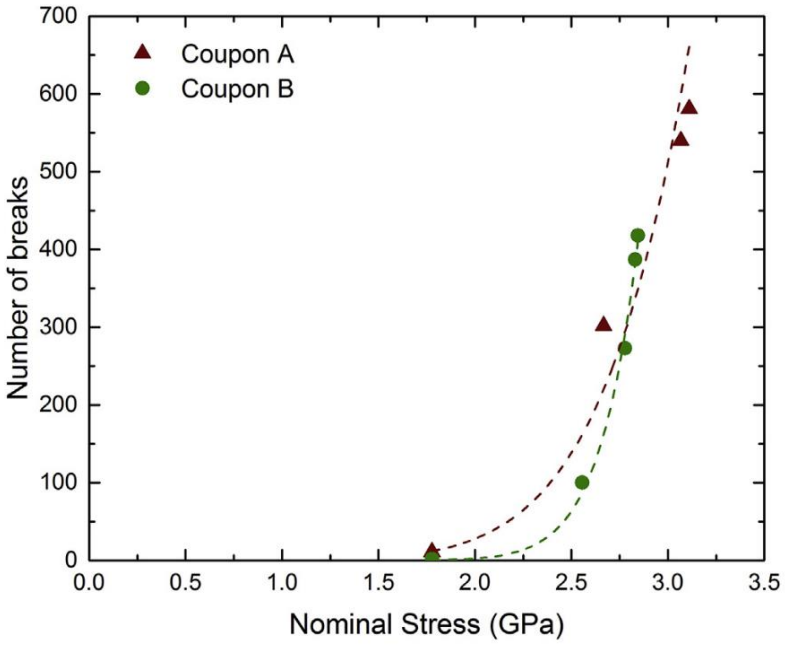

Figure 2-23 – Total number of fibre breaks as a function of applied stress in the load bearing reduced cross-section of 0.45 mm^2 for the two specimens subjected to in situ continuous tensile testing [71].

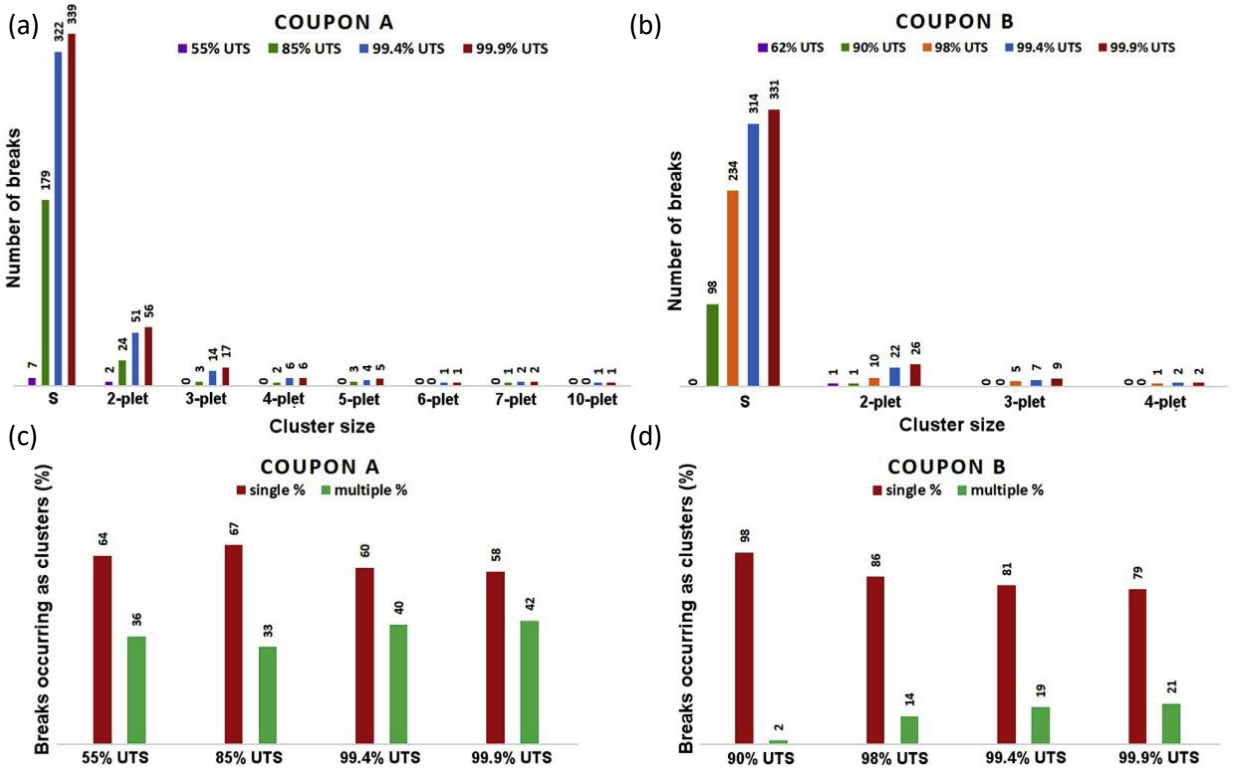

Figure 2-24 – Distribution of fibre breaks at different UTS levels: (a) and (b) total number of breaks, (c) and (d) proportion of breaks occurring as clusters of breaks [71].

Rosini *et al.* [72] performed detailed morphological measurements, which focused on identifying relationships between fibre orientations and local fibre packing in causing tensile failure. They used proprietary CFRP systems, with a $[90_2/0_2]_s$ layup and 5.4 µm nominal fibre diameter. The double-edge specimen geometry was retained, albeit with the specimen length increased from 66 mm to 100 mm, compared to the previous studies [2, 3, 60, 71, 104]. Two specimens were subjected to *in situ* SRCT testing, at voxel size of 0.65 µm. A beam energy of 19.5 keV was used, in conjunction with 2996 projections and 50 ms exposure time, respectively. They have shown, that on a statistical basis, the local background environment of intact fibre and single break sites is different. More precisely, the distribution of fibre orientations at single break sites exhibited a consistently higher standard deviation, when compared to the distribution at intact fibre sites. In contrast, no statistically significant differences were reported with respect to the local fibre packing at the damaged sites. Furthermore, as also noted by Scott *et al.* [3], fibres were shown to have a tendency to fracture in a nearest neighbouring fashion, indicating the presence of local load shedding. Overall, the findings suggested that the microstructural dependence of fibre breaks site formation is complex.

2.3 Computed Tomography

2.3.1 X-ray generation and interaction with matter

As shown in **Figure 2-25**, X-rays can be found at the short wavelength (high-energy) end of the electromagnetic spectrum, with wavelengths ranging from 10^{-11} m to 10^{-8} m, or 0.01 nm to 10 nm [109].

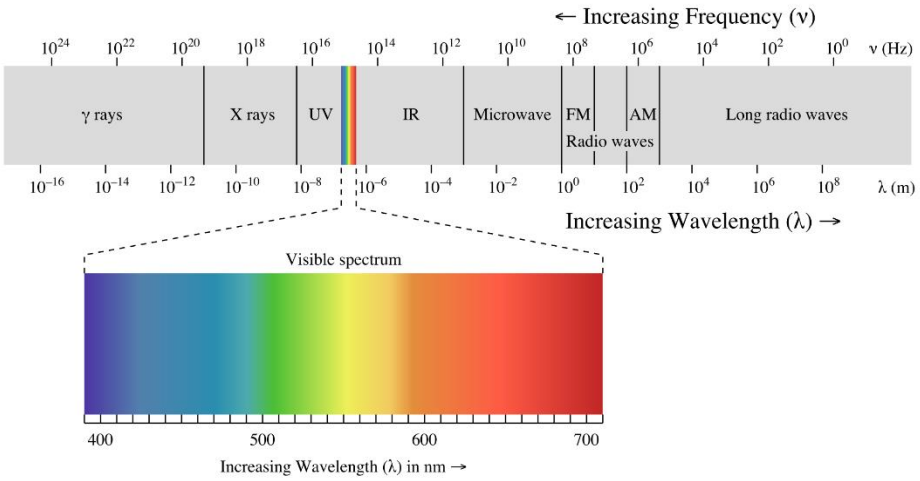

Figure 2-25 – Electromagnetic spectrum [110].

X-rays with wavelengths in the range of 10 nm (124 eV) to 0.1 nm (12.4 keV) are generally identified as 'soft' X-rays due to their inability to penetrate thicker material layers. These X-rays have limited value in real space imaging (*i.e.* radiographic) of structural materials, in which wavelengths of ~0.1 nm and below (energy greater than ~12.4 keV) are commonly required, *i.e.* 'hard' X-rays [109]. For science and engineering purposes, X-rays photons are conventionally generated as a result of bombarding a high atomic number metal (*e.g.* W, Mo) with high-speed electrons. The intensity or 'brightness' of the photon stream is proportional to the atomic number of the target material and to the number of electrons bombarding the target [111].

Upon hitting the target material, different types of interactions take place [109, 112]:

- High-speed electrons are decelerated by the electric field of a target nuclei, resulting in Bremsstrahlung radiation. This is a continuous band also known as 'white' radiation, which spans the entire range of the energy spectrum.
- High-speed electrons strike one of the inner-shell electrons of a target atom, ejecting it from its shell. As an outer-shell electron fills in the vacant shell, X-rays are produced at characteristic frequencies.
- The entire kinetic energy is converted into bremsstrahlung radiation as an electron directly hits the nucleus of an atom.

In relation to X-ray generation, it is useful to make the distinction between kVp (electric potential) and keV (energy). The units of kVp are typically used to describe a laboratory CT scanner. As an example, a 120 kVp CT indicates that the applied electric potential across the X-ray tube is 120 kV. In this case, the electrons that hit the target are characterized by 120 keV of energy and the highest energy photons that can be produced are 120 keV [109]. The average photon energy of such a beam will be on the order of one third to one half of the accelerating potential.

Once X-rays are produced, these can be used to interact with matter (*i.e.* specimen to be imaged). In the typical photon energy *'E'* range of 20 keV to 140 keV, the fundamental interactions are: the photoelectric effect, the Compton effect and coherent (Rayleigh) scattering, respectively [109, 112, 113].

The photoelectric effect portrays a state in which the X-ray photon energy is slightly higher than the binding energy of an electron; under such circumstances, the entire energy of an X-ray photon contributes to liberating an electron from a deep shell. The free electron released is typically called a 'photoelectron', and the photon ceases to exist. As the vacant inner-shell is filled by an outer-shell electron which is at a higher energy state, characteristic radiation results. The photoelectric effect produces a positive ion, as the affected atom lacks an electron to maintain its neutral charge [109].

The Compton effect is the second way in which X-rays can interact with matter. In this type of interaction, the energy of the X-ray photon is much higher than the binding energy of an electron. As the incident X-ray photon hits an electron, it will be freed from the atom. This leads to the formation of a positive ion, a 'recoil' electron and a scattered photon, respectively. The angle at which the photon is scattered can vary from 0 to 180° [109 ,114].

The third and final type of interaction with matter is known as coherent or Rayleigh scattering. In this type of interaction, no kinetic energy conversion takes place and ionization does not occur, but an electromagnetic wave with an oscillating electric field sets the electrons in the atom into a momentary vibration. These oscillating electrons are responsible for emitting radiation of the same wavelength. As this is a cooperative phenomenon, it is called coherent scattering [109].

The type of interaction, and consequently the percentage of energy transferred from each type of interaction, is governed by the level of energy, in conjunction with the atomic number used. At the energies available in this project, which are on the order of 20 keV, the percentage of energy transferred after interaction is mainly associated with the photoelectric effect, with the Compton effect assuming a more predominant role at significantly higher energies [109]. The probability of the photoelectric effect is approximately inversely proportional to the cube of the photon energy and proportional to the cube of the atomic number of the interacting atoms [109, 115]. Thus, for a given energy, small differences in composition of a material produce

large differences in the probabilities of the photoelectric effects, causing dissimilar absorption rates, and in turn, enabling greater contrast [109].

The overall effect of the aforementioned interactions is that some of the X-ray photons are scattered or absorbed upon passing through a specimen. Thus, the output is given by an attenuated intensity, which is recorded by the detector [109, 112, 113, 116]. For a monochromatic (monoenergetic) incident X-ray beam and homogenous (uniform density) material of atomic number *'Z'*, the attenuation can be expressed through the following exponential relationship (Beer-Lambert law [117]):

$$I = I_0 e^{-\mu x}$$

Equation 2-5

or

$$\mu = \frac{1}{x} ln \frac{I_0}{I}$$

Equation 2-6

where *'I_0'* and *'I'* indicate the incident and the emerging X-ray intensity, respectively, *'μ'* is the linear attenuation coefficient of the material and *'x'* is the thickness of the material. The attenuation coefficient is the sum of the individual attenuation coefficients of the photoelectric, Compton and coherent scattering interactions [109], with the photoelectric effect being dominant here as earlier mentioned. For this particular case, the attenuation coefficient for a specific point (X, Y, Z) within the material, is given by [91].

$$\mu\ (X, Y, Z) = K\rho \frac{Z^4}{E^3}$$

Equation 2-7

subsequently

$$\mu\ (X, Y, Z) \propto \frac{Z^4}{E^3}$$

Equation 2-8

where *'K'* is a constant and *'ρ'* is the density.

2.3.2 Principles of operation

The operation principle of X-ray CT relies on the ability to record the attenuation profiles of X-ray photons as part of their interaction with matter. As shown in **Figure 2-26**, a specimen is typically placed on a rotation stage, and a number of attenuation measurements are conducted in a non-invasive manner for different angular positions, to obtain a series of 2D projections images (radiographs) [116].

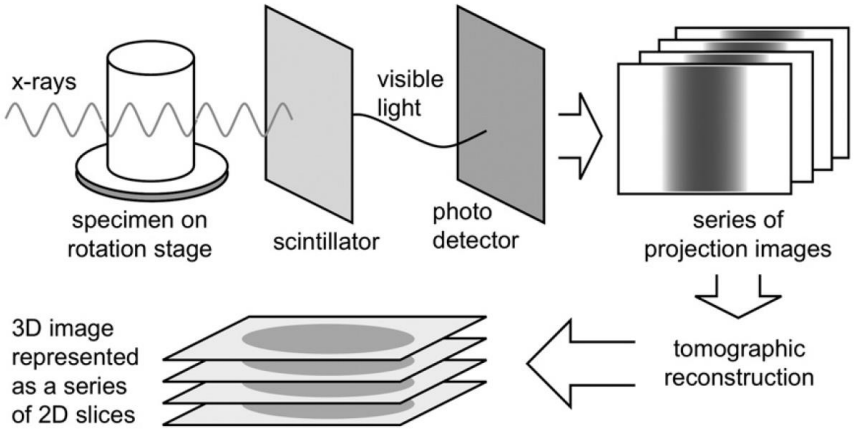

Figure 2-26 – Schematic illustration of the X-ray CT acquisition and reconstruction process [116].

Acquisition is typically performed over a rotation of 180° for tomographic systems which are characterized by monochromatic and parallel beams (*i.e.* synchrotron X-ray sources), while a rotation 360° is utilized for conventional laboratory systems which employ polychromatic and conical beams (thereby achieving full angular coverage at all positions in the object) [118]. As such, the intensity of the emerging X-ray beam is recorded for a finite number of angular increments, given by the ratio of the rotation to the number of projections used [119]. Modern 2D X-ray detectors, such as the ones employed here, typically have a size of ∼2000 × ∼2000 pixels [112], noting that in order to realize most of the advantages of the CT methods used, imaging is limited to relatively small specimens (less than ∼2 mm in cross-section). Finally, the projections are effectively combined as they undergo a variety of possible reconstruction methods (frequently a Filtered Back Projection or 'FBP' algorithm) to form a three-dimensional volume which is displayed and stored [116].

2.3.3 Micro-focus Computed Tomography

Micro-focus Computed Tomography relies on an X-ray tube to supply the necessary illumination to perform scans. Even though the size and appearance of the X-ray tube have changed considerably since its creation by Röntgen in 1895, the principles of X-ray generation remain fundamentally the same [109]. As illustrated in **Figure 2-27**, the main constituents of an X-ray tube are the anode and the cathode. Electrons are supplied through the cathode, while the anode acts as the target [109, 112].

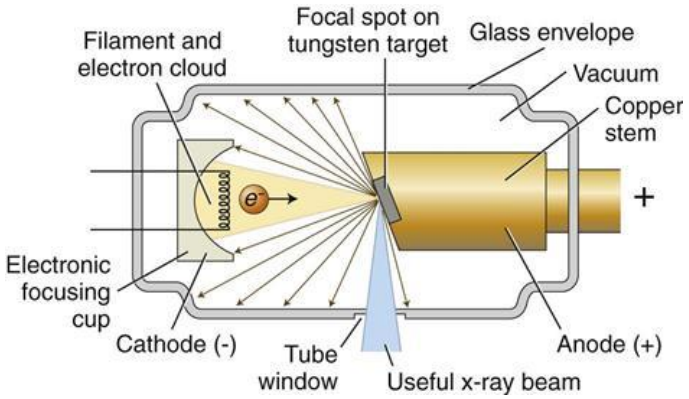

Figure 2-27 – Schematic illustration of an X-ray (cathode) tube and its main constituents [120].

In micro-focus tubes, X-ray radiation is produced when a target is bombarded by high-speed micrometre-sized 'spot' of electrons (hence the name) generated at the cathode (see **Section 2.3.1**) through a process known as 'thermionic emission', but then focused and aligned via a variety of electromagnetic lenses [111, 112]. The energy (or wavelength) of the generated X-ray beam, which in turn yields the penetrating power of the photons, is controlled by the electric potential difference applied between the cathode and the anode. In contrast, the intensity (*i.e.* flux or the number of X-ray quanta) of the X-ray spectrum is controlled primarily by the anode current [111, 112]. The quantum efficiency of the conversion from kinetic energy into X-ray radiation is very low, on the order of ~1 %. As such, the remaining of ~99 % of the kinetic energy is transferred locally to the lattice, heating up the anode, and thus, requiring extensive cooling solutions [111, 112].

To minimize geometric unsharpness, radiation is originated from as small a notional point-source or 'focal spot' as possible [111-113, 116, 121]. Nevertheless, as the source size is increased, the X-rays can take different paths from the origin to the detector, hence reducing the definition of small intricate geometries such as notches. As such, the focal spot size impacts the spatial resolution [116, 121]. Two types of targets may be identified as in **Figure 2-28**: (a) reflection, and (b) transmission target [122]. For achieving superior spatial resolutions, an X-ray tube equipped with a transmission target is generally preferred, due to the intrinsic thinner target which is capable of generating a smaller 'focal spot' [123].

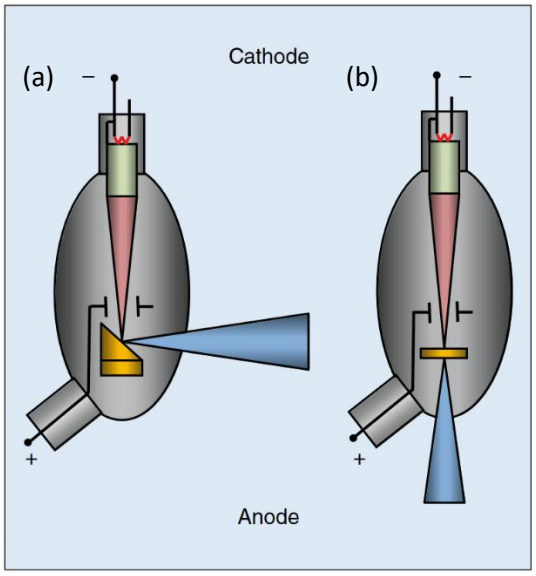

Figure 2-28 – Schematic illustration of the target system of an X-ray tube: (a) reflection, (b) transmission [122].

With respect to the data acquisition, three configurations are distinguishable as shown in **Figure 2-29**: (a) planar fan beam, (b) cone beam, and (c) parallel beam configuration [124].

In a planar fan beam configuration, the X-ray flux is collimated, and a linear detector array is employed. Collimation is employed to reduce the impact of X-ray scattering which can lead to spurious rays reaching the detector from different spots, and not along the source-detector pathway. Linear detector arrays are commonly more efficient that than planar ones but have the limitation that data can be acquired only for one slice at a time [124].

In the cone beam arrangement, the linear detector array is replaced with a planar detector and the beam is no longer collimated (*i.e.* beam is fully divergent). The one-slice acquisition limitation no longer exists and data for an entire specimen can be acquired during a single rotation. However, the cone beam setup is subjected to some blurring as well as distortion, the further one deviates from the central plane corresponding to a single slice-acquisition. In addition, considerable artefacts due the beam scattering may be expected if high energy sources are used. Nonetheless, the advantage of improved rate of data procurement is considerable, as well as the benefit, that as more acquisition time can be spent at each angular position, image noise can potentially be reduced [124].

Finally, the parallel (or more specifically, near parallel) beam configuration is typically reserved for laboratory systems that use microscope optics in conjunction with a micro-focus source (*e.g.* Zeiss Xradia Versa range [125]). In this case, no (or minimal) distortion is present in the volumetric data acquired. However, if there is no geometrical magnification, the object size is limited by the size of the beam itself and high-resolution must

be achieved at the detector itself. Thus, careful selection of the beam must be made according to the specimen dimensions; and as such the versatility of the setup in some senses is lower [124].

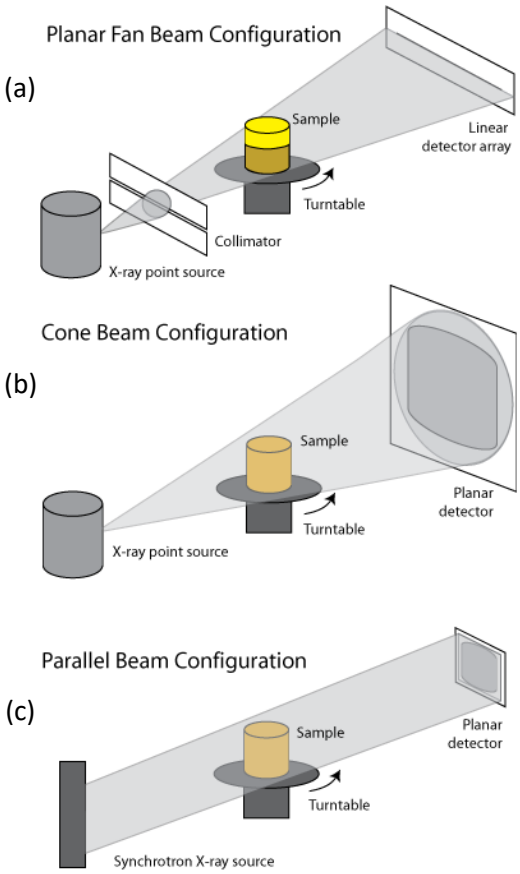

Figure 2-29 – Schematic illustration of the different data acquisition configurations and radiation flux geometries: (a) planar fan beam, (b) cone beam, (c) parallel beam [124].

2.3.4 Synchrotron Radiation Computed Tomography

Synchrotron radiation is produced by ultra-relativistic electrons, which are subjected to a change in direction by a magnetic field. The electrons respond by emitting short pulses of electromagnetic radiation, also known as 'synchrotron light' [116, 126, 127]. Such an ultra-low emittance source, as shown in **Figure 2-30**, can be found for instance at the European Synchrotron Radiation Facility (ESRF) in Grenoble, France.

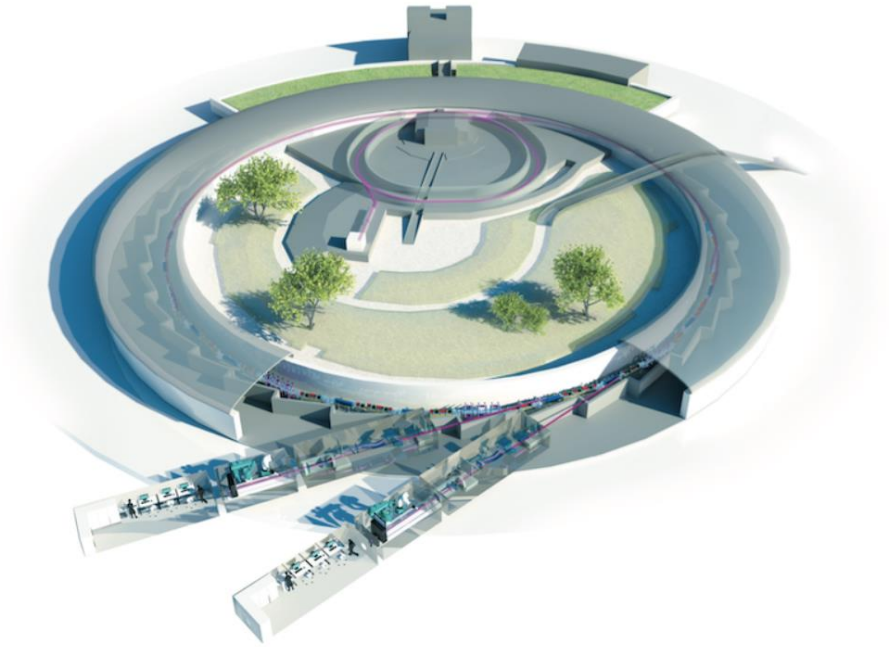

Figure 2-30 – Overview of a synchrotron facility (courtesy of ESRF [128]*).*

As noted in [128], the main components of the ESRF are as follows (although, the same general equipment is applicable for other synchrotron radiation facilities):

I. Linear accelerator

The linear accelerator (or 'Linac') is effectively an electron gun that generates electrons similar to a cathode tube. The electron stream is then accelerated through a small orifice and assisted by a high potential difference (200 MeV), is injected into the booster ring.

II. Booster ring

The booster ring takes the electrons generated by the Linac and accelerates them further, gaining a little more energy with every lap travelled. This is achieved via magnetic fields that are constantly adapted to the corresponding energy of the electrons. Once the electrons reach their final energy 6 billion electronvolts (6 GeV), they are injected into the storage ring. At ESRF, the booster ring structure measures 300 metres in circumference.

III. Storage ring

The storage ring is a very low pressure ($\sim 10^{-9}$ mbar) operated tube in which the electrons circulate close to the speed of light. As the electrons travel round, they pass through a series of magnets, and in the process produce X-ray radiation (or 'synchrotron light'). At ESRF, the storage ring structure

measures 844 m metres in circumference and it is comprised of 32 straight and 32 curved sections in alternating order. In turn, each curved section contains two large bending magnets, while each straight section houses several focusing magnets and insertion devices, respectively (**Figure 2-31**).

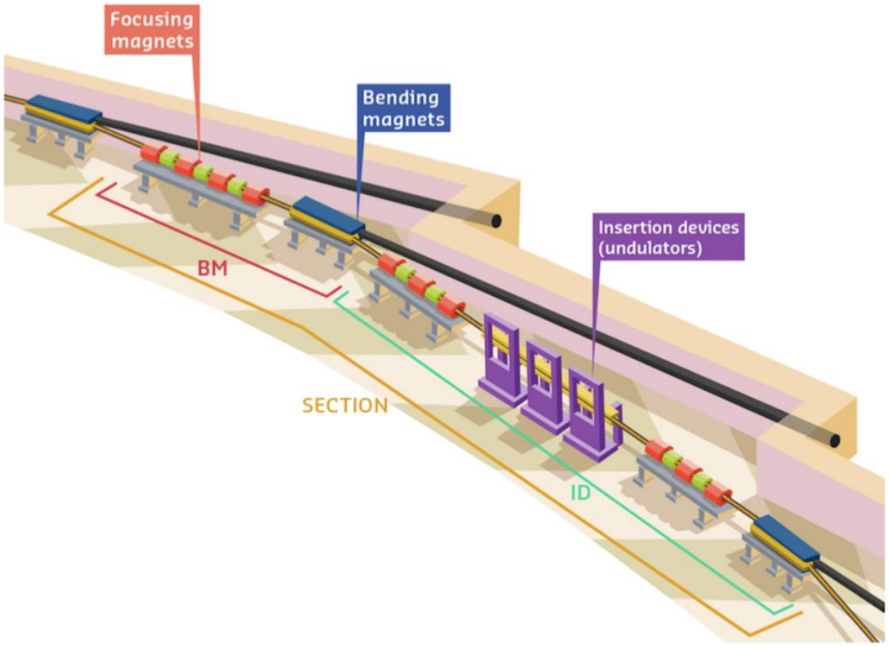

Figure 2-31 – Main components of a storage ring [128].

IV. Bending magnets

As the name suggests, the main function of bending magnets is to 'bend' the electrons in an orbital track. As the electrons are bent from their straight path, X-ray radiation is emitted tangentially to the plane of the electron beam (**Figure 2-32**). The subsequent synchrotron light covers a wide range of energies, from microwaves to hard X-rays and is less focused and bright when compared to the radiation emitted from the insertion devices.

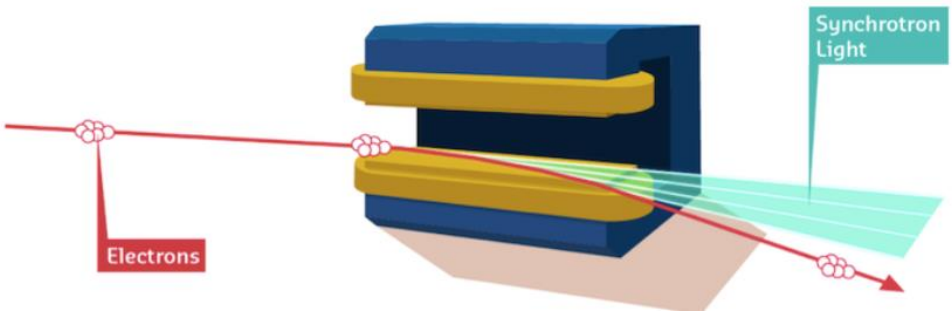

Figure 2-32 – Schematic illustration of a bending magnet [128].

V. Insertion devices

Insertion devices (IDs) are a complex array of small magnets that force electrons into an undulating, or wavy trajectory (**Figure 2-33**). These are inserted into a straight section of the storage ring (hence the term 'insertion device'). Radiation emitted at each consecutive bend is overlaid and interferes with that from other bends, generating a much more brilliant beam when compared to that generated by a bending magnet.

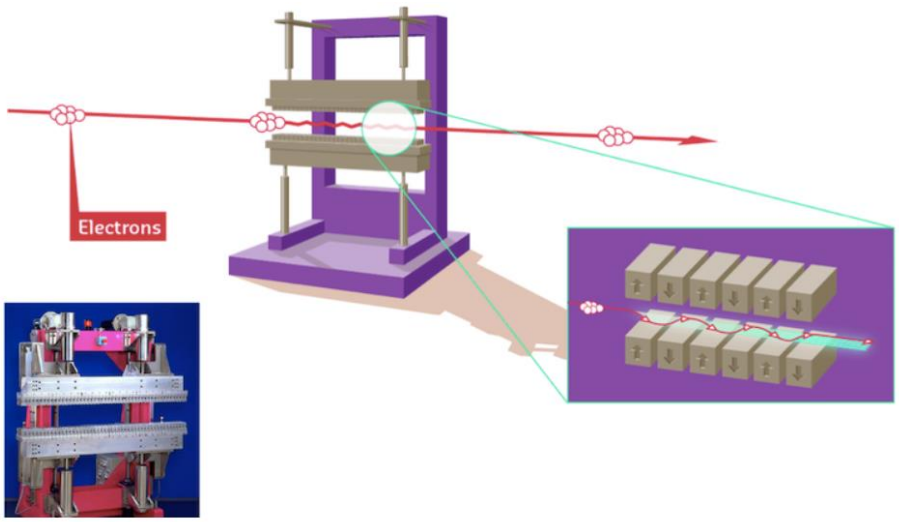

Figure 2-33 – Insertion device and it's schematic illustration [128].

VI. Beamlines

Radiation emitted by the deflected electrons paths are directed toward 'beamlines', which are situated tangentially around the storage ring. As each beamline has its own insertion device, bending magnets, and an array of X-ray optics (monochromators, collimators, mirrors *etc.*), the properties of the beam can be tuned to fit the needs of a particular research experiment.

2.3.5 Advantages of Synchrotron Radiation Computed Tomography

The use of a conventional or synchrotron radiation source has a considerable practical impact on the imaging results (signal- and contrast-to-noise ratio, spatial resolution, artefacts) and acquisition time (temporal resolution), respectively. This is primarily due to the nature of the beam, which is polychromatic and divergent for laboratory CT scanners (see **Section 2.3.3**), while synchrotron light is several orders of magnitude brighter, monochromatic, coherent and parallel. Taken together, the advantages of Synchrotron Radiation Computed Tomography are [71, 91, 116, 124, 126, 129-131]:

- High signal-to-noise ratio due to available flux. In turn, this results in a superior spatial resolution at equivalent voxel sizes, which allows finer microstructural details to be distinguished.
- Absence of beam hardening artefacts, which is preferable for studying low contrast materials (such as carbon-fibre reinforced polymers).
- High phase-contrast and contrast-to-noise ratio, respectively. This results in improved edge detection, which permits smaller microstructural discontinuities to be resolved (*e.g.* matrix cracks connecting cluster of fibre breaks and nucleation of very fine cracks generated by individual fibre fractures in carbon/epoxy specimens), while at the same time minimizing the measurement uncertainty of the DVC.
- Inherently fast acquisition times (now on the order of ≥ ∼1 tomograph per second *cf.* hours on laboratory systems), which is of fundamental value for *in situ* experiments, in order to minimize hold-at-load and movement artefacts. However, SRCT X-rays are typically lower in energy than what may be achieved in micro-focus CT machines, which in turn can present difficulties when imaging specimens with high atomic numbers.

It is worth noting that the latest laboratory CT systems, as the ones used in this project, have reduced the gap to synchrotron sources. For example, the Zeiss Xradia Versa range [125], employs a microscope objective turret, that combined with geometric magnification can deliver true sub-micrometre spatial resolutions while still enabling some degree of phase contrast [132]. Nonetheless, the increased predisposition to noise and long acquisition times remain a fundamental characteristic of laboratory CT systems compared to synchrotron facilities.

2.3.6 Artefacts

Artefacts are imaging errors associated with discrepancies between the reconstructed greyscale intensities in an image, and the 'true' attenuation coefficients of a specimen. Artefacts may stem from spatial sampling technologies and detector array arrangements, defective detector elements (*i.e.* pixels), and/or simplifications of the reconstruction method used (typically, FBP assumes a monochromatic incident X-ray beam with a continuous projection signal). As artefacts contain nearly all aspects of nonideal images, the discussion is limited here to the most common imaging errors [91, 112, 129, 133, 134]:

I. Beam hardening

Beam hardening is a phenomenon associated with the use of polychromatic radiation. This occurs due to the fact the average photon energy of the incident X-ray beam increases along its path (*i.e.* with

increasing material thickness), as the lower energy photons are absorbed at a significantly higher rate compared to the more energetic counterparts (photoelectric effect). As a result, the beam becomes proportionately richer in high-energy photons (*i.e.* 'harder', with more penetrating power); hence the term 'beam hardening'. In conjunction with beam scattering, this leads to streaking and shading artefacts, as well as cupping in the reconstructed slices of a uniformly dense object, that is, a radial gradient in attenuation: low values at the interior centre and high values at the periphery. As noted in **Section 2.3.5**, beam hardening is not common in SRCT, where monochromatic radiation is used.

II. Metal artefacts

Highly attenuating metal inclusions may cause under-range values to be registered by the acquisition electronics. In turn, this leads to photon starvation, with the reconstructed slices being dominated by high intensity streak patterns. Given that the probability of the photoelectric effect is approximately proportional to the cube of the atomic number of the interacting atom (see **Section 2.3.1**), the presence of heavy metal inclusions also promotes excessive beam hardening.

III. Ring artefacts

Rings artefacts are identifiable as concentric dark or bight rings around the centre of rotation (*i.e.* rotation axis) of the reconstructed volumes. These occur due to electronic defects, that is, the failure or miscalibration of an individual detector element or corresponding processing channel. Therefore, during image acquisition, the erroneous greyscale information associated with a malfunctioning detector element causes the development of rings.

IV. Motion artefacts

Changes in the morphology of an object to be imaged (*e.g.* due to loading), misalignment of the mid-axis of the specimen relative to the centre of rotation of the stage, and temporal variations of the attenuation coefficients, produces reconstructions with fluctuating data biases (*i.e.* data acquired during rotation is inconsistent). Typically, this is visible as blurring in the reconstructed slices. As motion artefacts are minimized considerably by decreasing the acquisition time, they are not so frequently encountered in synchrotron-based experiments (see **Section 2.3.5**).

V. Scattering artefacts

Scattering artefacts are common in conventional X-ray sources, particularly for cone beam configurations (see **Section 2.3.3**). Excluding geometric unsharpness, these are generated by spurious rays not traveling along the source-detector pathway due to the Compton effect. This implies that not all of the radiation that reaches the detector is comprised of primary photons (*i.e.* generated by the

photoelectric effect) – notwithstanding, that at the energies used in this project, the photoelectric effect remains dominant (see **Section 2.3.1**). The random deflection angle of the scattered photons yields an intensity distribution at the detector described by a low frequency background signal. When this is merged with the primary photon attenuation, the superimposed signal results in a projection with a diminished contrast. Overall, low frequency scatter signal provides little information with respect to the specimen imaged, however, it promotes projection noise. As such, scattering artefacts causes a reduction in the signal- and contrast-to-noise ratio.

It is worth stating that some artefacts (*e.g.* ring artefacts) can be corrected using various post-processing tools, others mitigated during the experimental campaign (*e.g.* motion artefacts), while some are inherent to the imaging hardware used (*e.g.* beam hardening).

2.4 Digital Volume Correlation

2.4.1 Bulk deformation and strain measurement methods

Characterizing volumetric deformation and damage is a challenging task. In conjunction with non-destructive, non-invasive imaging methods, Digital Volume Correlation is one of the few tools currently in existence capable of quantifying the internal/bulk microstructural responses of a material between different load states, by extracting relevant parameters (*e.g.* local displacements and strains) [135]. High-resolution Micro-focus Computed Tomography (μCT) remains the primary image modality used to capture the underlying volume images required for DVC [131, 136-145], although not unique [131]. For example, Confocal Microscopy (CM) [146, 147], Magnetic Resonance Imaging (MRI) [148, 149] and Optical Coherence Tomography (OCT) [150] techniques have also been paired with DVC – notwithstanding that OCT requires semi-transparent, light scattering materials, and is an alternative imaging approach to fluorescence microscopy. As a result, for opaque materials, such as carbon-fibre reinforced polymers, X-ray CT is preferred. While both μCT and SRCT can deliver usable sub-micrometre voxel resolution levels, superior scans are commonly achieved through SRCT. Furthermore, as noted in **Section 2.3.5**, μCT is characterised by significantly longer scanning times on the order of hours, as opposed to seconds for SRCT [91], particularly at sub-micrometre resolutions. This may be expected to promote hold-at-load artefacts near composite failure, whereby the viscoelastic response of the polymer matrix may result in time-dependent strain variation and subsequent failure of UD composites [151-154].

Small-angle X-ray scattering (SAXS) and wide-angle X-ray diffraction (WAXD) using brilliant synchrotron radiation sources are two effective alternatives to DVC for investigating bulk structure changes of materials during deformation. Sugimoto *et al.* [155] performed *in situ* SAXS and WAXD measurements during axial compression tests of composite strands of PAN-based carbon-fibres and investigated the changes in the microvoid and crystallite structure, respectively. They have shown that the longitudinal length of microvoids, the orientation parameter of the carbon layer stacks and the orientation parameter of the microvoids decreased approximately linearly with increasing axial compression stress on to the fibre. Loidl *et al.* [156] conducted *in situ* WAXD during tensile tests of single carbon-fibres (both PAN and pitch) and determined the Young and shear modulus, respectively, of the carbon layer stacks. They have shown that the moduli varied between the different fibre types (*i.e.* processing), depending on the initial orientation of the respective carbon layer stacks. Kobayashi *et al.* [157] performed *in situ* WAXD during tensile tests of PAN-based carbon-fibre specimens with a different Young bulk modulus, and determined the corresponding 'apparent' modulus of the carbon layer stacks (*i.e.* crystallites). The crystallite modulus was reported to be different for specimens with a different bulk modulus, suggesting that the stress distribution in the carbon-fibres is not homogenously

distributed between the crystalline and amorphous regions, thereby giving rise to stress concentrations, and triggering fibre fracture.

Other bulk deformation and strain measurement methods involve the use of optical fibres. Sánchez *et al.* [158] embedded a single optical fibre sensor in a carbon-fibre/epoxy-based panel to measure the development of residual strain through *in situ* and in real-time monitoring of the manufacturing process, from the resin infusion to the curing cycle. This was placed from the top to the bottom layers, resulting in multi-layer configuration with a continuous measurement. They have shown that it was possible to track the strain induced along the composite panel throughout the curing and cooling stages, giving information about the distribution of the resin, its physical changes and the thermal effects this had within the composite ply. Munzke *et al.* [159] distributed a series of optical sensors, which were wrapped during the hoop and helical winding of a hybrid type IV composite pressure vessel, resulting in a multi-layer configuration with multiple measurement channels. Strain sensing was performed across the helical and hoop layers for a total number of 252,000 load cycles until vessel burst. They have shown that fatigue could be monitored and spatially localized (*e.g.* strain evolution was more significant in the dome with the connection port), with critical material changes observed at 17,000 cycles before failure. Strain sensing was accompanied by acoustic emission analysis, which was useful to detect predominantly fast damage processes such as fibre breaks and/or matrix cracks.

One limitation of the techniques described above is the difficulty in superimposing the strain onto the underlying bulk microstructure, as often there is no direct visualization at a volumetric level. DVC is, therefore, the only tool that offers the possibility of full-field strain investigations directly overlaid with the internal microstructure of an opaque material (*i.e.* deep structure) under load. The underlying prerequisite for DVC is that volume images ideally contain a stochastic, isotropic contrast pattern for reliable tracking of unique regions in all directions [7]. The contrast pattern deforms together with the specimen, acting as a carrier of deformation information [160], and may be given by an array of naturally occurring inclusions (*e.g.* Al-Si alloys [131]), the material texture (*e.g.* polyurethane foam [139], bone [141], citrus fruits [144]), or by artificially introduced features (*e.g.* Cu particles [138], $ZrSiO_4$-bearing ceramic spheres [145]). This is a fundamental difference from the two-dimensional DIC technique, in which such a pattern, with adjustable homogeneity and contrast, can be readily applied on the surface of a specimen (*e.g.* through the application of black/white paint), resulting in what is commonly known as a 'speckle pattern' [160]. Undoubtedly, this may be a considerable challenge, as in order to apply DVC to materials lacking a suitable microstructure, it is necessary to enhance the available bulk contrast by modifying the internal architecture of the material, whilst preserving the mechanical behaviour of the particle-free counterpart; a notable example being unidirectional carbon-fibre reinforced polymer composites as used in this project.

In addition, the noise and sensitivity of the DVC measurements are affected by a series of factors, such as the imaging hardware used (*e.g.* µCT or SRCT) and the nature of the material/specimen under investigation [140, 142]. Likewise, DVC is affected by the processing parameters used (*i.e.* sub-set size, overlap percentage *etc*., see below), and exhibits spatial resolution limitations, meaning that accurate measurements are not trivial at the smallest possible scale [161]. This implies that the apparent local displacement and/or strain fields cannot always be directly correlated with the 'true' response of the microstructure. However, these spatial resolution limitations have been somewhat resolved, given the significant steps forward achieved in recent years, by the use of X-ray CT combined with *in situ* loading to identify detailed sequences of damage accumulation down to fibre-level, in 3D, within the bulk of real engineering materials under load [2, 3, 60, 71, 72, 104]. As such, given the direct visualization capabilities, it is valuable to consider the coupling of state-of-the-art CT imaging methods with Digital Volume Correlation for a strain-based quantification of the local deformation surrounding fibre break sites in representative CFRPs subjected to a continuously applied load.

2.4.2 Technique description

Digital Volume Correlation is essentially an extension of the white-light illumination, two-dimensional DIC technique [160]. DVC was developed for volumetric measurements, and initially demonstrated by Bay *et al.* [162] as a means to estimate the effective continuum (level) strain tensor in trabecular bone subjected to axial compression. The global spatial domain is composed of a number of voxels (rather than area pixels) rendered for visual display, that in reality is a 3D digital array of discrete greyscale intensity levels (**Figure 2-34**). In the context of X-ray Computed Tomography, these values represent the radiation interaction (attenuation) averaged over a voxel.

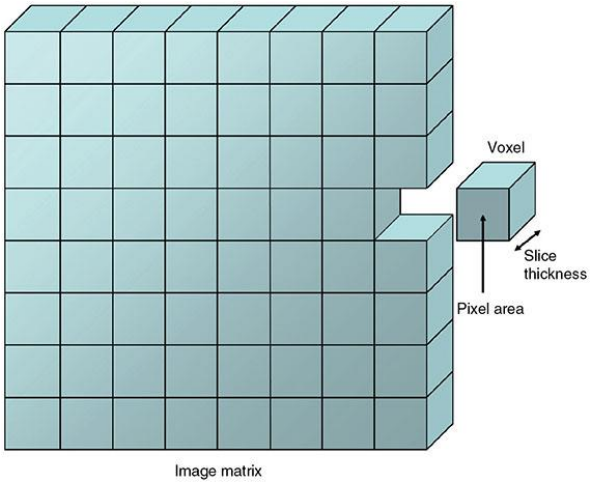

Figure 2-34 – Image matrix showing the in-plane domain (pixels) and volumetric domain (voxels) [163].

The DVC process (**Figure 2-35**) essentially starts with the selection of a region of interest, comprising a number of voxels, over which displacements are expected to be computed. It is critical that the same region exists in both of the undeformed and deformed volumes. Next, the initial region of interest is divided into sub-sets (typically cubic in shape), followed by the correlation of each individual sub-set. Analogous to DIC, the sub-sets are sized proportionally to the scale of the contrast pattern available, *i.e.* a microscale contrast pattern allows for smaller sub-sets to be used, while a macroscale contrast pattern typically requires coarser sub-sets. The deformed dataset is then systematically searched for these corresponding sub-sets, allowing the local 3D shift (displacement) vector to be estimated between the centroids of the initial undeformed (reference) and deformed (target) sub-sets [7]. Finally, 3D strain field estimation may be carried out through a centred finite difference scheme to determine the numerical derivatives of the vector field [140, 139, 164, 165].

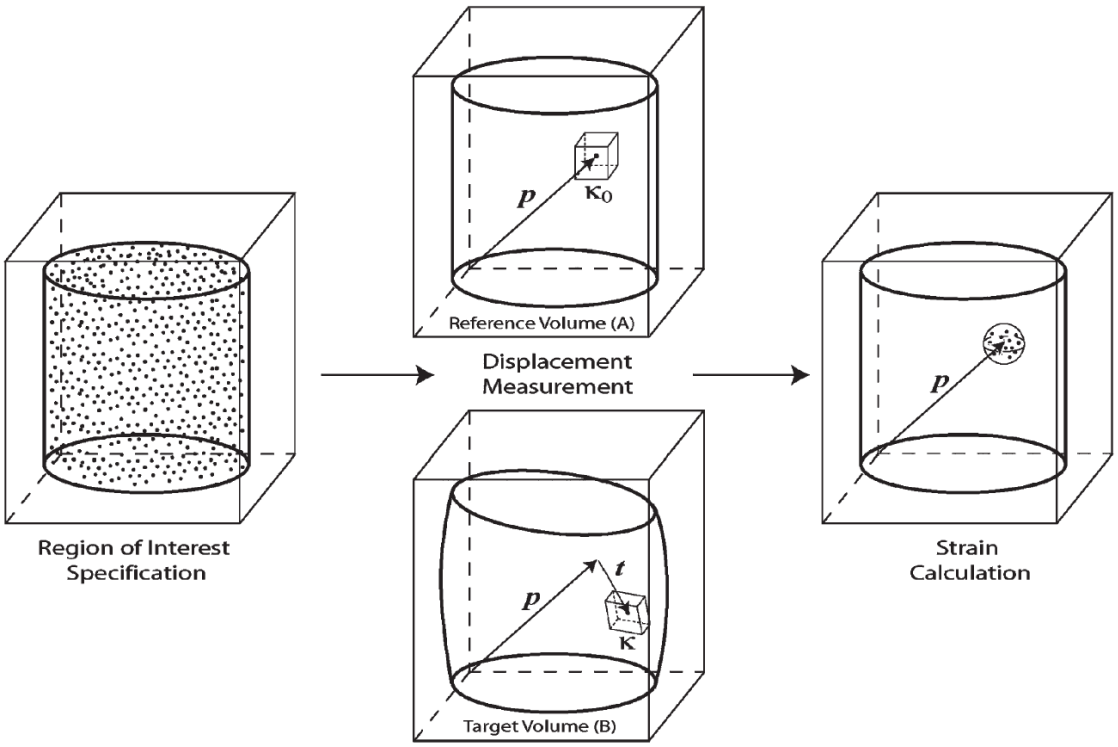

Figure 2-35 – Schematic diagram of the DVC process. For a given measurement point 'p', the displacement is given by the vector 't', which connects the centroids of the reference sub-set 'k_0' and deformed sub-set 'k', respectively [7].

Mathematically, the degree of matching may be quantified with the correlation coefficient *'C'*, which is maximal for an optimized conservation of the grey-levels between a reference and deformed sub-set [140, 164, 166, 167]. In the simplest one-dimensional (1D) form, this may for example be given by the following cross-correlation function [166]:

$$C_i = \sum_{i=x_0}^{x_0+N-1} A(i)B(i+dx)$$

Equation 2-9

where *'A(i)'* is the is the grey-level intensity of a voxel at position *'i'* in a reference sub-set *'A'*, *'B(i+dx)'* is the intensity of a voxel at the shifted position *'(i+dx)'* in a deformed sub-set *'B'*, *'dx'* is the current shift and *'N'* is the window size or number of overlaps. By varying the shift *'dx'* over a certain range, as shown in **Figure 2-36**, a symmetrical correlation peak is obtained. The optimized match is obtained when the shift *'dx'* provides a maximal value of this objective function [166].

Real images are prone to experiencing grey-level intensity fluctuations between deformation states. To account for such imaging inconsistencies, most cross-correlation algorithms utilize a normalized form of the correlation function [140, 164, 166-168]. In this normalized form, the correlation peak associated with a hypothetical perfect match will return a height of 1.0 [166]:

$$C_{norm}(i) = \frac{\sum_{i=x_0}^{x_0+N-1}(A(i)-\langle A\rangle)(B(i+dx)-\langle B\rangle)}{\sqrt{\sum_{i=x_0}^{x_0+N-1}(A(i)-\langle A\rangle)^2}\sqrt{\sum_{i=x_0}^{x_0+N-1}(B(i+dx)-\langle B\rangle)^2}}$$

Equation 2-10

where

$$\langle A\rangle = \sum_i \frac{A(i)}{N}$$

and

$$\langle B\rangle = \sum_i \frac{B(i+dx)}{N}$$

The simple 1D example can be expanded for two, or three dimensions. In case of 2D images, the correlation implies a range of shifts *'dx'* and *'dy'*, while for 3D datasets, *'dz'* is also accounted for [166].

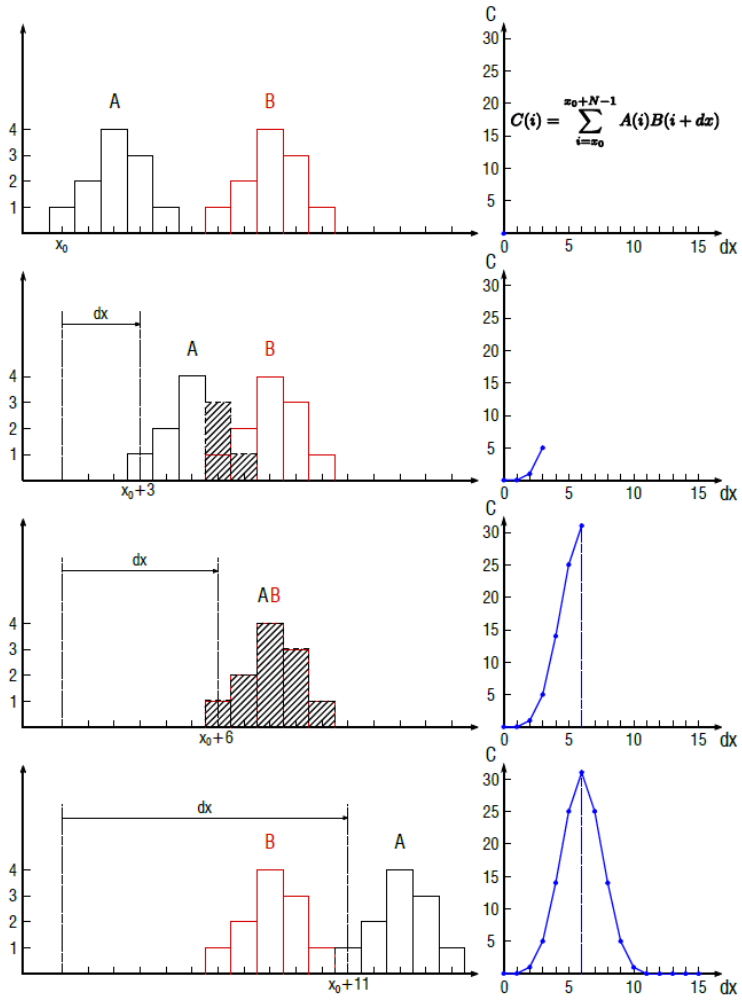

Figure 2-36 – An example of a simple 1D cross-correlation. The reference pattern 'A' is shifted through the space of the displaced pattern 'B' by integer increments of 'dx'. For each shift 'dx' the product of the height of pairs of overlapping bars from A and B is calculated, and the sum of these products returns the corresponding correlation coefficient (right-hand side of the figure). The correlation coefficient reaches its maximum at 'dx = 6', when the patterns exhibits an optimized match. Increasing the shift 'dx' even further causes the correlation coefficient to decrease. As a result, the best match is given by the maximum of the correlation peak [166].

From an implementation perspective, the recognition of matching sub-sets between the deformation states may be performed either via a Fast Fourier Transform (FFT) implementation, referred to as 'FFT', or via a multi-step strategy, whereby a global pre-shift is computed through the 'FFT' approach, followed by Direct Correlation – 'DC' [141, 166]. While both algorithms use a normalized form of the cross-correlation function and support a multi-pass approach for a successive refinement of the vector field [140, 141, 164, 166], the key difference between 'FFT' and 'DC' lies in the use of a Fourier space for the calculation in the former, rather than a direct coupling for the latter (*i.e.* it directly sums the products of voxel grey-level intensities of the initial and deformed sub-sets to form a 3D correlation map) [141]. Furthermore, 'FFT' is characterized by inherently faster processing times [141], and always returns the full correlation map for all possible shifts within the constraints of the volume analysed [166]. Hence, it is ideally suited to be used as an initial step to find large

shifts, such as those caused by rigid body displacements. In contrast, the computational cost of 'DC' scales with the size of the correlation map (*i.e.* the cube of the peak search radius). As the search radius must be large enough to encompass the local displacement, this may involve extended processing times for large deformation gradients [166].

To fulfil the correlation objective, the sub-sets may be considered to undergo deformation. This is characterised by a transformation, which is also known as a shape function. Typically, translation is the primary transformation of interest, as this provides the initial estimate of the displacement vector (*e.g.* as illustrated in **Figure 2-36**). Other transformations such as normal strain, shear strain and rotation may be invoked to improve the degree of matching, when the associated modes are significant over a sub-set. Each of the transformations adds degrees of freedom (DOFs) to the system, and the advantage of using a linear (affine) transformation for example, is that of managing computational cost by allowing the selection/deselection from the correlation process [7]. In this regard, Smith *et al.* [168] have shown that when non-translational deformations were present within the volumetric region of interest, such as rigid body rotations (15° of uniaxial rotation), mean displacement errors during correlation were relatively high if only a translation-capable shape function was implemented (3.328 voxels or 116.47 µm), compared to allowing linear transformations with higher DOFs (0.0057 voxels or 0.20 µm); which included both translation and rotation, respectively.

The commercial DaVis v10 code [166], for example, employs for both 'FFT' and 'DC' an equivalent of a piece-wise linear shape function for the reference-deformed mapping. However, a trilinear interpolation is used in 'FFT', and a third-order spline interpolation in 'DC', to compute the greyscale intensities of each displayed voxel at non-integer positions (*i.e.* sub-voxel measurements) [140, 141, 164]. Palanca *et al.* [141] have shown that measurement uncertainties both in terms of displacement and strain were up to several orders of magnitude higher for 'FFT' than for 'DC', depending on the sub-set size and material used (cortical or trabecular bone). As it is expected that a linear interpolator will not represent sub-voxel measurement as well as its spline counterpart, the majority of the DVC analyses performed in this project rely on the 'DC' algorithm, which benefits from the superior interpolator.

2.4.3 Effect of sub-set size

One of the key parameters that affect the DVC output measurements is the size of the sub-set. The sub-set must be large enough to ensure that during the correlation process it encompasses a sufficiently unique contrast pattern, that can be distinguished from other sub-sets to avoid a case of false correlation [169].

As extensively reported in the literature by Wang *et al.* [131], Liu *et al.* [136], Gillard *et al.* [140], Palanca *et al.* [142] and Borstnar *et al.* [167], the use of smaller sub-sets produces higher displacement measurement errors,

which in turn are responsible for lower strain resolutions. An excessively large sub-set on the other hand will compromise spatial resolution [170], as the underlying deformation will not be captured (*i.e.* the sub-set size effectively smooths or filter the underlying strain patterns). The latter occurs because the final displacement of the sub-set is calculated by the average displacement of all the voxels contained within [167]. As a result, an optimal sub-set size may be identifiable, above which no further significant improvements are made.

2.4.4 Effect of sub-set overlap

One possible approach to resolve the spatial sampling issues arising from finite sub-set sizes is the use of overlapping. Instead of placing neighbouring sub-sets directly next to each other, they may be positioned at a distance *'d'* away from the centroid of the first sub-set, where *'d'* is smaller than the edge length *'L'* of the sub-set in voxel. As shown in **Figure 2-37**, the sub-sets are now overlapped, with the spacing between the sub-sets given by *'d'*, which is also known as the step size. The overlapping percentage *'P'* is given by [166]:

$$P = \frac{L - d}{L} \times 100$$

Equation 2-11

Overlapping provides the opportunity to increase the spatial density of the grid, and implicit that of the vector field, without reducing the actual size of the sub-set. Nevertheless, it must be highlighted that as the sub-set size remains unchanged, displacements are still averaged over the same region of space [166].

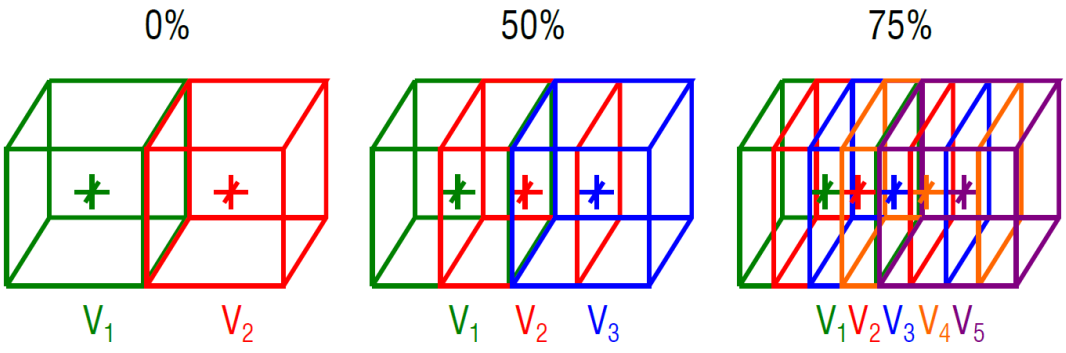

Figure 2-37 – Schematic illustration showing different sub-set overlapping percentages. Spatial density of sub-sets is increased, without reducing the actual size [166].

2.4.5 Previous uses of Digital Volume Correlation on fibre-reinforced polymers

Literature on the DVC technique applied to fibre-reinforced materials is relatively sparse, however, several studies may be identified to be relevant. Brault *et al.* [138] investigated transverse shear effects in a ten-ply unidirectional CFRP subjected to a three-point bending test. A combination of *in situ* μCT and DVC were used. To generate individual features unique to a particular sub-set, which provided X-ray contrast/attenuation, they have introduced Cu particles (150 μm, 5 wt. %) within the epoxy matrix. The DVC was shown to give a good evaluation (uncertainty of 0.04 voxels, 52 μm voxel size) of the mechanical response of the composite specimen under bending load, highlighting the transverse shear effects, including the warping of the cross-section. Tensile tests in the direction of the fibres were also conducted to analyse the response of the composite with and without particles. Results yielded a difference of only 1 % on the longitudinal modulus of the two configurations, concluding that the addition of particles did not have a major impact on the mechanical behaviour of the material.

Borstnar *et al.* [167] presented the first use of DVC on particle-toughened CFRPs to map out the strain fields ahead of a Mode I delamination using *in situ* SRCT. They investigated the behaviour of a sixteen-ply unidirectional laminate, which included three different secondary-phase thermoplastic particles (∼13 % vol.). These were confined to a ∼30 μm interlayer at each ply interface. One system (Mat. 'A') was identified with 5-20 μm irregularly shaped particles, while another (Mat. 'B') with a more regular geometry and a size between 5 and 10 μm. The third system (Mat. 'C') was recognized as a hybrid, containing particles as featured in Mat. 'A' as well as other particles which could not be resolved in the CT data. The particles were shown to respond to the applied load: particle debonding occurred ahead of the crack tip, followed by crack coalesce and the formation of bridging ligaments (*i.e.* bulk resin located between debonded particles or a mixture of resin and debonded particles) in the crack wake. In this regard, Mat. 'A' and Mat. 'B' were characterized by a more gradual increase in opening strain, compared to Mat. 'C'. This was found to be consistent with the micromechanical observations, whereby Mat. 'C' failed in a different manner featuring both inter- and intralaminar failure. A clear distinction needs to be made, in that here the particles were present already in the material to improve the interlaminar toughness of the composite, while in [138], they fulfilled the role of a fiducial marker system only. While the underlying role of the particles is distinctly different (mechanical *vs.* imaging), for the DVC technique, the contribution of the particles is equivalent, improving sub-set trackability. As such, displacement measurements in [167] were only accurate within the interlayers, where the contrast pattern was unique to a specific sub-set.

Lecomte-Grosbras *et al.* [171] investigated the free-edge effects in a glass-fibre reinforced polymer (GFRP) composite with a $[15/-15]_s$ stacking sequence, subjected to uniaxial tension. *In situ* DIC was combined with μCT-based DVC to measure the displacements upon loading/unloading at different scales, and to extract the

3D residual displacement field following the removal of the specimen from the loading rig. They have shown that at a mesoscopic scale (corresponding to a plane orthogonal to the ply direction), the displacement component along the loading axis exhibited sharp variations at the ply interfaces between the different orientations. At a macroscopic scale (corresponding to a plane parallel to the specimen length), steep displacement gradients were obtained close to the free surface of the sample. The residual displacement fields revealed displacement discontinuities at the interlaminar interfaces, which in turn were linked with initiation of delamination, as well as accumulation of irreversible strains near the delaminated interface. Microscopy was used to validate the DIC/DVC analysis, by means of which delamination microcracking was observed on the edges of the samples. It is also worth noting in a GFRP composite, the contrast between the glass-fibres and the epoxy matrix is superior, which allowed for reliable DVC measurements, albeit at a tow-level. In addition, for a given voxel and sub-set size, the effective resolution is improved (*i.e.* material is scaled up) due to the larger fibres, which are on the order of 20 μm (compared to ~7 μm for carbon).

Mendoza *et al.* [172] used Digital Volume Correlation as comparison (differentiating) tool, based on full-field displacement and strain measurements of woven composites under static conditions. In conjunction with μCT, they have shown that it was feasible to study the 'metric' (*e.g.* yarn displacements/deformations) and 'topological differences' (*e.g.* weaving anomalies, such as the occurrence of missing/extra yarns), respectively, within the textile. The 'metric differences' focused on a pair of volumes, which corresponded to two preform specimens manufactured after a specific weaving pattern. These specimens only contained the woven yarns, *i.e.* the reinforcement phase of the composite, with neither of the specimens containing anomalies. However, being different samples, their yarn disposition was not strictly identical. The 'topological differences' relied on a second pair of volumes, which corresponded to two injected specimens manufactured with a different weaving pattern from the first pair. In contrast to the first pair, these specimens contained intentional weaving anomalies, such as missing yarns. The study, thereby, provided insight into the variability of the manufacturing processes, and served as a non-destructive testing technique, through which microstructural anomalies were identified.

2.5 Summary and conclusions

The failure of CFRP laminates in tension is recognized to encompass multiple interacting damage mechanisms, occurring over varying length-scales, whereby that the failure of fibres within 0° plies is regarded as a controlling final failure mechanism. Carbon-fibres are brittle in nature, and exhibit fibre strength stochasticity, which is typically presumed to follow a Weibull distribution. The accuracy of the parameters of a particular Weibull model are, however, noted to be strongly influenced by the testing methodology (*e.g.* the gauge length adopted, as well the number of specimens tested). In parallel with the fibre strength, the level of

adhesion between the matrix and fibres is reported to have a fundamental role in the load-bearing capacity of such composites. More specifically, the ineffective length of a broken fibre, and the associated stress concentrations in the neighbouring intact fibres, were reported to be distributed over greater distances for a poor interfacial adhesion. This may lead to the development of earlier and larger clusters of breaks, and subsequently promote premature failure. Ultimately, this implies that predicting the failure of a UD composite laminate loaded in tension is not a trivial task, leaving unanswered questions with regards to the actual mechanisms governing the final failure of representative specimens (*i.e.* with realistic fibre volume fractions, containing thousands of fibres embedded in the matrix material).

Contemporary models (such as those summarized in [97]) have revealed that despite using the same input parameters, the estimate of failure strength and strain, as well as the behaviour of fibre breaks and clusters, can be distinctly different. A key element responsible for these discrepancies was the size of the affected gauge volume surrounding a fibre break, which in turn is given by the ineffective and overload length, respectively. Ultimately, this provides a specific indicator of the stress/strain transfer processes, that can then be compared against models developed by fellow researchers. However, to date, such detailed measurements in relation to fibre failure events are not available from the bulk of representative materials.

In this context, and building on the latest SRCT work available in the literature, there is an interest in visualizing fibre breaks and clustering events at a sufficiently high level of detail to quantify/map the local load shedding phenomenon, whilst providing the acquisition speed to minimize hold-at-load artefacts and beam exposure, with sufficient throughput of load steps. Whilst determination of internal displacement/strain measurements via SRCT and DVC within deforming microstructures has become popular in recent years, the work of Borstnar *et al.* [167] has revealed significant uncertainties in analysing the fibres contained within the individual plies that make up a representative composite specimen. This is due to the cylindrical structure and smooth surfaces of the filaments which lack a well-defined, trackable contrast pattern along the fibre direction, leading to poor image correlation, and correspondingly inaccurate displacement estimates parallel to this axis [167]. However, as noted by Brault *et al.* [138], this intrinsic limitation for DVC can be resolved by doping the matrix with sparse populations of particles. These act as displacement trackers (*i.e.* fiducial markers) by providing the required X-ray contrast/attenuation. Nonetheless, it is acknowledged that the particle composition, size and concentration must be chosen such that macro- and micromechanical responses of the doped CFRP must be understood to confirm suitability as a model system for mechanistic investigations.

2.6 References

[1] P. J. Schilling, B. R. Karedla, A. K. Tatiparthi, M. A. Verges and P. D. Herrington, "X-ray computed microtomography of internal damage in fiber reinforced polymer matrix composites," *Composites Science and Technology,* vol. 65, no. 14, pp. 2071-2078, 2005.

[2] P. Wright, A. J. Moffat, I. Sinclair and S. M. Spearing, "High resolution tomographic imaging and modelling of notch tip damage in a laminated composite," *Composites Science and Technology,* vol. 70, no. 10, pp. 1444-1452, 2010.

[3] A. E. Scott, M. N. Mavrogordato, P. Wright, I. Sinclair and S. M. Spearing, "In situ fibre fracture measurement in carbon-epoxy laminates using high resolution computed tomography," *Composites Science and Technology,* vol. 71, no. 12, pp. 1471-1477, 2011.

[4] Y. Swolfs, R. M. McMeeking, I. Verpoest and L. Gorbatikh, "Matrix cracks around fibre breaks and their effect on stress redistribution and failure development in unidirectional composites," *Composites Science and Technology,* vol. 108, pp. 16-22, 2015.

[5] A. S. Kaddour, M. J. Hinton, P. A. Smith and S. Li, "The background to the third world-wide failure exercise," *Journal of Composite Materials,* vol. 47, no. 20-21, pp. 2417-2426, 2013.

[6] M. J. Hinton and P. D. Soden, "Predicting failure in composite laminates: The background to the exercise," *Composites Science and Technology,* vol. 58, no. 7, pp. 1001-1010, 1998.

[7] B. K. Bay, "Methods and applications of digital volume correlation," *Journal of Strain Analysis for Engineering Design,* vol. 43, no. 8, pp. 745-760, 2008.

[8] Y. Nukushina, J. Matsui and M. Itoh, "On the tensile load to elongation response of carbon fibre single filament samples," *Journal of the Japan Society for Composite Materials,* vol. 15, no. 5, pp. 210-221, 1989.

[9] F. Islam, S. Joannès and L. Laiarinandrasana, "Evaluation of critical parameters in tensile strength," *Journal of Composites Science,* vol. 3, no. 3, pp. 1-17, 2019.

[10] F. Mesquita, Y. Swolfs, S. Bucknell, Y. Leray, S. V. Lomov and L. Gorbatikh, "Tensile properties of single carbon fibres tested with automated equipment," in *The 22nd International Conference on Composites Materials*, Melbourne, Australia, 2019.

[11] G. J. Curtis, J. M. Milne and W. N. Reynolds, “Non-Hookean behaviour of strong carbon fibres,” *Nature,* vol. 220, pp. 1024-1025, 1968.

[12] M. Guigon, A. Oberlin and G. Desarmot, “Microtexture and structure of some high tensile strength, PAN-base carbon fibres,” *Fibre Science and Technology,* vol. 20, no. 1, pp. 55-72, 1984.

[13] Y. Huang and R. J. Young, “Non-linear elasticity in carbon fibres,” *Journal of Materials Science Letters,* vol. 12, pp. 92-95, 1993.

[14] Y. Swolfs, I. Verpoest and L. Gorbatikh, “A review of input data and modelling assumptions in longitudinal strength models for unidirectional fibre-reinforced composites,” *Composite Structures,* vol. 150, pp. 153-172, 2016.

[15] A. A. Griffith, “The phenomena of rupture and flow in solids,” *Philosophical Transactions of the Royal Society A,* vol. 221, no. 582-593, pp. 163-198, 1921.

[16] S. C. Bennett, D. J. Johnson and W. Johnson, “Strength-structure relationships in PAN-based carbon fibres,” *Journal of Materials Science,* vol. 18, pp. 3337-3347, 1983.

[17] F. Tanaka, T. Okabe, H. Okuda, I. A. Kinloch and R. J. Young, “Factors controlling the strength of carbon fibres in tension,” *Composites Part A,* vol. 57, pp. 88-94, 2014.

[18] K. L. Pickering and T. L. Murray, “Weak link scaling analysis of high-strength carbon fibre,” *Composites Part A,* vol. 30, no. 8, pp. 1017-1021, 1999.

[19] J. D. H. Hughes, “The evaluation of current carbon fibres,” *Journal of Physics D,* vol. 20, no. 3, pp. 276-285, 1987.

[20] I. J. Beyerlein and S. L. Phoenix, “Statistics for the strength and size effects of microcomposites with four carbon fibers in epoxy resin,” *Composites Science and Technology,* vol. 56, no. 1, pp. 75-92, 1996.

[21] W. Weibull, “A statistical distribution function of wide applicability,” *Journal of Applied Mechanics,* vol. 18, no. 3, pp. 293-297, 1951.

[22] S. Mahesh, S. L. Phoenix and I. J. Beyerlein, “Strength distributions and size effects for 2D and 3D composites,” *International Journal of Fracture,* vol. 115, pp. 41-85, 2002.

[23] J. Watanabe, F. Tanaka, H. Okuda and T. Okabe, “Tensile strength distribution of carbon fibers at short gauge lengths,” *Advanced Composite Materials,* vol. 23, no. 5-6, pp. 535-550, 2014.

[24] J. Yao, W. Yu and D. Pan, “Tensile strength and its variation of PAN-based carbon fibers. III. Weak-link analysis,” *Journal of Applied Polymer Science,* vol. 110, no. 6, pp. 3778-3784, 2008.

[25] J. B. Jones, J. B. Barr and R. E. Smith, “Analysis of flaws in high-strength carbon fibres from mesophase pitch,” *Journal of Materials Science,* vol. 15, pp. 2455-2465, 1980.

[26] W. A. Curtin, “Tensile strength of fiber-reinforced composites: III. Beyond the traditional Weibull model for fiber strengths,” *Journal of Composite Materials,* vol. 34, no. 15, pp. 1301-1332, 2000.

[27] F. C. Campbell, Structural composite materials. Chapter 1 – Introduction to composite materials, 1st ed., Russell Township, OH, USA: ASM International, 2010, pp. 1-29.

[28] A. N. Netravali, R. B. Henstenburg, S. L. Phoenix and P. Schwartz, “Interfacial shear strength studies using the single-filament-composite test. I: Experiments on graphite fibers in epoxy,” *Polymer Composites,* vol. 10, no. 4, pp. 226-241, 1989.

[29] J. M. Hedgepeth, “Stress concentrations in filamentary structures (NASA-TN-D-882, L-1502),” NASA Langley Research Center, Hampton, VA, USA, 1961.

[30] J. M. Hedgepeth and P. Van Dyke, “Local stress concentrations in imperfect filamentary composite materials,” *Journal of Composite Materials,* vol. 1, no. 3, pp. 294-309, 1967.

[31] C. Zweben, “Tensile failure of fiber composites,” *AIAA Journal,* vol. 6, no. 12, pp. 2325-2331, 1968.

[32] H. Fukuda, “Stress concentration factors in unidirectional composites with random fiber spacing,” *Composites Science and Technology,* vol. 22, no. 2, pp. 153-163, 1985.

[33] Z. Xia, W. A. Curtin and T. Okabe, “Green's function vs. shear-lag models of damage and failure in fiber composites,” *Composites Science and Technology,* vol. 62, no. 10-11, pp. 1279-1288, 2002.

[34] Z. Xia, T. Okabe and W. A. Curtin, “Shear-lag versus finite element models for stress transfer in fiber-reinforced composites,” *Composites Science and Technology,* vol. 62, no. 9, pp. 1141-1149, 2002.

[35] Y. Huang and R. J. Young, “Analysis of the fragmentation test for carbon-fibre/epoxy model composites by means of Raman spectroscopy,” *Composites Science and Technology,* vol. 52, no. 4, pp. 505-517, 1994.

[36] M. R. Piggott, “Why interface testing by single-fibre methods can be misleading,” *Composites Science and Technology,* vol. 57, no. 8, pp. 965-974, 1997.

[37] T. H. Cheng, J. Zhang, S. Yumitori, F. R. Jones and C. W. Anderson, “Sizing resin structure and interphase formation in carbon fibre composites,” *Composites,* vol. 25, no. 7, pp. 661-670, 1994.

[38] M. Guigon and E. Klinklin, “The interface and interphase in carbon fibre-reinforced composites,” *Composites,* vol. 25, no. 7, pp. 534-539, 1994.

[39] S. Yumitori, D. Wang and F. R. Jones, “The role of sizing resins in carbon fibre-reinforced polyethersulfone (PES),” *Composites,* vol. 25, no. 7, pp. 698-705, 1994.

[40] J. P. Favre and J. Perrin, “Carbon fibre adhesion to organic matrices,” *Journal of Materials Science,* vol. 7, pp. 1113-1118, 1972.

[41] A. Paipetis and C. Galiotis, “Effect of fibre sizing on the stress transfer efficiency in carbon/epoxy model composites,” *Composites Part A,* vol. 27, no. 9, pp. 755-767, 1996.

[42] L. T. Drzal, M. J. Rich and P. F. Lloyd, “Adhesion of graphite fibers to epoxy matrices: I. The role of fiber surface treatment,” *The Journal of Adhesion,* vol. 16, no. 1, pp. 1-30, 1983.

[43] L. T. Drzal, M. J. Rich, M. F. Koenig and P. F. Lloyd, “Adhesion of graphite fibers to epoxy matrices: II. The effect of fiber finish,” *The Journal of Adhesion,* vol. 16, no. 2, pp. 133-152, 1983.

[44] Michelman, “Industrial manufacturing – Reinforced plastic composites – Fiber Sizing,” [Online]. Available: https://www.michelman.com/Industrial-Manufacturing/Reinforced-Plastic-Composites/Fiber-Sizing/. [Accessed 16 07 2020].

[45] C. DiFrancia, T. C. Ward and R. O. Claus, “The single-fibre pull-out test. 1: Review and interpretation,” *Composites Part A,* vol. 27, no. 8, pp. 597-612, 1996.

[46] B. Miller, P. Muri and L. Rebenfeld, “A microbond method for determination of the shear strength of a fiber/resin interface,” *Composites Science and Technology,* vol. 28, no. 1, pp. 17-32, 1987.

[47] M. J. Pitkethly and J. B. Doble, “Characterizing the fibre/matrix interface of carbon fibre-reinforced composites using a single fibre pull-out test,” *Composites,* vol. 21, no. 5, pp. 389-395, 1990.

[48] M. Nishikawa, T. Okabe, K. Hemmi and N. Takeda, “Micromechanical modeling of the microbond test to quantify the interfacial properties of fiber-reinforced composites,” *International Journal of Solids and Structures,* vol. 45, no. 14-15, pp. 4098-4113, 2008.

[49] D. Tripathi and F. R. Jones, “Single fibre fragmentation test for assessing adhesion in fibre reinforced composites,” *Journal of Materials Science,* vol. 33, pp. 1-16, 1998.

[50] T. H. Cheng, F. R. Jones and D. Wang, “Effect of fibre conditioning on the interfacial shear strength of glass-fibre composites,” *Composites Science and Technology,* vol. 48, no. 1-4, pp. 89-96, 1993.

[51] C. Ageorges, K. Friedrich and L. Ye, “Experiments to relate carbon-fibre surface treatments to composite mechanical properties,” *Composites Science and Technology,* vol. 59, no. 14, pp. 2101-2113, 1999.

[52] A. Kelly and W. R. Tyson, “Tensile properties of fibre-reinforced metals: Copper/tungsten and copper/molybdenum,” *Journal of the Mechanics and Physics of Solids,* vol. 13, no. 6, pp. 329-350, 1965.

[53] T. Ohsawa, A. Nakayama, M. Miwa and A. Hasegawa, “Temperature dependence of critical fiber length for glass fiber-reinforced thermosetting resins,” *Journal of Applied Polymer Science,* vol. 22, no. 11, pp. 3203-3212, 1978.

[54] P. W. J. van den Heuvel, T. Peijs and R. J. Young, “Analysis of stress concentrations in multi-fibre microcomposites by means of Raman spectroscopy,” *Journal of Materials Science Letters,* vol. 15, no. 21, pp. 1908-1911, 1996.

[55] V. Chohan and C. Galiotis, “Interfacial measurements and fracture characteristics of 2D microcomposites using remote laser Raman microscopy,” *Composites Part A,* vol. 27, no. 9, pp. 881-888, 1996.

[56] F. M. Zhao and N. Takeda, “Effect of interfacial adhesion and statistical fiber strength on tensile strength of unidirectional glass fiber/epoxy composites. Part II: Comparison with prediction,” *Composites Part A,* vol. 31, no. 11, pp. 1215-1224, 2000.

[57] F. M. Zhao and N. Takeda, “Effect of interfacial adhesion and statistical fiber strength on tensile strength of unidirectional glass fiber/epoxy composites. Part I: Experiment results,” *Composites Part A,* vol. 31, no. 11, pp. 1203-1214, 2000.

[58] L. Mishnaevsky Jr. and P. Brøndsted, “Micromechanical modeling of damage and fracture of unidirectional fiber reinforced composites: A review,” *Computational Materials Science,* vol. 44, no. 4, pp. 1351-1359, 2009.

[59] T. Watanabe, Y. Takeichi, Y. Niwa, M. Hojo and M. Kimura, “Nanoscale in situ observations of crack initiation and propagation in carbon fiber/epoxy composites using synchrotron radiation X-ray computed tomography,” *Composites Science and Technology,* vol. 197, p. 108244, 2020.

[60] Y. Swolfs, H. Morton, A. E. Scott, L. Gorbatikh, P. A. S. Reed, I. Sinclair, S. M. Spearing and I. Verpoest, “Synchrotron radiation computed tomography for experimental validation of a tensile strength model for unidirectional fibre-reinforced composites,” *Composites Part A,* vol. 77, pp. 106-113, 2015.

[61] P. W. J. van den Heuvel, M. K. Wubbolts, R. J. Young and T. Peijs, “Failure phenomena in two-dimensional multi-fibre model composites. Part 5 – A finite element study,” *Composites Part A,* vol. 29, no. 9-10, pp. 1121-1135, 1998.

[62] B. W. Rosen, “Tensile failure of fibrous composites,” *AIAA Journal,* vol. 2, no. 11, pp. 1985-1991, 1964.

[63] C. Marston, B. Gabbitas, J. Adams, S. Nutt, P. Marshall and C. Galiotis, “Failure characteristics in carbon/epoxy composite tows,” *Composites Part A,* vol. 27, no. 12, pp. 1183-1194, 1996.

[64] P. W. J. van den Heuvel, T. Peijs and R. J. Young, “Failure phenomena in two-dimensional multi-fibre model composites. Part 2 – A Raman spectroscopic study of the influence of inter-fibre spacing on stress concentrations,” *Composites Science and Technology,* vol. 57, no. 8, pp. 899-911, 1997.

[65] Y. Swolfs, L. Gorbatikh, V. Romanov, S. Orlova, S. V. Lomov and I. Verpoest, “Stress concentrations in an impregnated fibre bundle with random fibre packing,” *Composites Science and Technology,* vol. 74, pp. 113-120, 2013.

[66] M. R. Nedele and M. R. Wisnom, “Three-dimensional finite element analysis of the stress concentration at a single fibre break,” *Composites Science and Technology,* vol. 51, no. 4, pp. 517-524, 1994.

[67] M. R. Nedele and M. R. Wisnom, “Stress concentration factors around a broken fibre in a unidirectional carbon fibre-reinforced epoxy,” *Composites,* vol. 25, no. 7, pp. 549-557, 1994.

[68] A. E. Scott, I. Sinclair, S. M. Spearing, A. Thionnet and A. R. Bunsell, “Damage accumulation in a carbon/epoxy composite: Comparison between a multiscale model and computed tomography experimental results,” *Composites Part A,* vol. 43, no. 9, pp. 1514-1522, 2012.

[69] A. Thionnet, H. Y. Chou and A. R. Bunsell, “Fibre break processes in unidirectional composites,” *Composites Part A,* vol. 65, pp. 148-160, 2014.

[70] Y. Swolfs, I. Verpoest and L. Gorbatikh, “Issues in strength models for unidirectional fibre-reinforced composites related to Weibull distributions, fibre packings and boundary effects,” *Composites Science and Technology,* vol. 114, pp. 42-49, 2015.

[71] S. C. Garcea, I. Sinclair, S. M. Spearing and P. J. Withers, “Mapping fibre failure in situ in carbon fibre reinforced polymers by fast synchrotron X-ray computed tomography,” *Composites Science and Technology,* vol. 149, pp. 81-89, 2017.

[72] S. Rosini, M. N. Mavrogordato, O. Egorova, E. S. Matthews, S. E. Jackson, S. M. Spearing and I. Sinclair, “In situ statistical measurement of local morphology in carbon-epoxy composites using synchrotron X-ray computed tomography,” *Composites Part A,* vol. 125, pp. 1-14, 2019.

[73] M. R. Wisnom and D. Green, “Tensile failure due to interaction between fibre breaks,” *Composites,* vol. 26, no. 7, pp. 499-508, 1995.

[74] Y. Swolfs, C. Breite, S. V. Lomov and L. Gorbatikh, “Fibre break interactions in unidirectional composites under longitudinal tensile loading,” in *The 7th European Community on Computational Methods in Applied Sciences*, Girona, Spain, 2019.

[75] P. W. J. van den Heuvel, T. Peijs and R. J. Young, “Failure phenomena in two-dimensional multi-fibre microcomposites. Part 4 – A Raman spectroscopic study on the influence of the matrix yield stress on stress concentrations,” *Composites Part A,* vol. 31, no. 2, pp. 165-171, 2000.

[76] Y. Huang and R. J. Young, “Interfacial behaviour in high temperature cured carbon fibre/epoxy resin model composite,” *Composites,* vol. 26, no. 8, pp. 541-550, 1995.

[77] S. L. Gao and J. K. Kim, “Three-dimensional characterization of impact damage in CFRPs,” *Key Engineering Materials,* Vols. 141-143, pp. 35-54, 1997.

[78] B. S. Hayes and L. M. Gammon, Optical microscopy of fiber-reinforced composites. Chapter 3 – Rough grinding and polishing, 1st ed., Russell Township, OH, USA: ASM International, 2010, pp. 43-66.

[79] ASTM International, “Standard guide for Computed Tomography (CT) imaging: E 1441 – 97,” West Conshohocken, PA, USA, 1997.

[80] T. Gómez-del Río, R. Zaera, E. Barbero and C. Navarro, “Damage in CFRPs due to low velocity impact at low temperature,” *Composites Part B,* vol. 36, no. 1, pp. 41-50, 2005.

[81] T.-W. Shyr and Y.-H. Pan, “Impact resistance and damage characteristics of composite laminates,” *Composite Structures,* vol. 62, no. 2, pp. 193-203, 2003.

[82] MicroscopeMaster, “Scanning Electron Microscope – Advantages and disadvantages in imaging components and applications,” [Online]. Available: https://www.microscopemaster.com/scanning-electron-microscope.html. [Accessed 09 06 2020].

[83] F. Aymerich and S. Meili, “Ultrasonic evaluation of matrix damage in impacted composite laminates,” *Composites Part B,* vol. 31, no. 1, pp. 1-6, 2000.

[84] R. Suvarna, V. Arumugam, D. J. Bull, A. R. Chambers and C. Santulli, “Effect of temperature on low velocity impact damage and post-impact flexural strength of CFRP assessed using ultrasonic C-scan and micro-focus computed tomography,” *Composites Part B,* vol. 66, pp. 58-64, 2014.

[85] L. Mencattelli and S. T. Pinho, “Realising bio-inspired impact damage-tolerant thin-ply CFRP Bouligand structures via promoting diffused sub-critical helicoidal damage,” *Composites Science and Technology,* vol. 182, no. 29, p. 107684, 2019.

[86] L. Vergani, C. Colombo and F. Libonati, “A review of thermographic techniques for damage investigation in composites,” *Fracture and Structural Integrity,* vol. 8, no. 27, pp. 1-12, 2014.

[87] V. Munoz, B. Valès, M. Perrin, M. L. Pastor, H. Welemane, A. Cantarel and M. Karama, “Damage detection in CFRP by coupling acoustic emission and infrared thermography,” *Composites Part B,* vol. 85, pp. 68-75, 2016.

[88] M. T. Kortschot and C. J. Zhang, “Characterization of composite mesostructures and damage by de-ply radiography,” *Composites Science and Technology,* vol. 53, no. 2, pp. 175-181, 1995.

[89] J. Kastner, B. Plank and C. Heinzl, “Advanced X-ray computed tomography methods: High resolution CT, quantitative CT, 4DCT and phase contrast CT,” in *Digital Industrial Radiology and Computed Tomography*, Ghent, Belgium, 2015.

[90] D. J. Bull, L. Helfen, I. Sinclair, S. M. Spearing and T. Baumbach, “A comparison of multi-scale 3D X-ray tomographic inspection techniques for assessing carbon fibre composite impact damage,” *Composites Science and Technology,* vol. 75, pp. 55-61, 2013.

[91] S. C. Garcea, Y. Wang and P. J. Withers, “X-ray computed tomography of polymer composites,” *Composites Science and Technology,* vol. 156, pp. 305-319, 2018.

[92] E. Dilonardo, M. Nacucchi, F. De Pascalis, M. Zarrelli and C. Giannini, “High resolution X-ray computed tomography: A versatile non-destructive tool to characterize CFRP-based aircraft composite elements,” *Composites Science and Technology,* vol. 192, no. 108093, 2020.

[93] R. P. Tavares, F. Otero, A. Turon and P. P. Camanho, “Effective simulation of the mechanics of longitudinal tensile failure of unidirectional polymer composites,” *International Journal of Fracture,* vol. 208, pp. 269-285, 2017.

[94] R. P. Tavares, J. M. Guerrero, F. Otero, A. Turon, J. A. Mayugo, J. Costa and P. P. Camanho, “Effects of local stress fields around broken fibres on the longitudinal failure of composite materials,” *International Journal of Solids and Structures,* Vols. 156-157, pp. 294-305, 2019.

[95] C. M. Landis and R. M. McMeeking, “A shear-lag model for a broken fiber embedded in a composite with a ductile matrix,” *Composites Science and Technology,* vol. 59, no. 3, pp. 447-457, 1999.

[96] M. J. Hinton and A. S. Kaddour, “The background to the second world-wide failure exercise,” *Journal of Composite Materials,* vol. 46, no. 19-20, pp. 2283-2294, 2012.

[97] A. Bunsell, L. Gorbatikh, H. Morton, S. Pimenta, I. Sinclair, S. M. Spearing, Y. Swolfs and A. Thionnet, “Benchmarking of strength models for unidirectional composites under longitudinal tension,” *Composites Part A,* vol. 111, pp. 138-150, 2018.

[98] Toray Industries Inc., *Toray Composite Materials,* Tokyo, Japan, 2019.

[99] Hexcel Corp., *HexPly M21 Product Data Sheet,* Stamford, CT, USA, 2007.

[100] A. S. Kaddour, M. J. Hinton, P. A. Smith and S. Li, "Mechanical properties and details of composite laminates for the test cases used in the third world-wide failure exercise," *Journal of Composite Materials,* vol. 47, no. 20-21, pp. 2427-2442, 2013.

[101] E. M. Odom and D. F. Adams, "Specimen size effect during tensile testing of an unreinforced polymer," *Journal of Materials Science,* vol. 27, pp. 1767-1771, 1992.

[102] T. Hobbiebrunken, B. Fiedler, M. Hojo and M. Tanaka, "Experimental determination of the true epoxy resin strength using micro-scaled specimens," *Composites Part A,* vol. 38, no. 3, pp. 814-818, 2007.

[103] R. P. Tavares, F. Otero, J. Baiges, A. Turon and P. P. Camanho, "A dynamic spring element model for the prediction of longitudinal failure of polymer composites," *Computational Materials Science,* vol. 160, pp. 42-52, 2019.

[104] A. J. Moffat, P. Wright, J.-Y. Buffiere, I. Sinclair and S. M. Spearing, "Micromechanisms of damage in 0° splits in a [90/0]s composite material using synchrotron radiation computed tomography," *Scripta Materialia,* vol. 59, no. 10, pp. 1043-1046, 2008.

[105] P. Wright, X. Fu, I. Sinclair and S. M. Spearing, "Ultra high resolution computed tomography of damage in notched carbon fiber-epoxy composites," *Journal of Composite Materials,* vol. 42, no. 19, pp. 1993-2002, 2008.

[106] A. E. Scott, "Analysis of a hybrid composite pressure vessel using multi-scale computed tomography techniques – PhD Thesis," University of Southampton, Southampton, UK, 2011.

[107] H. Morton, "3D Imaging of the tensile failure mechanisms of carbon fibre composites – PhD Thesis," University of Southampton, Southampton, UK, 2014.

[108] A. E. Scott, I. Sinclair, S. M. Spearing, M. N. Mavrogordato and W. Hepples, "Influence of voids on damage mechanisms in carbon/epoxy composites determined via high resolution computed tomography," *Composites Science and Technology,* vol. 90, pp. 147-153, 2014.

[109] J. Hsieh, Computed Tomography: Principles, design, artifacts, and recent advances. Chapter 2 – Preliminaries, 2nd ed., Bellingham, WA, USA: Wiley, 2009, pp. 23-53.

[110] Wikimedia Commons, “EM spectrum,” [Online]. Available: https://upload.wikimedia.org/wikipedia/commons/f/f1/EM_spectrum.svg. [Accessed 02 05 2020].

[111] J. Hsieh, Computed Tomography: Principles, design, artifacts, and recent advances. Chapter 6 – Major components of the CT scanner, Bellingham, WA, USA: Wiley, 2009, pp. 179-205.

[112] T. M. Buzug, Springer handbook of medical technology. Chapter 16 – Computed tomography, 1st ed., R. Kramme, K. Hoffmann and R. S. Pozos, Eds., Berlin-Heidelberg, Germany: Springer, 2011, pp. 311-342.

[113] R. Hanke, T. Fuchs, M. Salamon and S. Zabler, Materials characterization using Nondestructive Evaluation (NDE) methods. Chapter 3 – X-ray microtomography for materials characterization, 1st ed., G. Hübschen, I. Altpeter, R. Tschuncky and H. Herrmann, Eds., Cambridge, UK: Woodhead Publishing, 2016, pp. 45-79.

[114] HyperPhysics, “Compton scattering equation,” [Online]. Available: http://hyperphysics.phy-astr.gsu.edu/hbase/quantum/compeq.html. [Accessed 31 10 2020].

[115] J. A. Seibert and J. M. Boone, “X-Ray Imaging Physics for Nuclear Medicine Technologists. Part 2: X-Ray Interactions and Image Formation,” *Journal of Nuclear Medicine Technology,* vol. 33, no. 1, pp. 3-18, 2005.

[116] E. N. Landis and D. T. Keane, “X-ray microtomography,” *Materials Characterization,* vol. 61, no. 12, pp. 1305-1316, 2010.

[117] V. Busignies, B. Leclerc, P. Porion, P. Evesque, G. Couarraze and P. Tchoreloff, “Quantitative measurements of localized density variations in cylindrical tablets using X-ray microtomography,” *European Journal of Pharmaceutics and Biopharmaceutics,* vol. 64, no. 1, pp. 38-50, 2006.

[118] R. Bernhardt, D. Scharnweber, B. Müller, P. Thurner, H. Schliephake, P. Wyss, F. Beckmann, J. Goebbels and H. Worch, “Comparison of microfocus- and synchrotron X-ray tomography for the analysis of osteointegration around Ti6Al4V implants,” *European Cells and Materials,* vol. 7, pp. 42-51, 2004.

[119] J. Fu, B. Jiang, B. Li, P. Li and Q. Wang, “Methods determining the angular increment of a continuous scan cone-beam CT system,” *Transactions on Nuclear Science,* vol. 57, no. 3, pp. 1071-1076, 2010.

[120] Pocket Dentistry, “Chapter 1 – Physics,” [Online]. Available: https://pocketdentistry.com/1-physics/. [Accessed 03 05 2020].

[121] NDT Resource Center, “Geometric unsharpness,” [Online]. Available: https://www.nde-ed.org/EducationResources/CommunityCollege/Radiography/Physics/GeometricUnsharp.htm. [Accessed 03 05 2020].

[122] R. Christoph and H. J. Neumann, X-ray tomography in industrial metrology, Munich, Germany: Süddeutscher Verlag GmbH, 2011.

[123] Werth Inc., “X-ray source,” [Online]. Available: https://werthinc.com/x-ray-source-2/. [Accessed 01 11 2020].

[124] Integrating Research and Education, “Geochemical instrumentation and analysis – X-ray Computed Tomography (CT),” [Online]. Available: https://serc.carleton.edu/research_education/geochemsheets/techniques/CT.html. [Accessed 03 05 2020].

[125] Carl Zeiss AG, “Zeiss X-ray tomography solutions – Xradia Versa,” [Online]. Available: https://www.zeiss.com/microscopy/int/products/x-ray-microscopy.html. [Accessed 07 05 2020].

[126] E. Maire, J.-Y. Buffière, L. Salvo, J. J. Blandin, W. Ludwig and J. M. Létang, “On the application of X-ray microtomography in the field of materials science,” *Advanced Engineering Materials,* vol. 3, no. 8, pp. 539-546, 2001.

[127] Deutsches Elektronen-Synchrotron (DESY), “Synchrotron radiation – How does a synchrotron radiation source work ?,” [Online]. Available: https://photon-science.desy.de/research/students__teaching/primers/synchrotron_radiation/index_eng.html. [Accessed 04 05 2020].

[128] European Synchrotron Radiation Facility (ESRF), “What is a synchrotron ?,” [Online]. Available: https://www.esrf.eu/about/synchrotron-science/synchrotron. [Accessed 05 05 2020].

[129] S. R. Stock, “X-ray microtomography of materials,” *International Materials Reviews,* vol. 44, no. 4, pp. 141-164, 1999.

[130] S. C. Garcea, I. Sinclair and S. M. Spearing, “In situ synchrotron tomographic evaluation of the effect of toughening strategies on fatigue micromechanisms in carbon fibre reinforced polymers,” *Composites Science and Technology,* vol. 109, pp. 32-39, 2015.

[131] L. Wang, N. Limodin, A. El Bartali, J.-F. Witz, R. Seghir, J.-Y. Buffiere and E. Charkaluk, “Influence of pores on crack initiation in monotonic tensile and cyclic loadings in lost foam casting A319 alloy by using 3D in-situ analysis,” *Materials Science & Engineering A,* vol. 673, pp. 362-372, 2016.

[132] B. Yu, R. S. Bradley, C. Soutis and P. J. Withers, “A comparison of different approaches for imaging cracks in composites by X-ray microtomography,” *Philosophical Transactions of the Royal Society A,* vol. 374, no. 2071, pp. 1-15, 2016.

[133] G. R. Davis and J. C. Elliott, “Artefacts in X-ray microtomography of materials,” *Materials Science and Technology,* vol. 22, no. 9, pp. 1011-1018, 2006.

[134] J. Hsieh, Computed Tomography: Principles, design, artifacts, and recent advances. Chapter 7 – Image artifacts: Appearances, causes, and corrections, Bellingham, WA, USA: Wiley, 2009, pp. 207-299.

[135] F. Xu, “Quantitative characterization of deformation and damage process by digital volume correlation: A review,” *Theoretical & Applied Mechanics Letters,* vol. 8, no. 2, pp. 83-96, 2018.

[136] L. Liu and E. F. Morgan, “Accuracy and precision of digital volume correlation in quantifying displacements and strains in trabecular bone,” *Journal of Biomechanics,* vol. 40, no. 15, pp. 3516-3520, 2007.

[137] K. Madi, G. Tozzi, Q. H. Zhang, J. Tong, A. Cossey, A. Au, D. Hollis and F. Hild, “Computation of full-field displacements in a scaffold implant using digital volume correlation and finite element analysis,” *Medical Engineering & Physics,* vol. 35, no. 9, pp. 1298-1312, 2013.

[138] R. Brault, A. Germaneau, J. C. Dupré, P. Doumalin, S. Mistou and M. Fazzini, “In-situ analysis of laminated composite materials by X-ray micro-computed tomography and digital volume correlation,” *Experimental Mechanics,* vol. 53, pp. 1143-1151, 2013.

[139] F. Pierron, S. A. McDonald, D. Hollis, J. Fu, P. J. Withers and A. Alderson, “Comparison of the mechanical behaviour of standard and auxetic foams by X-ray computed tomography and digital volume correlation,” *Strain,* vol. 49, no. 6, pp. 467-482, 2013.

[140] F. Gillard, R. P. Boardman, M. N. Mavrogordato, D. Hollis, I. Sinclair, F. Pierron and M. Browne, “The application of Digital Volume Correlation (DVC) to study the microstructural behaviour of trabecular bone during compression,” *Journal of the Mechanical Behavior of Biomedical Materials,* vol. 29, pp. 480-499, 2014.

[141] M. Palanca, G. Tozzi, L. Cristofolini, M. Viceconti and E. Dall'Ara, “Three-dimensional local measurements of bone strain and displacement: Comparison of three digital volume correlation approaches,” *Journal of Biomedical Engineering,* vol. 137, no. 7, pp. 1-14, 2015.

[142] M. Palanca, L. Cristofolini, E. Dall’Ara, M. Curto, F. Innocente, V. Danesi and G. Tozzi, “Digital volume correlation can be used to estimate local strains in natural and augmented vertebrae: An organ-level study,” *Journal of Biomechanics,* vol. 49, no. 16, pp. 3882-3890, 2016.

[143] D. Kytýř, P. Zlámal, P. Koudelka, T. Fíla, N. Krčmářová, I. Kumpová, D. Vavřík, A. Gantar and S. Novak, “Deformation analysis of gellan-gum based bone scaffold using on-the-fly tomography,” *Materials & Design,* vol. 134, pp. 400-417, 2017.

[144] B. Wang, B. Pan and G. Lubineau, “Morphological evolution and internal strain mapping of pomelo peel using X-ray computed tomography and digital volume correlation,” *Materials & Design,* vol. 137, pp. 305-315, 2018.

[145] J. Adam, M. Klinkmüller, G. Schreurs and B. Wieneke, “Quantitative 3D strain analysis in analogue experiments simulating tectonic deformation: Integration of X-ray computed tomography and digital volume correlation techniques,” *Journal of Structural Geology,* vol. 55, pp. 127-149, 2013.

[146] B. A. Roeder, K. Kokini, J. P. Robinson and S. L. Voytik-Harbin, “Local, three-dimensional strain measurements within largely deformed extracellular matrix constructs,” *Journal of Biomechanical Engineering,* vol. 126, no. 6, pp. 699-708, 2004.

[147] C. Franck, S. Hong, S. A. Maskarinec, D. A. Tirrell and G. Ravichandran, “Three-dimensional full-field measurements of large deformations in soft materials using confocal microscopy and digital volume correlation,” *Experimental Mechanics,* vol. 47, pp. 427-438, 2007.

[148] C. L. Gilchrist, J. Q. Xia, L. A. Setton and E. W. Hsu, “High-resolution determination of soft tissue deformations using MRI and first-order texture correlation,” *Transactions on Medical Imaging,* vol. 23, no. 5, pp. 546-553, 2004.

[149] G. D. O'Connell, W. Johannessen, E. J. Vresilovic and D. M. Elliott, "Human internal disc strains in axial compression measured noninvasively using magnetic resonance imaging," *Spine,* vol. 32, no. 25, pp. 2860-2868, 2007.

[150] J. Fu, F. Pierron and P. D. Ruiz, "Elastic stiffness characterization using three-dimensional full-field deformation obtained with optical coherence tomography and digital volume correlation," *Journal of Biomedical Optics,* vol. 18, no. 12, pp. 121512 (1-16), 2013.

[151] J. M. Lifshitz and A. Rotem, "Time-dependent longitudinal strength of unidirectional fibrous composites," *Fibre Science and Technology,* vol. 3, no. 1, pp. 1-20, 1970.

[152] S. Blassiau, A. R. Bunsell and A. Thionnet, "Damage accumulation processes and life prediction in unidirectional composites," *Proceedings of the Royal Society A,* vol. 463, no. 2080, pp. 1135-1152, 2007.

[153] A. R. Bunsell and A. Thionnet, "Life prediction for carbon fibre filament wound composite structures," *Philosophical Magazine,* vol. 90, no. 31-32, pp. 4129-4146, 2010.

[154] A. R. Bunsell and A. Thionnet, "Failure processes governing long term reliability of carbon fibre composites structures," *Composites and Nanostructures,* vol. 7, no. 4, pp. 216-224, 2015.

[155] Y. Sugimoto, T. Kato, M. Shioya, T. Kobayashi, K. Sumiya and M. Fujie, "Structure change of carbon fibers during axial compression," *Carbon,* vol. 57, pp. 416-424, 2013.

[156] D. Loidl, H. Peterlik, M. Müller, C. Riekel and O. Paris, "Elastic moduli of nanocrystallites in carbon fibers measured by in-situ X-ray microbeam diffraction," *Carbon,* vol. 41, no. 3, pp. 563-570, 2003.

[157] T. Kobayashi, K. Sumiya, Y. Fujii, M. Fujie, T. Takahagi and K. Tashiro, "Stress-induced microstructural changes and crystallite modulus of carbon fiber as measured by X-ray scattering," *Carbon,* vol. 50, no. 3, pp. 1163-1169, 2012.

[158] D. M. Sánchez, M. Gresil and C. Soutis, "Distributed internal strain measurement during composite manufacturing using optical fibre sensors," *Composites Science and Technology,* vol. 120, pp. 49-57, 2015.

[159] D. Munzke, E. Duffner, R. Eisermann, M. Schukar, A. Schoppa, M. Szczepaniak, J. Strohhäcker and G. Mair, “Monitoring of type IV composite pressure vessels with multilayer fully integrated optical fiber based distributed strain sensing,” *Materials Today: Proceedings,* p. In press, 2020.

[160] B. Pan, K. Qian, H. Xie and A. Asundi, “Two-dimensional digital image correlation for in-plane displacement and strain measurement: A review,” *Measurement Science and Technology,* vol. 20, no. 6, pp. 1-17, 2009.

[161] H. Leclerc, J.-N. Périé, F. Hild and S. Roux, “Digital volume correlation: What are the limits to the spatial resolution?,” *Mechanics & Industry,* vol. 13, no. 6, pp. 361-371, 2012.

[162] B. K. Bay, T. S. Smith, D. P. Fyhrie and M. Saad, “Digital volume correlation: Three-dimensional strain mapping using X-ray tomography,” *Experimental Mechanics,* vol. 39, no. 3, pp. 217-226, 1999.

[163] Radiology Key, “Chapter 7 – Protocol optimization,” [Online]. Available: https://radiologykey.com/protocol-optimization/. [Accessed 25 05 2020].

[164] M. P. Fernández, A. H. Barber, G. W. Blunn and G. Tozzi, “Optimization of digital volume correlation computation in SR-microCT images of trabecular bone and bone-biomaterial systems,” *Journal of Microscopy,* vol. 272, no. 3, pp. 213-228, 2018.

[165] E. M. C. Jones and M. A. Iadicola, “A good practices guide for digital image correlation,” International Digital Image Correlation Society (iDICs), 2018.

[166] LaVision GmbH, *DaVis v10 StrainMaster (Digital Volume Correlation),* Göttingen, Germany, 2018.

[167] G. Borstnar, F. Gillard, M. N. Mavrogordato, I. Sinclair and S. M. Spearing, “Three-dimensional deformation mapping of Mode I interlaminar crack extension in particle-toughened interlayers,” *Acta Materialia,* vol. 103, pp. 63-70, 2015.

[168] T. S. Smith, B. K. Bay and M. M. Rashid, “Digital volume correlation including rotational degrees of freedom during minimization,” *Experimental Mechanics,* vol. 42, no. 3, pp. 272-278, 2002.

[169] B. C. Roberts, E. Perilli and K. J. Reynolds, “Application of the digital volume correlation technique for the measurement of displacement and strain fields in bone: A literature review,” *Journal of Biomechanics,* vol. 47, no. 5, pp. 923-934, 2014.

[170] S. Yaofeng and J. H. L. Pang, “Study of optimal subset size in digital imagecorrelation of speckle pattern images,” *Optics and Lasers in Engineering,* vol. 45, no. 9, pp. 967-974, 2007.

[171] P. Lecomte-Grosbras, J. Réthoré, N. Limodin, J.-F. Witz and M. Brieu, “Three-dimensional investigation of free-edge effects in laminate composites using X-ray tomography and digital volume correlation,” *Experimental Mechanics,* vol. 55, no. 1, pp. 301-311, 2015.

[172] A. Mendoza, J. Schneider, E. Parra, E. Obert and S. Roux, “Differentiating 3D textile composites: A novel field of application for Digital Volume Correlation,” *Composite Structures,* vol. 208, pp. 735-743, 2019.

Chapter 3 Materials and methods

This chapter contains a general overview of the materials and methods used throughout the course of the project. As this thesis follows a three-paper format, the materials and experimental procedures described here are less detailed than those in the results **Chapters 4** to **6**, whereby the specific procedure developments are highlighted. As such, this chapter aims to provide a road map to the reader, in order to avoid progressing through unnecessary repetition of similar details.

3.1 Material development and manufacturing

All materials were developed and manufactured by the author. As outlined below, drum winding was identified as the most flexible and accessible fabrication route for essentially unidirectional prepregs with continuous reinforcements, which is the incumbent makeup of aerospace laminates. This manufacturing technique allowed the introduction of sub-micrometre particles within the polymer matrix to achieve a sufficiently stochastic, isotropic array of fiducial markers which provided the required X-ray contrast/attenuation for DVC processing.

Drum winding manufacturing processes at an industrial scale have the advantage of good representability; as large sheets of prepreg (meter size range) can be produced and cured, out of which a large number of samples can be cut. In contrast, open mold processes do not offer very good representability due to the manual labor involved which can easily alter the mechanical properties of from one cured material to another. Closed mold processes require the machining of the shaping dies to match the shape of the piece and are thus manufacturing processes reserved for complex geometries and sandwich structures. For manufacturing simple CFRP sheets, the close mold manufacturing route is not cost effective, although the major advantage would be that no particles are filtered during the resin transfer process, as it is essentially a closed system. Complications can arise however, for particles to uniformly flow in very tight and remote areas of the mold.

For specific details with respect to the material development and manufacturing, the reader is referred to **Section 4.2.1**. From the experimental matrix, two recurring sets of materials are highlighted: a modified CFRP with barium titanate particles (400 nm, ∼1.44 vol. %) identified as ‘doped material’, and a standard production material without the application of any fiducial markers (‘undoped material’). The manufacturing process of the doped material is reiterated succinctly in **Sections 5.2.1** and **6.2.1**, with the only additional element being **Figure 5-1** – which shows a schematic illustration of the prepreg manufacturing (drum winding) process.

3.2 Specimen geometry and loading

3.2.1 Microstructural analysis

Unnotched specimens, representative of each material manufactured, were prepared for qualitative analysis of the different microstructures. To reduce the overall scanning time, multiple specimens were stacked together to form essentially longer ‘matchsticks’ for standard Micro-focus Computed Tomography scanning. For specific details with respect to the specimen geometry prepared for the microstructural analysis, the reader is referred to **Section 4.2.2.1**, while **Section 4.2.3** describes the imaging hardware and settings used.

3.2.2 Double-edge notched tensile tests

In conjunction with *in situ* Synchrotron Radiation Computed Tomography, double-edge notched specimens were prepared for two tensile studies:

- **Chapter 4** – to compare the micromechanical behaviour of the doped material alongside its undoped counterpart.
- **Chapter 6** – to perform mechanistically-consistent 3D strain measurements in relation to fibre failure events.

Both studies benefited from identical specimen dimensions, which were loaded *in situ* using the same modified CT5000 single-actuator electromechanical rig (Deben Ltd., Woolpit, Suffolk, UK [1]) and equivalent displacement rates. For specific details with respect to the specimen geometry prepared for the double-edge notched tensile tests, the associated loading conditions and the dimensions of the reaction tube, the reader is referred to **Section 4.2.2.2**. These details are reiterated in **Section 6.2.2** for the doped material, noting that the same particle-modified specimen was shared for the analyses in **Chapters 4** and **6**.

3.2.3 Four-point bending test

'Matchsticks' specimens were prepared in accordance with the D 7264/D 7264M – 07 test method [2] from the doped material for the four-point bending study outlined in **Chapter 5**. These were placed in a custom loading rig designed by the author and used in conjunction with *ex situ* Micro-focus Computed Tomography, *i.e.* with specimen scanning being performed under load, notwithstanding that the loading was performed outside the CT scanner. For specific details with respect to the specimen geometry prepared for the flexural test and associated loading conditions, the reader is referred to **Section 5.2.2**.

3.3 Imaging methods

3.3.1 Micro-focus Computed Tomography

Micro-focus computed tomography (*i.e.* using laboratory X-ray facilities) was applied for two studies:

- **Chapter 4** – to perform a qualitative analysis of the different material microstructures manufactured.
- **Chapter 5** – to validate and demonstrate the effectiveness of Digital Volume Correlation in measuring local strains parallel to the fibre direction.

While the same imaging equipment was used to perform both studies, the main difference in the methodology is that conventional static scanning (*i.e.* no load applied) was used in **Chapter 4**, while **Chapter 5** used *ex situ* scanning. For specific details with respect to imaging hardware and settings used for the different experiments (*e.g.* flux, energy, exposure, propagation distance, voxel size *etc.*), the reader is referred to **Sections 4.2.3** and **5.2.3**. **Figure 5-4** presents the experimental setup used in the context of the four-point bending test.

3.3.2 Synchrotron Radiation Computed Tomography

The methodology concerning the application of Synchrotron Radiation Computed Tomography is identical in **Chapters 4** and **6**. As outlined above, this imaging method was used in conjunction with double-edge notched specimens for *in situ* tensile testing. **Figure 4-4** shows the experimental setup. For specific details with respect to imaging hardware and settings used, the reader is referred to **Section 4.2.4**. The details are reiterated in **Section 6.2.3**.

3.4 Digital Volume Correlation

Digital Volume Correlation was applied for two studies:

- **Chapter 5** – to validate and demonstrate the effectiveness of Digital Volume Correlation in measuring local strains parallel to the fibre direction.
- **Chapter 6** – to perform mechanistically-consistent 3D strain measurements in relation to fibre failure events.

The methodology was identical, with the same algorithm being employed for both studies. Digital Volume Correlation was performed using the commercial DaVis v10 software with StrainMaster DVC package (LaVision GmbH, Göttingen, Germany [3]). Differences arise in the correlation settings/parameters used (*e.g.* size of sub-sets, percentage of sub-set overlap *etc.*), as well as the physical size of the underlying volume images and acquisition methods used to obtain them; which in **Chapter 5** are obtained via *ex situ* Micro-focus Computed Tomography, while in **Chapter 6** are obtained via *in situ* Synchrotron Radiation Computing Tomography. A key aspect regarding DVC processing is the larger spatial filtering used, and implicit the lower spatial resolution achieved in **Chapter 5**, compared to **Chapter 6**. This strategy was desirable to balance the poorer signal-to-noise available using conventional CT methods.

For specific details with respect to the DVC implementation for the different studies, the reader is referred to **Sections 5.2.4** and **6.2.4**, noting that the two workflow diagrams (**Figures 5-5** and **6-1**) are complementary.

3.5 Image processing

Excluding DVC analyses, significant image processing was performed in the context of **Chapters 4** and **5**. More specifically, **Section 4.2.5** details the extraction of fibre break centroids in Fiji ImageJ [4], alongside the geometrical (distance-based) criterion used to define interacting breaks – required to compare the micromechanical behaviour of the doped material alongside its undoped counterpart. **Section 5.2.5** details the steps taken in Fiji ImageJ, VGSTUDIO Max v2.1 (Volume Graphics GmbH, Heidelberg, Germany [5]), GOM Inspect 2018 (GOM GmbH, Braunschweig, Germany [6]) and SOLIDWORKS 2015 (Dassault Systèmes SE, Vélizy-Villacoublay, France [7]) to evaluate the radius of curvature of the bent specimen – necessary to compute the analytical strain prediction, and validate/demonstrate the effectiveness of DVC in measuring local strains parallel to the fibre direction.

3.6 References

[1] Deben Ltd., *CT5000 5kN in-situ tensile stage for µXCT applications,* Woolpit, Suffolk, UK, 2019.

[2] ASTM International, "Standard Test Method for Flexural Properties of Polymer Matrix Composite Materials D 7264/D 7264M – 07," West Conshohocken, PA, USA, 2007.

[3] LaVision GmbH, *DaVis v10 StrainMaster (Digital Volume Correlation),* Göttingen, Germany, 2018.

[4] J. Schindelin, I. Arganda-Carreras, E. Frise, V. Kaynig, M. Longair, T. Pietzsch, S. Preibisch, C. Rueden, S. Saalfeld, B. Schmid, J.-Y. Tinevez, D. J. White, V. Hartenstein, K. Eliceiri, P. Tomancak and A. Cardona, "Fiji: An open-source platform for biological-image analysis," *Nature Methods,* vol. 9, pp. 676-682, 2012.

[5] Volume Graphics GmbH, *VGSTUDIO Max v2.1,* Heidelberg, Germany, 2011.

[6] GOM GmbH, *GOM Inspect 2018,* Braunschweig, Germany, 2018.

[7] Dassault Systèmes SE, *SOLIDWORKS,* Vélizy-Villacoublay, France, 2015.

Chapter 4 A novel particle-filled Carbon-Fibre Reinforced Polymer model composite tailored for the application of Digital Volume Correlation and Computed Tomography

This chapter presents the development of novel Carbon-Fibre Reinforced Polymer laminates, tailored for the application of Digital Volume Correlation and Computed Tomography to experimental mechanics analyses of these materials. Analogous to surface-based Digital Image Correlation, DVC is a relatively novel volumetric method that utilizes CT data to quantify internal three-dimensional displacements and implicit strain fields. The highly anisotropic and somewhat regular/self-similar microstructures found in well-aligned unidirectional materials at high fibre volume fractions are intrinsically challenging for DVC, especially along the fibre direction at microstructural length-scales on the order of a few fibre diameters. To permit the application of DVC to displacement and/or strain measurements parallel to the fibre orientation, the matrix was doped with a sparse population of sub-micrometre particles to act as displacement trackers (*i.e.* fiducial markers). Barium titanate particles (400 nm, ∼1.44 vol. %) were found to offer the most favourable compromise between contrast in CT images and the ability to obtain a homogeneous distribution in 3D space with sufficient particle compactness for local DVC analyses. This property combination was selected following an extensive Micro-focus Computed Tomography-based qualitative assessment on a wide test matrix, that included 38 materials manufactured with a range of possible particle compositions, mean sizes and concentrations. By comparing the tensile behaviour of the particle-adapted material alongside its particle-free counterpart, it is demonstrated through the application of *in situ* Synchrotron Radiation Computed Tomography that the macro- and micromechanical responses of the newly developed CFRP are consistent with standard production materials indicating its suitability as a model system for mechanistic investigations. This chapter has been reprinted from *Journal of Composite Materials,* in press, 2020, E. Schöberl, C. Breite, S. Rosini, Y. Swolfs, M. N. Mavrogordato, I. Sinclair and S. M. Spearing, "A novel particle-filled carbon-fibre reinforced polymer model composite tailored for the application of digital volume correlation and computed tomography".

4.1 Introduction

One of the many strategies for achieving a carbon neutral economy by the 2050s is the use of lightweight, adaptable materials, with high specific properties for transport applications. In this regard, Carbon-Fibre Reinforced Polymers outperform many monolithic materials, and are increasingly used in transport applications due to their desirable strength- and stiffness-to-weight characteristics. However, any material to be certified for use in high performance and safety critical structural applications, must be accompanied by a good understanding of its mechanical behaviour [1]. As such, knowledge of damage initiation and propagation in composites, and the transition from subcritical to critical damage is key to the design process, along with the development of improved materials [2, 3].

CFRPs are known to display complex failure modes, typically involving multiple interacting damage mechanisms, occurring over varying length-scales. For example, fibre breaks are highly localized forms of damage, and are limited to a few micrometers in scale. Delaminations on the other hand may occur over millimetre to metre scales, depending on the structure's size and geometry [4]. In tension, the failure of fibres within 0° plies is regarded as a critical damage mechanism, with the strength of an axially loaded unidirectional composite being dominated by fibre strength [4-6]. Understanding the fibre fracture process, therefore, becomes essential for achieving a comprehensive interpretation of CFRP tensile failure, alongside the various other forms of composite sub-critical damage [7, 8].

A range of predictive models have been developed and adapted to simulate the processes that lead to ultimate failure in fibre fracture-dominated situations [4]. These commonly include the following concepts:

- Fibre strength as a stochastic quantity [9]. This is typically presumed to follow a Weibull distribution [10].
- Stress (or strain) transfer mechanisms, or load shedding rules [11]. Around single fibre breaks, the surrounding matrix transfers load, primarily in shear, into adjacent fibres [9]. This stress transfer mechanism reintroduces stress into the broken fibre [12], while the break (*i.e.* crack) also triggers local stress concentrations in the nearby intact fibres [13, 14]. The stress (or strain) concentration factors, defined as the relative change in the average stress (or strain) over the cross-section of an adjacent fibre due to the presence of a fibre break, increases the probability of fracture in these intact fibres [1, 13, 15, 16].
- Evolution of fibre breaks with ongoing loading. Fibre breaks are initially spatially distributed and evolve into cluster of breaks. These clusters consist of multiple interacting fibre breaks, prior to the onset of unstable failure [1, 4, 5, 17-20].

- The propagation of a 'critical cluster' in an unstable, self-sustaining manner. This is associated with the catastrophic failure of the composite [9, 13, 18, 20].

Acknowledging that damage in composite materials is a three-dimensional problem, and in the endeavour to validate these underpinning assumptions of fibre failure-based strength theories, recent years have seen a departure from 'traditional' damage assessment methods (*e.g.* optical microscopy and material sectioning [21], acoustic emission [2, 6, 21], scanning electron microscopy [22] *etc.*) in favour of X-ray Computed Tomography; with this non-invasive 3D imaging technique being further divided into Micro-focus Computed Tomography and Synchrotron Radiation Computed Tomography. While both acquisition methods can deliver usable micrometre and sub-micrometre voxel resolution levels, superior scans are commonly achieved through SRCT (the beam is brighter, monochromatic, coherent and parallel, thereby avoiding issues such as beam hardening and cone beam artefacts, and facilitating phase enhanced imaging [23]). Moreover, µCT is characterised by significantly longer scanning times, on the order of hours, as opposed to seconds for SRCT, especially at sub-micrometre resolutions [23]. Near composite failure this may be expected to promote hold-at-load artefacts, whereby the viscoelastic response of the polymer matrix may result in time-dependent strain variation and subsequent failure of UD composites [6, 24-26].

The pairing of SRCT with in situ tensile loading has led to a paradigm shift in identifying detailed sequences of damage accumulation down to fibre-level, in 3D, within the bulk of real engineering materials under load [1, 4, 19, 20, 27, 28]. As such, considerable progress was made in terms of model validation [29] by specifically studying the evolution of breaks with ongoing loading [1, 4, 19, 20]. Recently, developments have seen the use of uninterrupted scan strategies [19] (but at the expense of image quality), mainly aimed at capturing the critical nature of damage required to trigger final failure. Nevertheless, this remains a somewhat hypothetical concept, as even the latest SRCT instruments do not permit observations to be made at sufficiently high temporal resolution to capture the final state of damage in the last instant prior to failure [19].

Experimental studies involving the stress (or strain) transfer mechanisms associated with fibre fracture have received limited attention despite developments in CT methods. Therefore, direct experimental evidence to validate one of the underpinning assumptions of fibre failure-based strength theories remains primarily based on Raman spectroscopy studies [30-33]. These measurements are, however, limited to the surface of the material (as they require visible light transmission), and have been generally performed on model microcomposites with a sparse distribution of fibres, which may not exhibit fully-representative stress/strain states.

To bridge this gap in the literature the authors have considered the coupling of *in situ* SRCT with Digital Volume Correlation for a strain-based quantification of the local deformation surrounding fibre break sites in representative materials subjected to a continuously applied load [8]. An extension of the two-dimensional Digital Image Correlation technique [34], DVC was developed for volumetric measurements, and initially demonstrated as a means to estimate the effective continuum strain tensor in trabecular bone subjected to axial compression [35]. The general objective of the DVC is to track a set of multiple reference volumes between the undeformed and subsequent deformed states of a structure, in order to determine the associated displacement vectors. This may be achieved by employing a correlation criterion (function) to identify underlying patterns within a time (applied load)-series volumetric data set [35, 36]. In combination with high-resolution 3D imaging, DVC is a tool capable of quantifying the internal/bulk microstructural responses of a material between different load states, by extracting relevant parameters (*e.g.* local displacements and strains) [37].

Ideally, X-ray-based DVC analysis requires the presence of a sufficiently stochastic, isotropic array of features (or texture) which provides X-ray contrast/attenuation [38, 39]. The highly anisotropic and somewhat regular/self-similar microstructures found in conventional unidirectional CFRPs at high fibre volume fractions are, therefore, intrinsically challenging for DVC, particularly for the analysis of displacements/strains along the fibre direction. The simple cylindrical structure and relatively smooth surfaces of the filaments yields little structural variation along the fibre direction, leading to poor image correlation, and correspondingly inaccurate displacement estimates in this direction within a given ply [40].

This study is the first from a series documenting the application of DVC to displacement and/or strain measurements parallel to the fibre orientation, ultimately aimed at mapping strain fields at fibre break sites [7, 8] and other damage critical sites. Here focus is made on the material development required to perform such measurements. Following a similar approach to that taken by Brault *et al.* [41] to generate individual features unique to a particular sub-set, the authors have explored the insertion of sparse populations of significantly smaller particles (< 1 μm, as opposed to 150 μm used in [41]) within the matrix to act as displacement trackers – *i.e.* fiducial markers.

Whilst adding particles to a material clearly changes its microstructure, previous studies have shown that for low particle concentrations, the mechanical properties of thermosetting matrices can be largely preserved [42, 43]. This work represents the first detailed evaluation of potential fiducials for DVC on CFRP materials at truly micromechanical levels, resulting in the development of a model system, which may have wide utility for understanding fundamental mechanisms of failure and quantitatively informing mathematical model development.

4.2 Materials and methods

4.2.1 Material development

4.2.1.1 Carbon-fibre and resin system

Fibres suitable for drum winding and prepreg production were selected, specifically, a 12K non-twisted TORAYCA T700SC-50C tow (Toray Industries Inc., Tokyo, Japan [44]). This is a PAN-based high strength (4900 MPa), standard-modulus (230 GPa) fibre, with a 7 μm nominal diameter [44]. This fibre type has been extensively used in previous works [1, 4, 5, 19, 28], providing a database of comparable measurements. A SiPreg SR 8500/KTA 313 dual-component epoxy matrix was used (Sicomin, Châteauneuf-les-Martigues, France [45]). As per the manufacturer specifications, the resin is characterized by a low initial viscosity (7.0 Pa.s at 20°C), low reactivity, and upon curing has a 65 MPa and 3.7 GPa tensile strength and tensile modulus, respectively. For this work, the former characteristics are considered desirable, allowing for both particle doping and fibre impregnation, without inducing premature curing during manufacture (**Section 4.2.1.3**).

4.2.1.2 Particle systems

To create microstructural fiducial patterns, the resin was filled with dilute concentrations of a range of commercially available particles of approximately spherical shape (US Research Nanomaterials Inc., Houston, TX, USA [46]). In absorption mode X-ray CT, the imaging contrast arises from the different linear attenuation coefficients of the constituent phases [23, 47, 48]. **Figure 4.1** presents the mass attenuation coefficient *'μ/ρ'* (see **Section 2.3.1**) for relevant elemental media and compounds, based on data obtained from the National Institute of Standards and Technology (NIST) [49]. As materials with low atomic number exhibit low X-ray attenuation (*e.g.* carbon), and, therefore, poor imaging contrast relative to the fibres and epoxy resin, the particle systems were selected such that they are characterized by attenuation coefficients higher than that of the composite constituents. **Table 4-1** presents the different concentrations of particles used, expressed in weight % of the amount of resin used, while **Table 4-2** shows the different particles sizes investigated.

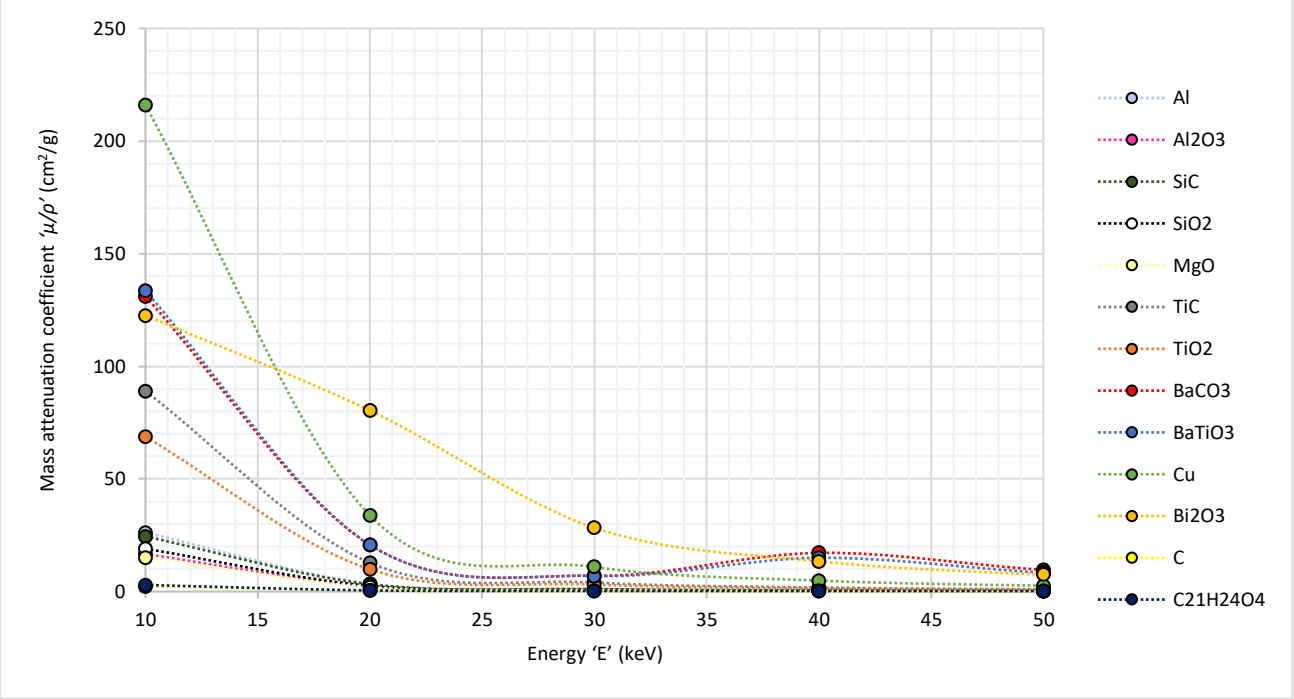

Figure 4-1 – Attenuation profiles for elemental media and compounds, representative of the different phases: matrix, carbon-fibres and fiducial markers. The attenuation of the matrix was estimated using bisphenol A diglycidyl ether (DGEBA), $C_{21}H_{24}O_4$. Based on NIST data [49].

	Weight % in resin *									
	0.25	0.5	1	2	3	4	5	7.5	10	15
Al	x		x				x		x	x
Al_2O_3								x	x	
SiC	x	x								x
SiO_2								x	x	
MgO								x	x	
TiC	x	x								
TiO_2							x	x	x	
$BaCO_3$		x								
$BaTiO_3$	x	x	x	x	x	x		x		
Cu	x	x	x							
Bi_2O_3									x	

*Table 4-1 – Experimental matrix showing the particle compositions in conjunction with the concentrations used. *Approximate values based on element (or compound) density.*

	Particle mean size (nm) *					
	300	400	500	580	600	800
Al						x
Al_2O_3	x		x			x
SiC					x	
SiO_2		x				
MgO	x				x	
TiC						x
TiO_2	x		x			
$BaCO_3$						x
$BaTiO_3$		x				
Cu				x		
Bi_2O_3						x

*Table 4-2 – Experimental matrix showing the particle compositions in conjunction with the nominal particle sizes used (*as specified by the manufacturer).*

4.2.1.3 Material manufacturing

Cross-ply laminates, with a $[90/0]_s$ layup and thickness of ~1 mm were manufactured by drum winding at KU Leuven, Belgium. Prior to fibre impregnation, the particles were dispersed in the epoxy system using a combination of high-shear mixing and heated ultra-sonication (U100H bath, Ultrawave Ltd., Cardiff, UK [50]). No additional treatment was applied to the particle surfaces. To remove entrapped air, the thermosetting mixture was degassed for 10 minutes at ambient temperature. The amount of resin used was 150 g, with 31.5 g of hardener, following the manufacturer's specified mixing ratio of 100/21 (by weight). A nominal 25 % tow overlap was targeted during the winding process, with a maximum spool tension of 0.53 N. To control the volume fraction of the matrix following impregnation, the tow was passed through a metering die with an orifice slot of 0.2 mm × 9 mm. The temperature of the tow spreader and final guide roller were set to 50°C. The fibre sizing was left intact. For a schematic diagram of the manufacturing setup, the reader is referred to **Figure 5-1**. The drum winding process resulted in uniaxial prepreg tape, ~0.25 mm thick × ~350 mm × ~1900 mm, which was cut and laid up to produce the desired $[90/0]_s$ cross-ply layup. As indicated in **Figure 4-2**, the prepreg stack was cured in an autoclave for 280 minutes at 0.5 MPa (5 bar) and a maximum temperature of 120°C. To minimize void content in the cured material, a vacuum of ~0.07 MPa (~0.7 bar) was maintained throughout the autoclave process. The particle-modified CFRP is identified as 'doped material' throughout the rest of this work.

A subsequent set of similar cross-ply laminates was fabricated, without the application of any fiducial markers ('undoped material'). Identical processing parameters (including shear mixing and sonication) were used in the fabrication of both composite types.

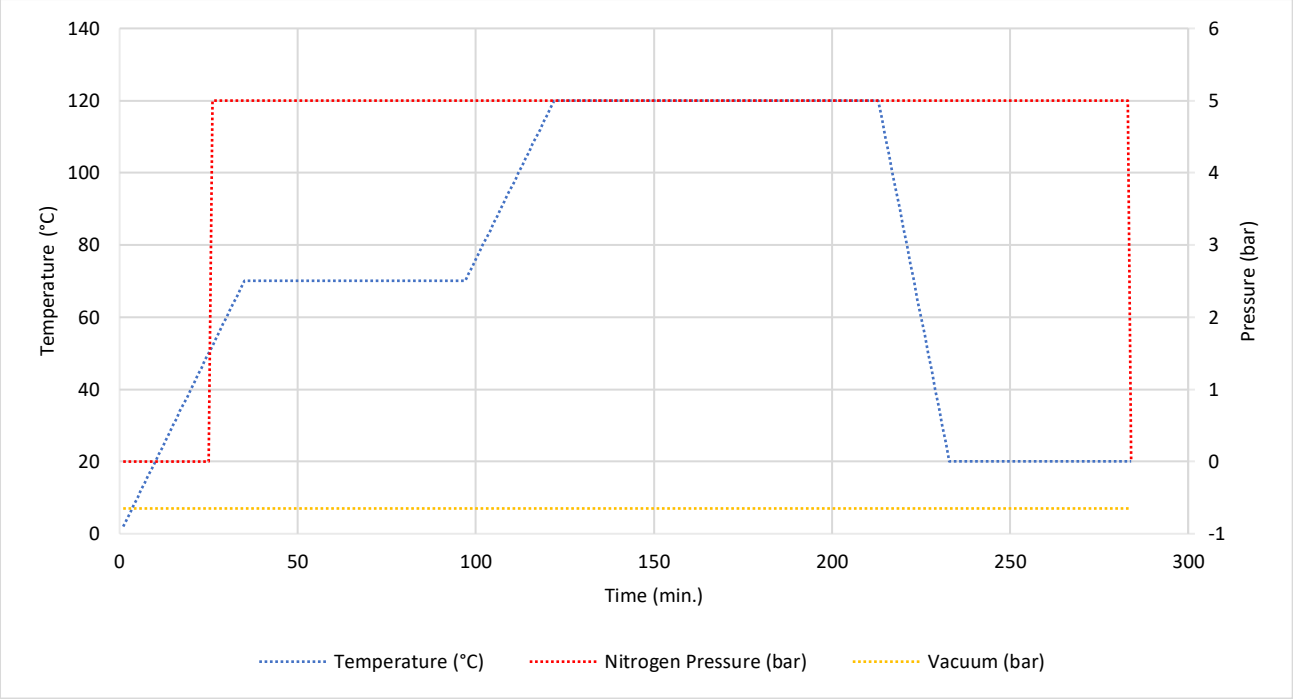

Figure 4-2 – Schematic illustration of the cure cycle used as part of the autoclave process.

4.2.2 Specimen geometry

4.2.2.1 Microstructural analysis

Unnotched specimens (~1 mm × ~15 mm × ~1 mm) were machined via water-jet cutting from the manufactured CFRP plates. Three to six specimens, each representative of a different material, were stacked together to form 75 mm long 'matchsticks' for conventional static µCT scanning (*i.e.* no load applied) – see **Section 4.2.3**.

4.2.2.2 Tensile testing

Double-edge notched specimens were machined via water-jet cutting for *in situ* SRCT imaging (see **Section 4.2.4**). The geometry is based on previous work of Scott, Schöberl, Garcea, Rosini, Moffat, Wright and co-workers [4, 5, 8, 19, 20, 27, 28], although here the total specimen length was increased to 100 mm, as reported in [8] and [20]. This was performed to (a) minimize the risk of pull-out from the central 0˚ portion of the gauge region, and (b) to accommodate a smaller X-ray propagation distance, by providing sufficient clearance between the top of the loading rig and detector optics. Once cut, the T-shaped sections of the specimens were tabbed with 1.5 mm thick aluminium sheet. Aerospace-grade adhesive, Scotch-Weld EC-9323 B/A (3M Company, Maplewood, MN, USA [51]), was used to bond the tabs onto the CFRP surface. Adhesive curing was performed at 65°C for 2 h according to the manufacturer's recommendations. The key specimen dimensions,

the tabbed assembly and an exemplar microstructure with high contrast fiducial markers are collectively shown in **Figure 4-3**. Tensile loading was performed *in situ* by using a modified CT5000 single-actuator electromechanical rig (Deben Ltd., Woolpit, Suffolk, UK [52]) retrofitted with a Poly(Methyl Methacrylate) – PMMA reaction tube (25 mm outer diameter and 3 mm wall thickness). Using position control, loading was performed at a displacement rate of 0.2 mm/min up to a prescribed load point. A small applied preload was used (max. 75 N) to ensure that the specimen did not move during initial acquisition and/or manipulator stage translation. Typically, ten load steps were applied for stepwise *in situ* measurements, with somewhat smaller load increments being made at high loads, close to failure. This was applied on the basis of the work of Scott *et al.* [4], where fibre breaks have been shown to accumulate exponentially with applied stress, with the majority of breaks occurring above ~90 % UTS. To alleviate potential effects of specimen relaxation under load (and thus potential movement during CT acquisition), scanning was carried out with a slight reduction in load (~10 %) from the most recent peak level applied.

Based on µCT imaging, three specimens were subjected to SRCT-based tensile testing: one doped with $BaTiO_3$ particles (400 nm, ~1.44 vol. %, see **Section 4.3.1**) and two undoped: 'A' and 'B'. **Table 4-3** summarizes the double-notched specimens studied, together with the associated fibre volume fractions *'V_f',* measured through digital segmentation. Due to experimental time constraints, the undoped specimen 'B' was not loaded to fracture.

Specimen label	Particle system	Fibre volume fraction
Doped	$BaTiO_3$, 400 nm, ~1.44 vol. %	~55 %
Undoped 'A'	N/A	~63 %
Undoped 'B'		~58 %

Table 4-3 – Basic characteristics of the double-notched specimens subjected to SRCT-based tensile testing.

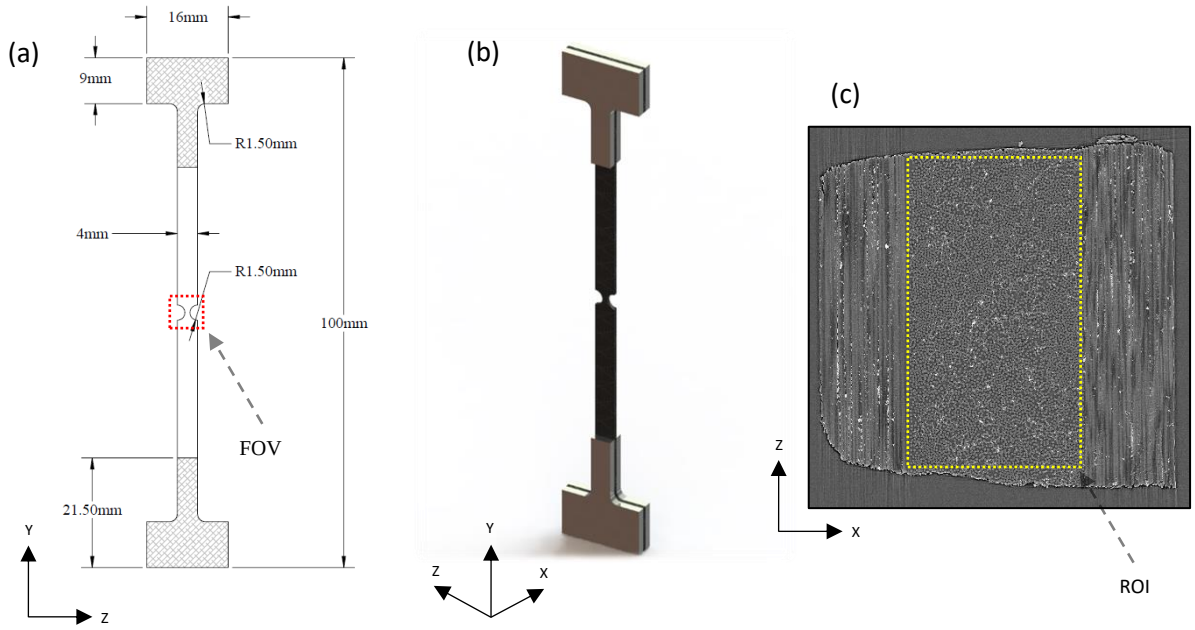

Figure 4-3 – Tensile specimens: (a) key specimen dimensions and field of view (FOV), (b) tabbed assembly (CFRP plus aluminium tabs), (c) SRCT slice showing a cross-section of the notch region doped with high contrast fiducial markers ($BaTiO_3$, 400 nm, ~1.44 vol. %), including the region of interest (ROI), which encompasses the 0° plies.

4.2.3 Micro-focus Computed Tomography

Micro-focus CT measurements were carried out at the µ-VIS X-Ray Imaging Centre at the University of Southampton, UK. Scans were conducted in a Xradia 510 Versa (Carl Zeiss AG, Oberkochen, Germany [53]) polychromatic system, equipped with a tungsten transmission target. A 2048 × 2048-pixel detector was used, with a chip size of 13.5 µm. To achieve matching SRCT voxel resolution levels, a two-stage magnification approach was implemented (Resolution at a Distance or RaaD [53]), combining the geometric magnification of the X-Ray imaging with a set of barrel-mounted scintillator lenses. Scans were conducted at 20 × magnification, yielding a voxel size ranging from ~0.65 µm to ~0.77 µm. A 2 × detector 'binning' was used, resulting in a maximum field of view (FOV) of ~0.74 mm × ~0.75 mm × ~0.76 mm. The beam energy was set to 50 kVp and the current to 80 µA. The number of projections acquired per scan was 1601, at a maximum exposure of 7 s, resulting in ~3.11 h per tomograph. Acquisition was performed over a rotation of ± 180°. A source-to-object and object-to-detector distance of ~13 mm and ~13 mm, respectively, was used. The data was reconstructed using conventional absorption-based FBP.

4.2.4 Synchrotron Radiation Computed Tomography

In situ SRCT measurements were performed at the ID19 beamline, European Synchrotron Radiation Facility, Grenoble, France. A 2560 × 2160-pixel detector was used, with a chip size of 6.5 µm. Scans, with a monochromatic beam, were conducted at a 10 × magnification, yielding a voxel size of 0.65 µm and a FOV of ~1.66 mm × ~1.40 mm × ~1.66 mm. The beam energy was set to 19 keV, with 2996 projections acquired per scan, at an exposure of 25 ms, resulting in ~75 s per tomograph. Acquisition was performed over a rotation of 180°. A propagation distance of ~30 mm was used, while the data was reconstructed using conventional absorption-based FBP. **Figure 4-4** illustrates the SRCT experimental setup.

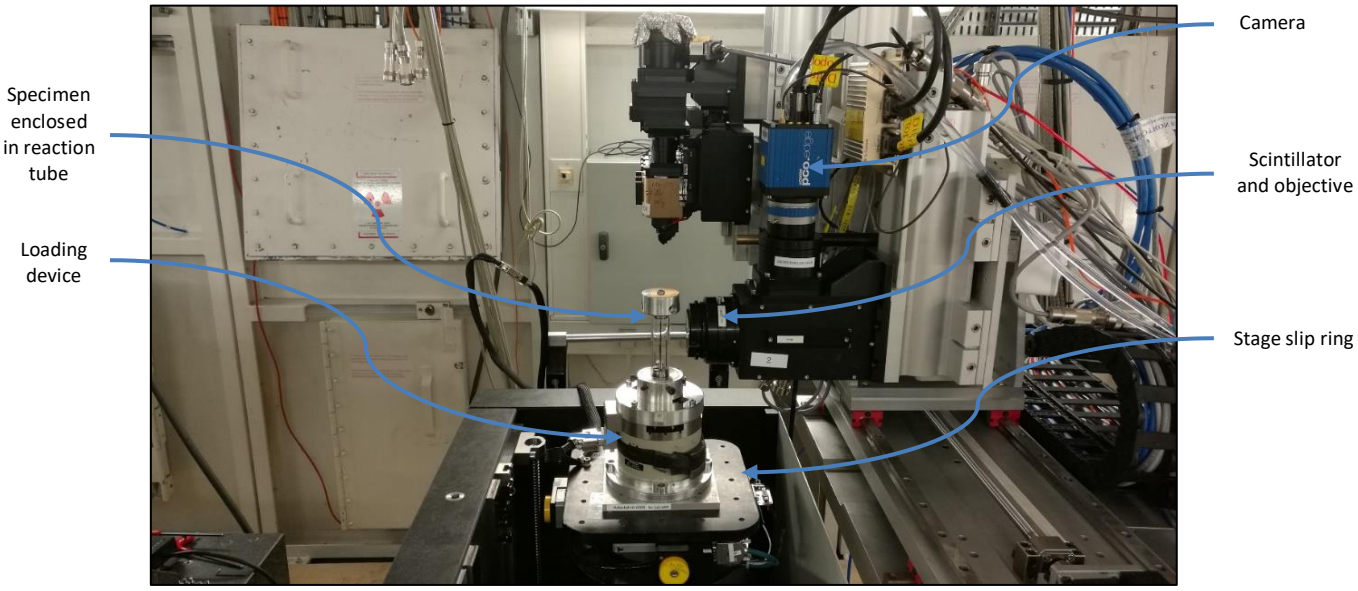

Figure 4-4 – SRCT experimental setup illustrating the key components (ID19 beamline, ESRF).

4.2.5 Image processing

Volume images were extracted from the centre-notch gauge section of the 0° plies, ensuring that the same region of interest (ROI) exists across each load step, for each specimen in part (**Table 4-4**). Fibre breaks were hand-counted within the volume stack to minimize false positives/negatives. To ensure that no fibre breaks were omitted (and/or mislabelled), three distinct counts (iterations) were performed across each of the volume stacks. The location of each fibre break was marked in Fiji ImageJ [54] with the centroid coordinates being extracted. Attention was given to centre each mark onto the associated fibre break in 3D space, to within a single-voxel. Fibre break centroids were finally sorted into single, non-interacting fibre breaks ('singlets') or clusters of fibre breaks ('N-plets'), whereby *N* indicates the number of interacting breaks within a given cluster (*e.g.* three 7-plets are the equivalent of three fibre break clusters, each comprising 7 interacting breaks, and accounting for 21 breaks in total).

Following a similar geometrical (proximity) criterion to that used by Swolfs *et al.* [1] and Scott *et al.* [4], a cluster is defined here as two or more broken fibres with an axial and radial separation of 10 and 2 fibre diameters, respectively, measured from centre-to-centre. A fibre diameter of 6.8 µm (as opposed to 7 µm) was used to set this criterion, as detailed in [55]. This essentially creates a 'bounding cylinder' measuring 136 µm in the fibre direction (2 × 10 × 6.8 µm) and 27.2 µm in diameter (2 × 2 × 6.8 µm) for each fibre break centroid. If more than one fibre break is located within the boundary of this cylinder, then the respective fibre breaks are considered to be part of the same fibre break cluster. It is important to note that the term 'cluster' does not have a consistent definition throughout the literature, so results from different studies must be compared carefully [19]. As noted in **Table 4-4**, all post-processing is conducted within a volume of ~0.34 mm^3, extracted from the 0° plies. Additionally, for computational cost reduction reasons, a 32-bit floating point to 8-bit integer conversion was performed for the SRCT data.

Slice dimension (voxels)	Doped specimen	Undoped specimen 'A'	Undoped specimen 'B'	ROI volume (mm^3)
Coordinate 'X'	650	640	640	~0.34
Coordinate 'Z'	1150	1250	1250	
Coordinate 'Y'	1670	1560	1560	

Table 4-4 – ROI from the 0° plies used for fibre break data quantification (SRCT data, 1 voxel = 0.65 µm).

4.3 Results and discussion

4.3.1 Microstructural analysis

Given the number of materials manufactured, and the evident microstructural variations, initial triage of microstuctures was carried out qualitatively, based on µCT data. This rationale was used to determine the combination of particle composition, size and concentration that results in reasonably homogeneous distributions in 3D space, with sufficient particle compactness for local DVC analyses, without gross anomalies (large voids, clumping *etc.*). Representative µCT slices from each material are provided in **Appendix A**. To preserve the tensile behaviour of a commercially representative material, whilst still allowing the application of DVC parallel to the fibre direction [7, 8, 40], the authors have established a series of considerations:

- Particles must be reasonably attenuating (more so than the carbon-filaments), without introducing X-ray imaging artefacts (particularly streak patterns).

- Particle size must be small enough to allow for incorporation between individual fibres, essentially creating parallel ‘strips’ of fiducial marks with respect to the fibre direction (Y), minimising influence on fibre packing (and hence misalignment and presence of resin-rich regions).
- Particles should be sufficiently large to be detectable at the available voxel resolution levels (on the order of three voxels across).
- Particle concentration must be low enough to prevent agglomeration, yet sufficient for DVC analyses at microstructural length-scales (on the order of one fibre diameter).

Following the above considerations, the materials doped with various particle system are ranked in **Table 4-5**. For more detailed comments, the reader may consult **Appendix B**. A 'three-tick' system was used to summarize the overall attributes (one tick = poor, two ticks = adequate, three ticks = excellent).

Fiducial marker system	Overall ranking	Imaging contrast	Spatial distribution	Lack of agglomerates	Key comment
Al	✓✓✓	✓✓	✓✓✓	✓✓✓	At a concentration of 10 wt. %, aluminium appears to satisfy the imaging requirements for local DVC analyses.
Al_2O_3	✓	✓	✓✓	✓✓	The 300 nm aluminium oxide system appears to yield a slightly superior particle deposition between the individual carbon-filaments, compared to the 500 nm and 800 nm counterparts, respectively.
SiC	✓	✓✓	✓	✓	The doping with silicon carbide at a concentration of 15 wt. % results in a microstructure abundant with gross microstructural anomalies. This fails to satisfy the established considerations.
SiO_2	✓✓	✓	✓✓	✓✓✓	Silicon dioxide (7.5 wt. % and 10 wt. %) with a particle size of 400 nm performs similar to the 500 nm aluminium oxide and 500 nm titanium oxide systems, respectively, at similar concentrations.
MgO	✓	✓	✓	✓	The microstructure doped with magnesium oxide is characterized by an abundance of agglomerates, particularly at the higher concentrations. These have a 'crystal-like' appearance and are differentiated by sharp edges from the other compositions examined.
TiC	✓	✓✓✓	✓	✓✓	At a size of 800 nm, titanium carbide particles are identifiable at a concentration of 0.25 wt. % and 0.5 wt. %, respectively. The imaging requirements for local DVC analyses are, however, not satisfied given the sparse spatial distribution associated with these low concentration levels.
TiO_2	✓✓	✓✓✓	✓✓	✓	Compared to the magnesium oxide counterpart, titanium oxide agglomerates are no longer characterized by sharp edges and the overall abundance is slightly reduced within the microstructure, notwithstanding that the particle distribution does not match that of barium titanate, particularly in terms of inter-fibre deposition.
$BaCO_3$	✓	✓✓✓	✓	✓✓	The doping with barium carbonate yields similar results to those obtained by the titanium carbide system.
$BaTiO_3$	✓✓✓	✓✓✓	✓✓✓	✓✓✓	The particle distribution remains homogenous throughout the concentrations investigated, with the desirable particle compactness for local DVC analyses achieved at the highest concentration of 7.5 wt. %. Also, the barium titanate system does not appear to be prone to agglomerate formation.
Cu	✓	✓✓✓	✓✓	✓✓	The copper system is overly attenuating (see **Figure 4-1**), such that at the energies available, it promoted imaging artefacts, visible as streak patterns surrounding the fiducial markers.
Bi_2O_3	✓	✓✓✓	✓	✓	Like copper, bismuth oxide is too attenuating compared to carbon at the beam energies available in the present work.

Table 4-5 – Ranking system highlighting the overall attributes of the different materials manufactured.

Based on this qualitative analysis, two fiducial markers systems appear to outperform the others on balance: (1) barium titanate (400 nm, 7.5 wt. %) and aluminium (800 nm, 10 wt. %) – **Figure 4-5**. This can be further reduced to the barium titanate system based on the following considerations:

- A better inter-fibre deposition is achieved, which may be attributed to a smaller particle size.
- Higher intrinsic density, which translates into a lower volumetric content of ∼1.44 vol. % *vs.* ∼4.17 vol. % (considered favourable for preserving the mechanical behaviour of standard production materials).
- More attenuating at the energies available, which results in a superior imaging contrast next to the carbon-filaments.

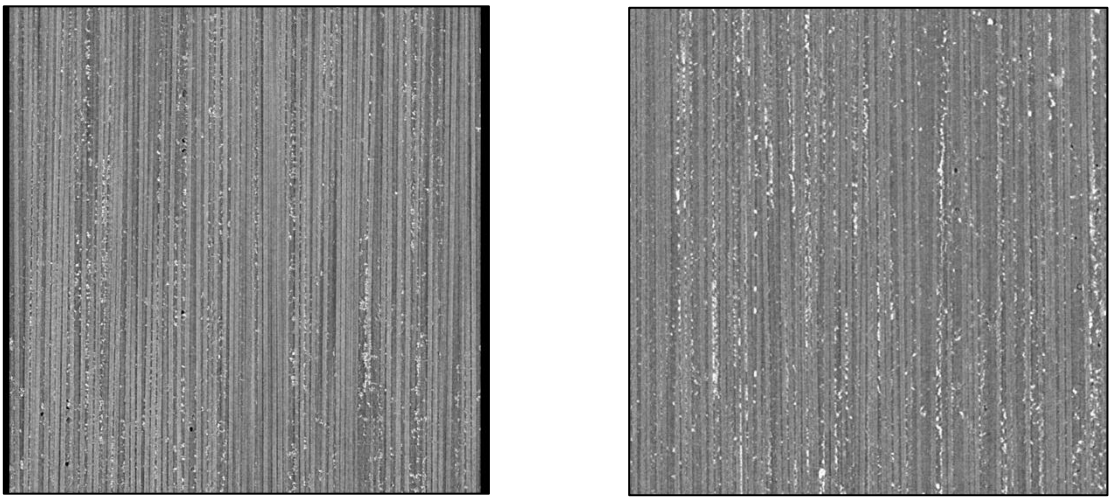

Al 800 nm, 10 wt. % (slice 423)

$BaTiO_3$ 400 nm, 7.5 wt. % (slice 457)

Figure 4-5 – Representative µCT slices showing the doping of the CFRP with aluminium and barium titanate, respectively (0° plies shown).

As such, the barium titanate particles (400 nm, ∼1.44 vol. %) were judged to offer the most favourable compromise between contrast in CT images and the ability to obtain a homogeneous distribution in 3D space with a sufficiently fine particle distribution for local DVC analyses. Using a threshold of 48/255 for a fully stretched greyscale, the average microvoid content for this material was computed at ∼0.1 vol. %, with a corresponding standard deviation of ∼0.04 % across the stack (*i.e.* individual CT slices). The result is consistent with the acceptable levels of less than 1 vol. % in aerospace-grade applications [56]. The low levels of microvoid content are primarily attributed to the autoclave curing, rather than being an intrinsic characteristic of the drum winding manufacturing process. This becomes more obvious if the CT slices shown here are compared to those in [57], whereby the lack of autoclave curing in a similar filament wound material resulted in fewer voids, but with a substantially larger size: 15 µm in diameter and 105 µm in length, where the length of the void was aligned with the fibre axis.

4.3.2 Fibre break behaviour

A summary of fibre break behaviour as a function of loading is shown in **Table 4-6**. Load is presented as a function of force applied, stress (minimum nominal cross-section of the 0° plies, as in [1, 4, 19]) and fraction of specimen UTS, respectively. It is clear that the undoped specimens achieve significantly higher peak nominal stress (in excess of ~3000 MPa) *cf.* the doped composite (~2300 MPa). Of the undoped samples, only specimen 'A' was taken to final fracture, failing at 3651 MPa. The different failure stresses can be expected to be somewhat governed by difference in the volume fraction of fibres (~55 % *vs.* ~63 %), rather than just the presence of the fiducial marker system. It is noted that:

- It is not the doped specimen that manifests an anomalous behaviour, but rather the undoped specimen 'A'. More specifically, the failure stress of the composite is surprisingly high for the fibre type used, even if the higher volume fraction is accounted for – on the order of 15 % above an equivalent fibre strength of 4900 MPa.
- The double-edge notched specimens used are expected to experience high specimen-to-specimen variability due to the small gauge volumes. This is because any intrinsic flaws (or the lack of) in the fibres will have a higher impact on such a small gauge volume. In this context, according to the weakest link theory (*i.e.* Weibull distribution), very small volumes are found to exhibit high strengths [1]. For example, Tanaka *et al.* [58] have shown that the average size of critical flaws decreased with decreasing gauge length, whereby a higher fibre strength was reported in conjunction with smaller flaw sizes. Likewise, an experimental size-scaling is reported by Okabe and Takeda [59]. Therefore, it seems possible that the undoped specimen 'A' may have been simply a region which was characterized by fewer flaws within the load bearing section of ~1 mm^3.
- As noted in the introduction, the mechanical properties of the thermosetting matrices can be preserved, provided that the particle concentration used is low; and since the matrix is responsible for the load transfer around a fibre break, it may also be expected that the micromechanical response of the composite is not fundamentally interfered with.

Figure 4-6 shows that fibre breaks accumulate exponentially with applied stress in all three specimens, as reported in [1, 4, 5, 19]. The two undoped specimens 'A' and 'B' show reasonable consistency in terms of accumulation rate, with a slightly more rapid accumulation in the latter. Conversely, the doped specimen exhibits the most rapid accumulation of breaks, particularly noticeable above a composite stress of ~2000 MPa. This trend holds if the volume fraction differences are accounted for in terms of equivalent fibre stresses for the two materials, in spite of the subsequent shift that results over the horizontal axis – position of the

undoped specimen curves are swapped, with undoped specimen ‘A’ exhibiting a slightly earlier (lower stress) onset of fibre breaks, *cf.* undoped specimen ‘B’.

Figure 4-7 exemplifies the same effect in terms of fraction of specimen UTS. Likewise, it indicates that the total number of breaks close to fracture is on the same order for doped and undoped materials (913 and 873 breaks, respectively), resulting in a difference of less than ∼5 % – notwithstanding the slightly different fraction of UTS achieved in each case (98 % and 95 %, respectively). Given the lower fibre volume fraction of the doped specimen it can be noted that the proportion of fibres fractured is actually higher in the doped case. However, the statistical nature of fibre behaviour should be recognised, that otherwise identical specimens, representative of T700-series composite, have been reported to exhibit greater variability than seen between the current doped and undoped materials. This is particularly reported in [19], whereby specimens were characterised by 581 and 418 breaks, respectively, at 99.9 % UTS within the load bearing reduced cross-section of 0.45 mm^2 – implying that one material presented ∼40 % variation in number of breaks. In this context, the presence of $BaTiO_3$ particles does not appear to have had an exceptional effect on the total number of breaks at fracture, and from this perspective, the doped material replicates the essential behaviours of the undoped counterpart, allowing it to be considered as a useful model system.

It is noted that the accumulation rates may be influenced by the volume fraction of fibres. A high fibre volume fraction material has more intact fibres closely-packed around any given broken one, which may be anticipated to result in a stronger ‘shielding effect’ [13]. On this basis, numerical models indicate that for a random packing, the nearest (intact) neighbouring fibres shield the second nearest neighbouring fibres from the stress concentration associated with a fibre break. Indeed, a higher fibre volume fraction results, on average, in more intact fibres at small distances from the break, and thus with high SCFs. However, when the SCFs are compared at a fixed radial distance from a broken fibre, the higher fibre volume fraction results in a lower SCF [13]. In turn, this ‘shielding effect’ may translate into an overall accumulation of breaks, with the shallower trend seen in the undoped specimen ‘A’.

(a) - Doped specimen	Load (N)	600	750	800	850	900	950
	Stress in 0° plies (MPa)	1432	1790	1909	2029	2148	2267
	Specimen UTS (fraction)	0.62	0.77	0.82	0.88	0.93	0.98
	Number of total breaks	1	14	47	108	357	913
	% of total breaks	0.11	1.53	5.15	11.83	39.10	100
Failure load (N)	970						
Failure stress in 0° plies (MPa)	2315						
Minimum cross-sectional area of 0° plies (mm^2)	0.419						

(b) - Undoped specimen 'A'	Load (N)	900	1200	1250	1300	1350	1450
	Stress in 0° plies (MPa)	2163	2885	3005	3125	3245	3486
	Specimen UTS (fraction)	0.59	0.79	0.82	0.86	0.89	0.95
	Number of total breaks	20	283	385	490	612	873
	% of total breaks	2.29	32.42	44.10	56.13	70.10	100
Failure load (N)	1519						
Failure stress in 0° plies (MPa)	3651						
Minimum cross-sectional area of 0° plies (mm^2)	0.416						

(c) - Undoped specimen 'B'	Load (N)	900	1050	1200	1350
	Stress in 0° plies (MPa)	2055	2397	2740	3082
	Specimen UTS (fraction)	N/A			
	Number of total breaks	25	102	266	661
	% of total breaks	3.78	15.43	40.24	100
Failure load (N)	N/A				
Failure stress in 0° plies (MPa)	N/A				
Minimum cross-sectional area of 0° plies (mm^2)	0.438				

Table 4-6 – Summary of fibre break behaviour as a function of applied load, stress and % UTS: (a) doped specimen, (b) undoped specimen 'A', (c) undoped specimen 'B'. Based on in situ SRCT tensile data.

The total number of fibre breaks found in the present work is consistently higher than that previously reported in the literature, based on an aerospace-grade CFRP with similar reinforcing fibres (*i.e.* T700-series) [1, 4, 19]. For example, Swolfs *et al.* [1] reported less than 500 breaks/mm^3 at 94 % specimen UTS, which is reasonably consistent with that reported by Scott *et al.* [4] and Garcea *et al.* [19], respectively. While it is beyond the scope of this work to establish why this is the case, the higher number of fibre breaks reported here may be associated with intrinsic defects arising from the prepreg drum winding process (*e.g.* abrasion of the fibre

surfaces by the metering die, guide rollers *etc.*) and/or during the lay-up stage, which was not automated, and thus involved extensive manual intervention. The fact that a CFRP based on T700-series fibres and manufactured via filament winding can exhibit a considerably higher number of breaks, as opposed to its aerospace-grade counterpart, is also shown by Scott [60] and Morton [61], acknowledging that the filament wound materials in [60] and [61] were not subjected to autoclave curing. It is also worth noting that given the combination of individual microvoids and a low void volume fraction, no obvious/direct mechanistic correlation was found between the location of the broken fibres and the location of microvoids, nor between the total number of breaks and the volume fraction of microvoids. This is in contrast to that reported in [57], whereby significantly larger, and more numerous voids (by vol.), than found in the present work, were shown to have a clear influence on fibre break location. In [57], a significant proportion of fibre breaks occurred within half a fibre diameter of a void.

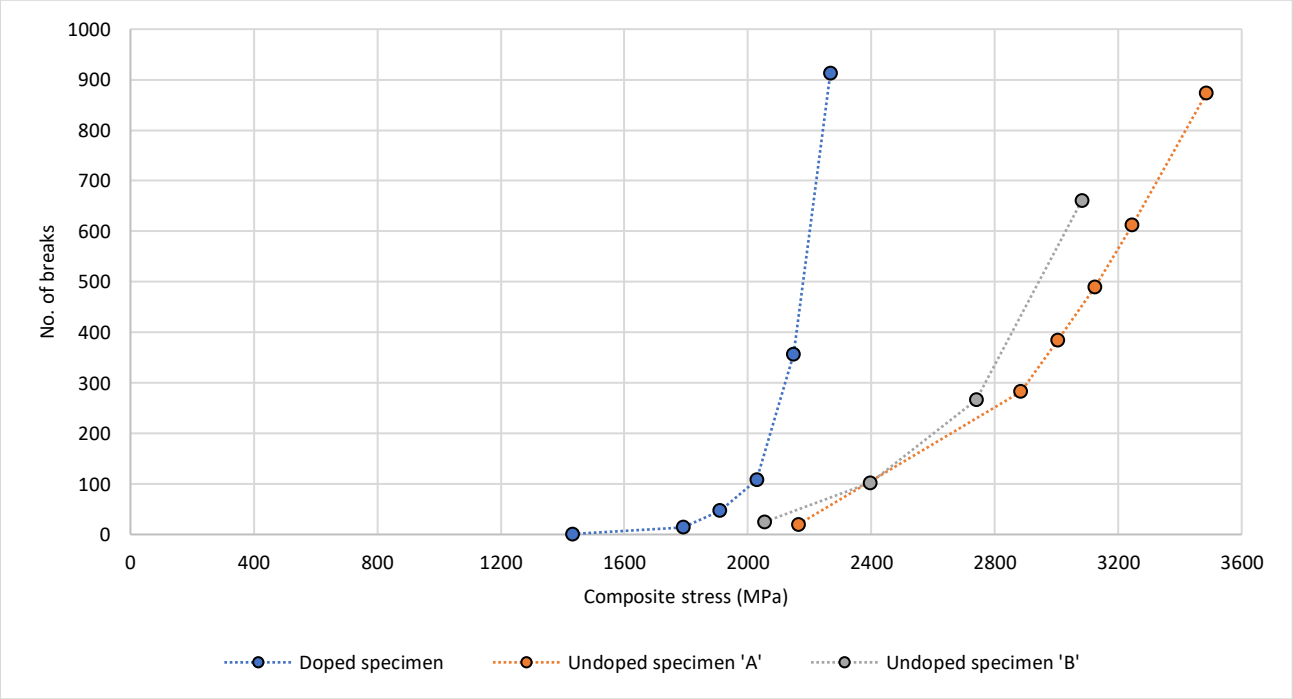

Figure 4-6 – Fibre break accumulation as a function of applied stress for the three specimens subjected to in situ SRCT tensile testing. Data shown for an equivalent ROI volume of ~0.34 mm^3 for each specimen.

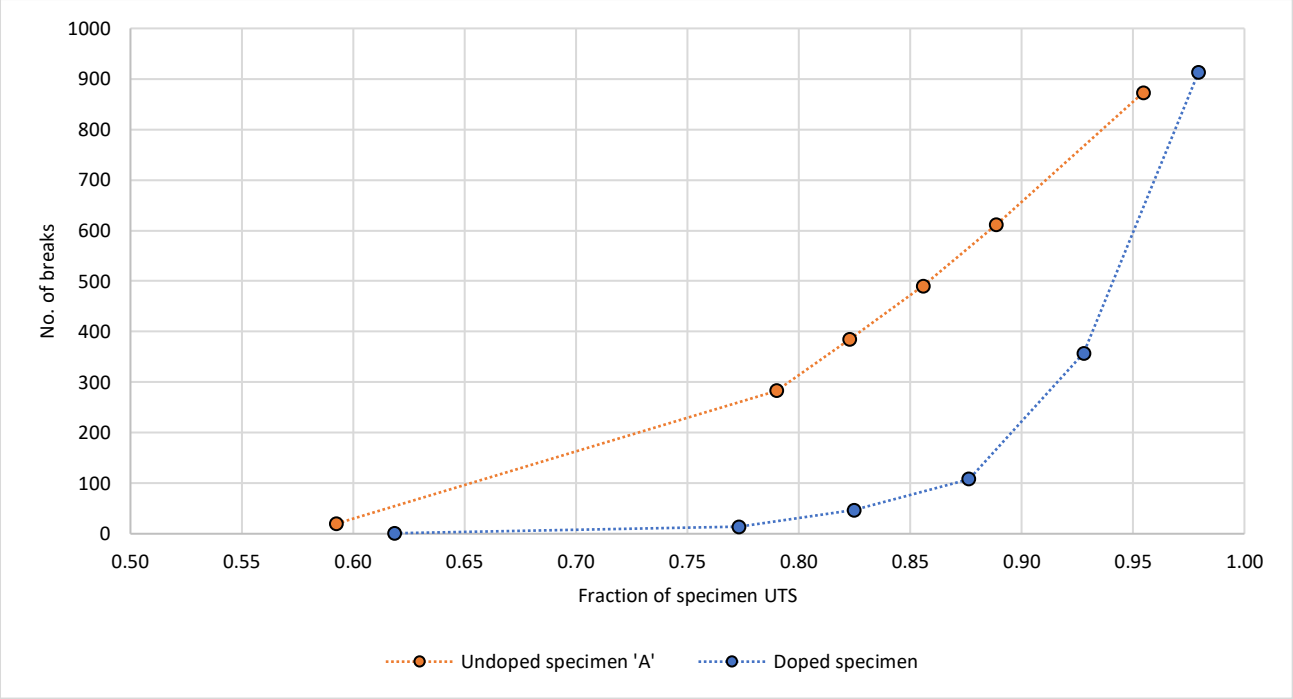

Figure 4-7 – Fibre break accumulation as a function of % UTS for the two specimens loaded to fracture. Based on in situ SRCT data. Data shown for an equivalent ROI volume of ~0.34 mm^3 for each specimen.

The specimen variability becomes even more evident if the fibre break behaviour is decoupled into singlets (**Figure 4-8**) and fraction of singlets to N-plets (**Figure 4-9**), respectively. It can be observed that the rate of singlet accumulation in the undoped specimen 'B' matches more to that in the doped specimen, as opposed to that in the undoped specimen 'A'.

The doped specimen is also associated with the lowest number of singlets (421), which is ultimately linked to the lowest fraction of singlets to N-plets (46 %). As the difference in the number of singlets between the specimens is considerably higher compared to that reported in the literature (*e.g.* 339 *vs.* 331 at 99.9 % UTS in [19]), it would initially appear that doping with barium titanate has had an effect on the distribution of non-interacting fibre breaks. However, also shown in [19] is that even larger differences can be expected in terms of the proportion of singlets to N-plets (*cf.* total number of breaks), for identical specimens: 58 % and 79 %, respectively – a difference which is undoubtedly higher than found here between the doped and undoped specimen 'A'.

Furthermore, while **Figure 4-9** shows a general decrease in the proportion of singlets to N-plets, the trend is only monotonic in the case of the undoped specimen 'A'. This occurs due to the appearance of clusters of breaks at relatively low applied stresses, that unlike singlets, do not exhibit a particularly steep evolution until closer to failure (*i.e.* above ~90 % UTS) – *e.g.* the largest cluster (12-plet) in the undoped specimen 'B', appears at an intermediate applied stress of 2397 MPa – forming an 'early cluster'. Taken together, these observations

indicate that there is variability in damage progression irrespective of the inclusion of $BaTiO_3$ particles, which is consistent with the specimen-to-specimen variability in fibre break evolution observed in other material systems [19, 61].

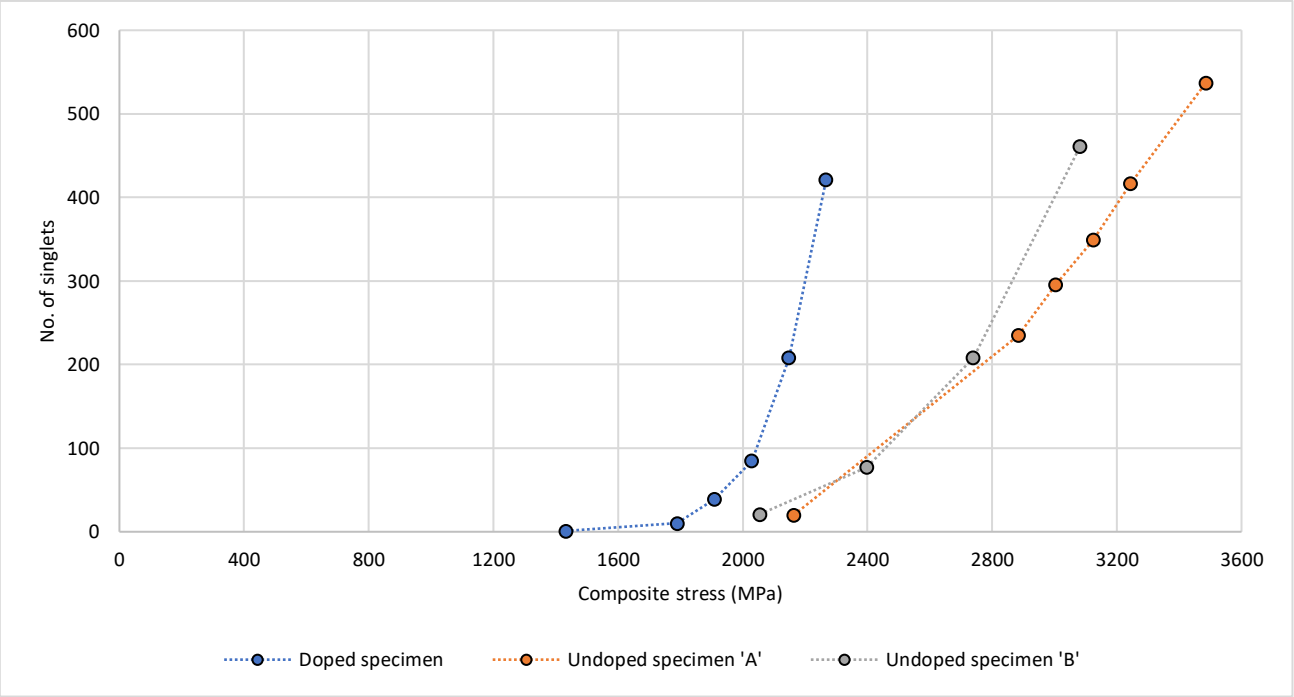

Figure 4-8 – Number of singlets as a function of applied stress for the three specimens subjected to in situ SRCT tensile testing. Data shown for an equivalent ROI volume of ~0.34 mm³ for each specimen.

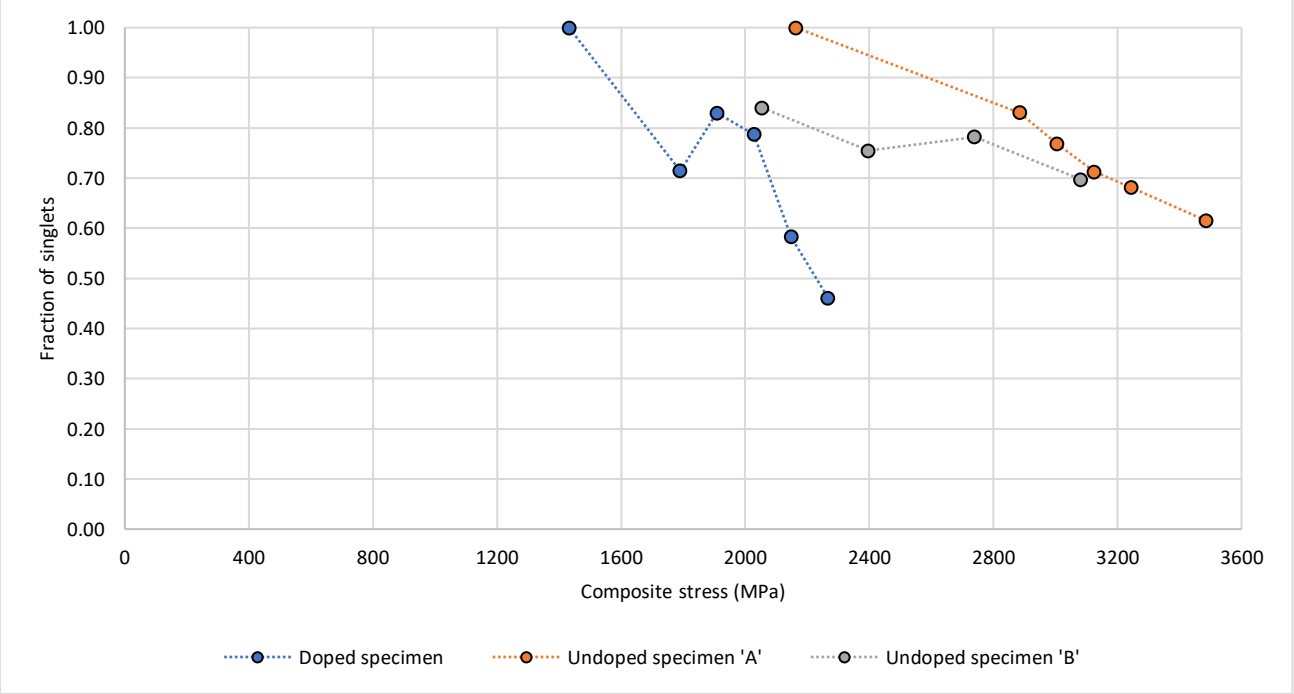

Figure 4-9 – Fraction of singlets to N-plets as a function of applied stress for the three specimens subjected to in situ SRCT tensile testing. Data shown for an equivalent ROI volume of ~0.34 mm³ for each specimen. Nomenclature example: three 7-plets are counted as 21 breaks in total).

4.3.3 Cluster behaviour

The accumulation of clusters of breaks as a function of applied stress is summarized in **Figure 4-10**, while **Figure 4-11** presents the visual distribution of these clusters in 3D, at the maximum stress recorded prior to fracture.

The largest clusters found in this work were: a 19-plet in the doped specimen, two 9-plets in the undoped specimen 'A' and an 'early' 12-plet in the undoped specimen 'B'. It was also noted that the largest cluster(s) of one 19-plet in the doped specimen encompasses a similar number of breaks to the two 9-plets in the undoped specimen 'A' (19 *vs.* 18); with the two 9-plets forming adjacent to each other (**Figure 4-11**).

The 19-plet found in the doped specimen is larger than the 14-plet at 94 % UTS reported in [4], as well as than the 10-plet and 4-plet, respectively, at 99.9 % UTS reported in [19] – notwithstanding that in [19] a cluster of breaks only encompassed breaks that were directly adjacent to one another, potentially making an equivalent 'distance-based' cluster significantly larger (see **Section 4.2.5**). At 93 % UTS, which is closer to the maximum value reported in [4], the largest cluster of breaks in the doped material is a 7-plet, making it half the size of the largest cluster reported in [4]. In terms of the morphology of largest clusters, this is consistent between the doped and undoped materials. It is important to note, that these are all diffuse clusters (**Figure 4-11**), meaning that unlike the largest cluster reported in [4], they are separated by greater axial and radial distances.

Figure 4-10 shows a similar trend to that reported in [1, 4, 5, 19], whereby larger clusters typically appear with increasing stress. Overall, the undoped specimen 'A' exhibits the shallowest rate of cluster accumulation, followed by the undoped specimen 'B' and doped specimen, respectively. As such, there is distinct variability in behaviour, consistent with that reported in [19]. **Figure 4-10** also shows that for both material types, large clusters of breaks generally form without a reduction in the number of smaller clusters. Furthermore, a 'break-by-break' accumulation with applied stress is not observed for the larger clusters. A notable example is the 'early' 12-plet in the undoped specimen 'B', which formed in a single increment or 'burst', and does not exhibit any further growth. This behaviour generally agrees with the experimental data previously reported in [1] and [4] for hold-at-load scans. Again, the doped material is seen to replicate the key behaviour (cluster formation) of undoped, and more broadly, other carbon-fibre composite systems, validating its use as a model system, with the capability to allow tracking of local strains [7].

Ultimately, within the statistical power of the current sample gauge volumes, it appears that the behaviour of clusters is stochastic, whereby specimen failure is likely to be determined by intrinsic stochastic factors, such as fibre strength and local microstructure [19], rather than particularly the inclusion of barium titanate. A much larger number of specimens would need to be examined to provide a statistically significant conclusion regarding the relative contribution of the fiducial markers compared to the intrinsic variability. This, however,

is not trivial to achieve in practice due to the limited availability and cost of the SRCT beam time required to achieve such results.

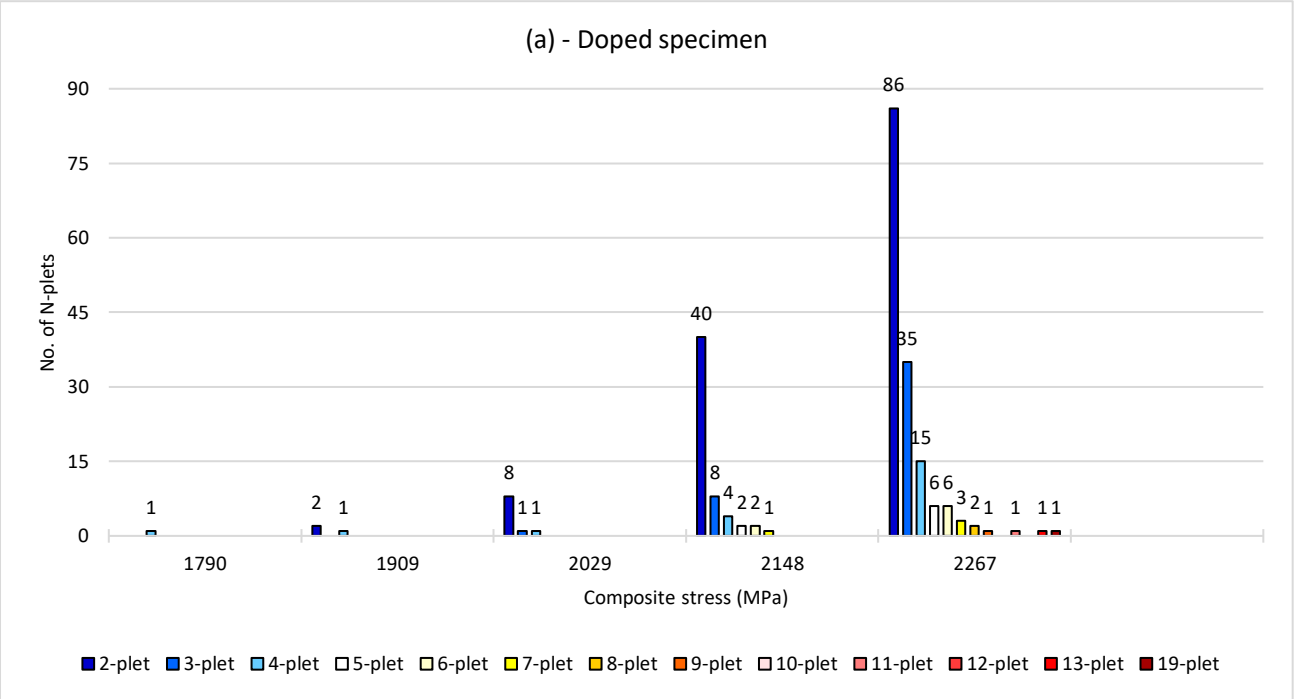

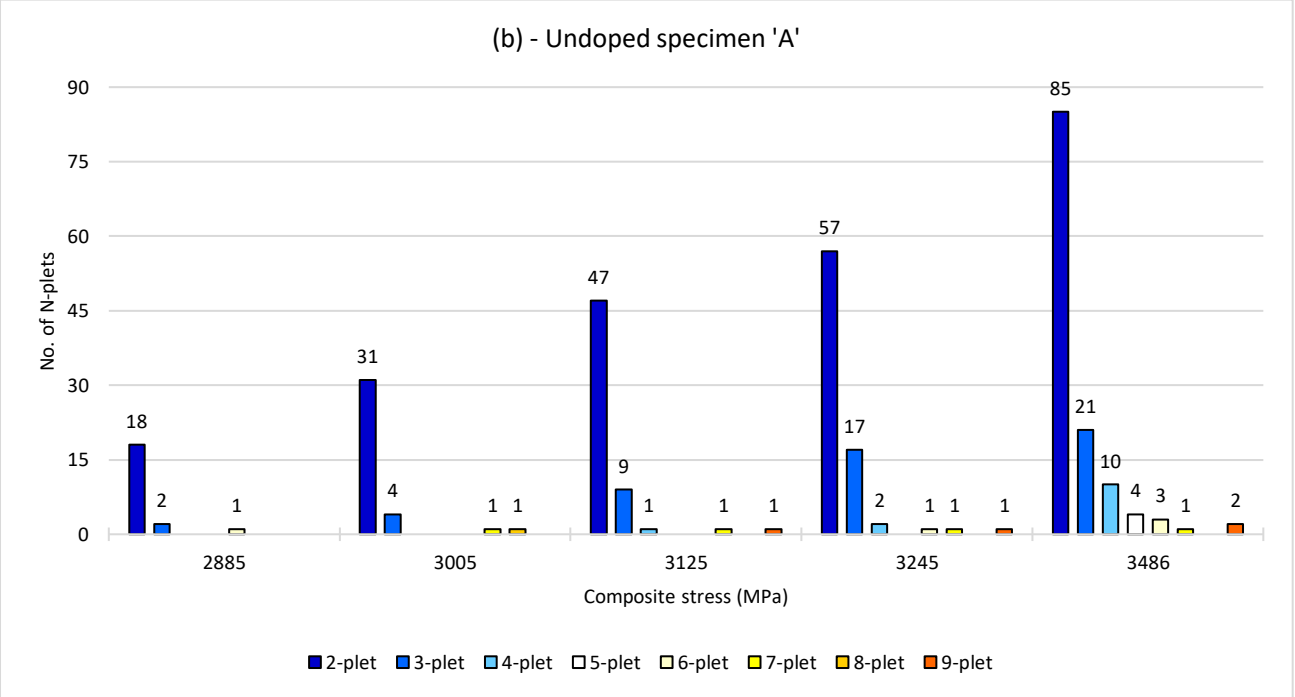

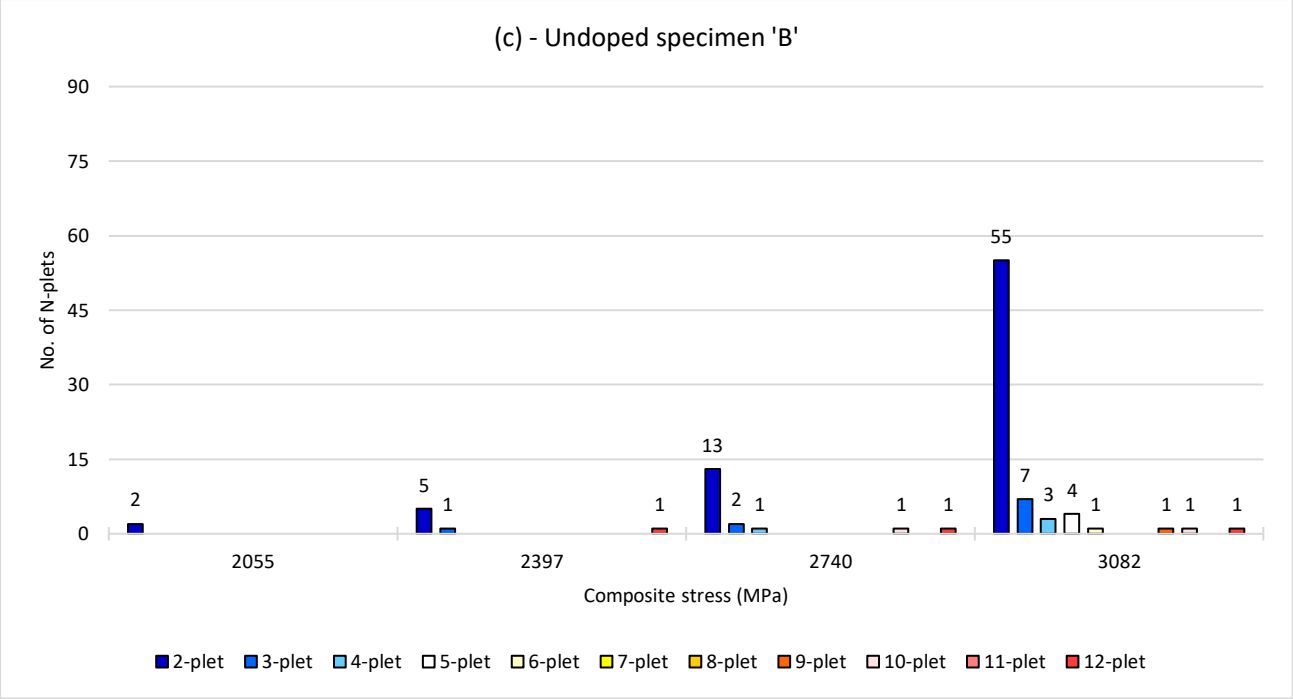

Figure 4-10 – Distribution of N-plets as a function of applied stress for the three specimens subjected to in situ SRCT tensile testing: (a) doped specimen, (b) undoped specimen 'A', (c) undoped specimen 'B'. Data shown for an equivalent ROI volume of ~0.34 mm^3 for each specimen.

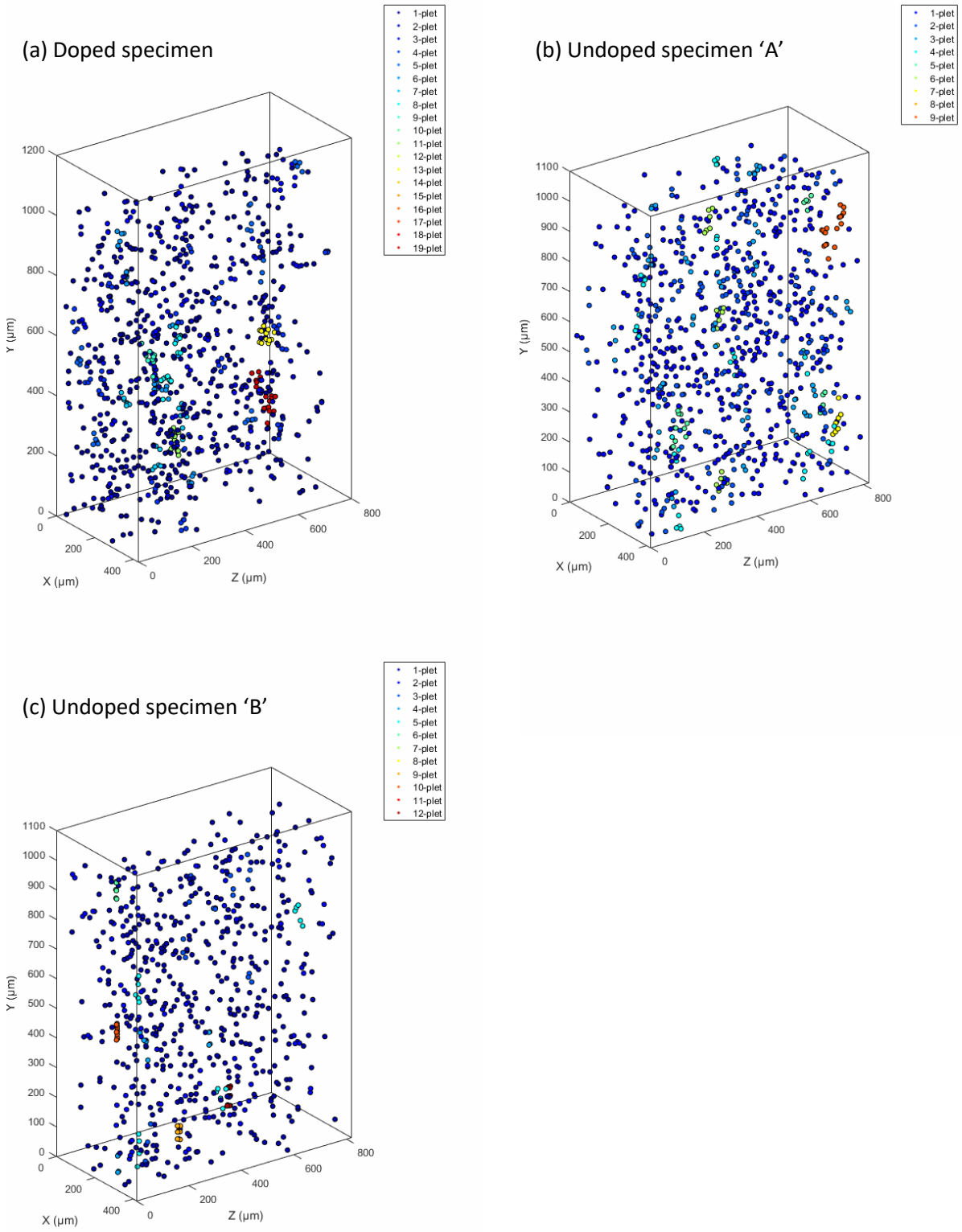

Figure 4-11 – Distribution of N-plets in 3D space at the maximum stress recorded prior to fracture: (a) doped specimen – 2267 MPa, (b) undoped specimen 'A' – 3486 MPa, (c) undoped specimen 'B' – 3082 MPa. Visualizations reconstructed from break centroid coordinates. Each volume corresponds to ~0.34 mm^3.

4.4 Summary and conclusions

A model Carbon-Fibre Reinforced Polymer composite was developed to permit the application of Digital Volume Correlation to displacement and/or strain measurements parallel to the fibre orientation, with the ultimate goal of allowing the mapping of strain fields at fibre break sites. To generate individual features unique to a particular sub-set, the work has explored the insertion of sparse populations of sub-micrometre particles within the matrix to act as fiducial markers.

To preserve the tensile behaviour of a commercially representative material, whilst still allowing the application of DVC parallel to the fibre direction, a series of considerations were established. The key trade-off required ensuring that the volume fraction of fiducial markers was able to satisfy the imaging requirements, yet was low enough to minimize any substantial disruption in the separation and packing of fibres at tow-level. Out of the 38 test materials manufactured, barium titanate particles (400 nm, ~1.44 vol. %) were found to offer the most favourable compromise between contrast in CT images and the ability to obtain a homogeneous distribution in 3D space with sufficient particle compactness for local DVC analyses. This property combination was selected following an extensive µCT-based qualitative assessment on a range of possible particle compositions, mean sizes and concentrations.

In situ SRCT and subsequent image analysis has shown that the response of the doped material is mechanistically representative of undoped materials made by the same manufacturing route, and is consistent with other materials made by other processes – at least in terms of the fibre fracture response. Some variability in mechanical behaviour is discerned between individual specimens, and material types (doped and undoped), which may be attributable to both manufacturing inconsistency and a potential contribution of the doping particles. Notwithstanding these effects, the doped material is identified as a suitable model to characterise for the first time the localised, three-dimensional load shedding processes associated with fibre break accumulation within the bulk of CFRPs.

While the development of the present material is mainly intended to promote the understanding of the fundamental aspects of UD composite tensile failure, a similar methodology may be applied to off-axis ply orientations. Furthermore, acknowledging that the benefits of displacement/strain mapping should outweigh differences in the material behaviour, the methodology may be adapted to probe the understanding of composite behaviour not only under different loading conditions (*e.g.* compression, torsion, time-varying), but also at larger length-scales (*e.g.* up to the structural level) and in the context of multiaxial or discontinuous reinforcements.

4.5 Appendix A – Micro-focus Computed Tomography

Representative µCT slices from each of the CFRPs fabricated. FOV of ~730 µm x ~730 µm per slice.

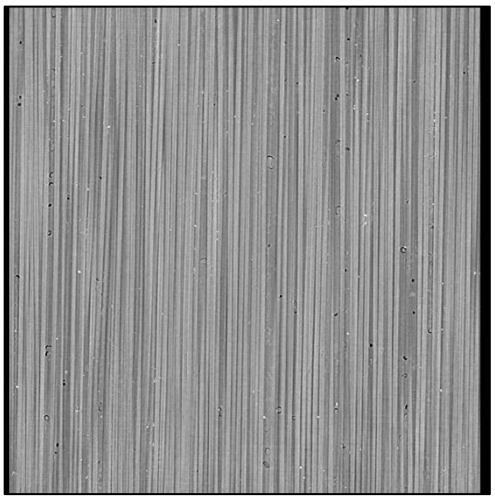

Al 800 nm, 0.25 wt. % (slice 426)

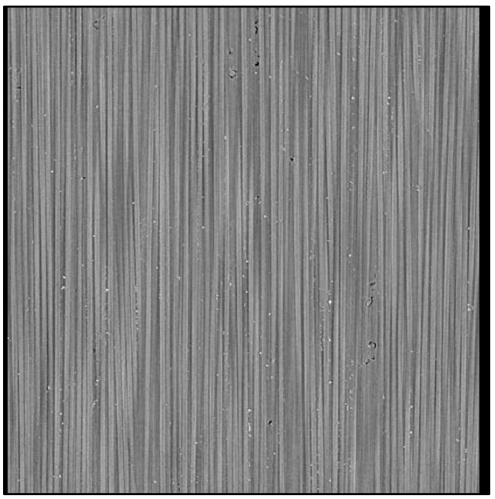

Al 800 nm, 1 wt. % (slice 542)

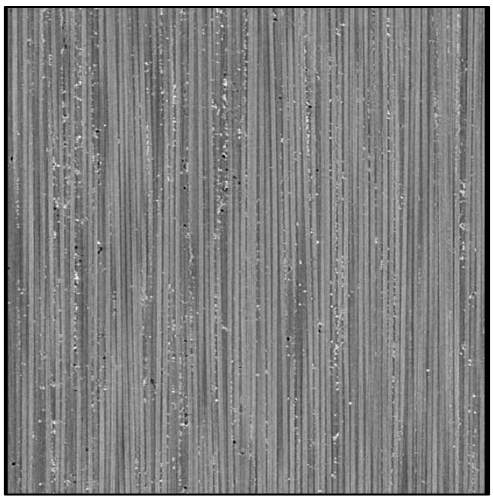

Al 800 nm, 5 wt. % (slice 541)

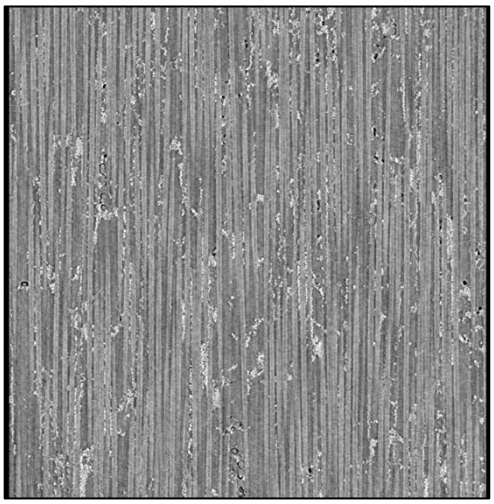

Al 800 nm, 15 wt. % (slice 583)

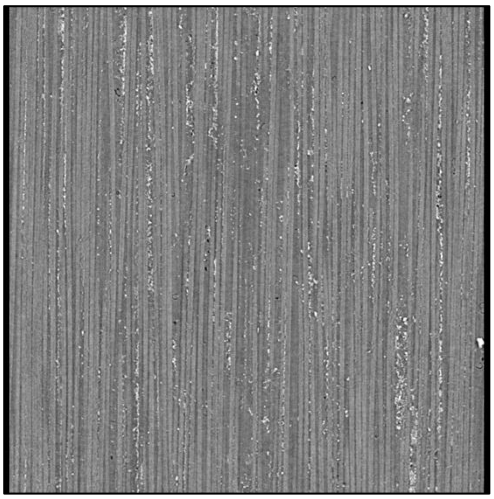

Al_2O_3 300 nm, 7.5 wt. % (slice 435)

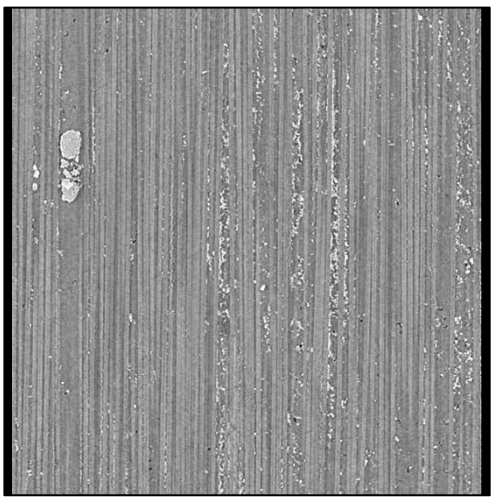

Al_2O_3 300 nm, 10 wt. % (slice 402)

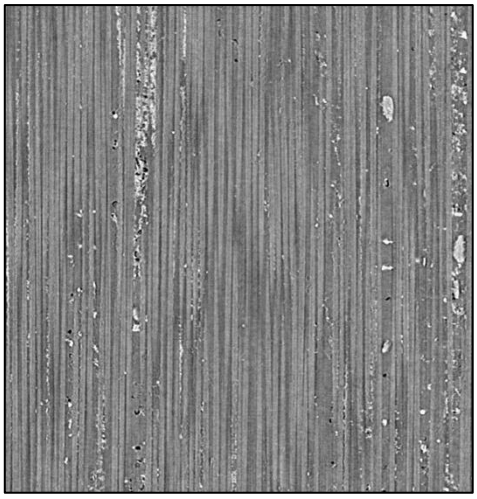

Al_2O_3 500 nm, 7.5 wt. % (slice 386)

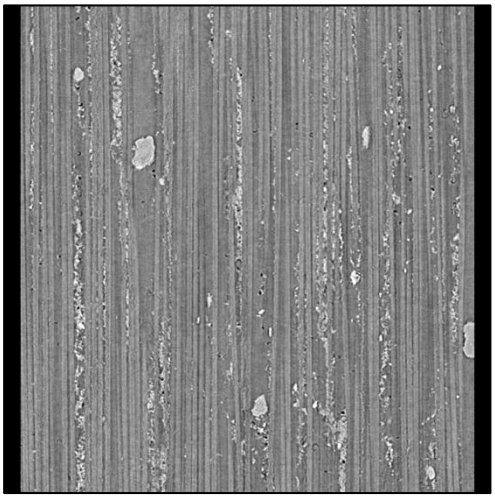

Al_2O_3 500 nm, 10 wt. % (slice 341)

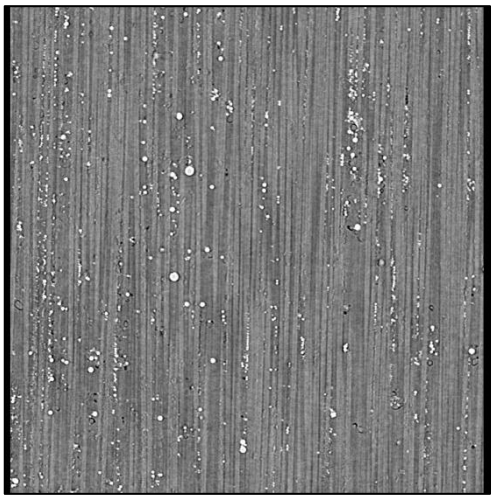

Al_2O_3 800 nm, 7.5 wt. % (slice 420)

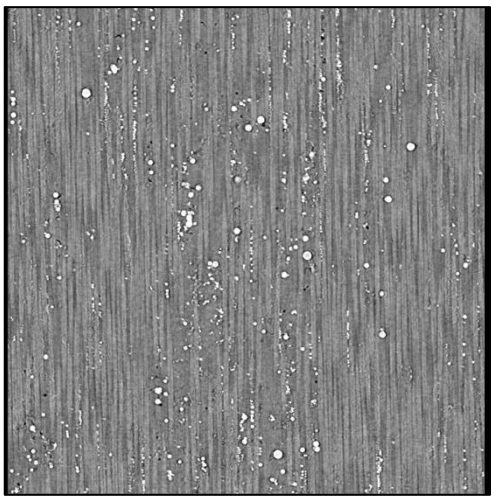

Al_2O_3 800 nm, 10 wt. % (slice 546)

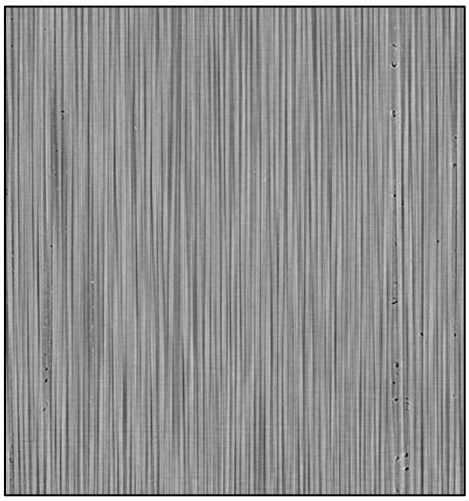

SiC 600 nm, 0.25 wt. % (slice 644)

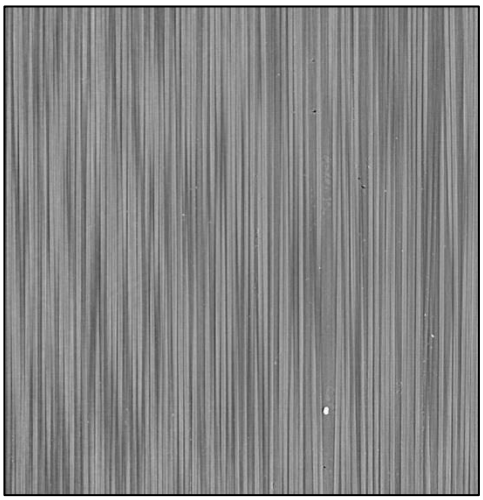

SiC 600 nm, 0.5 wt. % (slice 552)

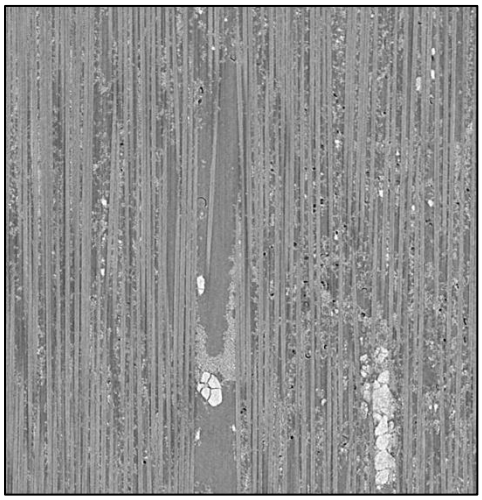

SiC 600 nm, 15 wt. % (slice 425)

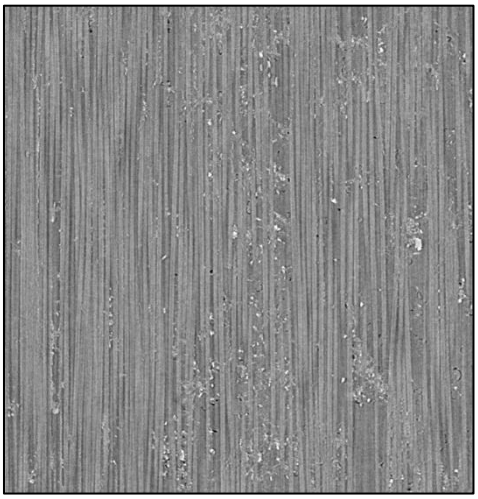

SiO_2 400 nm, 7.5 wt. % (slice 562)

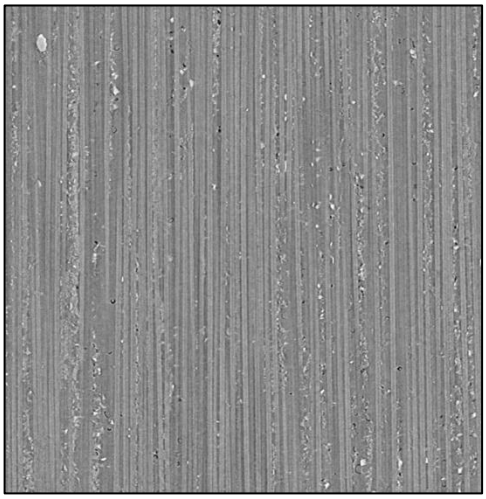

SiO_2 400 nm, 10 wt. % (slice 480)

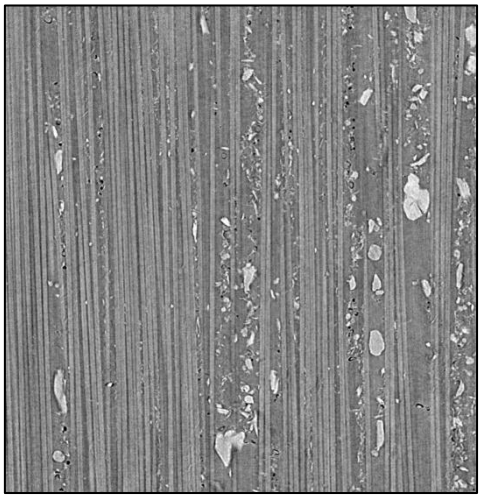

MgO 300 nm, 7.5 wt. % (slice 425)

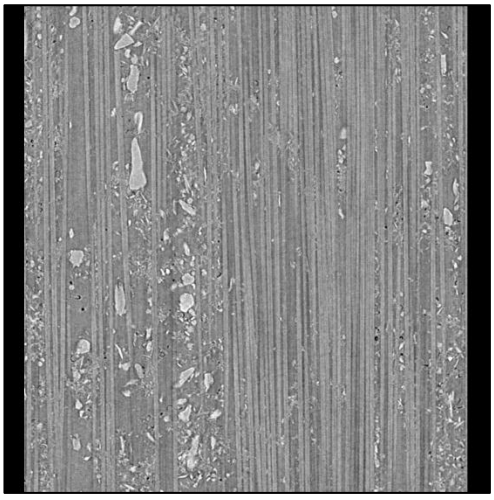

MgO 300 nm, 10 wt. % (slice 320)

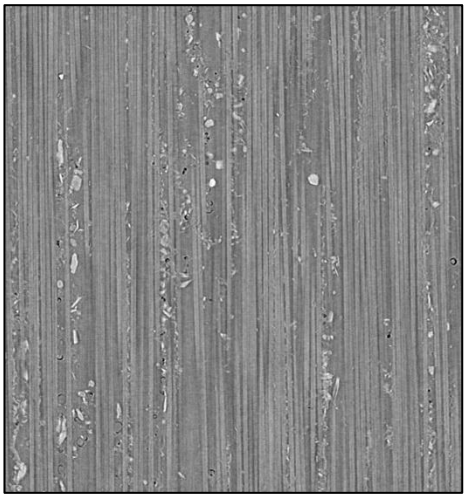

MgO 600 nm, 7.5 wt. % (slice 370)

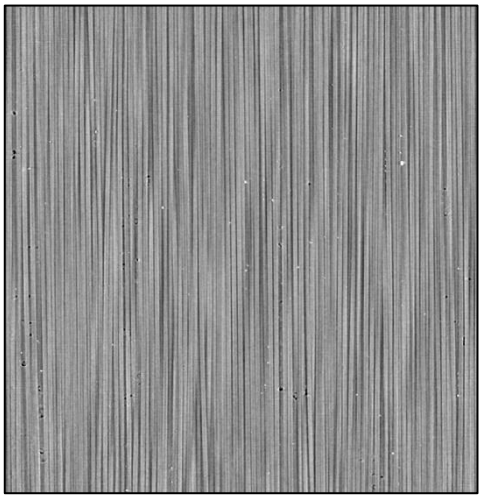

TiC 800 nm, 0.25 wt. % (slice 556)

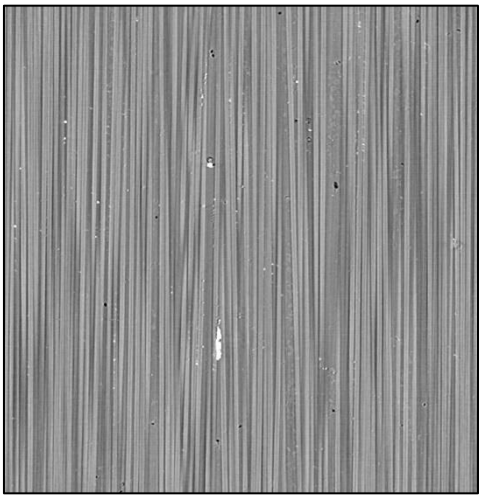

TiC 800 nm, 0.5 wt. % (slice 451)

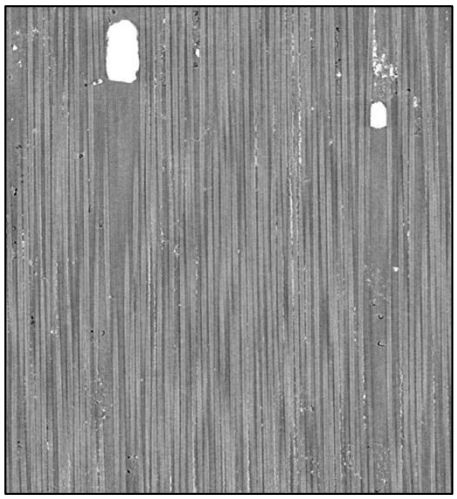

TiO_2 300 nm, 5 wt. % (slice 656)

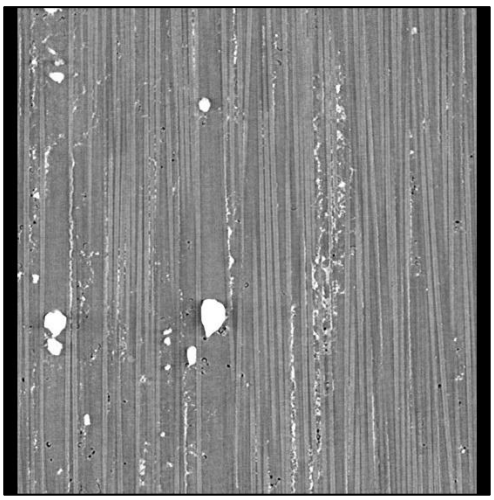

TiO_2 300 nm, 7.5 wt. % (slice 631)

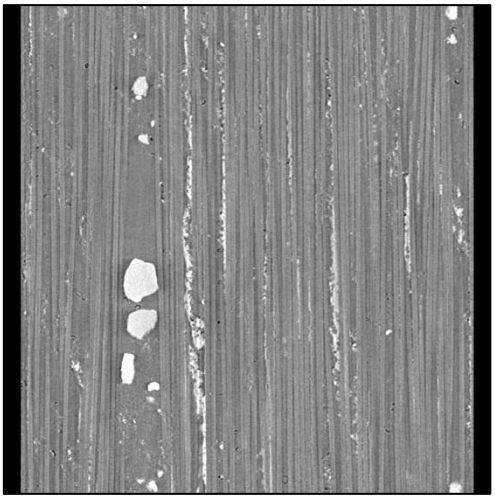

TiO_2 300 nm, 10 wt. % (slice 343)

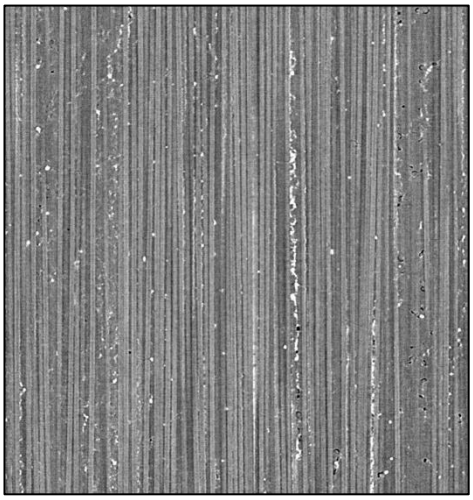

TiO_2 500 nm, 7.5 wt. % (slice 615)

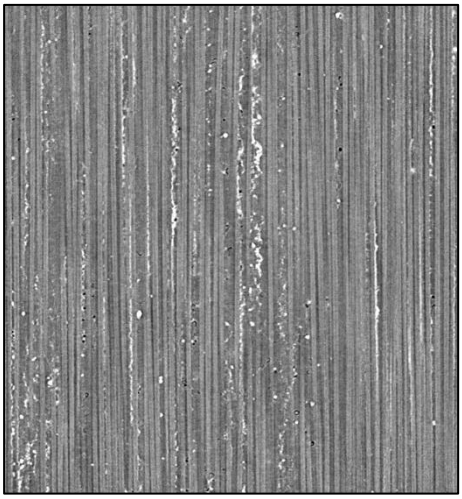

TiO_2 500 nm, 10 wt. % (slice 355)

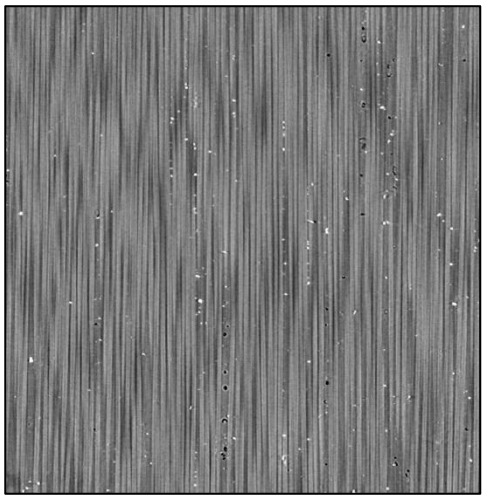

$BaCO_3$ 800 nm, 0.5 wt. % (slice 507)

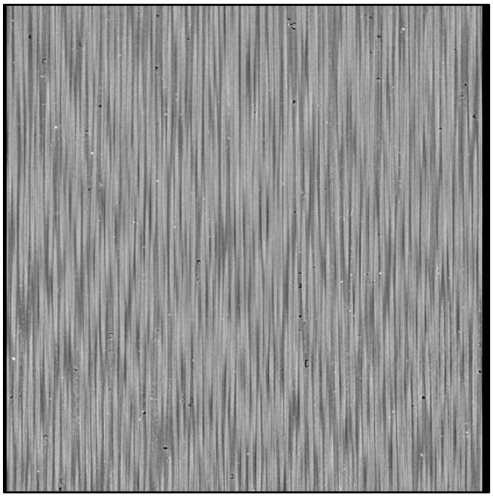

$BaTiO_3$ 400 nm, 0.25 wt. % (slice 458)

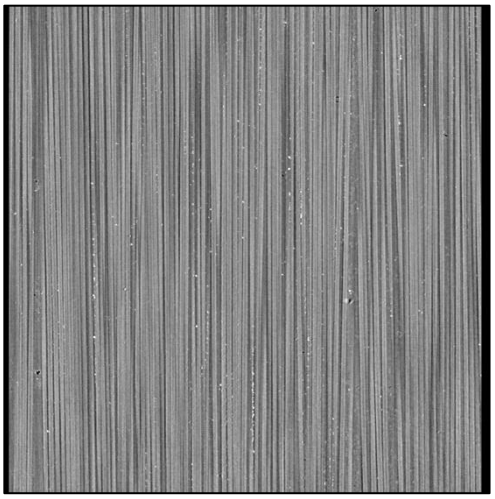

$BaTiO_3$ 400 nm, 0.5 wt. % (slice 441)

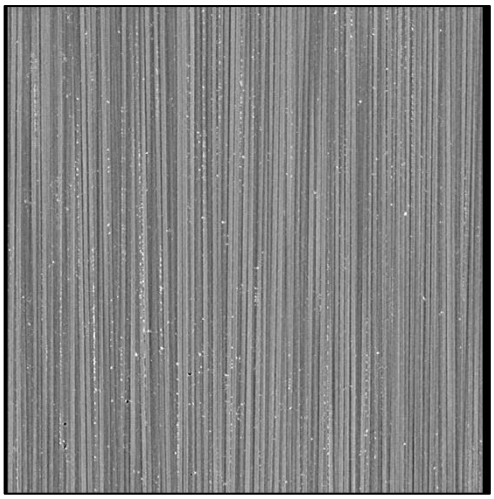

$BaTiO_3$ 400 nm, 1 wt. % (slice 470)

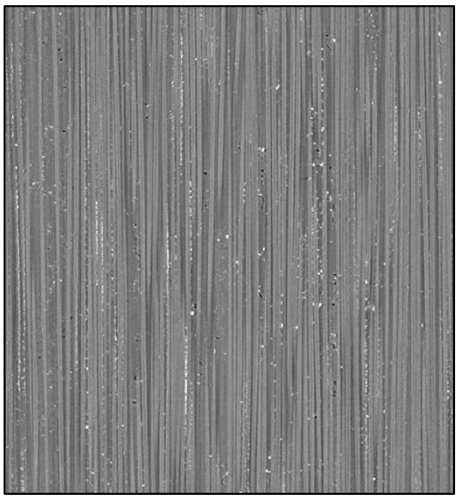

$BaTiO_3$ 400 nm, 2 wt. % (slice 346)

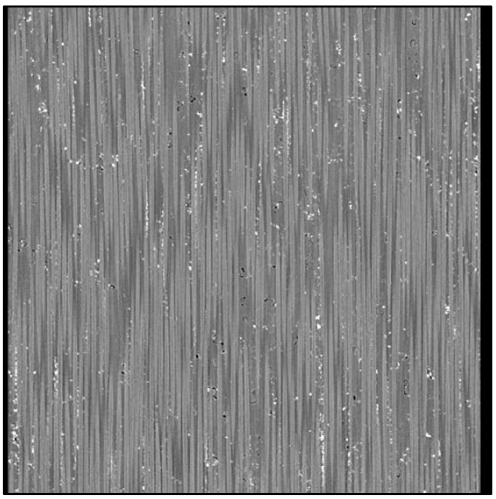

$BaTiO_3$ 400 nm, 3 wt. % (slice 452)

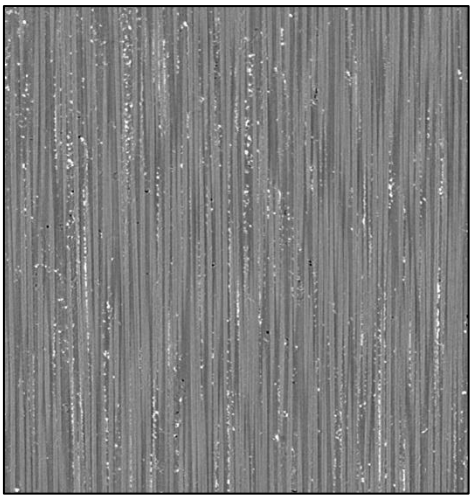

$BaTiO_3$ 400 nm, 4 wt. % (slice 394)

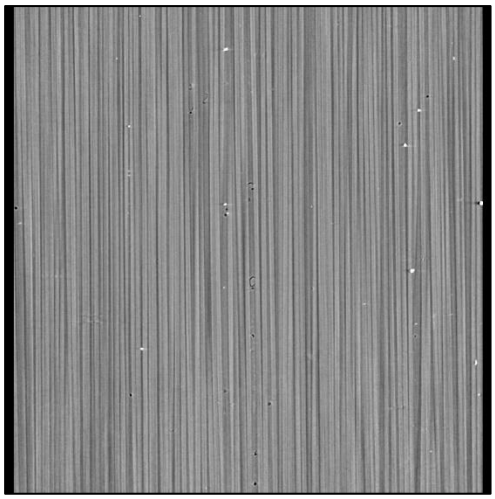

Cu 580 nm, 0.25 wt. % (slice 398)

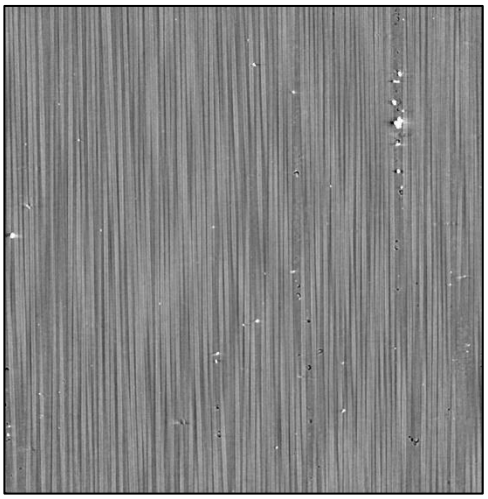

Cu 580 nm, 0.5 wt. % (slice 452)

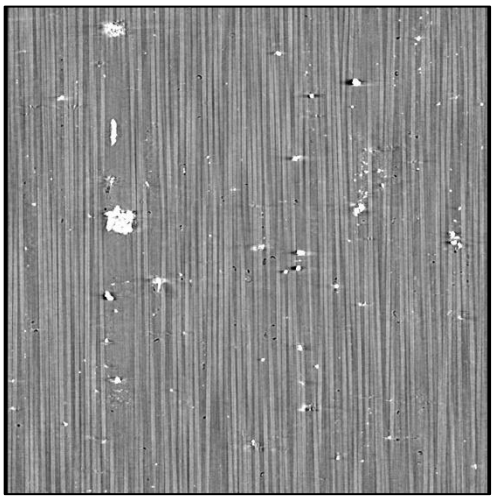

Cu 580 nm, 1 wt. % (slice 452)

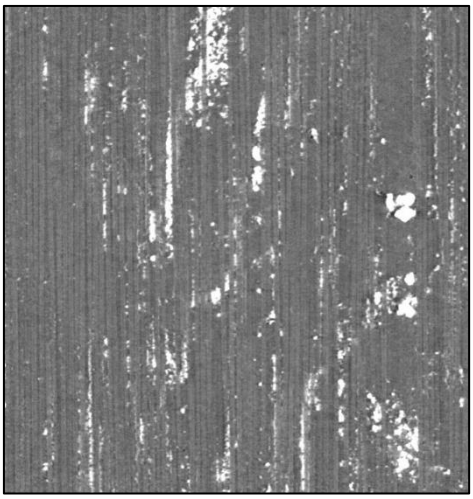

Bi_2O_3 800 nm, 10 wt. % (slice 487)

4.6 Appendix B – Microstructural analysis

Fiducial marker system	Ranking	Detailed list of comments
Al	✓✓✓	• The 800 nm aluminium particles are identifiable from the lowest concentration used of 0.25 wt. %, albeit with a sparse spatial distribution. • Increasing the concentration to 1 wt. % results in a marginal improvement. • The spatial distribution is improved at a concentration of 5 wt. % and 10 wt. %, respectively. • At a concentration of 10 wt. %, aluminium is deposited between individual fibres, forming the desired 'strips' of fiducial markers in the fibre direction, without introducing gross microstructural anomalies. This appears to satisfy the imaging requirements for local DVC analyses. • The highest concentration investigated of 15 wt. % causes particles to clump significantly, forming heterogeneous 'bands' of fiducial markers along the fibre direction, and subsequently generating substantial disruption in the separation and packing of fibres at tow-level.
Al_2O_3	✓	• The 300 nm and 500 nm aluminium oxide particle sizes yield a relatively sparse spatial distribution at a concentration of 7.5 wt. % (*e.g.* compared to the 800 nm aluminium particles at a concentration of 10 wt. %). • The homogeneity of the spatial distribution does not improve, for either particle size, if the concentration is increased to 10 wt. %; on the contrary, the prominence of particle 'bands' increases, in conjunction with a greater agglomerate presence. • Agglomerates represent the heaviest form of local particle clumping detected, with the accompanying microstructural disruption being considerably higher than that caused by the particle 'bands'. • The 300 nm system appears to yield a slightly superior particle deposition between the individual carbon-filaments compared to the 500 nm counterpart. This may be attributed to less filtering as the fibre tow was drawn through the metering die, and thus as a superior deposition of aluminium oxide during manufacture. • At the largest aluminium oxide particle size of 800 nm investigated, the spatial distribution is sparse compared to the 300 nm and 500 nm counterpart (applicable to both concentrations investigated of 7.5 wt. % and 10 wt. %, respectively). • The 800 nm system appears not to be associated with the formation of agglomerates, but rather with the presence of individual particles of evidently larger size, if compared alongside the mean stated by the manufacturer. In turn, this may be explained through a large variability in particle size for this system. • At a concentration of 10 wt. %, the spatial distribution of the 800 nm aluminium oxide particles is sparse compared to the 800 nm aluminium system.
SiC	✓	• At a concentration of 0.25 wt. % and 0.5 wt. %, respectively, the spatial distribution of the 600 nm silicon carbide system is sparse. This is similar to the other materials doped with very low particle concentrations (< 1 wt. %). • Increasing the concentration to 15 wt. % results in a microstructure abundant with gross microstructural anomalies (both particle 'bands' and agglomerates), which fails to satisfy the established considerations. • Compared to the more attenuating compounds (*e.g.* TiC, $BaTiO_3$), the imaging contrast obtained between the silicon carbide particles and the carbon-filaments is noticeably less – this is consistent with the attenuation profiles shown in **Figure 4-1**.
SiO_2	✓✓	• Silicon dioxide (7.5 wt. % and 10 wt. %) with a particle size of 400 nm performs similar to the 500 nm aluminium oxide (7.5 wt. %) and 500 nm titanium oxide (7.5 wt. %) systems, respectively. • Compared to the silicon carbide (15 wt. %) system, gross anomalies are reduced for both concentrations of 7.5 wt. % and 10 wt. %, respectively. • The particle distribution homogeneity and local compactness do not match that achieved by the 800 nm aluminium (10 wt. %) and 400 nm barium titanate (7.5 wt. %) systems, respectively.

MgO	✓	• Doping the matrix with 300 nm magnesium oxide particles at a concentration 7.5 % and 10 %, respectively, results in a cured material with the highest departure from the established considerations. • The microstructure is characterized by an abundance of agglomerates, particularly at the higher concentrations. • The magnesium oxide agglomerates have a 'crystal-like' appearance, differentiated by sharp edges from the other compositions examined. It may be envisaged that under applied load, these sharp edges would act as stress raisers (concentrations), promoting extensive matrix microcracking. • In conjunction with the substantial disruption in the separation and packing of fibres at tow-level, the doping of the matrix with magnesium oxide may be expected to significantly reduce the overall mechanical performance of the composite. • Doubling the particle size of the magnesium oxide (*i.e.* 600 nm) for a concentration of 7.5 wt. % results in no substantial improvements with respect to the 300 nm counterpart at the equivalent concentration.
TiC	✓	• At a size of 800 nm, titanium carbide particles are identifiable despite the very low concentrations investigated (0.25 wt. % and 0.5 wt. %). • The imaging requirements for local DVC analyses are not satisfied at these concentrations. • Agglomerates are identified within the visible region, indicating that the system is generally prone to early-onset clumping. • Given the very low particle concentrations, it is also conceivable that the large agglomerates pre-existed in the powder, and are thus not associated with the manufacturing process.
TiO_2	✓✓	• The doping of the matrix with 300 nm titanium oxide (5 wt. %, 7.5 wt. % and 10 wt. %) yields a marginal improvement compared to the magnesium oxide systems (300 nm and 600 nm, respectively). • Similarly, compared to the magnesium oxide counterpart, agglomerates no longer have sharp edges and the overall abundance is slightly reduced within the microstructure. However, the CFRP is mainly characterized by lighter forms of clumping (*i.e.* heterogeneous 'bands' of fiducial markers). • As in the case of aluminium (800 nm, 15 wt. %), these particle 'bands' significantly affect the separation and packing of fibres. • The homogeneity of the spatial distribution appears to decrease with increasing particle concentration – indicating that the titanium oxide system is prone to clumping at the higher concentrations used. • The homogeneity of the spatial distribution is improved considerably by increasing the particle size to 500 nm, at a concentration of 7.5 wt. % (this is contrary to the magnesium oxide system, which did not respond substantially to a change in particle size). • Increasing the concentration to 10 wt. % for the 500 nm system, results in a decrease in the distribution's homogeneity, however, still superior to the 300 nm counterpart system at the equivalent concentration. • Overall, the particle distribution does not match that of barium titanate, particularly in terms of inter-fibre deposition.
$BaCO_3$	✓	• At a concentration of 0.5 wt. %, the 800 nm barium carbonate system yields similar results to those obtained by the titanium carbide system. • A marginally improved particle distribution homogeneity may be observed compared to the titanium carbide system.

$BaTiO_3$	✓✓✓	• At a size of 400 nm, barium titanate exhibits a progressive improvement in particle distribution homogeneity with increasing concentration: 0.25 wt. %, 0.5 wt. %, 1 wt. %, 2 wt. %, 3 wt. %, 4 wt. %, and 7.5 wt. %. • The particle distribution remains homogenous throughout the higher concentrations, with the desirable particle compactness for local DVC analyses achieved at the highest concentration of 7.5 wt. %. • The 7.5 wt. % system also presents a reduced level of microstructural anomalies, with instances being isolated and generally limited to less than ~10 µm within the visible region. In this respect, it is similar to the aluminium 800 nm system (10 wt. %). • Even though, at a concentration of 7.5 wt. %, the microstructure is not completely free of particle 'bands', a desirable compromise is achieved between the local deposition of particles in the fibre direction and any potential mechanical property detriment. • Also, the barium titanate system does not appear to be prone to agglomerate formation.
Cu	✓	• At a concentration of 0.25 wt. %, the 580 nm copper particles are well-recognizable, despite a sparse spatial distribution. • The spatial distribution is somewhat improved at a concentration of 0.5 wt. % and 1 wt. %, respectively, notwithstanding that copper appears to be particularly prone to agglomerate development with increasing concentration, and thus a departure from a homogenous distribution within the composite bulk. • This system is overly attenuating (see **Figure 4-1**), such that at the energies available, it promoted imaging artefacts, visible as streak patterns surrounding the fiducial markers. As with any artefact, it is not desirable for DVC analyses as it may lead to an increased predisposition to noise.
Bi_2O_3	✓	• At a size of 800 nm and concentration of 10 wt. %, the spatial distribution obtained by doping the matrix with bismuth oxide is sparse. • A combination of both particle 'bands' and agglomerates are observed along the fibre direction, causing substantial disruption in the local fibre packing at tow-level. • Similar to copper, bismuth oxide is too attenuating compared to carbon at the beam energies available in the present work.

Table 4-7 – Detailed comments complementing the ranking system in Table 4-5.

4.7 References

[1] Y. Swolfs, H. Morton, A. E. Scott, L. Gorbatikh, P. A. S. Reed, I. Sinclair, S. M. Spearing and I. Verpoest, "Synchrotron radiation computed tomography for experimental validation of a tensile strength model for unidirectional fibre-reinforced composites," *Composites Part A,* vol. 77, pp. 106-113, 2015.

[2] J. Bohse, "Acoustic emission characteristics of micro-failure processes in polymer blends and composites," *Composites Science and Technology,* vol. 60, no. 8, pp. 1213-1226, 2000.

[3] N. De Greef, L. Gorbatikh, A. Godara, L. Mezzo, S. V. Lomov and I. Verpoest, "The effect of carbon nanotubes on the damage development in carbon fiber/epoxy composites," *Carbon,* vol. 49, no. 14, pp. 4650-4664, 2011.

[4] A. E. Scott, M. N. Mavrogordato, P. Wright, I. Sinclair and S. M. Spearing, "In situ fibre fracture measurement in carbon-epoxy laminates using high resolution computed tomography," *Composites Science and Technology,* vol. 71, no. 12, pp. 1471-1477, 2011.

[5] A. E. Scott, I. Sinclair, S. M. Spearing, A. Thionnet and A. R. Bunsell, "Damage accumulation in a carbon/epoxy composite: Comparison between a multiscale model and computed tomography experimental results," *Composites Part A,* vol. 43, no. 9, pp. 1514-1522, 2012.

[6] S. Blassiau, A. R. Bunsell and A. Thionnet, "Damage accumulation processes and life prediction in unidirectional composites," *Proceedings of the Royal Society A,* vol. 463, no. 2080, pp. 1135-1152, 2007.

[7] E. Schöberl, M. N. Mavrogordato, I. Sinclair and S. M. Spearing, "Fibre-direction strain measurement in a composite ply under pure bending using digital volume correlation and micro-focus computed tomography," *Journal of Composite Materials,* vol. 54, no. 14, pp. 1889-1911, 2020.

[8] E. Schöberl, C. Breite, A. Melnikov, Y. Swolfs, M. N. Mavrogordato, I. Sinclair and S. M. Spearing, "Fibre-direction strain measurement in a composite ply under quasi-static tensile loading using digital volume correlation and in situ synchrotron radiation computed tomography," *Composites Part A,* vol. 137, no. 105935, 2020.

[9] Y. Swolfs, I. Verpoest and L. Gorbatikh, "A review of input data and modelling assumptions in longitudinal strength models for unidirectional fibre-reinforced composites," *Composite Structures,* vol. 150, pp. 153-172, 2016.

[10] J. Watanabe, F. Tanaka, H. Okuda and T. Okabe, "Tensile strength distribution of carbon fibers at short gauge lengths," *Advanced Composite Materials,* vol. 23, no. 5-6, pp. 535-550, 2014.

[11] S. L. Phoenix and I. J. Beyerlein, Comprehensive composite materials. Chapter 1.19 – Statistical strength theory for fibrous composite materials, 1st ed., vol. 1, A. Kelly and C. Zweben, Eds., Oxford, UK: Pergamon Press, 2000, pp. 559-639.

[12] B. W. Rosen, "Tensile failure of fibrous composites," *AIAA Journal,* vol. 2, no. 11, pp. 1985-1991, 1964.

[13] Y. Swolfs, L. Gorbatikh, V. Romanov, S. Orlova, S. V. Lomov and I. Verpoest, "Stress concentrations in an impregnated fibre bundle with random fibre packing," *Composites Science and Technology,* vol. 74, pp. 113-120, 2013.

[14] Y. Swolfs, R. M. McMeeking, I. Verpoest and L. Gorbatikh, "Matrix cracks around fibre breaks and their effect on stress redistribution and failure development in unidirectional composites," *Composites Science and Technology,* vol. 108, pp. 16-22, 2015.

[15] M. R. Nedele and M. R. Wisnom, "Three-dimensional finite element analysis of the stress concentration at a single fibre break," *Composites Science and Technology,* vol. 51, no. 4, pp. 517-524, 1994.

[16] M. R. Nedele and M. R. Wisnom, "Stress concentration factors around a broken fibre in a unidirectional carbon fibre-reinforced epoxy," *Composites,* vol. 25, no. 7, pp. 549-557, 1994.

[17] A. Thionnet, H. Y. Chou and A. R. Bunsell, "Fibre break processes in unidirectional composites," *Composites Part A,* vol. 65, pp. 148-160, 2014.

[18] Y. Swolfs, I. Verpoest and L. Gorbatikh, "Issues in strength models for unidirectional fibre-reinforced composites related to Weibull distributions, fibre packings and boundary effects," *Composites Science and Technology,* vol. 114, pp. 42-49, 2015.

[19] S. C. Garcea, I. Sinclair, S. M. Spearing and P. J. Withers, "Mapping fibre failure in situ in carbon fibre reinforced polymers by fast synchrotron X-ray computed tomography," *Composites Science and Technology,* vol. 149, pp. 81-89, 2017.

[20] S. Rosini, M. N. Mavrogordato, O. Egorova, E. S. Matthews, S. E. Jackson, S. M. Spearing and I. Sinclair, "In situ statistical measurement of local morphology in carbon-epoxy composites using synchrotron X-ray computed tomography," *Composites Part A,* vol. 125, pp. 1-14, 2019.

[21] K. L. Pickering, M. G. Bader and A. C. Kimber, "Damage accumulation during the failure of uniaxial carbon fibre composites," *Composites Part A,* vol. 29, no. 4, pp. 435-441, 1998.

[22] N. J. Pagano, "On the micromechanical failure modes in a class of ideal brittle matrix composites. Part 1 – Coated-fiber composites," *Composites Part B,* vol. 29, no. 2, pp. 93-119, 1998.

[23] S. C. Garcea, Y. Wang and P. J. Withers, "X-ray computed tomography of polymer composites," *Composites Science and Technology,* vol. 156, pp. 305-319, 2018.

[24] J. M. Lifshitz and A. Rotem, "Time-dependent longitudinal strength of unidirectional fibrous composites," *Fibre Science and Technology,* vol. 3, no. 1, pp. 1-20, 1970.

[25] A. R. Bunsell and A. Thionnet, "Life prediction for carbon fibre filament wound composite structures," *Philosophical Magazine,* vol. 90, no. 31-32, pp. 4129-4146, 2010.

[26] A. R. Bunsell and A. Thionnet, "Failure processes governing long term reliability of carbon fibre composites structures," *Composites and Nanostructures,* vol. 7, no. 4, pp. 216-224, 2015.

[27] A. J. Moffat, P. Wright, J.-Y. Buffiere, I. Sinclair and S. M. Spearing, "Micromechanisms of damage in 0° splits in a [90/0]s composite material using synchrotron radiation computed tomography," *Scripta Materialia,* vol. 59, no. 10, pp. 1043-1046, 2008.

[28] P. Wright, A. J. Moffat, I. Sinclair and S. M. Spearing, "High resolution tomographic imaging and modelling of notch tip damage in a laminated composite," *Composites Science and Technology,* vol. 70, no. 10, pp. 1444-1452, 2010.

[29] A. Bunsell, L. Gorbatikh, H. Morton, S. Pimenta, I. Sinclair, S. M. Spearing, Y. Swolfs and A. Thionnet, "Benchmarking of strength models for unidirectional composites under longitudinal tension," *Composites Part A,* vol. 111, pp. 138-150, 2018.

[30] Y. Huang and R. J. Young, "Analysis of the fragmentation test for carbon-fibre/epoxy model composites by means of Raman spectroscopy," *Composites Science and Technology,* vol. 52, no. 4, pp. 505-517, 1994.

[31] Y. Huang and R. J. Young, “Interfacial behaviour in high temperature cured carbon fibre/epoxy resin model composite,” *Composites,* vol. 26, no. 8, pp. 541-550, 1995.

[32] P. W. J. van den Heuvel, T. Peijs and R. J. Young, “Analysis of stress concentrations in multi-fibre microcomposites by means of Raman spectroscopy,” *Journal of Materials Science Letters,* vol. 15, no. 21, pp. 1908-1911, 1996.

[33] P. W. J. van den Heuvel, T. Peijs and R. J. Young, “Failure phenomena in two-dimensional multi-fibre microcomposites. Part 4 – A Raman spectroscopic study on the influence of the matrix yield stress on stress concentrations,” *Composites Part A,* vol. 31, no. 2, pp. 165-171, 2000.

[34] B. Pan, K. Qian, H. Xie and A. Asundi, “Two-dimensional digital image correlation for in-plane displacement and strain measurement: A review,” *Measurement Science and Technology,* vol. 20, no. 6, pp. 1-17, 2009.

[35] B. K. Bay, T. S. Smith, D. P. Fyhrie and M. Saad, “Digital volume correlation: Three-dimensional strain mapping using X-ray tomography,” *Experimental Mechanics,* vol. 39, no. 3, pp. 217-226, 1999.

[36] J. Adam, M. Klinkmüller, G. Schreurs and B. Wieneke, “Quantitative 3D strain analysis in analogue experiments simulating tectonic deformation: Integration of X-ray computed tomography and digital volume correlation techniques,” *Journal of Structural Geology,* vol. 55, pp. 127-149, 2013.

[37] F. Xu, “Quantitative characterization of deformation and damage process by digital volume correlation: A review,” *Theoretical & Applied Mechanics Letters,* vol. 8, no. 2, pp. 83-96, 2018.

[38] B. K. Bay, “Methods and applications of digital volume correlation,” *Journal of Strain Analysis for Engineering Design,* vol. 43, no. 8, pp. 745-760, 2008.

[39] L. Wang, N. Limodin, A. El Bartali, J.-F. Witz, R. Seghir, J.-Y. Buffiere and E. Charkaluk, “Influence of pores on crack initiation in monotonic tensile and cyclicloadings in lost foam casting A319 alloy by using 3D in-situ analysis,” *Materials Science & Engineering A,* vol. 673, pp. 362-372, 2016.

[40] G. Borstnar, F. Gillard, M. N. Mavrogordato, I. Sinclair and S. M. Spearing, “Three-dimensional deformation mapping of Mode I interlaminar crack extension in particle-toughened interlayers,” *Acta Materialia,* vol. 103, pp. 63-70, 2015.

[41] R. Brault, A. Germaneau, J. C. Dupré, P. Doumalin, S. Mistou and M. Fazzini, "In-situ analysis of laminated composite materials by X-ray micro-computed tomography and digital volume correlation," *Experimental Mechanics,* vol. 53, pp. 1143-1151, 2013.

[42] L. M. McGrath, R. S. Parnas, S. H. King, J. L. Schroeder, D. A. Fischer and J. L. Lenhart, "Investigation of the thermal, mechanical, and fracture properties of alumina-epoxy composites," *Polymer,* vol. 49, no. 4, pp. 999-1014, 2008.

[43] C. Chen, R. S. Justice, D. W. Schaefer and J. W. Baur, "Highly dispersed nanosilica-epoxy resins with enhanced mechanical properties," *Polymer,* vol. 49, no. 17, pp. 3805-3815, 2008.

[44] Toray Industries Inc., *Toray Composite Materials,* Tokyo, Japan, 2019.

[45] Sicomin, *Epoxy Systems,* Châteauneuf-les-Martigues, France, 2018.

[46] US Research Nanomaterials Inc., *Micron Powders,* Houston, TX, USA, 2019.

[47] E. N. Landis and D. T. Keane, "X-ray microtomography," *Materials Characterization,* vol. 61, no. 12, pp. 1305-1316, 2010.

[48] E. Maire, J.-Y. Buffière, L. Salvo, J. J. Blandin, W. Ludwig and J. M. Létang, "On the application of X-ray microtomography in the field of materials science," *Advanced Engineering Materials,* vol. 3, no. 8, pp. 539-546, 2001.

[49] National Institute of Standards and Technology (NIST), "X-Ray Mass Attenuation Coefficients," Physical Measurement Laboratory (PML), 01 06 2017. [Online]. Available: https://www.nist.gov/pml/x-ray-mass-attenuation-coefficients.

[50] Ultrawave Ltd., *U100/U100H Ultrasonic Cleaning Bath,* Cardiff, UK, 2017.

[51] 3M Company, *Epoxy Adhesive,* Maplewood, MN, USA, 2019.

[52] Deben Ltd., *CT5000 5kN in-situ tensile stage for µXCT applications,* Woolpit, Suffolk, UK, 2019.

[53] Carl Zeiss AG, *Xradia 510 Versa,* Oberkochen, Germany, 2018.

[54] J. Schindelin, I. Arganda-Carreras, E. Frise, V. Kaynig, M. Longair, T. Pietzsch, S. Preibisch, C. Rueden, S. Saalfeld, B. Schmid, J.-Y. Tinevez, D. J. White, V. Hartenstein, K. Eliceiri, P. Tomancak and A. Cardona,

"Fiji: An open-source platform for biological-image analysis," *Nature Methods,* vol. 9, pp. 676-682, 2012.

[55] C. Breite, L. Gorbatikh, Y. Swolfs, M. Alves, S. Pimenta, E. Schöberl, M. Mavrogordato, I. Sinclair, S. M. Spearing, J. Rojek, A. Thionnet and A. Bunsell, "Benchmarking exercise II for longitudinal strength models of unidirectional composites – Instructions for participants," Marie Skłodowska-Curie European Training Network FiBreMoD, Leuven, Belgium, 2018.

[56] M. A. Suhot and A. R. Chambers, "The effect of voids on the flexural fatigue performance of unidirectional carbon fibre composites," in *16th International Conference on Composite Materials*, Kyoto, Japan, 2007.

[57] A. E. Scott, I. Sinclair, S. M. Spearing, M. N. Mavrogordato and W. Hepples, "Influence of voids on damage mechanisms in carbon/epoxy composites determined via high resolution computed tomography," *Composites Science and Technology,* vol. 90, pp. 147-153, 2014.

[58] F. Tanaka, T. Okabe, H. Okuda, I. A. Kinloch and R. J. Young, "Factors controlling the strength of carbon fibres in tension," *Composites Part A,* vol. 57, pp. 88-94, 2014.

[59] T. Okabe and N. Takeda, "Size effect on tensile strength of unidirectional CFRP composites – experiment and simulation," *Composites Science and Technology,* vol. 62, no. 15, pp. 2053-2064, 2002.

[60] A. E. Scott, "Analysis of a hybrid composite pressure vessel using multi-scale computed tomography techniques – PhD Thesis," University of Southampton, Southampton, UK, 2011.

[61] H. Morton, "3D Imaging of the tensile failure mechanisms of carbon fibre composites – PhD Thesis," University of Southampton, Southampton, UK, 2014.

Chapter 5 Fibre-direction strain measurement in a composite ply under pure bending using Digital Volume Correlation and Micro-focus Computed Tomography

This chapter presents an experimental demonstration and validation of high-resolution three-dimensional experimental strain measurement using Digital Volume Correlation on Carbon Fibre-Reinforced Polymers, via through-thickness strain analysis under a state of pure bending. To permit the application of DVC to displacements and/or strain measurements parallel to the fibre direction in well-aligned unidirectional materials at high volume fractions, a methodology was developed for the insertion of sparse populations of 400 nm $BaTiO_3$ particles within the matrix to act as displacement trackers (*i.e.* fiducial markers). For this novel material system, measurement sensitivity and noise are considered, along with the spatial filtering intrinsic to established DVC data processing. In conjunction with Microfocus Computed Tomography, the technique was applied to a simple standard specimen subjected to a four-point flexural test, which resulted in a linear strain distribution through the beam thickness. The high-resolution, fibre-level strain distributions (imaged at a voxel resolution of ~0.64 μm) were compared against the classical beam theory (Euler-Bernoulli) in incrementally decreasing averaging schemes and different sub-set sizes. Different sampling and averaging strategies are reported, showing that DVC outputs can be obtained that are in very good agreement with the analytical solution. A practical lower limit for the spatial resolution of strain is discerned for the present materials and methods. This study demonstrates the effectiveness of DVC in measuring local strains parallel to the fibre direction, with corresponding potential for calibration and validation of micromechanical models predicting various fibre-dominated damage mechanisms. This chapter has been reprinted from *Journal of Composite Materials,* vol. 54, no. 14, pp. 1889-1911, 2020, E. Schöberl, M. N. Mavrogordato, I. Sinclair and S. M. Spearing, "Fibre-direction strain measurement in a composite ply under pure bending using digital volume correlation and micro-focus computed tomography".

5.1 Introduction

Climate change continues to be a global challenge. In December 2015, the Paris agreement [1] established goals to limit temperature increase to less than 2°C, with ambitions to less than 1.5°C. Owing to high specific mechanical properties and the potential to engineer structural properties to precise applications and loading conditions, Carbon Fibre-Reinforced Polymers have been identified as a pivotal technology for lightweighting across the transport sector [2], where weight reduction remains the fundamental approach to reducing greenhouse gas emissions (*e.g.* CO_2, NO_x).

Due to the multiphase composition, anisotropy and heterogeneity of composite laminates, failure prediction remains difficult, even under the simplest loading conditions. As such, a fundamental understanding of the fibre fracture process is important for a complete interpretation of composite tensile failure, alongside the various other forms of damage that develop in these materials under load.

Characterizing volumetric material deformation and damage is, however, notoriously challenging, due to the opacity of the materials, the three-dimensional multiscale nature of damage, the coupling of multiple micromechanisms and the difficulty of distinguishing damage caused by load from cutting and polishing artefacts associated with traditional metallographic approaches. A significant step forward has been achieved in recent years by the use of X-ray computed tomography combined with *in situ* loading to identify detailed sequences of damage accumulation down to fibre level, in 3D, within the bulk of representative materials under load [3-7]. As a natural evolution, the coupling of CT with Digital Volume Correlation was identified.

An extension of the white-light illumination, two-dimensional Digital Image Correlation technique [8], DVC was developed for volumetric measurements, and initially demonstrated as a means to estimate the effective continuum strain tensor in trabecular bone subjected to axial compression [9]. The general objective of DVC is to track a pattern of the reference volume in the deformed volume image and to determine its associated shift vector. This may be achieved by employing a correlation criterion (function) to search for a digital pattern within a time-series volumetric data set. In the case of volume images, the pattern is given by an array of voxel grey-level intensities, *i.e.* a contrast pattern [9, 10]. As a result, DVC is a tool capable of quantifying the internal microstructural response of the material between different load states, by extracting essential failure parameters (*e.g.* local displacements and strains) [11].

In the field of composite mechanics, the application of DVC is less extensive, but previous work includes its use as a strain-based quantification of the deformation fields to investigate strain concentrations and strain transfer lengths associated with the fracture of continuous fibres [12, 13], free-edge effects [14], Mode I delamination induced damage in particle-toughened interlayers [15] and transverse shear effects [16]. DVC therefore appears to be a powerful tool for measuring volumetric displacements and computing strains, but

for X-ray CT, the noise and sensitivity of the measurements rely heavily on a series of factors. These include imaging hardware (beam stability, flux, energy, exposure, propagation distance, voxel size), the nature of the material type under investigation (sample shape, size, phase density distribution, trackable features) and imaging results (contrast-to- noise ratio, spatial resolution, artefacts), all of which influence the quality of the image volumes obtained [17, 18].

Consequently, an assessment of the reliability and accuracy of the measurements is required through validation experiments, where the displacement and/or strain field is known *a priori* [17]. The approach commonly involves two zero-strain pair analyses: a static repeat scan and a rigid body displacement (RBD) assessment [12, 13, 15, 18-20].

In the context of CFRP tensile failure [12, 13], and progressing from the conventional noise tests, this chapter proposes a more comprehensive validation study, specifically focused on an unidirectional material, through the application of a four-point flexural test to a simple standard specimen with a well-defined strain distribution. The advantage of this approach is that the strain gradient is linear through the beam thickness, related directly to the curvature (*i.e.* the reciprocal of the radius of curvature [21]) which is easily measured and does not need measurements of load or material elastic properties. Furthermore, this approach allows the exploration of the effects of averaging and the selection of sub-set size on the accuracy of the gradient of strain values.

The highly anisotropic and somewhat regular/self-similar microstructures found in conventional UD CFRPs at high volume fractions are intrinsically challenging for DVC, particularly along the fibre direction. The cylindrical structure and smooth surfaces of the filaments lack a well-defined, trackable contrast pattern along the fibre direction, leading to poor image correlation, and correspondingly inaccurate displacement estimates in this direction within a given ply [15]. Following a similar approach to that taken by Brault *et al*. [16] to generate individual features unique to a particular sub-set, the authors have explored the insertion of sparse populations of significantly smaller particles (400 nm as opposed to 150 μm) within the matrix to act as displacement trackers – *i.e.* fiducial markers. High-resolution, fibre-level strain distributions are specifically addressed (imaged at a voxel resolution of ~0.64 μm), as opposed to the ply-level studies in Brault *et al.* [16] (which used a voxel resolution of 52 μm). This chapter reports on the development of the fiducial-adapted CFRP, corresponding Micro-focus CT four-point flexural testing and DVC processing: micromechanical strain mapping results within the fibre bed to evidence the utility of the technique at very much higher resolutions than reported in the literature.

5.2 Materials and methods

5.2.1 Material manufacturing

Cross-ply laminates, with a $[90/0]_s$ layup, height *'h'* of ~1 mm and a nominal fibre volume fraction *'V_f'* of ~55% were manufactured by drum winding at KU Leuven, Belgium. A PAN-based 12K TORAYCA T700SC-50C (Toray Industries Inc., Tokyo, Japan [22]) non-twisted tow was used, with a 7 µm nominal fibre diameter.

To create microstructural fiducial patterns for the application of DVC, the resin was filled with commercially available tetragonal $BaTiO_3$ particles, nominal mean size of 400 nm and approximately spherical shape (US Research Nanomaterials Inc., Houston, TX, USA [23]). This property combination was selected following an extensive µCT-based qualitative assessment on a range of possible fiducial compositions (Al, Al_2O_3, SiC, SiO_2, MgO, TiC, TiO_2, $BaCO_3$, $BaTiO_3$, Cu and Bi_2O_3), mean particle sizes (300 nm to 800 nm) and concentrations (0.25 wt. % to 15 wt. % of the resin). From this test matrix, $BaTiO_3$ particles were found to offer the most favourable compromise between contrast in CT images (high attenuation coefficient), and the ability to obtain a homogeneous distribution in 3D space with sufficient particle compactness for local DVC analyses. The particles were dispersed in a SiPreg SR 8500/KTA 313 dual-component epoxy (Sicomin, Châteauneuf-les-Martigues, France [24]) using a combination of high-shear mixing and heated ultra-sonication (U100H bath, Ultrawave Ltd., Cardiff, UK [25]). No specific treatment was applied to the particle surfaces. To remove entrapped air, the thermosetting mixture was degassed for 10 min at ambient temperature. The amount of resin used was 150 g, with 31.5 g of hardener, following the manufacturer's specified mixing ratio of 100/21 (by weight). The $BaTiO_3$ fraction was set at 7.5 wt. % of the resin, equivalent to ~1.44 vol. %. A nominal 25 % tow overlap was targeted during the winding process. A maximum spool tension of 0.12 lb (54.43 g) was applied. To control the volume fraction of the matrix, following impregnation, the tow was passed through a flat die with an orifice of 0.2 mm × 9 mm. The temperature of the tow spreader and final guide roller were set to 50℃. The fibre sizing was left intact. A schematic of the manufacturing setup is shown in **Figure 5-1**. The drum winding process resulted in uniaxial prepreg tape, ~0.25 mm × ~350 mm × ~1900 mm, which was cut and laid up to produce the desired $[90/0]_s$ cross-ply layup. The prepreg stack was cured in an autoclave for 280 min at 0.5 MPa (5 bar) and maximum 120℃. To minimize void content in the cured material, a vacuum of ~0.07 MPa (~0.7 bar) was maintained throughout the autoclave process.

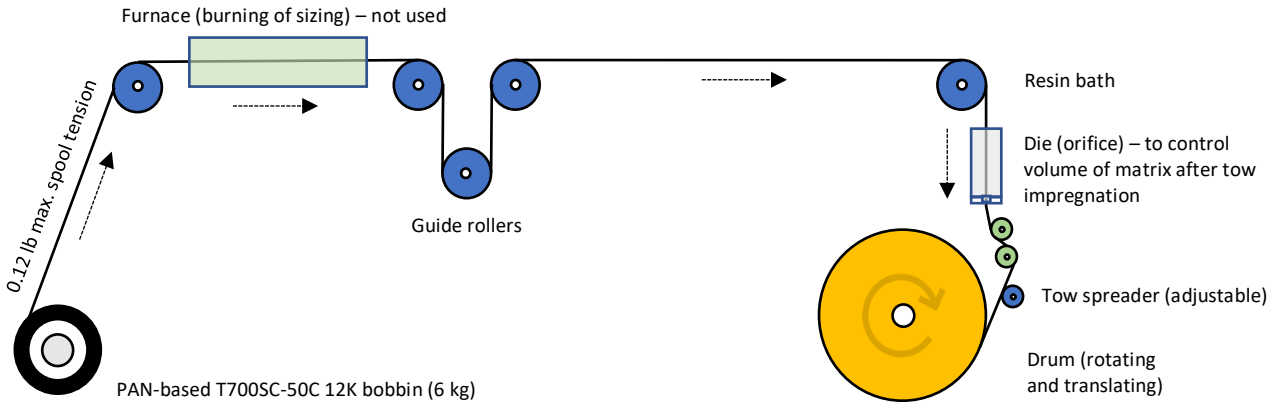

Figure 5-1 – Schematic illustration of the prepreg manufacturing (drum winding) process.

5.2.2 Specimen geometry and loading

Specimen preparation was carried out in accordance with the D 7264/D 7264M – 07 test method [26]. A standardized support span *'L'* to thickness *'t'* ratio of 20:1 was used. 'Matchsticks' (~1 mm × ~41.5 mm × ~1 mm) were prepared via water-jet cutting from the manufactured plates described in **Section 5.2.1**. The specimens were cut with additional length to ensure good alignment with the loading and support span, respectively. The specimen geometry, region of interest and direction of loading relative to the composite layup are shown in **Figure 5-2**.

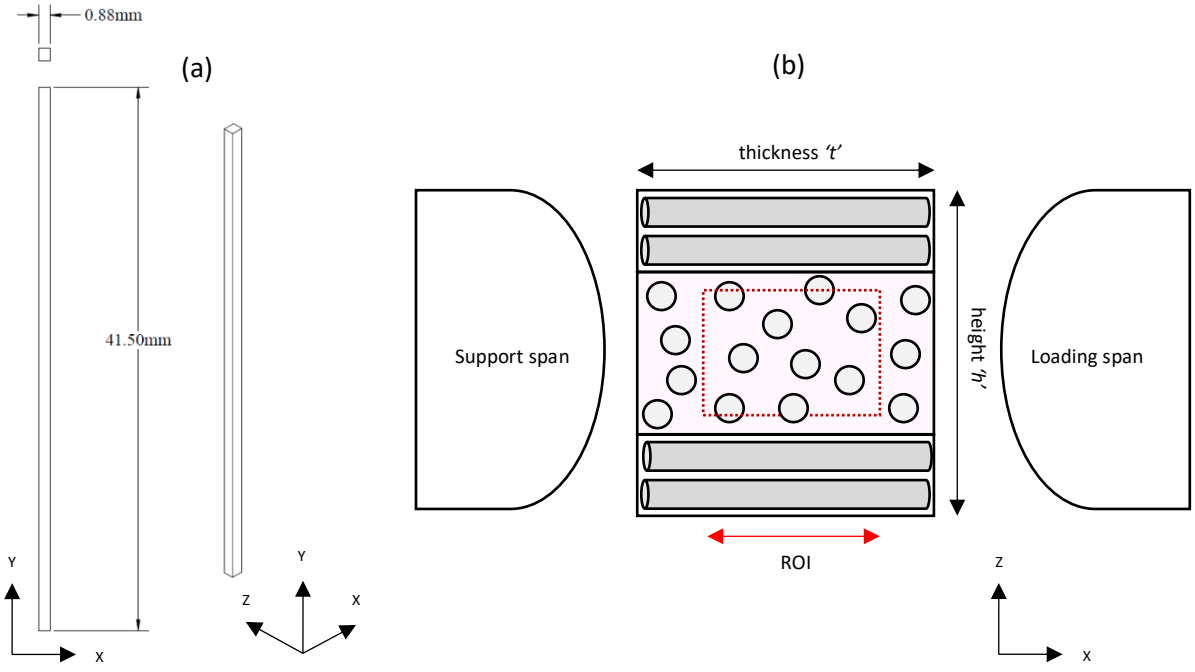

Figure 5-2 – (a) Specimen geometry (thickness as measured via CT), and (b) direction of loading relative to the composite layup (orthogonal to the 0° plies – XZ-plane shown). The ROI shown schematically corresponds to that of the cropped CT volume for DVC analysis.

The specimen was enclosed in a 58 mm long, 7 mm inner diameter and 10 mm outer diameter Poly(methyl methacrylate) (PMMA) reaction tube, illustrated in **Figure 5-3 (a)**. A polymer-based material was selected for the construction of the tube to minimize X-ray absorption. Holes were machined and threaded to accommodate M3 grub screws to act as the support (20 mm) and loading span (10 mm), respectively. Opposite the loading span, two cavities were designed to allow manipulation of the specimen once the tube was capped with the 3D printed acrylonitrile butadiene styrene, non-load bearing wedges as shown in **Figure 5-3 (b)**. Guide grooves (1.10 mm × 2.0 mm) were designed in the top and bottom wedges, aligned with the loading screws. A tolerance of 0.25 mm was provided around the specimen (Y- and Z-direction) to ensure that it did not come into contact with the wedge surfaces, thereby influencing the bending deformation. The wedges were designed with interlocking pins to ensure both good alignment and no movement relative to the tube. The assembly, as shown in **Figure 5-3 (c)**, was mounted onto the sample manipulator stage via a stand-off that screwed directly into the bottom wedge.

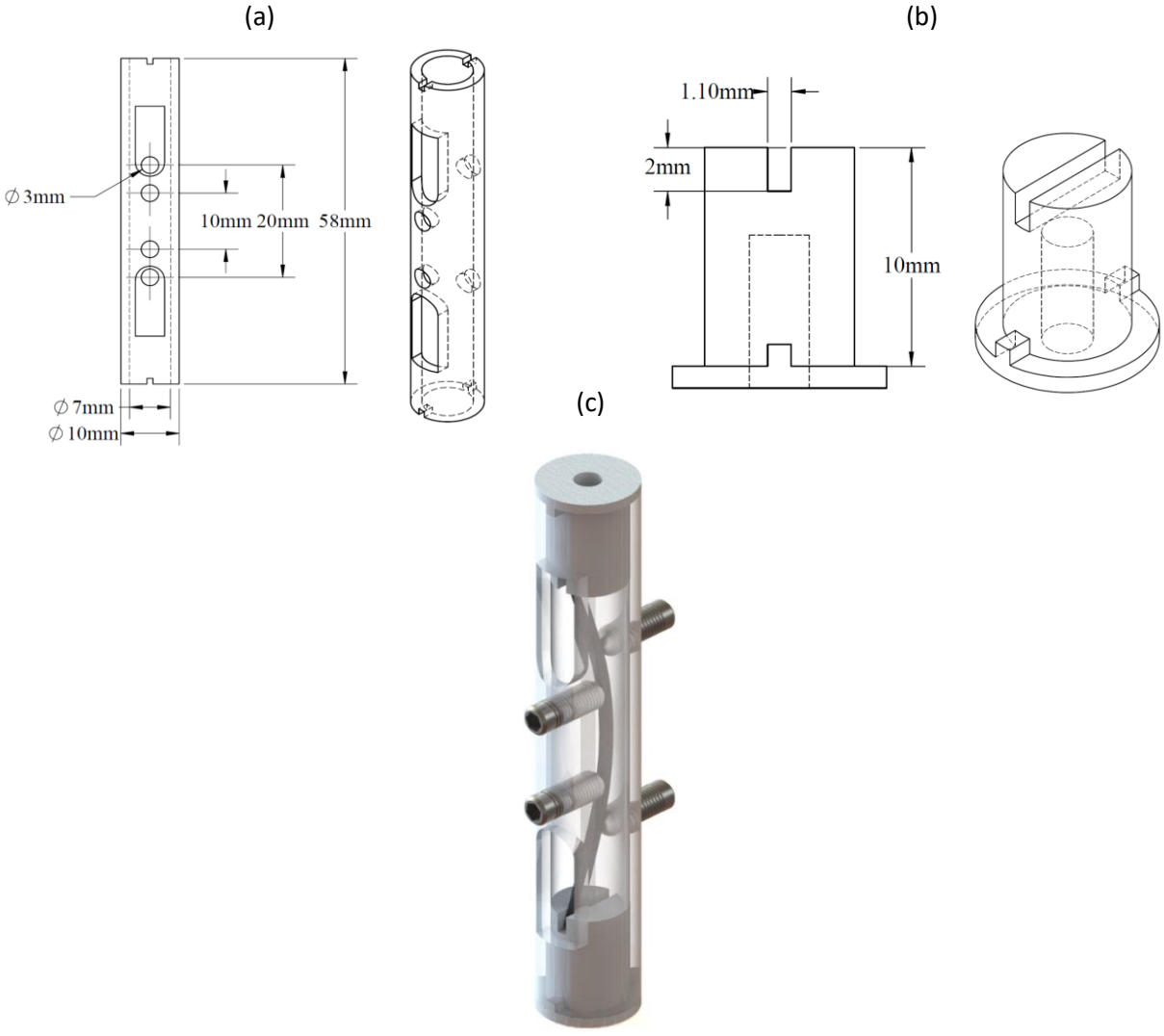

Figure 5-3 – (a) Reaction tube with relevant dimensions, (b) wedges designed to maintain optimum alignment of the specimen, (c) complete assembly – showing both a bent and unbent geometry to illustrate the operating principle.

The bending of the specimen was applied *ex situ*, by manually rotating both the grub screws simultaneously via a pair of Allen keys. Rotation of the screws was carried out in increments of $1/8^{th}$ of a turn until the desired curvature was reached. A relatively small deformation (large radius of curvature) was intended in order to (a) ensure that the classical beam theory (Euler-Bernoulli) is applicable [21], and (b) prevent microstructural damage occurring within the two 0° plies (*e.g.* fibre fractures, intra/interlaminar matrix cracks and delaminations) as such damage would significantly alter the local strain distribution [12, 13, 15]. Conversely, the radius of curvature attained was selected to be small enough, for the maximum strain within the ROI to exceed the anticipated experimental noise. A single load step (sequence) was performed.

5.2.3 Computed Tomography

Micro-focus CT measurements were carried out at the μ-VIS X-Ray Imaging Centre at the University of Southampton, UK. Scans were conducted in a Xradia 510 Versa (Carl Zeiss AG, Oberkochen, Germany [27]) polychromatic system, equipped with a tungsten transmission target. A 2048 × 2048-pixel detector was used, with a chip size of 13.5 μm. To achieve the desired voxel resolution levels, a two-stage magnification approach was implemented (Resolution at a Distance or RaaD [27]), combining the geometric magnification of the X-ray imaging with a set of barrel-mounted lenses. Scans on the specimen were conducted at different resolutions, depending on the designation: (a) low resolution – with greater field of view for the sole purpose of determining the radius of curvature, and (b) high resolution – used in order to determine fibre-level strain gradients through the application of DVC. The low-resolution scans were acquired through an objective with 4 × magnification, yielding a voxel size of ∼4.02 μm for the bent and unbent specimen, respectively. The high-resolution scans were conducted at 20 × magnification, yielding a voxel size of ∼0.64 μm for the bending configuration and noise assessment scans (static repeat and RBD), respectively. A 1 s exposure was used for the low-magnification scans. The number of projections per scan was set to 1601, giving a duration of ∼0.44 h per tomograph. For the high-magnification scan, the exposure time was increased to 30 s, resulting in a scan time of ∼13.34 h. The beam energy was set to 80 kVp and the current to 87 mA throughout. A 2 × detector 'binning' was used, with acquisition taking place over a rotation of ± 180°. The FOV corresponds to ∼4 mm × ∼4 mm × ∼4 mm and ∼0.58 mm × ∼0.62 mm × ∼0.64 mm for the low- and high-resolution scans, respectively. A source-to-object and object-to-detector distance of ∼17 mm and ∼18 mm, respectively, was used. The data were reconstructed using conventional absorption-based FBP. **Figure 5-4** illustrates the complete experimental setup.

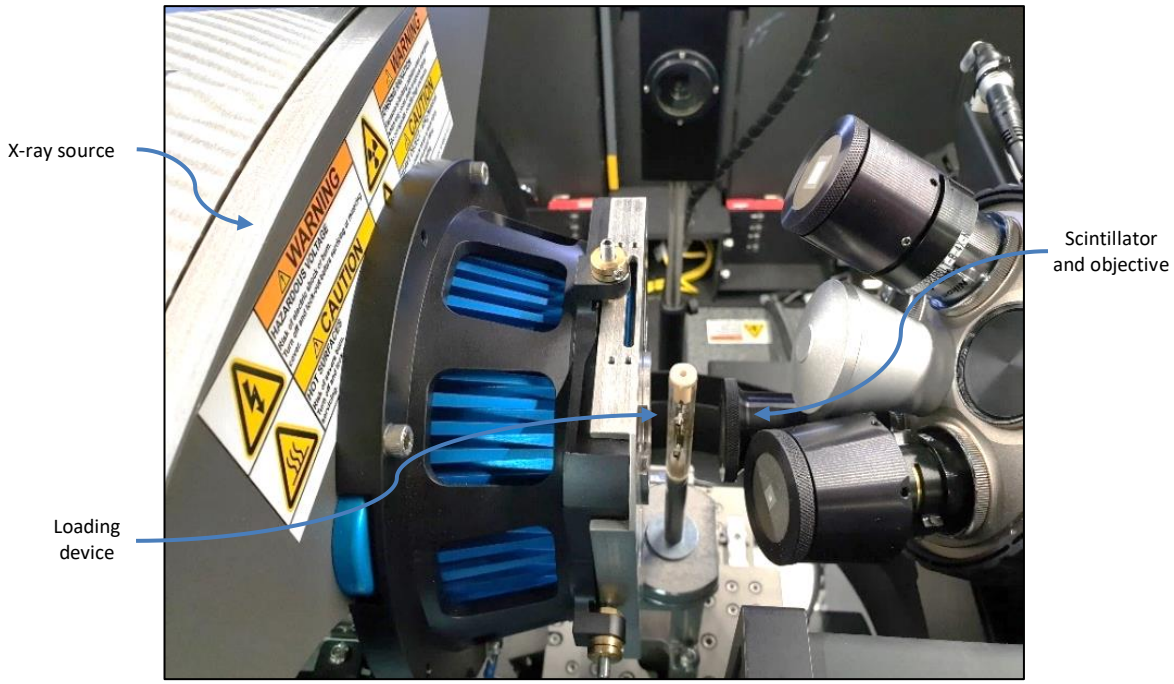

Figure 5-4 – Experimental setup illustrating the loading device in acquisition position.

5.2.4 Digital Volume Correlation

DVC was performed using the commercial DaVis v10 software with StrainMaster DVC package (LaVision GmbH, Göttingen, Germany [28]). StrainMaster employs a correlation criterion operating on the grey-level intensity values of 3D images [29]. In essence, the measurement volume is divided into smaller sub-sets, and the contrast pattern within each sub-set is then tracked from the reference to the deformed state independently (local approach [30]) as a discrete function of the grey levels [29]. A cross-correlation function is employed to measure the conservation of the grey levels between the original and displaced sub-set, with the position determined for which the correlation is closest to unity [15, 18, 29]. Analogous to DIC, the correlation coefficient can be used to evaluate the similitude between the sub-sets [18]. A coefficient of 1.0 implies that the sub-sets are completely related, whereas a value of 0 indicates that they are completely unrelated [18].

The workflow of the correlation process is illustrated schematically in **Figure 5-5**. The associated shift (3D displacement) is given by the vector connecting the sub-set centroids between the deformation states [28]. Finally, 3D strain field estimation may be carried out through a centred finite difference to determine the numerical derivatives of the vector field [18, 20, 29, 31].

Recognition of matching sub-sets between the deformation states was performed within the DVC software via a multi-step, multi-pass strategy, whereby a global pre-shift was computed through a Fast Fourier Transform approach, followed by Direct Correlation. The approach maximized the efficiency of using the DVC

algorithm by exploiting the $BaTiO_3$ particles as fiducial markers along the fibre direction, as the search for the corresponding sub-set in the deformed state was confined to a shift equal to the search radius (**Figure 5-6**). Furthermore, the approach allowed for the coarse displacements captured by larger sub-sets to be used as a predictor vector field for the subsequent and refined iterations, involving smaller sub-sets.

Both implementations use an equivalent of a piecewise linear shape function for the reference-deformed mapping and a normalized form of the cross-correlation function to quantify the conservation of the grey levels between the images [18, 28, 29, 32]. A trilinear interpolation is used in 'FFT', and a third-order spline interpolation in 'DC', to compute the greyscale intensities of each displayed voxel at non-integer positions (*i.e.* sub-voxel measurements) [32]. 'DC' also permits the use of a weighted window within sub-sets, an option which was implemented during the final iteration step of correlation (dual-pass). This results in a potentially improved representation of the local displacement field, as the voxels in the vicinity of the sub-set centroid carry more weight than voxels located at the edge of the sub-set. While the weighted window extends over two times the sub-set size, the implementation ensures that the effective spatial resolution is similar to that of a conventional sub-set, for which an arithmetic average is implemented [28].

As isotropic sub-sets were used throughout all present analyses, a specific notation is introduced, whereby the specified size of a sub-set is equivalent to a sub-set with its characteristic length cubed (*i.e.* sub-set size of N voxels is equivalent to a sub-set size with $N \times N \times N$ voxels or N^3 voxels).

To moderate the computational cost, two further strategies were implemented. First, a 16-bit to 8-bit integer conversion was performed. While the correlation results will always be imaging configuration dependent, Buljac *et al.* [34] have shown that histogram (grey level) rescaling has negligible impact on the DVC error. Similarly, the bit-depth of volumes was also reduced in Borstnar *et al.* [15] to achieve faster processing times. Secondly, the search radius was incrementally reduced from 8 to 6 and ultimately 4 voxels between the deformed and undeformed state. As reported in Schöberl *et al.* [12, 13] the latter value corresponds to a typical fibre-break opening (based on a 0.65 µm voxel size) in a T700SC-50C/epoxy-based cross-ply, implying that in the absence of fractured filaments and/or matrix cracks within the 0° plies, the elastic response of the microstructure cannot exceed the aforementioned displacement level.

To increase sampling, the overlap between the neighbouring sub-sets was set to 50 %, as reported in previous works [15, 18, 20]. This is less than the 75 % overlap reported in Schöberl *et al.* [12, 13]; however, it is desirable to balance the poorer signal-to-noise available using the present materials and methods (see **Section 5.3.1.2**). The relevant settings used are detailed in **Table 5-1**.

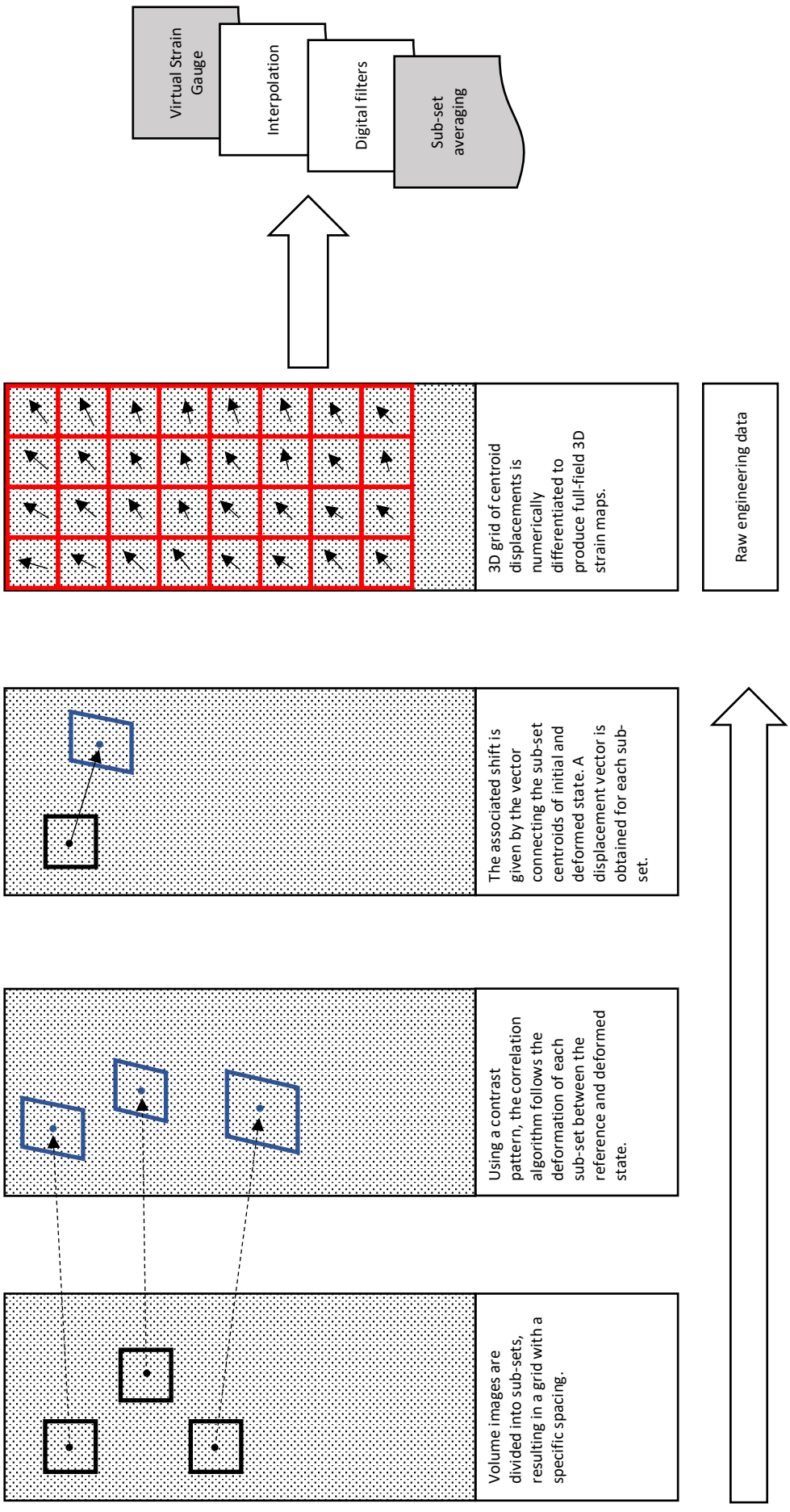

Figure 5-5 – Generalized workflow of the correlation process (for simplicity, the illustration is shown in 2D). Strain post-processing strategies employed in the present work are highlighted. Adapted from [40].

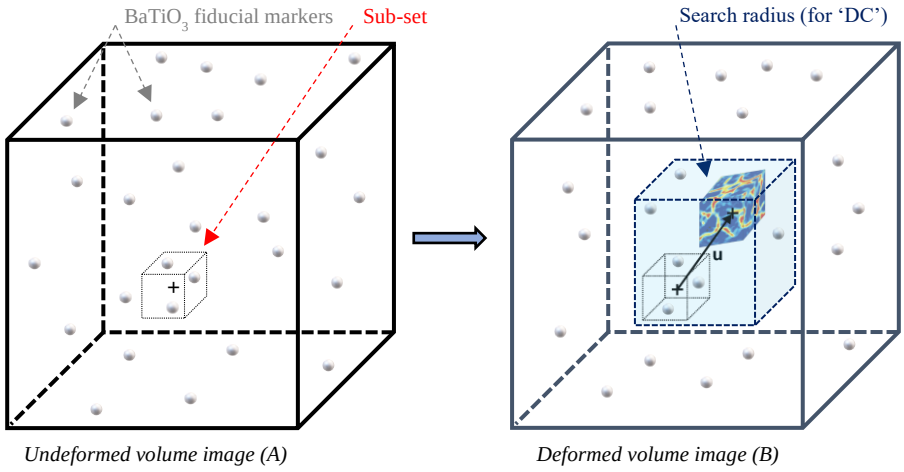

Figure 5-6 – Schematic diagram of the DVC process: inclusion of fiducials and presence of a user-specific search region when using the 'DC' method. Figure not to scale. Adapted from Xu [11] with permission from Elsevier and with permission from Jiroušek et al. [33].

Final sub-set size (voxels)	FFT pre-shift (voxels)	Step 1 (voxels)	Step 2 (voxels)	Step 3 (voxels)	No. of passes steps 1-3	Voxel binning step 1	Voxel binning step 2	Voxel binning step 3
40	80	80	48	40	2	4 × 4 × 4	2 × 2 × 2	NONE
48	80	80	56	48				
60	96	96	64	60				
72	128	128	88	72				
80	128	128	96	80				
100	144	144	112	100				
120	176	176	136	120				
148	192	192	160	148				
156	192	192	160	148				

Table 5-1 – Summary of 'DC' settings used in the multi-step, multi-pass approach (50 % sub-set overlap). Weighted windows used in the last iteration step (dual-pass).

To assess the noise and sensitivity associated with the DVC technique, conventional stationary and RBD tests were performed (see **Sections 5.3.1.1 and 5.3.1.2**). DVC was applied to cropped volumes from the 0° plies, measuring 795 × 885 × 230 voxels. As previously indicated in **Figure 5-2**, the Y-axis indicates the fibre direction; the X-axis is in-plane orthogonal to the fibre direction, while the Z-axis corresponds to the out-of-plane direction. The anisotropic volume represented the maximum available window to perform DVC, particularly limited in the Z-direction by the position of the FOV relative to the centre of the specimen and the height *'h'* of 0° plies. Volumes were carefully checked in advance against the presence of any significant CT artefacts and/or variations in sharpness within the visible region.

As summarized in **Table 5-2**, the number of DVC 'slices' (*i.e.* planes composed of volumetric sub-sets, one sub-set thick) is computed by dividing the height of the cropped volume (230 voxels) by the step size used in the correlation algorithm. Such an example is illustrated in **Figure 5-7**, where a stack comprising of four DVC slices can be observed. Likewise, the number of in-plane data points per DVC slice can be computed by dividing the sub-set plane dimensions (795 × 885 voxels) by the step size used (see **Table 5-3**).

Sub-sets positioned at the perimeter of the grid (XY-plane) as well as the planes of sub-sets located at the top ends of the stack (Z-direction) must be treated with special consideration (*e.g.* masked or truncated) if displacement vectors are computed, but not 100 % satisfied from a voxel validity perspective – *i.e.* notional sub-sets that overlap with the edge, due to cropping between deformation states and/or large RBDs, potentially causing the correlated data to be noisier [20] or incomplete.

Sub-set size (voxels)	Step size (voxels)	No. of DVC slices (Z-direction) *	No. of raw data slices per DVC slice
80	40	6	40
100	50	5	50
120	60	4	60
148	74	3	74

*Table 5-2 – Number of DVC slices (planes of sub-sets) for a given sub-set size with 50 % overlap, and the corresponding number of raw data slices per DVC slice. *Nomenclature: DVC slice numbering starts with 0.*

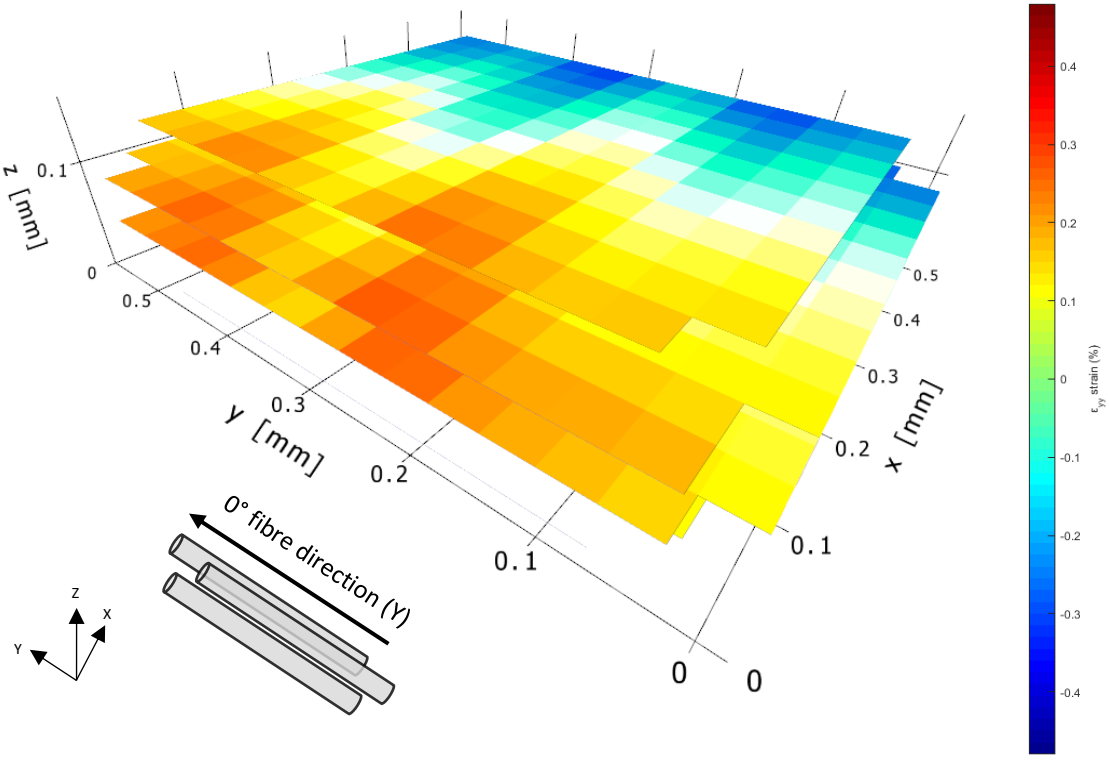

Figure 5-7 – Example stack comprised of 4 DVC slices in the Z-direction ('Z=0' to 'Z=3'), applicable to a sub-set size of 120 voxels with 50 % overlap. In turn, each DVC slice (i.e. plane of sub-sets, one volumetric sub-set thick) is representative for 60 raw CT data slices. Raw data volumes cropped from the 0° plies: 795 × 885 × 230 voxels. Y-axis indicates the fibre direction. X-axis is in-plane orthogonal to the fibre direction, while the Z-axis corresponds to the out-of-plane direction.

Sub-set size (voxels)	Step size (voxels)	No. of DVC slices (Z-direction)	No. of data points per slice (X-direction)	No. of data points per slice (Y-direction)
80	40	6	20	22
100	50	5	16	18
120	60	4	13	15
148	74	3	11	12

Table 5-3 – Number of in-plane data points (X- and Y-direction) per DVC slice, applicable to a sub-set with 50 % overlap.

A common post-processing aspect of strain computation via DVC (and related DIC algorithms) is the Virtual Strain Gauge (VSG). The VSG defines the local (effective) region of the image that is used for strain calculation at a specific location and is volumetrically analogous to the physical area that a metallic foil strain gauge covers [31]. Additionally, the VSG may also be considered to be a smoothing/denoising strategy as it represents a higher-order filtering stage for the computed strains. More details about the application of VSGs can be found in Jones and Iadicola [31].

Several key variables affect the VSG, such as the characteristic length (size) of the strain window *(L_{SW})*, step *(L_{ST})* and sub-set *(L_{SS})*. As the characteristic length *(L_{VSG})* of the VSG decreases, the noise typically increases, and the amount of global spatial filtering decreases. Similarly, as the size of the VSG decreases, the maximum strain amplitude along a line cut (extracted region of highest strain gradient) will generally increase [31]. In this chapter, a VSG with an L_{SW} of 3 × 3 × 3 and 3 × 3 × 1 neighbouring vectors was used for volumetric and planar strain computation, respectively. The application of a VSG implies that the effective volumetric gauge length over which each strain value is computed is larger than the size of a single subset, with **Equation 5-1** describing how the characteristic length of the VSG varies linearly with the aforementioned parameters [31].

$$L_{VSG} = (L_{SW} - 1) \times L_{ST} + L_{SS}$$

Equation 5-1

5.2.5 Image processing

The evaluation of the radius of curvature of the bent specimen was performed on the low-magnification scan (4 ×) by using an industrial 3D metrology toolkit – GOM Inspect 2018 (GOM GmbH, Braunschweig, Germany [35]). As the approach requires inspection of polygonally meshed surfaces, a series of operations were carried out in Fiji ImageJ [36] and VGSTUDIO Max v2.1 (Volume Graphics GmbH, Heidelberg, Germany [37]), respectively, to export the greyscale based tomographs as a 2D meshed surface. Surface determination and the construction of a best-fitting circle has been performed using the 'automatic' function, thus removing any user bias.

A second procedure was performed to check manually the result of the calculation described above. This was carried out in SOLIDWORKS 2015 (Dassault Systèmes SE, Vélizy-Villacoublay, France [38]), whereby the radius of curvature obtained through GOM Inspect 2018 was backfitted onto the edge of the bent specimen. The workflow consisted of fitting a three-point arc (to the nearest pixel) to a 2D edge performed extraction. The flowchart in **Figure 5-8** illustrates the process in detail.

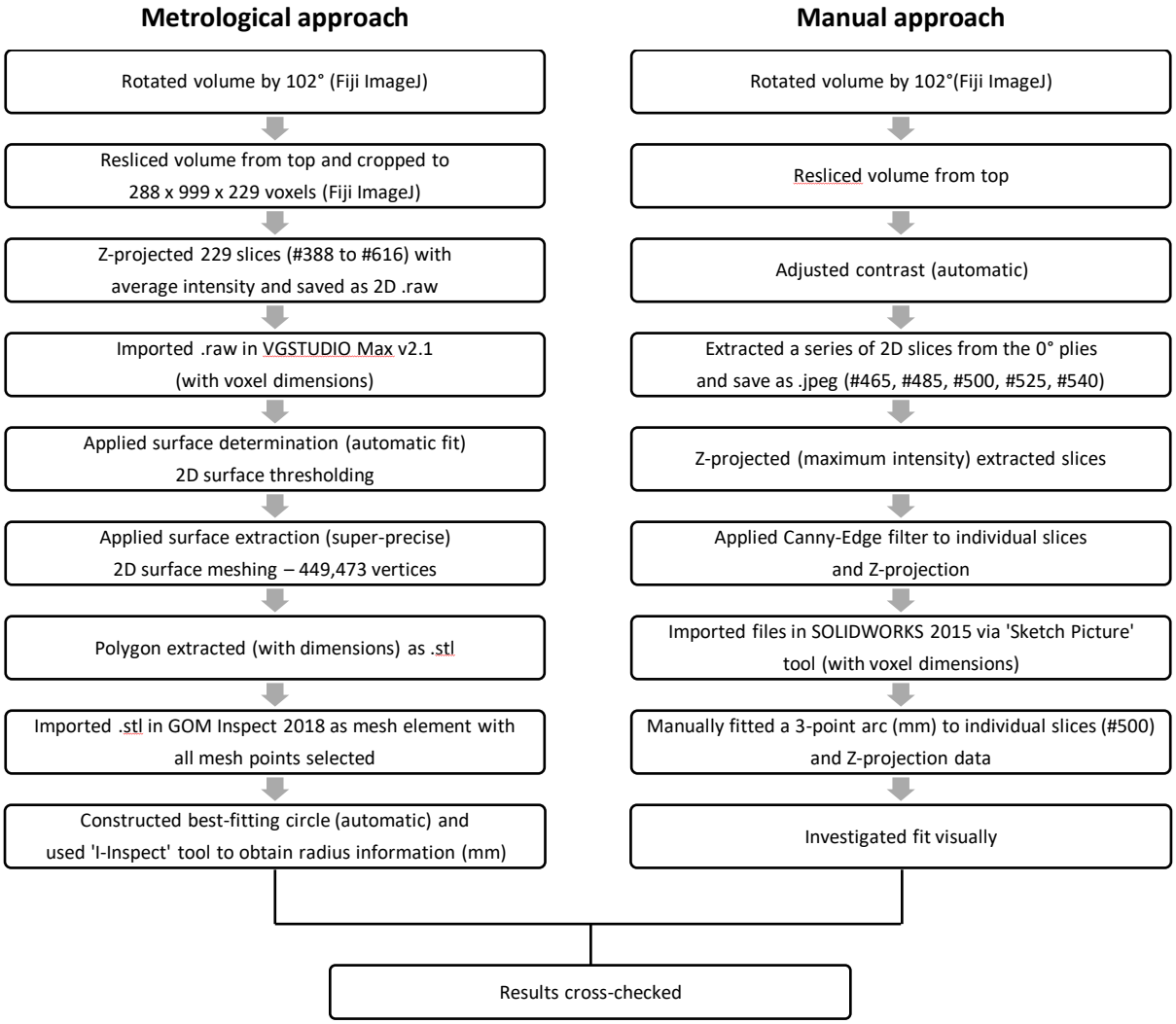

Figure 5-8 – Workflow illustrating the evaluation of radius of curvature of the bent specimen using GOM Inspect 2018 and validating the metrologically obtained results in SOLIDWORKS 2015.

5.3 Results and discussion

5.3.1 Noise and sensitivity

As noted above, to evaluate the metrological performance of the DVC technique, noise studies were conducted. The assessment involves two studies, with the approach being similar to that of Schöberl *et al.* [12, 13], Borstnar *et al.* [15], Gillard *et al.* [18] and Pierron *et al.* [20]. The first is a stationary analysis, which involves repeated scanning of the same specimen without any alterations in load (zero displacement, zero strain) or CT parameters (exposure, number of projections, beam energy, current or propagation distance). The purpose of this static noise test (SNT) is to quantify the intrinsic scanning noise and bias. The second study is an RBD in which the specimen was moved *in situ* by a predefined displacement, parallel to the fibre direction (Y-axis), using the manipulator stage. CT acquisition was performed between each specimen position to evaluate the magnitude of the displacement vector fields and to assess any interpolation and/or system errors associated with the DVC approach [15].

5.3.1.1 Static noise test

Under ideal conditions, the obtained displacement vector data and implicit computed strains should be equal to zero. Noise arising from the imaging system (*e.g.* photon counting statistics, electrical noise, scattered radiation) and the surrounding environment (*e.g.* induced vibrations, thermal changes) implies that this is never the case, and consequently, sub-set displacements will generate false strains within the results [12, 13, 15, 18, 20]. However, due to the novelty of the DVC technique, as yet there is no agreed standard for the assessment of the strain error (usually referred to as the strain resolution) [15, 32]. For example, one approach reports the maximum standard deviation of a given strain map (plane of sub-sets) [18, 20], while a second returns the standard deviation of the measured strain components within the volume [12, 13, 15]. Following the first approach, however, can result in overestimating the error, as results can be affected by unrepresentative localized scanning artefacts (*e.g.* rings, detector 'zingers'). In this work, the latter approach is taken for which the error is seen to form a normal distribution with a mean of ∼zero. The advantage of this approach is that both the stochastic noise in the imaging system and any biases in the correlation algorithm are captured and accounted for: Schöberl *et al.* [12, 13] and Borstnar *et al.* [15].

A typical effect of the sub-set size on the strain resolution is presented in **Figure 5-9**. As previously reported in the literature, a compromise can be achieved between strain and spatial resolution [12, 13, 15, 17-19]. Of specific interest in this work is the normal strain *'ε_{yy}'*, parallel to the fibre direction. Considering the normal components of the strain tensor, it can be observed that the lowest error is achieved in the fibre direction (Y), despite the fact that correlation along the fibres themselves has the lowest values, particularly in particle-free

CFRPs [15]. This may be rationalized, as the deposition of $BaTiO_3$ during the drum winding process occurred parallel to the fibre direction as the tow was drawn through the die, essentially creating longitudinal bands of fiducial markers in the Y-direction which assists the correlation process significantly, eliminating the self-similar microstructure. A similar effect, for the identical material, is also observed using SRCT [12, 13].

The compromise between strain and spatial resolution occurs as a smaller sub-set size will contain too few unique features, in this case, the $BaTiO_3$ particles. In contrast, a larger sub-set will compromise spatial resolution [39], as the underlying deformation is representative of the average displacement of all the voxels contained within the sub-set [15]. A larger sub-set size also implies a larger characteristic length for the VSG, which in turn has a negative impact on the global length-scale over which the strains are computed. **Figure 5-10** shows an isometric view of a typical subset, while **Figure 5-11** presents the number of particles as a function of sub-set size. As the fiducial markers are the main features used for correlating sub-sets between the different deformation states, it may be assumed that matrix deformation dominates the DVC output [12, 13].

A trade-off is identifiable in **Figure 5-9** at an isotropic sub-set size of 120 voxels, where the corresponding length of the VSG measures 240 voxels. The equivalent VSGs (for different sub-set sizes applied) are shown in **Figure 5-12**, alongside the strain resolution *(ε_{yy})* related to the SNT. From **Equation 5-1**, it can be observed that for the particular case of a 50 % sub-set overlap, the characteristic length of the VSG measures twice the size of the constituent sub-set dimension.

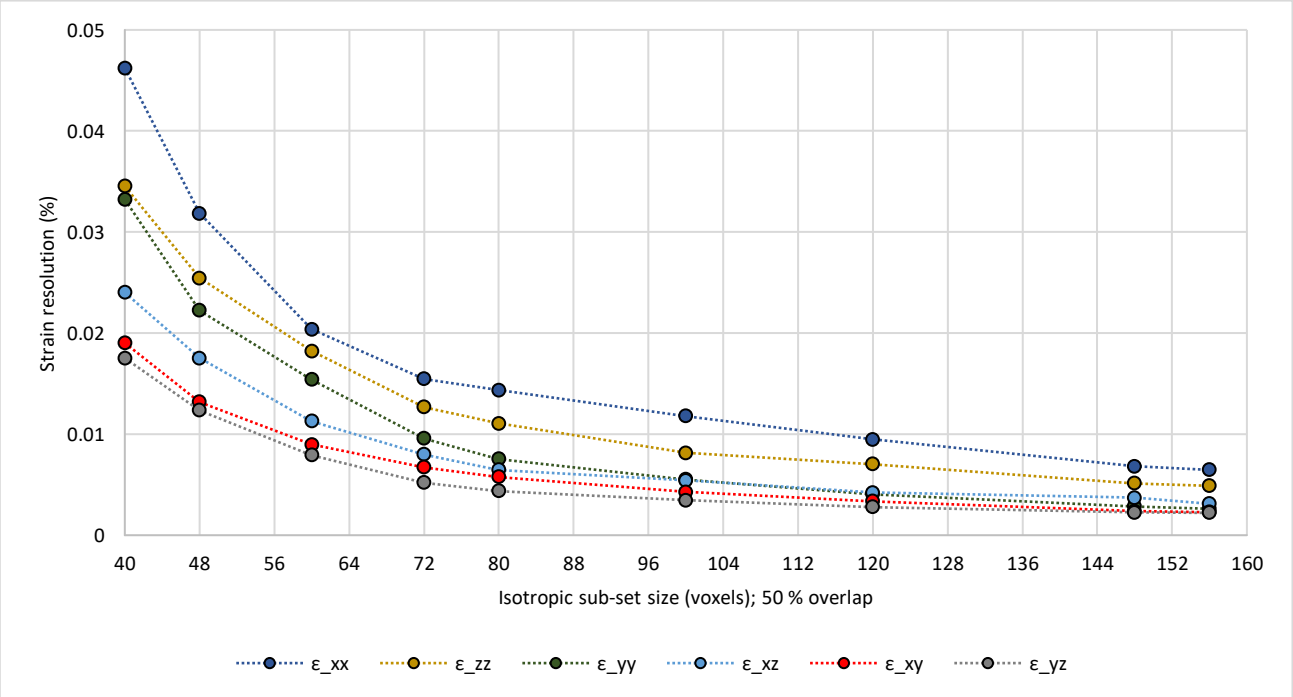

Figure 5-9 – Influence of sub-set size on the strain resolution during SNT scanning (expressed as the standard deviation of the measured strain values), illustrating the compromise between strain and spatial resolution. The 'ε_{yy}' component of the strain tensor denotes the longitudinal (fibre) strain, 'ε_{xx}' the in-plane transverse strain, while the out-of-plane strain component is given by 'ε_{zz}'.

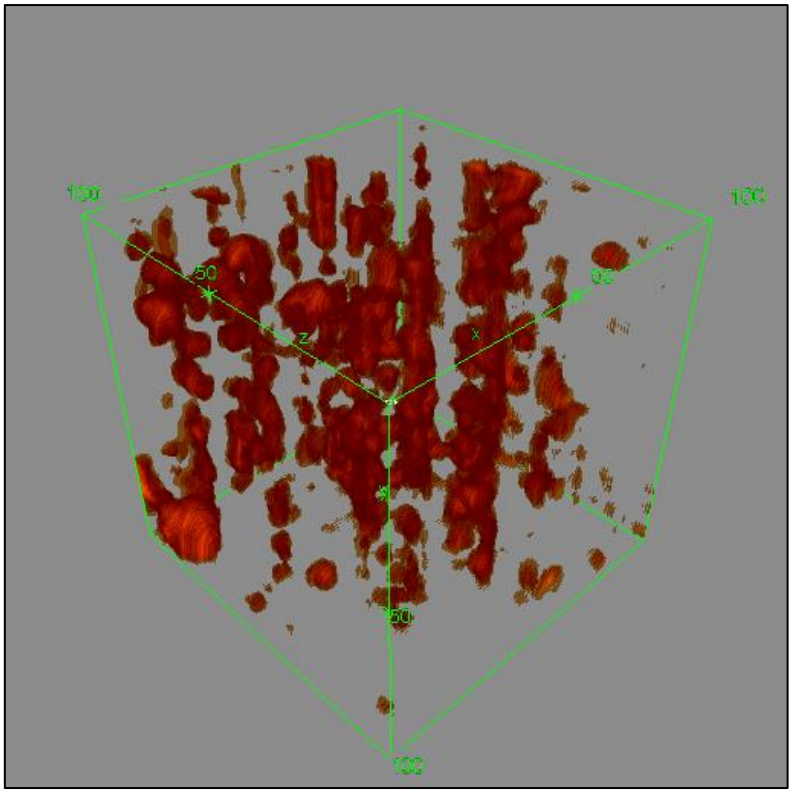

Figure 5-10 – 3D isometric CT view of an isotropic sub-set with a characteristic length of 100 voxels, containing segmented $BaTiO_3$ particles.

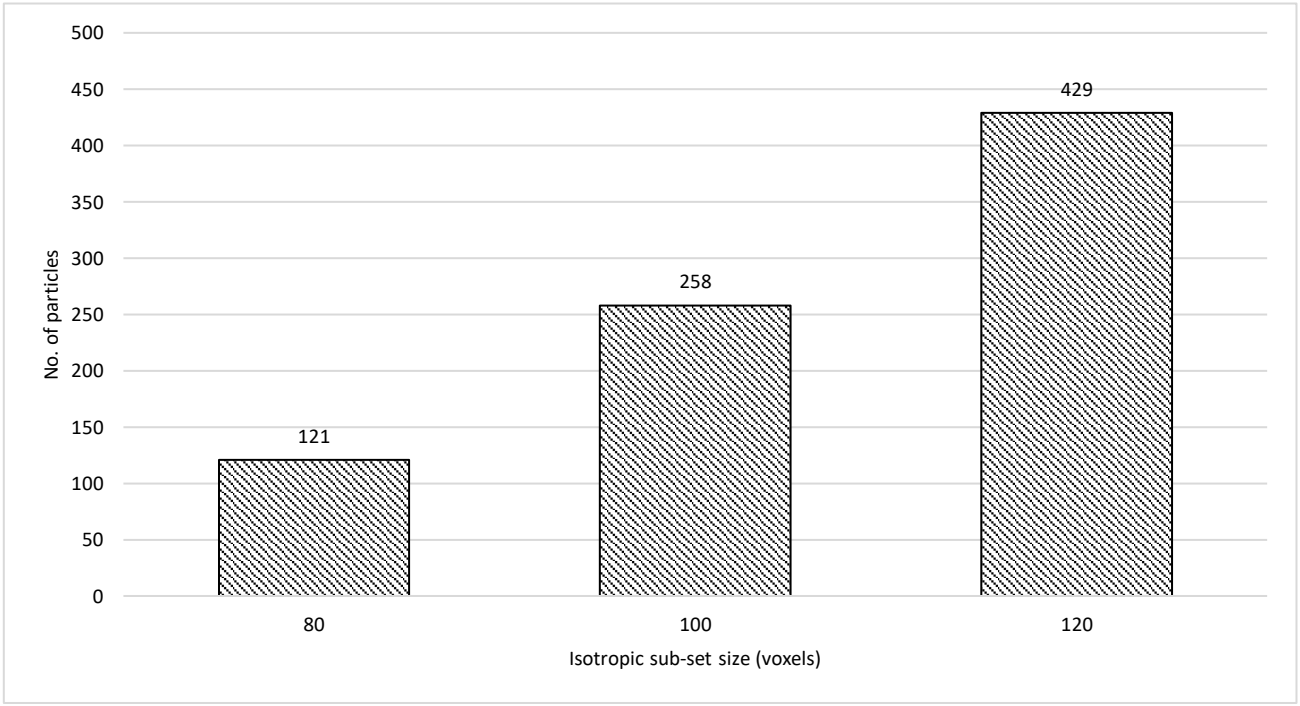

Figure 5-11 – Number of particles as function of sub-set size, using a grey-level threshold of 100/255.

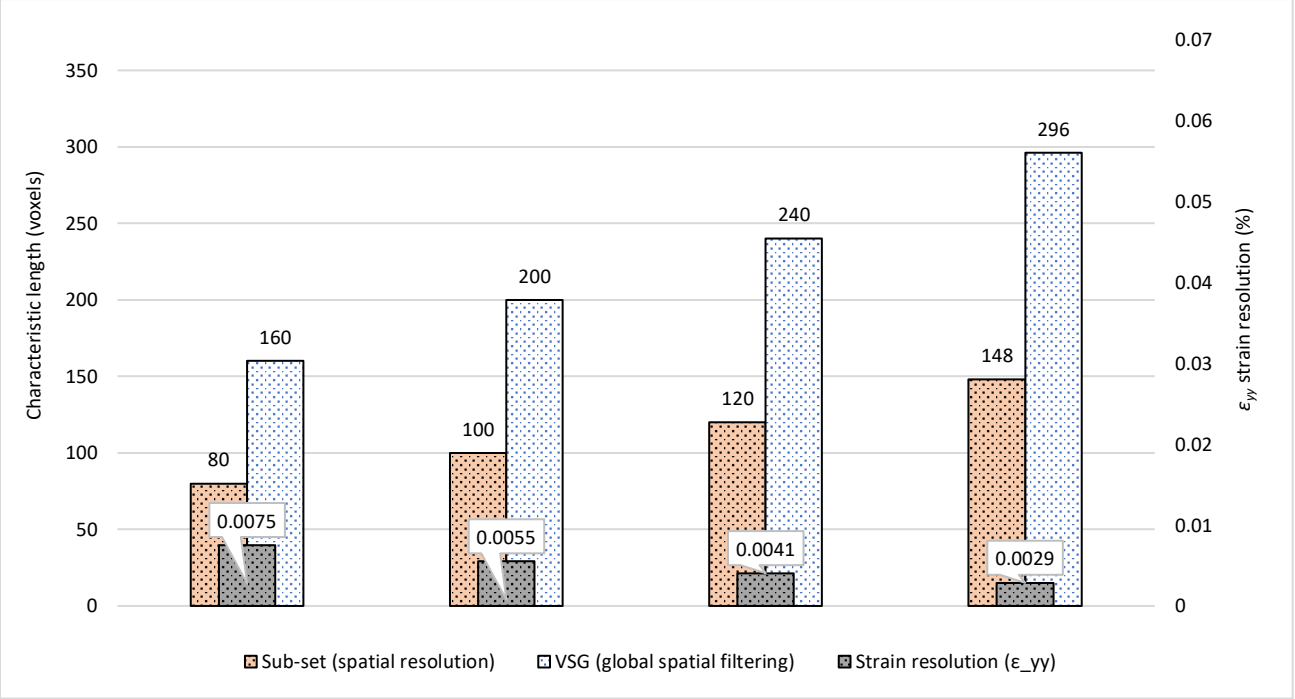

Figure 5-12 – Illustration of VSG and sub-set size, in conjunction with spatial resolution vs. strain resolution (ε_{yy}). Voxel size corresponds to ~0.64 µm.

5.3.1.2 Rigid body displacement

The displacement field following a movement parallel to the fibre direction was initially computed at a sub-set size of 120 voxels (50 % overlap). The measured variation in displacement via DVC is relatively small, with an average displacement reading of 9.713 µm and a standard deviation of 0.0148 µm. The induced Y-displacement was manually confirmed to the nearest pixel in Fiji ImageJ; multiple measurements were taken by determining the distance between a unique feature (*e.g.* a void or $BaTiO_3$ particle) and a reference point. The manual (average) measurement indicates a displacement of ~9.62 ± ~0.64 µm, which is within the accuracy of the DVC. As the present work is exclusively focused on fibre direction strain measurements, RBD analyses were limited to longitudinal tests. Although not an objective here, it is acknowledged that in order to perform reliable transverse (X-direction) and out-of-plane (Z-direction) strain measurements, additional noise assessment studies would be required (*e.g.* as in Borstnar *et al.* [15]).

A strain map indicating the rigid body correction is shown in **Figure 5-13**, where the magnitude of the longitudinal strain noise is shown on a map overlapped with the microstructure. For other sub-set sizes, the SNT and RBD-corrected errors *(ε_{yy})* are collectively summarized in **Figure 5-14**. Edge artefacts arising from volume displacements were geometrically masked prior to initiating the correlation process, measuring 795 × 16 invalid voxels (rounded to the closest integer), across each of the 230 raw data slices.

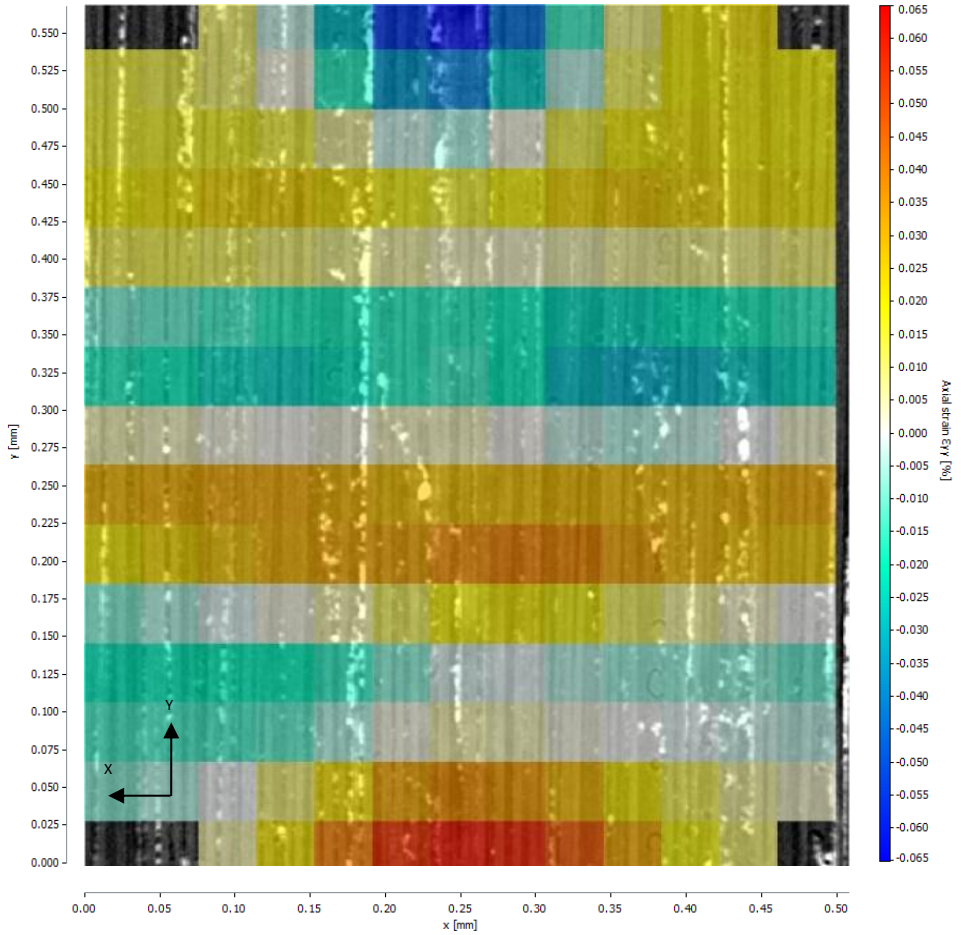

Figure 5-13 – DVC slice 'Z=2' illustrating the 'ε_{yy}' strain map (noise) overlaid with the microstructure following RBD correction. Masking applied (795 × 16 × 230 voxels) to remove edge artefacts for the Y-displaced scans. Map range: -0.065 to 0.065 %.

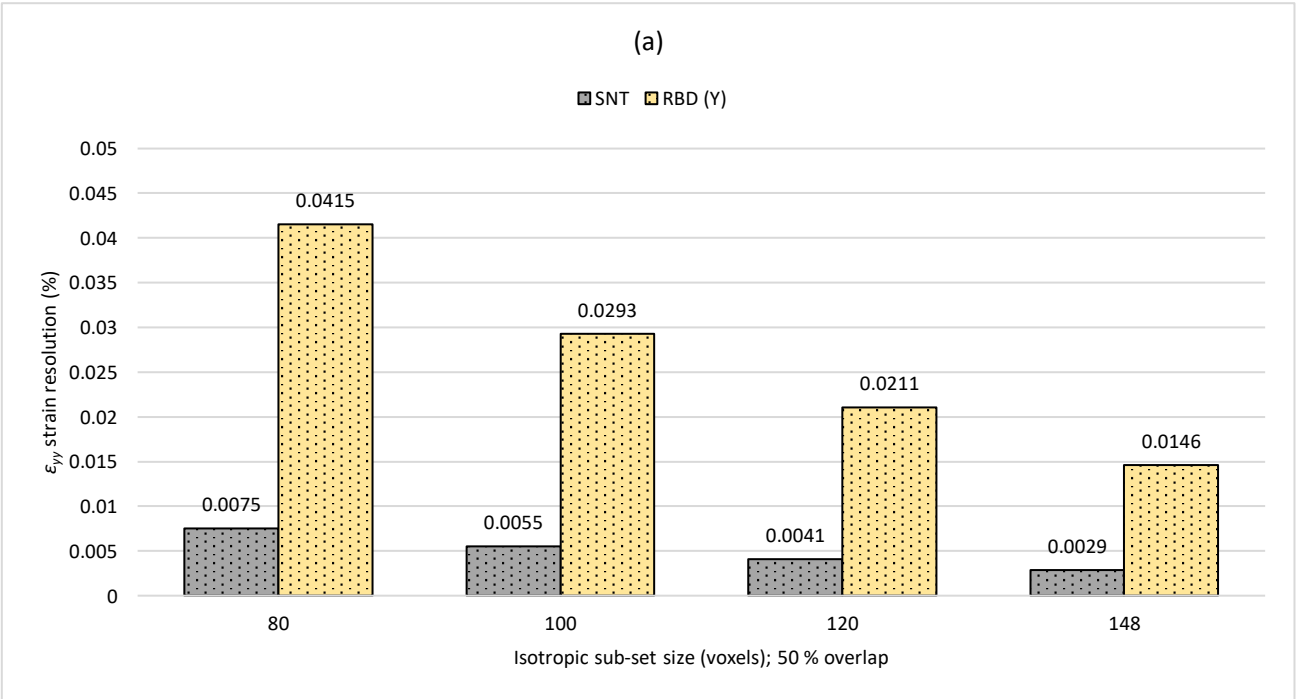

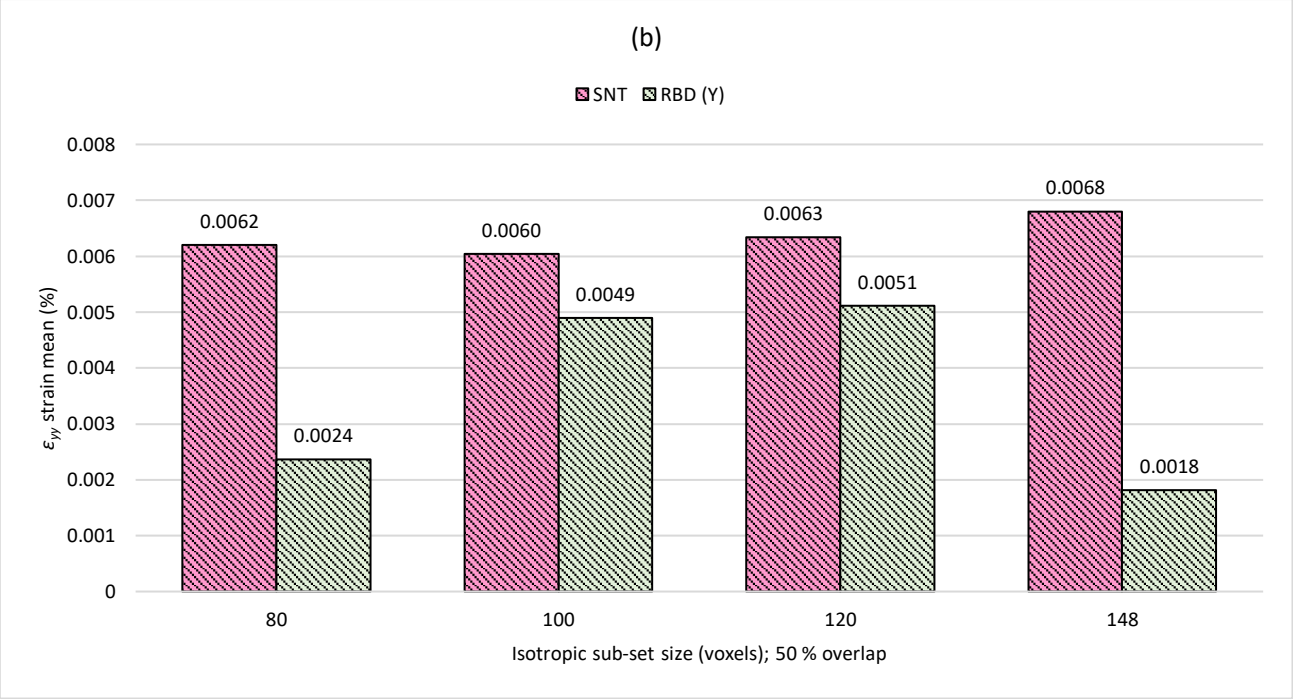

Figure 5-14 – (a) Strain resolution (ε_{yy}), and (b) strain mean (ε_{yy}) for the SNT and RBD corrected scans for various sub-set sizes with 50 % overlap. Masking applied (795 × 16 × 230 voxels) to remove edge artefacts for the Y-displaced scans. Voxel size corresponds to ~0.64 µm.

Figure 5-14 (a) shows that in all cases, the RBD-corrected error is higher than that of the SNT. This is consistent with previous studies which have shown that RBDs can induce higher errors, particularly in the translation direction, due to additional errors from the interpolation biases arising from the specimen movement [15, 18, 20]. Based on the *ex situ* configuration of the present experiment, the RBD strain resolution is considered as the major contribution to the experimental error.

For the equivalent material and similar voxel resolution levels, but in the context of SRCT, it was shown that the discrepancies between the RBD-corrected and SNT standard deviations for a given sub-set size are less than presented here [12, 13]. While it is not the aim of this study to investigate the performance of the DVC based on different imaging acquisition methods, this is a potential indicator that the strain error following an RBD is particularly influenced by the interpolation function, which in turn is affected by the quality of the scan and/or acquisition parameters – *e.g.* noticeable reduced sharpness in volumes obtained through conventional lab cathode tube as opposed to SRCT in Schöberl *et al.* [12, 13].

Despite the different sources of radiation and dissimilar DVC algorithms/parameters (yielding different spatial resolutions), the magnitude of the RBD-corrected strain resolutions are reasonably consistent with those reported in Schöberl *et al.* [12, 13] using $BaTiO_3$-filled CFRPs and in particle-toughened interlayer materials [15].

5.3.2 Evaluation of radius of curvature

The automatically generated radius of curvature generated in GOM Inspect 2018 is shown in **Figure 5-15**, where a close-up view of the best-fitted circle can be visualized. The obtained radius measures 65.38 mm or the equivalent of ~16,263 voxels (~4.02 µm voxel size). A key observation can be readily made regarding the dimension of the circle, which is large in relation to the geometry of the specimen captured within the FOV of the 4 × scan. This, however, follows the above-described methodology of the experiment, whereby a small deflection was intended in order to maintain compatibility with the classical beam theory as well as to avoid any microstructural damage within the 0° plies.

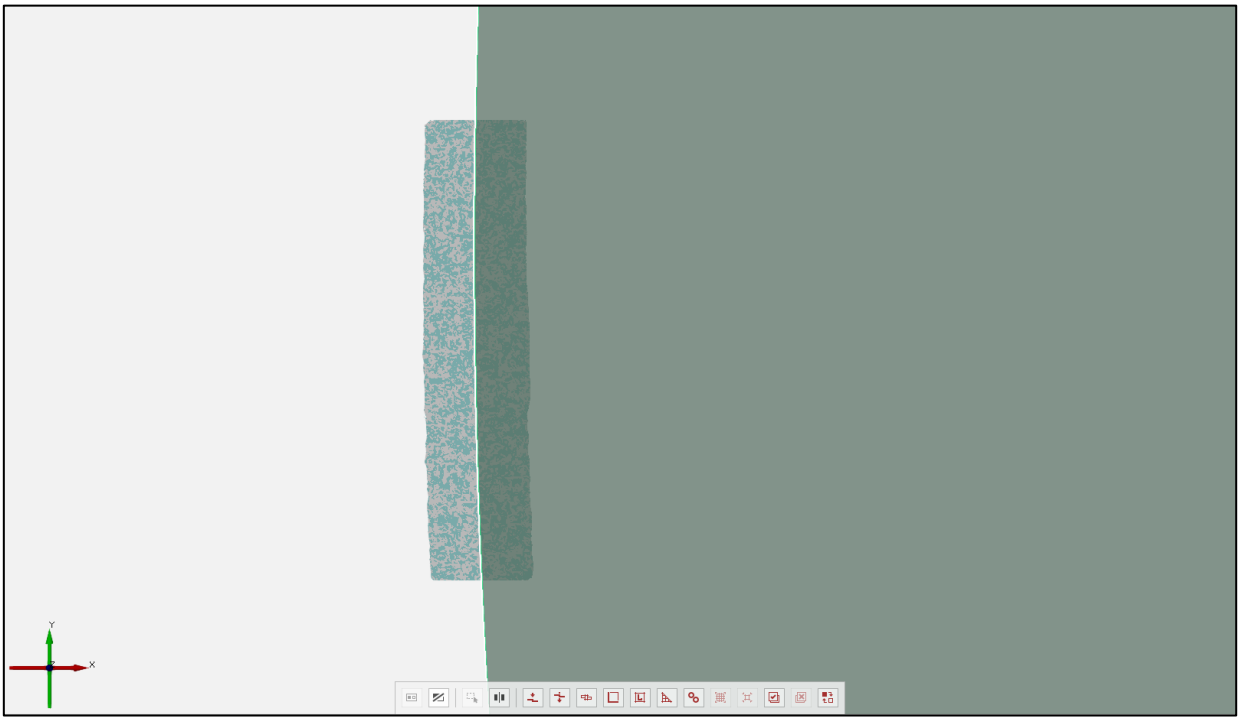

Figure 5-15 – Metrologically fitted circle with a radius of 65.38 mm on the specimen bent geometry (~1 mm × ~4 mm) captured within the FOV of the 4 × scan.

Following the workflow earlier described in **Section 5.2.5**, this result was manually back-fitted onto the specimen edge in SOLIDWORKS 2015. A good agreement was found between the two techniques, and therefore, the data generated by GOM Inspect 2018 is considered correct. The value of 65.38 mm is thus used in the evaluation of the strain profiles as a function of the specimen thickness (see **Section 5.3.3**).

5.3.3 Beam strain profiles

For an ideally homogeneous material, it is expected that deformation under elastic bending would yield a smooth linear gradient about the central neutral axis of the specimen. Divergence from this may be attributed to experimental errors (stochastic, systematic *etc.*) and/or variations in microstructure (*e.g.* local fibre misalignment).

Once the 3D grid of centroid displacements was numerically differentiated to produce full-field 3D strain maps, the constituent sub-sets can either be evaluated as standalone or averaged with the neighbouring sub-sets in various post-processing schemes for comparison purposes. An exemplar averaging scheme is presented schematically in **Figure 5-16**, initially carried out on a volumetric basis (through the entire DVC stack), followed by the analysis of an individual DVC slice – see **Table 5.2** and **Figure 5-7**. As such, for a centroid position along the X-axis, a column of sub-sets (Y-direction) was averaged both in the in-plane and in the out-of-plane direction (Z). Subsequently, the process was repeated incrementally for all permutations in the X-direction. For the grid obtained through a correlation with a sub-set size of 120 voxels with 50 % overlap (**Figure 5-16**), each of the columns contain 15 sub-sets and spans four DVC slices (planes) in the Z-direction – thereby representing an average of 60 subsets (with the exception of the corners of the overall volume, due to cropping/masking, where the total number of sub-sets per column are slightly less). Finally, each of the 13 averaged columns was compared against the Euler-Bernoulli prediction. The theoretical values, corresponding to the reciprocal of the radius of curvature (65.38 mm), were computed at the position of each sub-set column on the grid. The planar procedure is similar, with the only difference being that sub-set averaging was performed independently in each of the slices (*i.e.* limited to the in-plane direction: 15 sub-sets were averaged in one instance, as opposed to 60 for across whole volume). Next, the averaging scheme followed a decomposition into blocks comprised of a reduced number of sub-sets: 3 blocks of 5 sub-sets followed by 5 blocks of 3 sub-sets per each column, corresponding to a sub-set sampling of 33.33 % and 20 %, respectively, per column. Ultimately, the assessment was carried out based on standalone sub-sets (multiple rows) through the thickness of the beam.

A typical strain profile obtained through the four-point experiment can be seen in **Figure 5-17**, in which the microstructure is overlaid with the strain map. The expected strain distribution can be observed qualitatively through the beam thickness, *i.e.* fibres in tension on the left-hand side and in compression on the right-hand side, with a neutral plane of sub-sets (∼zero strain) located centrally.

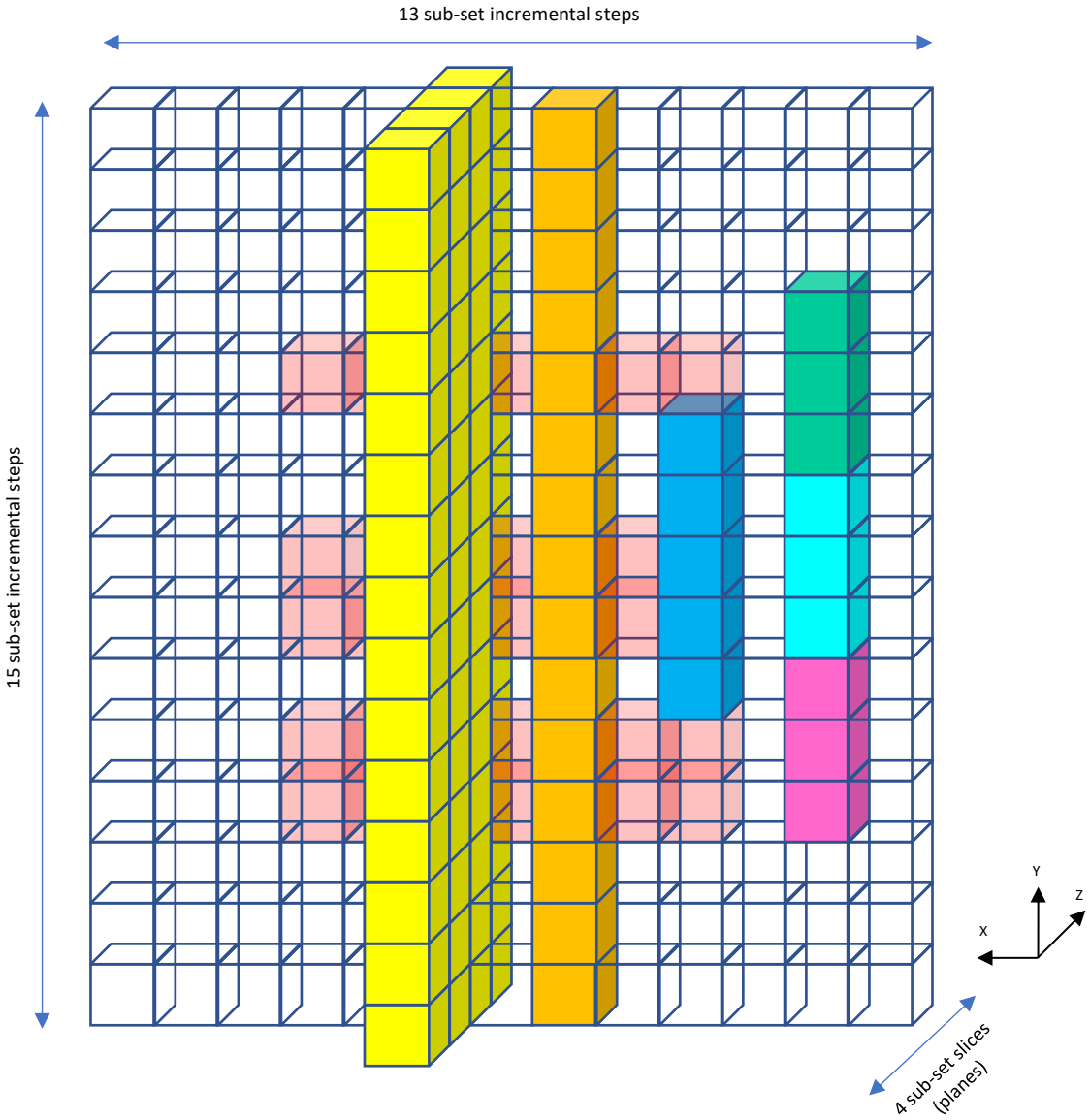

*Figure 5-16 – Schematic diagram illustrating the 3D grid of DVC sub-sets, applicable to matching volumes of 795 × 885 × 230 voxels, correlated with an isotropic sub-set size of 120 voxels and 50 % overlap. For simplicity, only overlapping windows (steps) are shown as opposed to the grid comprised of overlapped sub-sets. Displacement vectors, and implicit strain values are computed for each step (i.e. a distance of 60 voxels or ~38.4 µm). The sub-set averaging schemes are indicated as follows in decreasing stages (applicable to each permutation along the X-direction: **yellow** – volumetric across four slices (planes) of sub-sets, **orange** – planar, across a single slice of sub-sets, **blue** – planar, single median block of five sub-sets '2/3', **pink**, **cyan** and **green** – planar, three central blocks each consisting of three sub-sets '2/5', '3/5', '4/5' and **red** – planar, standalone sub-sets (rows) through the beam thickness compared with the analytical solution.*

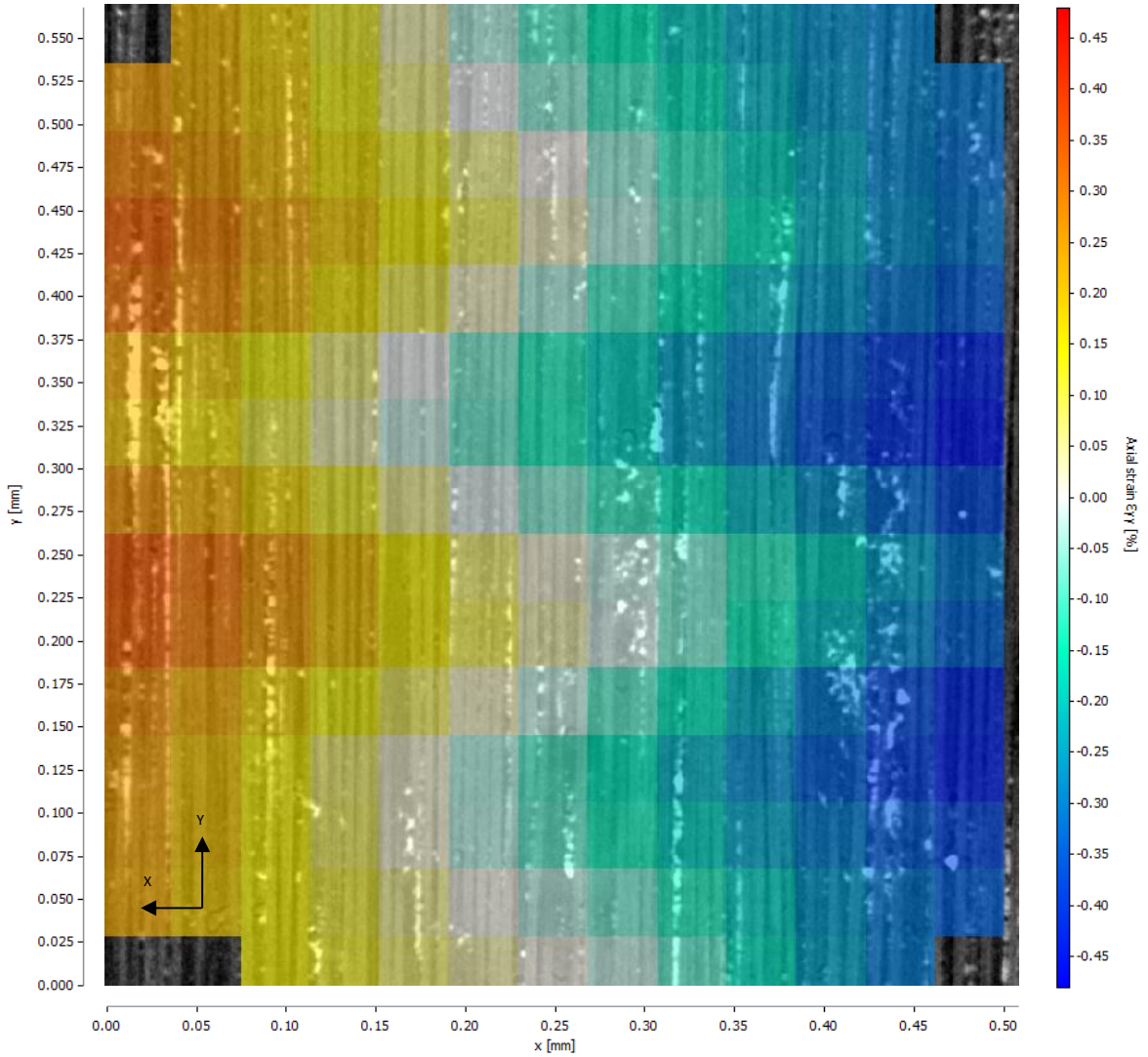

Figure 5-17 – Strain mapping illustration overlapped with the microstructure (795 × 885 voxels, ~0.64 µm voxel size), showing the through-thickness strain distribution. Fibres in tension on the left-hand side and in compression on the right-hand side. Sub-set size: 120 voxels with 50 % overlap. DVC slice number 'Z=2'. Interpolation/smoothing not applied to the strain map.

5.3.3.1 Volumetric sub-set averaging

Figure 5-18 (a) presents the strain data obtained from a correlation based on subset size of 120 voxels with 50 % overlap. Similarly, **Figure 5-18 (b)** and **(c)** presents the volumetrically averaged strain gradient, but at different spatial resolutions (100 voxels and 80 voxels sub-set size, respectively). As expected, the spatial sampling improves with decreasing sub-set size, but with an increased predisposition to noise – see **Table 5-3** and **Figure 5-9**.

Following the volumetric averaging scheme of subsets, the DVC output is found to be in concordance with the analytical solution for all three presented case studies. Even though the experimental error doubles (0.0415 % *vs.* 0.0211 %) from a sub-set size of 80 voxels to 120 voxels, the strain gradient is shown not to be affected.

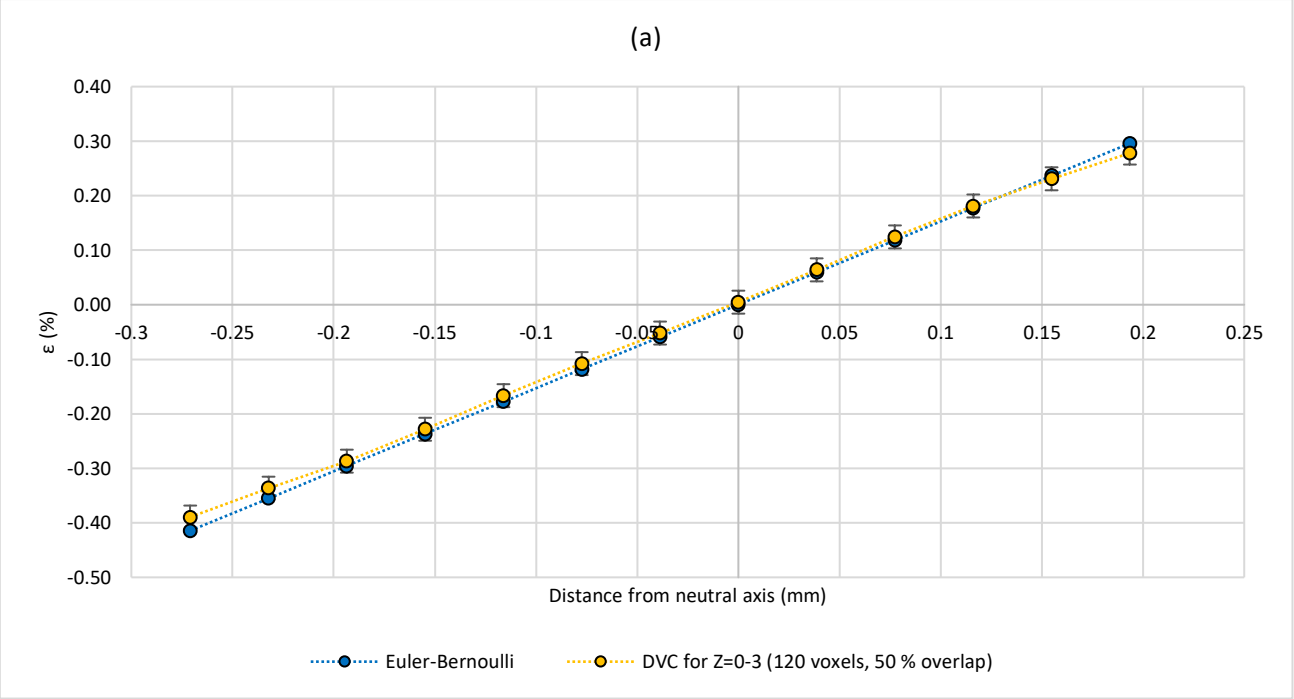
(a)
0.40
0.30
0.20
0.10
0.00
-0.10
-0.20
-0.30
-0.40
-0.50
ε (%)
-0.3
-0.25
-0.2
-0.15
-0.1
-0.05
0
0.05
0.1
0.15
0.2
0.25
Distance from neutral axis (mm)
Euler-Bernoulli
DVC for Z=0-3 (120 voxels, 50 % overlap)

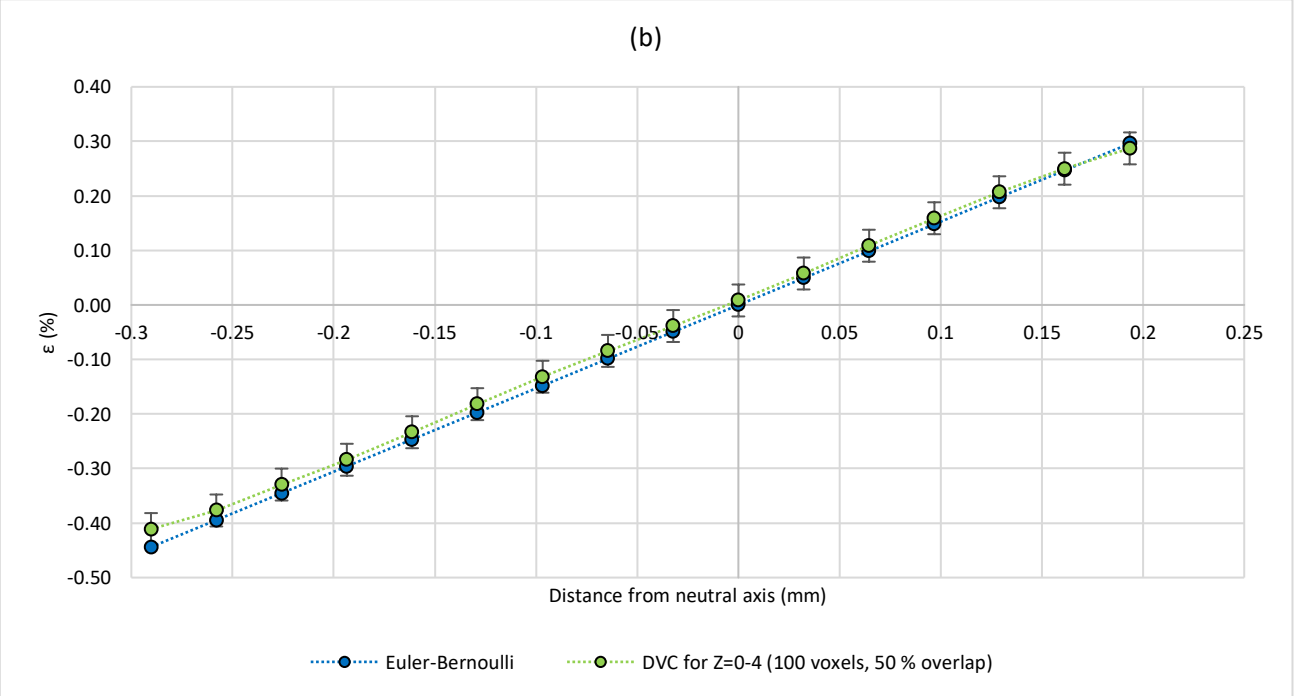
(b)
0.40
0.30
0.20
0.10
0.00
-0.10
-0.20
-0.30
-0.40
-0.50
ε (%)
-0.3
-0.25
-0.2
-0.15
-0.1
-0.05
0
0.05
0.1
0.15
0.2
0.25
Distance from neutral axis (mm)
Euler-Bernoulli
DVC for Z=0-4 (100 voxels, 50 % overlap)

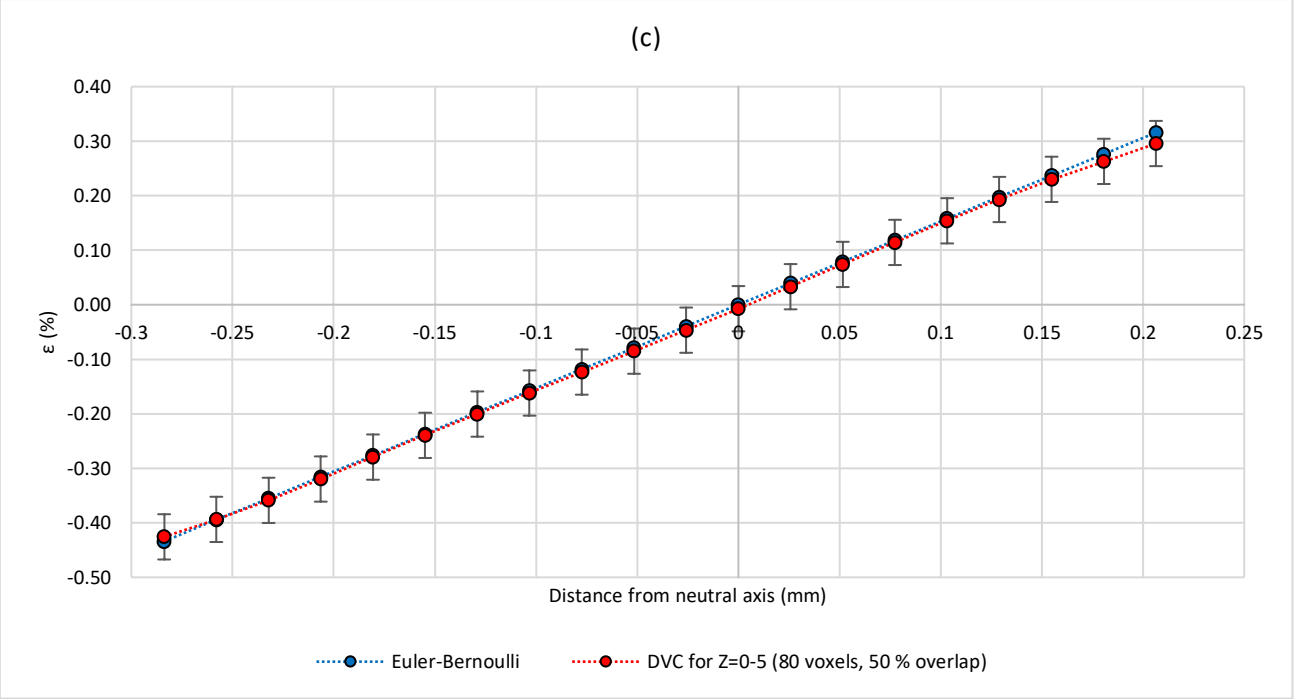

Figure 5-18 – Strain gradient obtained through the application of DVC vs. classical beam theory prediction. Sub-set size: (a) 120 voxels, (b) 100 voxels, (c) 80 voxels with 50 % overlap. Volumetric sub-set averaging through all DVC slices: (a) 'Z=0' to 'Z=3', (b) 'Z=0' to 'Z=4', (c) 'Z=0' to 'Z=5'. Number of averaged sub-sets per column: (a) 60 (15 × 4), (b) 72 (18 × 4), (c) 88 (22 × 4). Number of data points: (a) 13 columns, (b) 16 columns, (c) 20 columns. Indicated RDB corrected error of (a) 0.0211 %, (b) 0.0293 %, (c) 0.0415 %.

A key observation from **Figure 5-18** is related to what appears to be an offset of the neutral axis by ~76.8 µm to ~96 µm (depending on the sub-set grid spacing), leading to a higher number of data points in compression as opposed to the tension side of the beam, across all examples (*e.g.* 7 data points in compression *vs.* 5 data points in tension from the neutral axis, for the 120 voxel sub-set size case, with 50 % overlap). This effect is a direct experimental artefact arising from image acquisition, and not DVC processing, whereby the CT volumes of the deformed and undeformed state were slightly offset in relation to the geometrical neutral axis of the specimen. The reduced FOV at 20 × magnification made a perfect alignment at fibre-level challenging, which combined with the offset required to implement an eccentric centre of rotation relative to the mid-axis of the rig for the bent configuration resulted in matching volume images marginally orientated towards the compression side of the beam.

In addition, from **Figure 5-18**, a small degree of nonlinearity can be observed at the furthest distance from the neutral axis (corresponding to the highest negative/positive strain values within the FOV). This effect is consistent throughout the data sets and can be attributed to edge-based artefacts – see **Section 5.2.4**. The effect is confined to three grid positions nearest the edge of the FOV, which is the equivalent to the span of the VSG. This is anticipated, as a poorly correlated sub-set positioned at the edge of the matching volumes will have a detrimental impact on the entire corresponding VSG measurement of strain. Further DVC results have

been truncated to eliminate these edge artefacts located at the perimeter of the correlated volumes (XY-plane), at the expense of a reduced number of data points through the beam thickness (see **Section 5.3.3.2**). It can also be observed that as the sampling rate is increased (*i.e.* smaller sub-set size/higher spatial resolution), the gauge length of the affected area diminishes, confirming that this is an artefact of the image processing.

Following the above-described volumetric sub-set sampling and averaging strategy, the effectiveness of DVC in measuring local strains is shown to correlate well with Euler-Bernoulli beam theory, however, with a subtly reduced accuracy in the presence of edge artefacts.

5.3.3.2 Planar sub-set averaging

For brevity, correlation results in this section are based on a sub-set size of 120 voxels (50 % overlap), with averaging now being carried out in a single slice (plane) of the specimen. In the first instance, single-sliced columns of sub-sets are considered as opposed to columns averaged through the overall stack. **Figure 5-19** shows strain gradients obtained through the decomposition of the DVC stack into the component DVC slices. While there is a reduction in the number of sub-sets averaged per data point (column) by a quarter, *i.e.* from 60 to 15, the linearity of DVC output remains in good agreement with the analytical solution for the middle DVC slices shown here 'Z=1' and 'Z=2'. As noted in the previous section, the number of data points through the thickness of the specimen was reduced to eliminate edge-based artefacts.

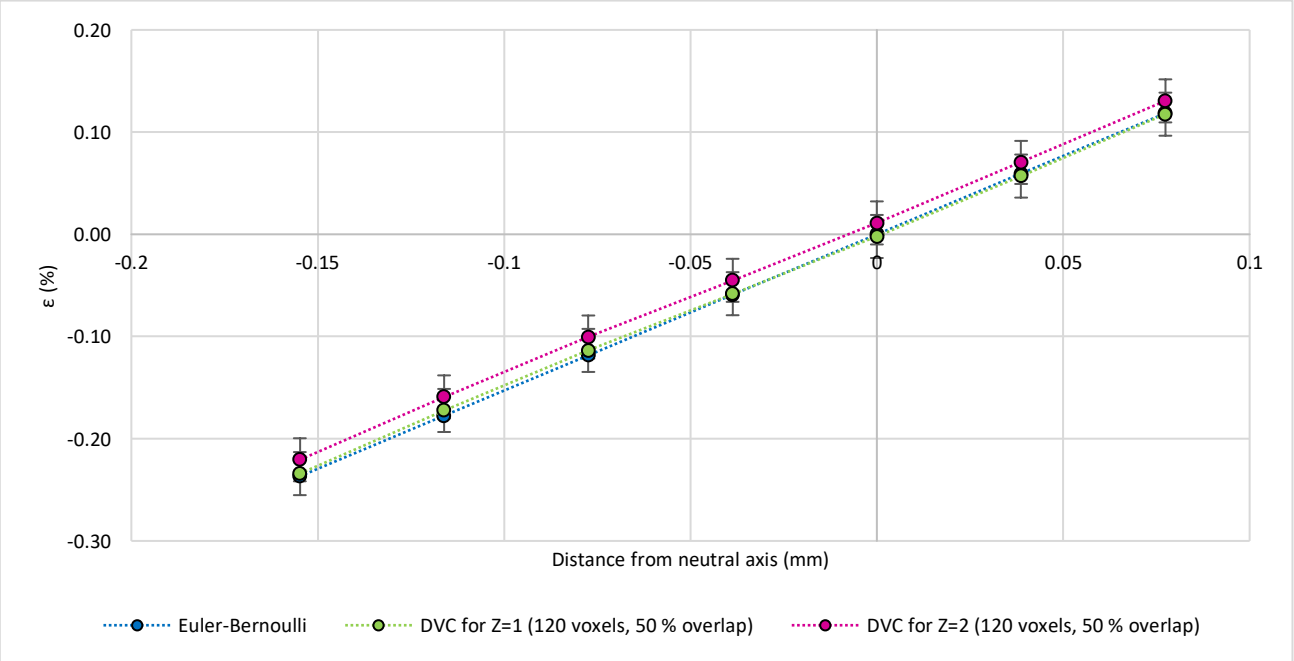

Figure 5-19 – Strain gradient obtained through the application of DVC vs. classical beam theory prediction. Sub-set size: 120 voxels with 50 % overlap. Planar sub-set averaging performed independently in both DVC slices 'Z=1' and 'Z=2'. Number of averaged sub-sets per column: 15 (15 × 1). Edge-artefacts located at the perimeter truncated (XY-plane), yielding 14 data points (7 columns × 2 DVC slices). Indicated RDB corrected error of 0.0211 %.

The two remainder DVC slices 'Z=0' and 'Z=3' are not discussed, as they are comparable to what was stated in **Section 5.3.3.1**; these planes of sub-sets also represent edge-artefacts, not being fully satisfied from a voxel perspective. However, in this particular instance, the outlier subsets are not positioned at the perimeter of the grid (XY-plane) for each DVC slice but are rather located at the top/bottom end of the 3D stack (Z-direction) – see **Section 5.2.4**. Consequently, due to missing pixel information, restoring the 'true' response of the material is more challenging in the aforementioned DVC slices.

Further decomposition of the averaging scheme concentrates on the results based on a single DVC slice, in particular slice 'Z=2'. Blocks are considered, being comprised of a reduced number of sub-sets (as opposed to full single-sliced columns) and remote from edge artefacts: median block number '2/3' comprised of 5 sub-sets (**Figure 5-20 (a)**) and central blocks '2/5', '3/5' and '4/5', each comprised of 3 sub-sets (**Figure 5-20 (b)**). Finally, the averaging scheme is removed completely, and an example is shown where single rows of sub-sets are compared against the theoretical prediction (**Figure 5-21**).

Decreasing the number of averaged sub-sets in a column even further, from 15 to 5, is also shown not to introduce fluctuations above the experimental error in the strain gradient (**Figure 5-20 (a)**). The level of nonlinearity is observed to increase slightly when only three sub-sets are averaged per column, as opposed to a number of five, but the DVC output still remains within the boundaries of the RBD-corrected error of 0.0211 % (**Figure 5-20 (b)**).

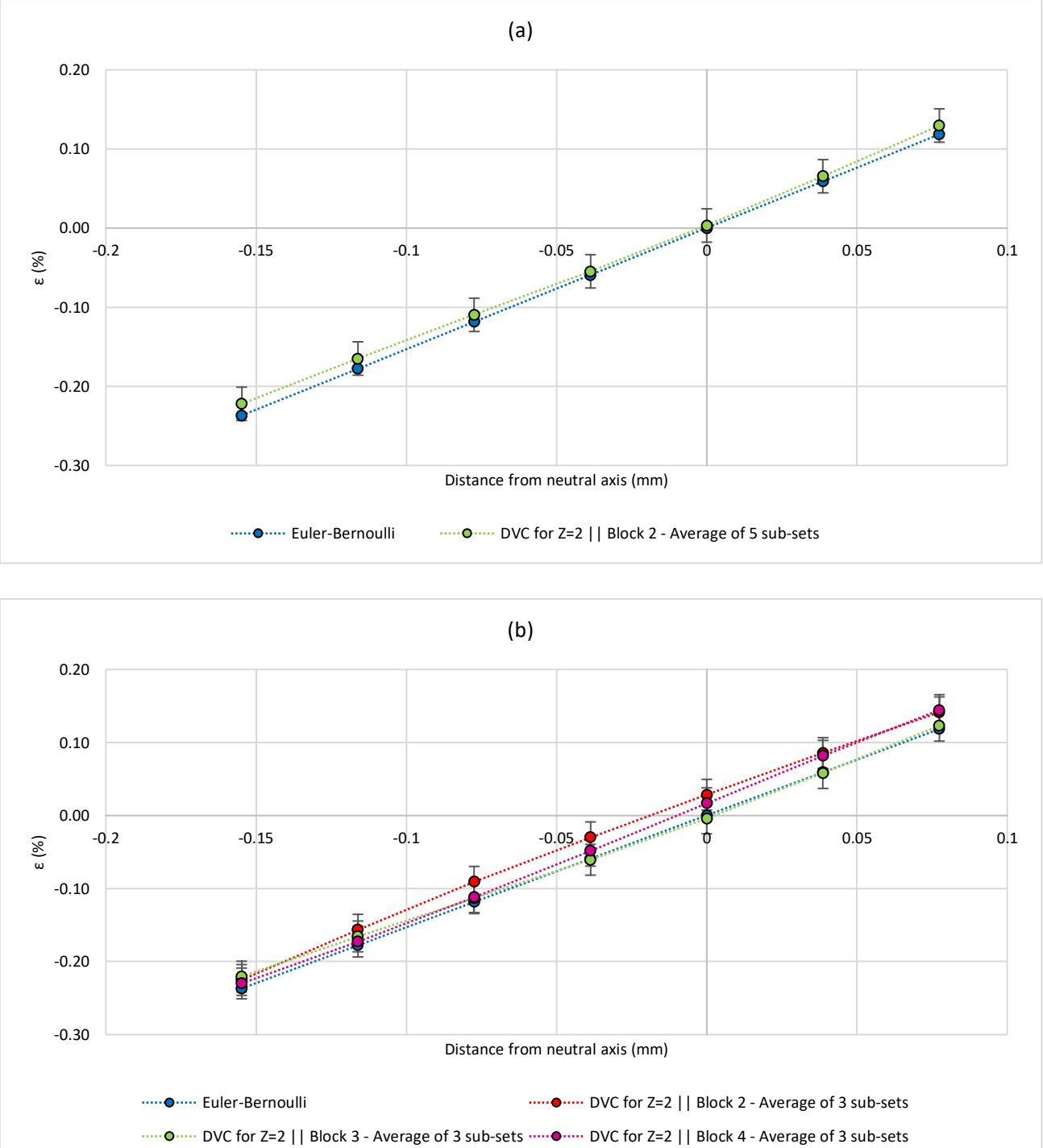

Figure 5-20 – Strain gradient obtained through the application of DVC vs. classical beam theory prediction. Sub-set size: 120 voxels with 50 % overlap. DVC slice number 'Z=2'. Planar averaging scheme: (a) single median block '2/3' containing 5 averaged sub-sets per column on the grid (block contains 33.33 % of the total number of sub-sets per column), and (b) central blocks '2/5', '3/5', '4/5' each containing 3 averaged sub-sets per column on the grid (one block contains 20 % of the total number of sub-sets per column). Edge-artefacts located at the perimeter and ends of the stack truncated (XY and Z-plane), resulting in: (a) 7 data points (1 block of averaged sub-sets × 7 columns), and (b) 21 data points (3 blocks of averaged sub-sets × 7 columns). Indicated RDB corrected error of 0.0211 %.

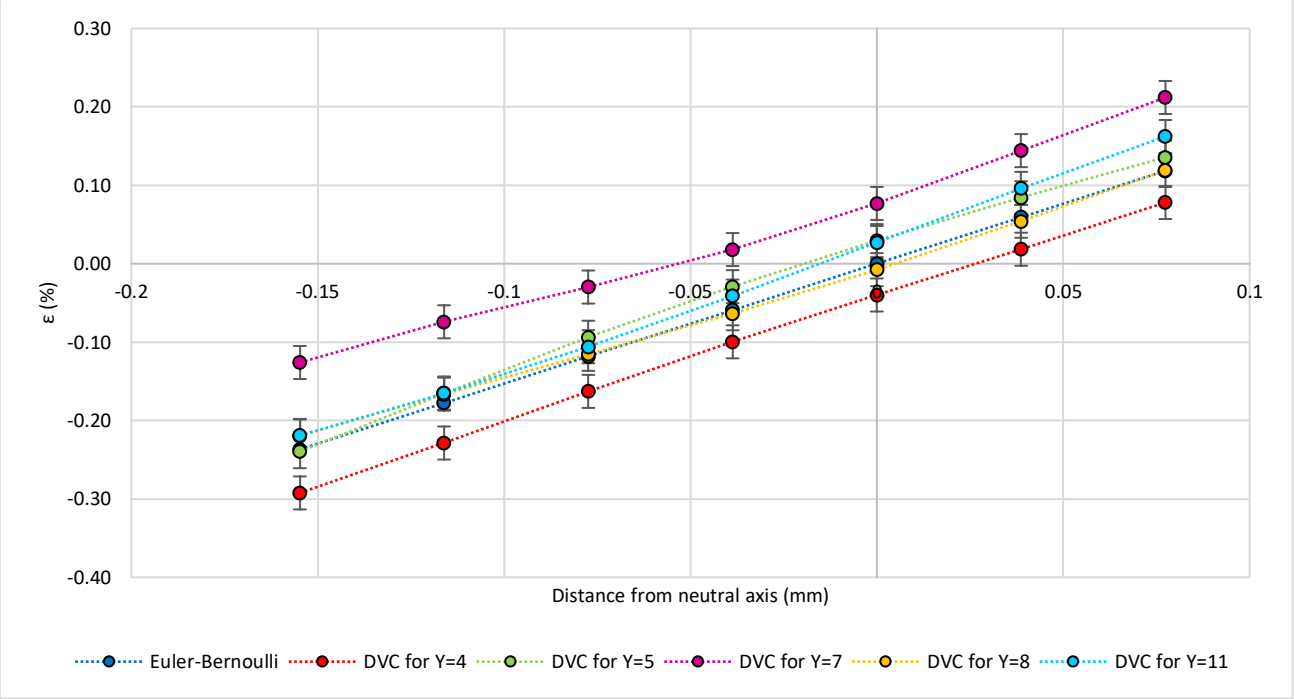

Figure 5-21 – Strain gradient obtained through the application of DVC vs. classical beam theory prediction. Sub-set size: 120 voxels with 50 % overlap. Sub-set averaging scheme removed (i.e. each data point corresponds to strain value of a standalone sub-set). Rows of sub-sets (Y-direction) plotted: 4/15, 5/15, 7/15, 11/15, resulting in 28 data points (7 sub-sets × 4 rows). Edge-artefacts located at the perimeter and ends of the stack truncated (XY and Z-plane). Indicated RDB corrected error of 0.0211 %.

Sampling standalone sub-sets with a size of 120 voxels (~76.8 µm or ~11 fibre diameters), as opposed to averaging entire columns or reduced blocks comprising multiple sub-sets, does reveal strain values through the beam thickness in which the nonlinearity and/or offset exceeds that of the computed experimental error (**Figure 5-21**). No conclusive explanation can be drawn as to why a deviation from the Euler-Bernoulli prediction occurs at such relatively small length-scales, but it is likely that this represents the practical limit of the current technique, linked to the effective sampling of the beam. More specifically, the eccentric centre of rotation relative to the mid-axis of the rig for the bent configuration could have resulted in tomographic reconstructions with underlying:

- Different attenuation profiles, due to varying X-ray path lengths and
- Oversampled/undersampled radiographs of the central gauge and edge region.

Additionally, the deviation may also be related to interpolation biases (**Figure 5-13**), as well as strain variations associated with local changes in the material microstructure, including fibre misalignment (fibre direction errors and waviness) and fibre-matrix volume fraction fluctuations. Raw CT data slices shown in **Figure 5-22** illustrate that the fabricated material presents such local microstructural changes. Voids represent an

additional variability; however, the implications are presumed second-order due to a relatively dispersed distribution within the CFRP.

Maintaining the overall argument that the experimental data agrees with the theoretical prediction, and that the effectiveness of the technique is validated, additional studies via DVC in conjunction with CT are envisaged within the 0° plies (not limited to elastic deformations): matrix plastic yielding, fibre-matrix interfacial debonding, longitudinal matrix microcracking, inter/intralaminar delaminations, *etc*. Furthermore, the technique can be applied to orientations different from the 0° plies (*e.g.* transverse matrix cracking), as well as in different loading scenarios (*e.g.* compression, torsion) and materials with multiaxial or discontinuous reinforcement.

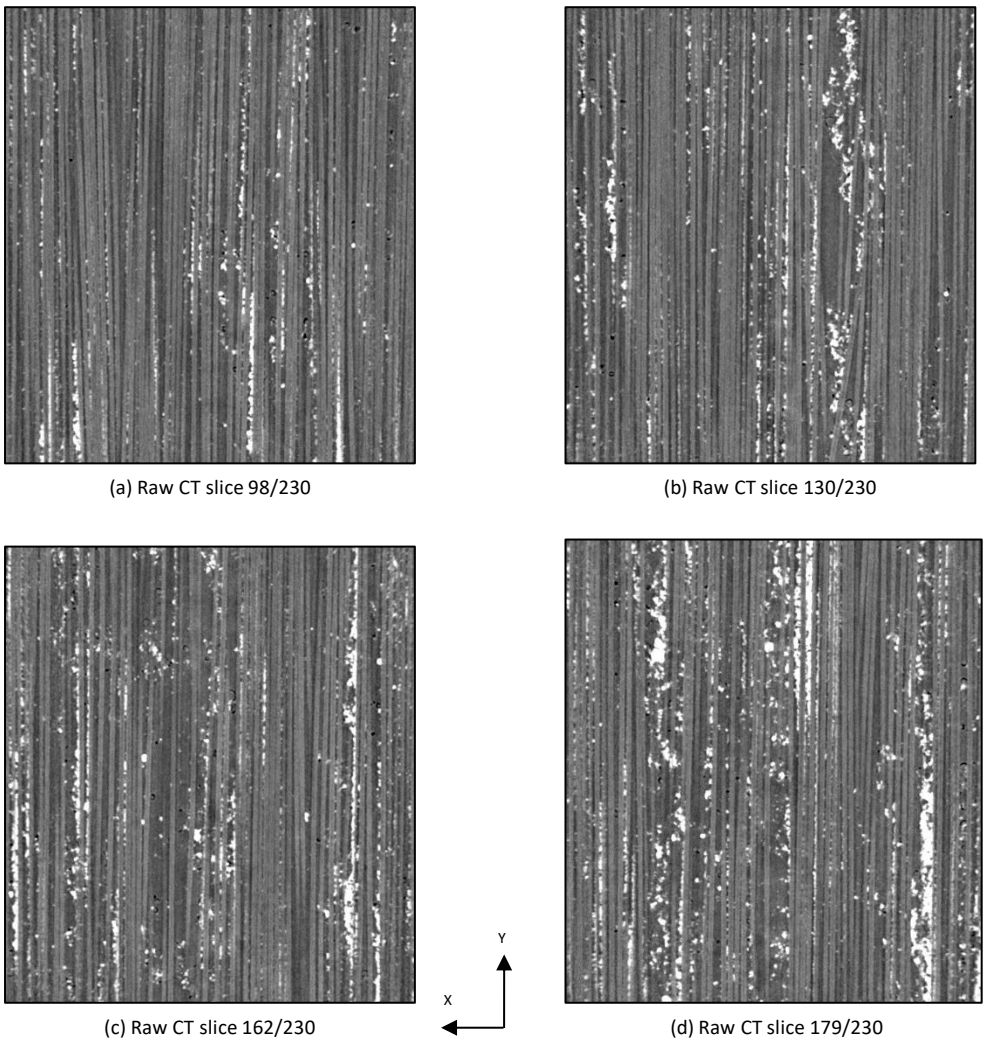

Figure 5-22 – Raw CT data slices showcasing changes in material microstructure, potentially accountable for an uneven strain distribution at fibre-level. Each slice has a FOV of 795 × 885 voxels (~0.64 µm voxel size): (a) illustrating tow-level misalignment, (b) large resin-rich channel coupled with fibre direction errors, (c) multiple, parallel resin-rich channels and fibre misalignment, (d) large resin-rich channel and fibre misalignment. The spatial distribution of particles is uniformly random, providing this is considered in 3D space.

5.3.4 Summary and conclusions

A comprehensive DVC study was performed at sub-micrometre resolution (~0.64 μm) on UD carbon-fibre composite plies to validate the methodology by comparison to the analytical result for the through-thickness strain distribution in a state of pure bending. To counteract the sub-optimal microstructures found in conventional UD CFRPs for the application of DVC, particularly along the fibre direction, $BaTiO_3$ particles with a mean size of 400 nm and volume fraction of ~1.44 % were introduced in the matrix. Micro-focus CT measurements were acquired from a simple beam-type specimen subjected to a four-point flexural test, which led to a well-defined strain distribution. A rigid body displacement test was also performed to determine the experimental error. The test also confirmed that that specimen translation parallel to the fibre direction is in line with the applied displacements, obviating a key problem in applying DVC to such uniformly aligned microstructures. DVC results were compared against the classical beam theory in incrementally decreasing averaging schemes, and at various spatial resolutions: 120 voxels, 100 voxels and 80 voxels sub-set size, with 50 % overlap applied between adjacent sub-sets. Good agreement was found between the Euler-Bernoulli beam theory and DVC output providing that the mean of three or more standalone sub-sets was taken, demonstrating the effectiveness of DVC in measuring local strains parallel to the fibre direction in UD laminae. Edge artefacts were shown to introduce subtle nonlinearities in the measurements, illustrating that any DVC results located at the edge of the cropped/masked volume image must be treated with caution. Deviations from the classical beam theory, exceeding that of the experimental error, were observed when sampling was performed with single 120 voxel size sub-sets. This represents a practical lower limit for the spatial resolution using the technique employed in the current work and may also be attributed to variations in the material microstructure. The methodology provides a framework for accessing unprecedented opportunities to identify the local strain distributions before and after damage formation in composite materials, in 3D, at relatively high spatial resolutions. **Chapter 6** will report mechanistically consistent measurements in relation to local fibre failure events, such as strain transfer lengths. To eliminate some of the present caveats, in particular related to spatial and strain resolutions achievable, detailed analyses will be conducted on SRCT data. This provides the opportunity to refine the understanding of composite tensile failure processes alongside the various other forms of composite damage that exist and is in turn expected to provide a valuable tool for developing and validating micromechanics models for composite damage and failure.

5.3.5 References

[1] United Nations, “Paris Agreement,” New York City, NY, USA, 2015.

[2] K. Van Acker, I. Verpoest, J. De Moor, J.-R. Duflou and W. Dewulf, “Lightweight materials for the automotive: Environmental impact analysis of the use of composites,” in *The 3rd International Seminar on Society & Materials*, Freiberg, Germany, 2009.

[3] A. J. Moffat, P. Wright, J.-Y. Buffiere, I. Sinclair and S. M. Spearing, “Micromechanisms of damage in 0° splits in a [90/0]s composite material using synchrotron radiation computed tomography,” *Scripta Materialia,* vol. 59, no. 10, pp. 1043-1046, 2008.

[4] P. Wright, A. J. Moffat, I. Sinclair and S. M. Spearing, “High resolution tomographic imaging and modelling of notch tip damage in a laminated composite,” *Composites Science and Technology,* vol. 70, no. 10, pp. 1444-1452, 2010.

[5] A. E. Scott, M. N. Mavrogordato, P. Wright, I. Sinclair and S. M. Spearing, “In situ fibre fracture measurement in carbon-epoxy laminates using high resolution computed tomography,” *Composites Science and Technology,* vol. 71, no. 12, pp. 1471-1477, 2011.

[6] S. C. Garcea, I. Sinclair, S. M. Spearing and P. J. Withers, “Mapping fibre failure in situ in carbon fibre reinforced polymers by fast synchrotron X-ray computed tomography,” *Composites Science and Technology,* vol. 149, pp. 81-89, 2017.

[7] S. Rosini, M. N. Mavrogordato, O. Egorova, E. S. Matthews, S. E. Jackson, S. M. Spearing and I. Sinclair, “In situ statistical measurement of local morphology in carbon-epoxy composites using synchrotron X-ray computed tomography,” *Composites Part A,* vol. 125, pp. 1-14, 2019.

[8] B. Pan, K. Qian, H. Xie and A. Asundi, “Two-dimensional digital image correlation for in-plane displacement and strain measurement: A review,” *Measurement Science and Technology,* vol. 20, no. 6, pp. 1-17, 2009.

[9] B. K. Bay, T. S. Smith, D. P. Fyhrie and M. Saad, “Digital volume correlation: Three-dimensional strain mapping using X-ray tomography,” *Experimental Mechanics,* vol. 39, no. 3, pp. 217-226, 1999.

[10] J. Adam, M. Klinkmüller, G. Schreurs and B. Wieneke, “Quantitative 3D strain analysis in analogue experiments simulating tectonic deformation: Integration of X-ray computed tomography and digital volume correlation techniques,” *Journal of Structural Geology,* vol. 55, pp. 127-149, 2013.

[11] F. Xu, “Quantitative characterization of deformation and damage process by digital volume correlation: A review,” *Theoretical & Applied Mechanics Letters,* vol. 8, no. 2, pp. 83-96, 2018.

[12] E. Schöberl, M. N. Mavrogordato, I. Sinclair and S. M. Spearing, “The mapping of damage behaviour in a unidirectional composite subjected to uniaxial loading using digital volume correlation,” in *The 12th International Conference on Composite Science and Technology*, Sorrento, Italy, 2019.

[13] E. Schöberl, C. Breite, A. Melnikov, Y. Swolfs, M. N. Mavrogordato, I. Sinclair and S. M. Spearing, “Mapping strains and fibre fracture in carbon fibre composites using in situ digital volume correlation,” in *The 22nd International Conference on Composites Materials*, Melbourne, Australia, 2019.

[14] P. Lecomte-Grosbras, J. Réthoré, N. Limodin, J.-F. Witz and M. Brieu, “Three-dimensional investigation of free-edge effects in laminate composites using X-ray tomography and digital volume correlation,” *Experimental Mechanics,* vol. 55, no. 1, pp. 301-311, 2015.

[15] G. Borstnar, F. Gillard, M. N. Mavrogordato, I. Sinclair and S. M. Spearing, “Three-dimensional deformation mapping of Mode I interlaminar crack extension in particle-toughened interlayers,” *Acta Materialia,* vol. 103, pp. 63-70, 2015.

[16] R. Brault, A. Germaneau, J. C. Dupré, P. Doumalin, S. Mistou and M. Fazzini, “In-situ analysis of laminated composite materials by X-ray micro-computed tomography and digital volume correlation,” *Experimental Mechanics,* vol. 53, pp. 1143-1151, 2013.

[17] M. Palanca, L. Cristofolini, E. Dall’Ara, M. Curto, F. Innocente, V. Danesi and G. Tozzi, “Digital volume correlation can be used to estimate local strains in natural and augmented vertebrae: An organ-level study,” *Journal of Biomechanics,* vol. 49, no. 16, pp. 3882-3890, 2016.

[18] F. Gillard, R. P. Boardman, M. N. Mavrogordato, D. Hollis, I. Sinclair, F. Pierron and M. Browne, “The application of Digital Volume Correlation (DVC) to study the microstructural behaviour of trabecular bone during compression,” *Journal of the Mechanical Behavior of Biomedical Materials,* vol. 29, pp. 480-499, 2014.

[19] L. Liu and E. F. Morgan, “Accuracy and precision of digital volume correlation in quantifying displacements and strains in trabecular bone,” *Journal of Biomechanics,* vol. 40, no. 15, pp. 3516-3520, 2007.

[20] F. Pierron, S. A. McDonald, D. Hollis, J. Fu, P. J. Withers and A. Alderson, “Comparison of the mechanical behaviour of standard and auxetic foams by X-ray computed tomography and digital volume correlation,” *Strain,* vol. 49, no. 6, pp. 467-482, 2013.

[21] S. P. Timoshenko, Strength of materials. Part 1 – Elementary theory and problems, 2nd ed., New York City, NY, USA: David Van Nostrand Company Inc., 1940, pp. 88-97.

[22] Toray Industries Inc., *Toray Composite Materials,* Tokyo, Japan, 2019.

[23] US Research Nanomaterials Inc., *Micron Powders,* Houston, TX, USA, 2019.

[24] Sicomin, *Epoxy Systems,* Châteauneuf-les-Martigues, France, 2018.

[25] Ultrawave Ltd., *U100/U100H Ultrasonic Cleaning Bath,* Cardiff, UK, 2017.

[26] ASTM International, “Standard test method for flexural properties of polymer matrix composite materials: D 7264/D 7264M – 07,” West Conshohocken, PA, USA, 2007.

[27] Carl Zeiss AG, *Xradia 510 Versa,* Oberkochen, Germany, 2018.

[28] LaVision GmbH, *DaVis v10 StrainMaster (Digital Volume Correlation),* Göttingen, Germany, 2018.

[29] M. P. Fernández, A. H. Barber, G. W. Blunn and G. Tozzi, “Optimization of digital volume correlation computation in SR-microCT images of trabecular bone and bone-biomaterial systems,” *Journal of Microscopy,* vol. 272, no. 3, pp. 213-228, 2018.

[30] K. Madi, G. Tozzi, Q. H. Zhang, J. Tong, A. Cossey, A. Au, D. Hollis and F. Hild, “Computation of full-field displacements in a scaffold implant using digital volume correlation and finite element analysis,” *Medical Engineering & Physics,* vol. 35, no. 9, pp. 1298-1312, 2013.

[31] E. M. C. Jones and M. A. Iadicola, “A good practices guide for digital image correlation,” International Digital Image Correlation Society (iDICs), 2018.

[32] M. Palanca, G. Tozzi, L. Cristofolini, M. Viceconti and E. Dall'Ara, “Three-dimensional local measurements of bone strain and displacement: Comparison of three digital volume correlation approaches,” *Journal of Biomedical Engineering,* vol. 137, no. 7, pp. 1-14, 2015.

[33] O. Jiroušek, I. Jandejsek and D. Vavřík, “Evaluation of strain field in microstructures using micro-CT and digital volume correlation,” in *The 12th International Workshop on Radiation Imaging Detectors*, Cambridge, UK, 2010.

[34] A. Buljac, T. Taillandier-Thomas, L. Helfen, T. F. Morgeneyer and F. Hild, “Evaluation of measurement uncertainties of digital volume correlation applied to laminography data,” *The Journal of Strain Analysis,* vol. 53, no. 2, pp. 49-65, 2018.

[35] GOM GmbH, *GOM Inspect 2018,* Braunschweig, Germany, 2018.

[36] J. Schindelin, I. Arganda-Carreras, E. Frise, V. Kaynig, M. Longair, T. Pietzsch, S. Preibisch, C. Rueden, S. Saalfeld, B. Schmid, J.-Y. Tinevez, D. J. White, V. Hartenstein, K. Eliceiri, P. Tomancak and A. Cardona, “Fiji: An open-source platform for biological-image analysis,” *Nature Methods,* vol. 9, pp. 676-682, 2012.

[37] Volume Graphics GmbH, *VGSTUDIO Max v2.1,* Heidelberg, Germany, 2011.

[38] Dassault Systèmes SE, *SOLIDWORKS,* Vélizy-Villacoublay, France, 2015.

[39] S. Yaofeng and J. H. L. Pang, “Study of optimal subset size in digital image correlation of speckle pattern images,” *Optics and Lasers in Engineering,* vol. 45, no. 9, pp. 967-974, 2007.

[40] Tampere University of Applied Sciences (TAMK), “Digital Image Correlation – IMPACT Multiscale Materials Testing Research Group,” [Online]. Available: https://research.tuni.fi/impact/equipment/digital-image-correlation/. [Accessed 30 01 2020].

Chapter 6 Fibre-direction strain measurement in a composite ply under quasi-static tensile loading using Digital Volume Correlation and *in situ* Synchrotron Radiation Computed Tomography

Digital Volume Correlation, in concert with *in situ* Synchrotron Radiation Computed Tomography, has been applied to Carbon-Fibre Reinforced Polymers under quasi-static tensile loading. DVC represents a relatively novel tool for quantifying full-field volumetric displacements and implicit strain fields. The highly anisotropic and somewhat regular/self-similar microstructures found in well-aligned unidirectional materials at high fibre volume fractions are shown to be intrinsically challenging for DVC, especially along the fibre direction. To permit the application of DVC to displacement and/or strain measurements parallel to the fibre orientation, the matrix was doped with a sparse population of sub-micrometre barium titanate particles to act as displacement trackers (*i.e.* fiducial markers). For the novel materials systems developed, measurement noise is considered along with the spatial filtering intrinsic to DVC data processing. Compared to volume images acquired through Micro-focus Computed Tomography, hold-at-load artefacts are mitigated through scan times on the order of seconds using SRCT, as opposed to hours. Instances of individually fractured fibres evolving into clusters of breaks are presented, together with the associated strain redistribution (imaged at a voxel resolution of 0.65 µm). It is shown that the distance over which strain is recovered in the broken fibres not only increases with the applied force, but also with the number of broken fibres, delineating aspects of the load shedding phenomenon. The study demonstrates that unprecedented, mechanistically-consistent three-dimensional strain measurements may be made in relation to fibre failure events, that can be used to validate micromechanical models for predicting UD tensile failure. This work presents the first application of DVC to the SRCT imaging of failure in CFRPs, achieving significantly higher resolution than reported previously within the literature. This chapter (excluding Appendix D and E) has been reprinted from *Composites Part A,* vol. 137, no. 105935, 2020, E. Schöberl, C. Breite, A. Melnikov, Y. Swolfs, M. N. Mavrogordato, I. Sinclair and S. M. Spearing, “Fibre-direction strain measurement in a composite ply under quasi-static tensile loading using digital volume correlation and in situ synchrotron radiation computed tomography”.

6.1 Introduction

Carbon-Fibre Reinforced Polymers are increasingly used in transport applications due to their desirable strength- and stiffness-to-weight properties. The tensile failure of these materials involves a complex sequence of interacting mechanisms, including fibre-matrix interfacial debonding, matrix microcracking, delamination, fibre fracture, sub-laminate and ply failure. The interactions between the different mechanisms make it challenging to predict accurately the structural performance of composite materials. While the different mechanisms are important for the damage development and property degradation, the ultimate tensile failure of composite parts is generally recognised to be dominated by fibre fracture within 0° plies. Understanding the fibre fracture process is thus of fundamental importance for a complete interpretation of CFRP tensile failure, alongside the various other forms of composite damage that exist.

A key concept in longitudinal tensile failure of unidirectional composites is that fibre strength is a stochastic quantity [1], which is typically presumed to follow a Weibull distribution [2]. Therefore, fibre breaks are initially spatially distributed, and accumulate with increasing load. Around individual fibre breaks, the surrounding matrix transfers load, primarily in shear, into adjacent fibres [3-8]. This stress transfer mechanism also reintroduces stress into the broken fibre, and the length over which this process occurs is commonly referred to as the 'ineffective length'. More specifically, Rosen [9] defined the ineffective length as twice the fibre length over which 90 % of strain recovery occurs. Complementary to this, is the 'overload length'; indicating the region over which the stress in immediately neighbouring filaments is increased. Nearby intact fibres will, therefore, carry local stress concentrations, but the magnitude decreases with increasing distance from the fibre break [10]. The stress (or strain) concentration factors, defined as the relative change in the average stress (or strain) over the cross-section of an adjacent fibre due to the presence of a fibre break, is expected to increase the probability of fracture in these intact fibres [6, 10-13]. With ongoing loading, this increased failure probability may lead to the development of clusters of breaks [13-19] which further increases the SCFs in the neighbouring fibres. Catastrophic failure is assumed to occur when sufficient neighbouring fibres are broken, and a critical cluster is formed, which grows in an unstable, self-sustaining manner [1, 10, 17, 19]. Therefore, apart from the fibre strength, the stress and strain redistribution around fibre breaks and the length over which it occurs becomes a key controlling parameter in predicting the tensile failure of UD composites. Raman spectroscopy [20-23] represents a useful approach to perform such experimental measurements, however, it is limited to surface measurements, and has often been performed on model microcomposites with a sparse distribution of fibres, which may not exhibit fully-representative stress/strain states. Characterizing volumetric material deformation and damage in the bulk of practical specimens with realistic fibre volume fractions thus becomes highly desirable. However, this is challenging, due to the opacity of the CFRPs, the three-dimensional multi-scale nature of damage, the coupling of multiple micromechanisms and

the difficulty of distinguishing damage caused by cutting and polishing artefacts associated with metallographic sectioning [24].

A significant step forward has been achieved in recent years by the use of X-ray Computed Tomography combined with *in situ* loading to identify detailed sequences of damage accumulation down to fibre-level, in 3D, within the bulk of real engineering materials under load [13, 14, 18, 19, 25, 26]. It is then interesting to consider the use of Digital Volume Correlation for a strain-based quantification of the local deformation surrounding fibre break sites in representative materials subjected to a continuously applied load. An extension of the white-light illumination, two-dimensional Digital Image Correlation technique [27], DVC is a relatively novel tool capable of quantifying the internal microstructural response of the material between different load states, by extracting essential deformation and failure parameters such as local displacements and strains [24, 28]. Whilst not addressed here, applications to other aspects of composite micro- and mesomechanics may be envisaged, such as quantifying the influences of porosity or ply drops on local load paths/partitioning.

For X-ray CT, the noise and sensitivity of the DVC measurements rely on several factors. These include imaging hardware (beam stability, flux, energy, exposure, propagation distance, voxel size), the nature of the material type under investigation (sample shape, size, phase density distribution, trackable features) and imaging results (contrast-to-noise ratio, spatial resolution, artefacts), all of which influence the quality of the image volumes obtained [24, 29, 30]. Consequently, an assessment of the reliability and accuracy of the measurements is required through validation experiments for the imaging conditions in question, where the displacement and/or strain field is known *a priori* [24, 29]. In this context, Schöberl *et al.* [24] have reported a four-point flexural validation study, in which it was demonstrated that the DVC measurement of the bending strain gradient through the thickness of the specimen was in good agreement with the Euler-Bernoulli beam theory [31] for the current material (see **Chapter 5**). Additionally, the authors have undertaken error estimation by conducting two zero-strain pair analyses: a static repeat scan and a rigid body displacement assessment.

The underlying volume images for DVC are typically acquired through Micro-focus Computed Tomography [24, 29, 30, 32-39] or less frequently through Synchrotron Radiation Computed Tomography [37, 40, 41]. While both acquisition methods can deliver usable sub-micrometre voxel resolution levels, superior scans are commonly achieved through SRCT (the beam is brighter, monochromatic, coherent and parallel, with a higher level of phase contrast and avoids beam hardening artefacts [42]). Furthermore, µCT is characterised by significantly longer scanning times, on the order of hours, as opposed to seconds for SRCT [42], particularly at sub-micrometre resolutions. This may be expected to promote hold-at-load artefacts near composite failure,

whereby the viscoelastic response of the polymer matrix may result in time-dependent strain variation and subsequent failure of UD composites [43-46].

Unlike many monolithic materials (*e.g.* Al-Si alloys), which contain well-distributed, small inclusions which provide X-ray contrast [37], the highly anisotropic and somewhat regular/self-similar microstructures found in conventional unidirectional CFRPs at high fibre volume fractions are intrinsically challenging for DVC, particularly along the fibre direction. The cylindrical structure and relatively featureless surfaces of the filaments lack a well-defined, trackable contrast pattern along the fibre direction, leading to poor image correlation, and correspondingly inaccurate displacement estimates in this direction within a given ply [40]. Following a similar approach to that taken by Brault *et al.* [34] to generate individual features unique to a particular sub-set, the authors have doped the matrix with a sparse population of particles (but significantly smaller, at 400 nm *vs.* 150 µm used in [34]) to act as displacement trackers – *i.e.* fiducial markers [24]. High-resolution, fibre-level strain distributions are specifically addressed (imaged at a voxel resolution of 0.65 µm), as opposed to the ply-level studies in [34]. The fraction of fiducial markers is selected such that any potential impact on the mechanical performance of the material is mitigated. Previous studies have shown that for low particle concentrations, the mechanical properties of thermosetting matrices can be largely preserved [47, 48]. In turn, by comparing the micromechanical behaviour of the particle-adapted material alongside its particle-free counterpart, it was demonstrated elsewhere [49] that the response of the newly developed CFRP is consistent with standard production materials suggesting its suitability as a model system for mechanistic investigations (see **Chapter 4**).

Using this approach, *in situ* SRCT tensile testing and micromechanical strain mapping results are reported for the regions immediately surrounding fibre breaks. A complex load shedding phenomenon is identified at fibre-level, whereby the distance over which strain is recovered in the broken fibre not only increases with the applied force, but also with the number of broken fibres. For the first time, key 3D strain measurements around fibre breaks have been made that can be compared to micromechanical Finite Element models. The work is intended to support material development and promote the understanding of the fundamental aspects of unidirectional composite tensile failure.

6.2 Materials and methods

6.2.1 Material manufacturing

Cross-ply laminates, with a $[90/0]_s$ layup, thickness of ~1 mm and a specimen fibre volume fraction *'V_f'* of ~55 % were manufactured by drum winding at KU Leuven, Belgium. A PAN-based 12K TORAYCA T700SC-50C (Toray Industries Inc., Tokyo, Japan [50]) non-twisted tow was used, with a 7 µm nominal fibre diameter.

To create microstructural fiducial patterns for the application of DVC, the resin was filled with commercially available tetragonal $BaTiO_3$ particles, nominal mean size of 400 nm and approximately spherical shape (US Research Nanomaterials Inc., Houston, TX, USA [51]). This property combination was selected following an extensive µCT-based qualitative assessment on a range of possible fiducial compositions (Al, Al_2O_3, SiC, SiO_2, MgO, TiC, TiO_2, $BaCO_3$, $BaTiO_3$, Cu and Bi_2O_3), mean particle sizes (300 nm to 800 nm) and concentrations (0.25 wt. % to 15 wt. % of the resin). From this test matrix, $BaTiO_3$ particles were found to offer the most favourable compromise between contrast in CT images (high attenuation coefficient), and the ability to obtain a homogeneous distribution in 3D space with sufficient particle compactness for local DVC analyses. The particles were dispersed in a SiPreg SR 8500/KTA 313 dual-component epoxy (Sicomin, Châteauneuf-les-Martigues, France [52]) using a combination of high-shear mixing and heated ultra-sonication (U100H bath, Ultrawave Ltd., Cardiff, UK [53]). No specific treatment was applied to the particle surfaces. To remove entrapped air, the thermosetting mixture was degassed for 10 minutes at ambient temperature. The amount of resin used was 150 g, with 31.5 g of hardener, following the manufacturer's specified mixing ratio of 100/21 (by weight). The $BaTiO_3$ fraction was set at 7.5 wt. % of the resin, equivalent to ~1.44 vol. %. A nominal 25 % tow overlap was targeted during the winding process. A maximum spool tension of 0.12 lb (54.43 g) was applied. To control the volume fraction of the matrix, following impregnation, the tow was passed through a metering die with an orifice slot of 0.2 mm × 9 mm. The temperature of the tow spreader and final guide roller were set to 50°C. The fibre sizing was left intact. For a schematic diagram of the manufacturing setup, the reader is referred to **Figure 5-1**. The drum winding process resulted in uniaxial prepreg tape, ~0.25 mm × ~350 mm × ~1900 mm, which was cut and laid up to produce the desired $[90/0]_s$ cross-ply layup. The prepreg stack was cured in an autoclave for 280 minutes at 0.5 MPa (5 bar) and maximum 120°C. To minimize void content in the cured material, a vacuum of ~0.07 MPa (~0.7 bar) was maintained throughout the autoclave process.

6.2.2 Specimen geometry and loading

Double-edge notched specimens were machined via water-jet cutting. The specimen geometry is based on previous work of Swolfs, Scott, Garcea, Rosini, Moffat, Wright and co-workers [13-15, 18, 19, 25, 26], although here the total specimen length was increased to 100 mm, as reported in [19]. This was performed to (a) minimize the risk of pull-out from the central 0˚ portion of the gauge region, and (b) to accommodate a smaller X-ray propagation distance, by providing sufficient clearance between the top of the loading rig and detector optics. Once cut, the T-shaped sections of the specimens were tabbed with 1.5 mm thick aluminium sheet. Aerospace-grade adhesive, Scotch-Weld EC-9323 B/A (3M Company, Maplewood, MN, USA [54]), was used to bond the tabs onto the CFRP surface. Adhesive curing was performed at 65°C for 2 hrs according to the manufacturer's recommendations. The key specimen dimensions, the tabbed assembly and the highly contrasted microstructure were collectively shown in **Figure 4-3**. Tensile loading was performed *in situ* by using a modified CT5000 single-actuator electromechanical rig (Deben Ltd., Woolpit, Suffolk, UK [55]) retrofitted with a Poly(Methyl Methacrylate) – PMMA reaction tube (25 mm outer diameter and 3 mm wall thickness). Using position control to ameliorate potential artefacts during scanning, loading was performed at a displacement rate of 0.2 mm/min up to a prescribed load point. Typically, ten load steps were applied for stepwise *in situ* measurements, with somewhat smaller load increments being made at high loads, close to failure. This was applied on the basis of the work of Scott *et al.* [14], where fibre breaks have been confirmed to accumulate exponentially with applied stress, with the majority of breaks occurring above ~90 % UTS. To alleviate potential effects of specimen relaxation under load (and thus potential movement during CT acquisition), scanning was carried out with a slight reduction in load (~10 %) from the most recent peak level applied. It is also worth stating that at the observable scale, the fact that the fibres are in a cross-ply has no effect on the fibre-scale stress transfer characteristics, as shown in [13] and [14]. That is because splitting and delamination occurs, which essentially creates a local UD composite in the notched region of the specimen after a certain strain (typically ~70% UTS [14]). Noise and sensitivity assessment scans (static repeat and rigid body displacement) for the DVC technique were conducted with a small applied preload, max. 75 N, to ensure that the specimen did not move during acquisition and/or manipulator stage translation.

6.2.3 Synchrotron Radiation Computed Tomography

In situ SRCT measurements were performed at the ID19 beamline, European Synchrotron Radiation Facility, Grenoble, France. A 2560 × 2160-pixel detector was used, with a chip size of 6.5 µm. Scans, with a monochromatic beam, were conducted at a 10 × magnification, yielding a voxel size of 0.65 µm and a field of view of ∼1.66 mm × ∼1.40 mm × ∼1.66 mm. The beam energy was set to 19 keV, with 2996 projections acquired per scan, at an exposure of 25 ms, resulting in ∼75 s per tomograph. Acquisition was performed over a rotation of 180°. A propagation distance of ∼30 mm was used, while the data was reconstructed using conventional absorption-based FBP.

6.2.4 Digital Volume Correlation

Digital Volume Correlation was performed using the commercial DaVis v10 software with StrainMaster DVC package (LaVision GmbH, Göttingen, Germany [56]). StrainMaster employs a correlation criterion operating on the grey-level intensity values of 3D images [41]. In essence, the measurement volume is divided into smaller sub-sets, and the contrast pattern within each sub-set is then tracked from the reference to the deformed state independently (local approach [33]) as a discrete function of the grey-levels [41]. A cross-correlation function is employed to measure the conservation of the grey-levels between the original and displaced sub-set, with the position determined for which the correlation is closest to unity [24, 30, 40, 41]. Analogous to DIC, the correlation coefficient can be used to evaluate the similitude between the sub-sets [24, 30]. A coefficient of 1.0 implies that the sub-sets are completely related, whereas a value of 0 indicates that they are completely unrelated [24, 30].

The correlation process between two adjacent volumes ‘A’ and ‘B’ was illustrated schematically in **Figure 5-6**, which is complemented by the workflow diagram in **Figure 6-1**. The associated shift (3D displacement) is given by the vector connecting the sub-set centroids between the deformation states [56]. Finally, 3D strain field estimation may be carried out through a centred finite difference to determine the numerical derivatives of the vector field [24, 30, 35, 41, 57].

Recognition of matching sub-sets between the deformation states was performed within the DVC software either via a Fast Fourier Transform implementation, or via a multi-step strategy, whereby a global pre-shift was computed through the ‘FFT’ approach, followed by Direct Correlation. Both implementations use an equivalent of a piece-wise linear shape function for the reference-deformed mapping, a normalized form of the cross-correlation function to quantify the similarity between the images, and support a multi-pass approach [30, 36, 41, 56]. A trilinear interpolation is used in ‘FFT’, and a third-order spline interpolation in ‘DC’, to compute the greyscale intensities of each displayed voxel at non-integer positions (*i.e.* sub-voxel

measurements) [36]. 'DC' also permits the use of a weighted window within sub-sets, an option which was implemented during the final iteration step of correlation (dual-pass). This results in a potentially improved representation of the local displacement field, as the voxels in the vicinity of the sub-set centroid carry more weight than voxels located at the edge of the sub-set. While the weighted window extends over two times the sub-set size, the implementation ensures that the effective spatial resolution is similar to that of a conventional sub-set, for which an arithmetic average is implemented [56]. As isotropic sub-sets were used throughout all present analyses, a specific notation is introduced, whereby the specified size of a sub-set is equivalent to a sub-set with its characteristic length cubed (*i.e.* sub-set size of N voxels is equivalent to a sub-set size with $N \times N \times N$ voxels or N^3 voxels). More information on LaVision's DVC implementation can be found in [30] for the 'FFT' and in [41] for the 'DC' method and/or by consulting the software guidelines [56].

The 'DC' approach can maximise the efficiency of using the DVC algorithm, as the search for the corresponding sub-set in the deformed state was confined to a shift equal to the search radius. Additionally, in 'DC' the coarse displacements, captured by using larger sub-sets, were used as a predictor vector field for the subsequent and refined iterations, based on smaller sub-sets. Although the latter implementation is also possible using 'FFT', the additional steps can outweigh the faster processing times associated with the frequency domain. Following a comprehensive parametric study and algorithm optimization process, respectively, it was established that 'DC' yields generally superior performance in terms of noise and sensitivity. A similar behaviour is also reported by Palanca *et al.* [36]. As a result, the Direct Correlation method was used throughout this work.

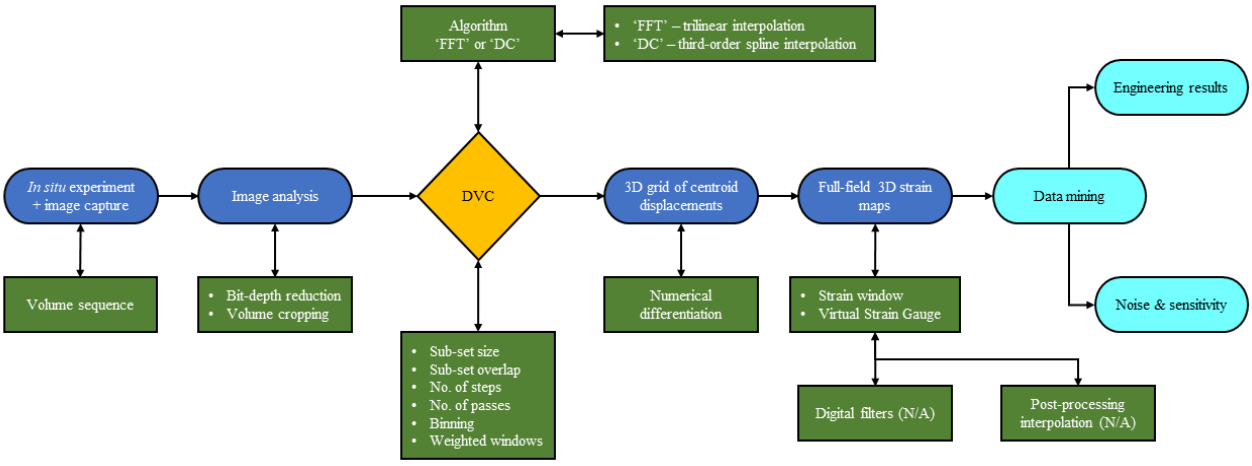

Figure 6-1 – Workflow diagram of the DVC process.

To moderate computational costs, two further strategies were used. First, a 32-bit floating point to 8-bit integer conversion was performed for the voxel data. While the correlation results will always be imaging configuration-dependent, Buljac *et al.* [58] have shown that histogram (grey-level) rescaling has negligible impact on the DVC error. Similarly, the bit-depth of volumes was also reduced in [40] to achieve faster

processing times. Secondly, for the Direct Correlation method, the search radius was incrementally reduced from 8 to 6 and ultimately 4 voxels between the deformed and undeformed state. The latter value corresponds to a typical fibre-break opening (based on a 0.65 µm voxel size) in a T700SC-50C/epoxy-based cross-ply, implying that in the absence of fractured fibres and/or matrix microcracks within the 0° plies, the elastic response of the microstructure cannot exceed the aforementioned displacement level. Nonetheless, for very small sub-set sizes and large clusters of breaks, a higher search radius may be required to fully characterise the local deformation.

To increase sampling, the overlap between the neighbouring sub-sets was set to 75 %. This represents a higher sampling rate than that previously reported in [24, 30, 35, 40], for which a 50 % sub-set overlap was used. Correlation was carried out relative-to-first, *i.e.* each volume was correlated with the initial undeformed scan. The relevant settings used are detailed in **Table 6-1.**

Final sub-set size (voxels)	FFT pre-shift (voxels)	Step 1 (voxels)	Step 2 (voxels)	Step 3 (voxels)	No. of passes steps 1-3	Voxel binning step 1	Voxel binning step 2	Voxel binning step 3
32	64	64	40	32	2	4 × 4 × 4	2 × 2 × 2	NONE
40	80	80	48	40				
48	80	80	56	48				
52	80	80	56	52				
60	96	96	64	60				
72	128	128	88	72				
80	128	128	96	80				
100	144	144	112	100				
120	176	176	136	120				

Table 6-1 – Summary of 'DC' settings used in the multi-step, multi-pass approach (75 % sub-set overlap). Weighted windows used in the last iteration step (dual-pass).

To assess the noise and sensitivity associated with the DVC technique, conventional stationary and rigid body displacement tests were performed. DVC was applied to cropped volumes from the 0° plies, measuring 600 × 600 × 600 voxels. Gross rigid body displacements were initially removed by carefully cropping the volumes with a voxel accuracy. As previously indicated in **Figure 4-3**, the Y-axis indicates the fibre direction, the X-axis is in-plane orthogonal to the fibre direction, while the Z-axis corresponds to the out-of-plane direction. Volumes were carefully checked against the presence of any significant CT artefacts (*e.g.* rings, streaks) and/or variations in sharpness within the visible region.

As summarized in **Table 6-2**, the number of DVC 'slices' (*i.e.* planes composed of volumetric sub-sets, one sub-set thick) is computed by dividing the height of the cropped volume (*e.g.* 600 voxels) by the step size used in the correlation algorithm. Such an example is illustrated in **Figure 6-2**, where a stack comprising of 33 DVC slices can be observed. As the in-plane voxel dimensions are equivalent (*i.e.* 600 × 600 voxels), the same number of DVC data points is obtained in-plane as per the slices in **Table 6-2**.

Sub-sets positioned at the perimeter of the grid (XY-plane) as well as the planes of sub-sets located at the top ends of the stack (Z-direction) must be treated with special consideration (*e.g.* masked or truncated) if displacement vectors are computed, but not 100 % satisfied from a voxel validity perspective – *i.e.* notional sub-sets that overlap with the edge, due to cropping between deformation states and/or large rigid body displacements, potentially causing the correlated data to be noisier or incomplete [24, 35].

Sub-set size (voxels)	Step size (voxels)	No. of DVC slices (Z-direction) *	No. of raw data slices per DVC slice
32	8	75	8
52	13	46	13
60	15	40	15
72	18	33	18

*Table 6-2 – Number of DVC slices (planes of sub-sets) for a given sub-set size with 75 % overlap, and the corresponding number of raw data slices per DVC slice. *Nomenclature: DVC slice numbering starts with 0. Applicable to a cropped volume of 600 × 600 × 600 voxels.*

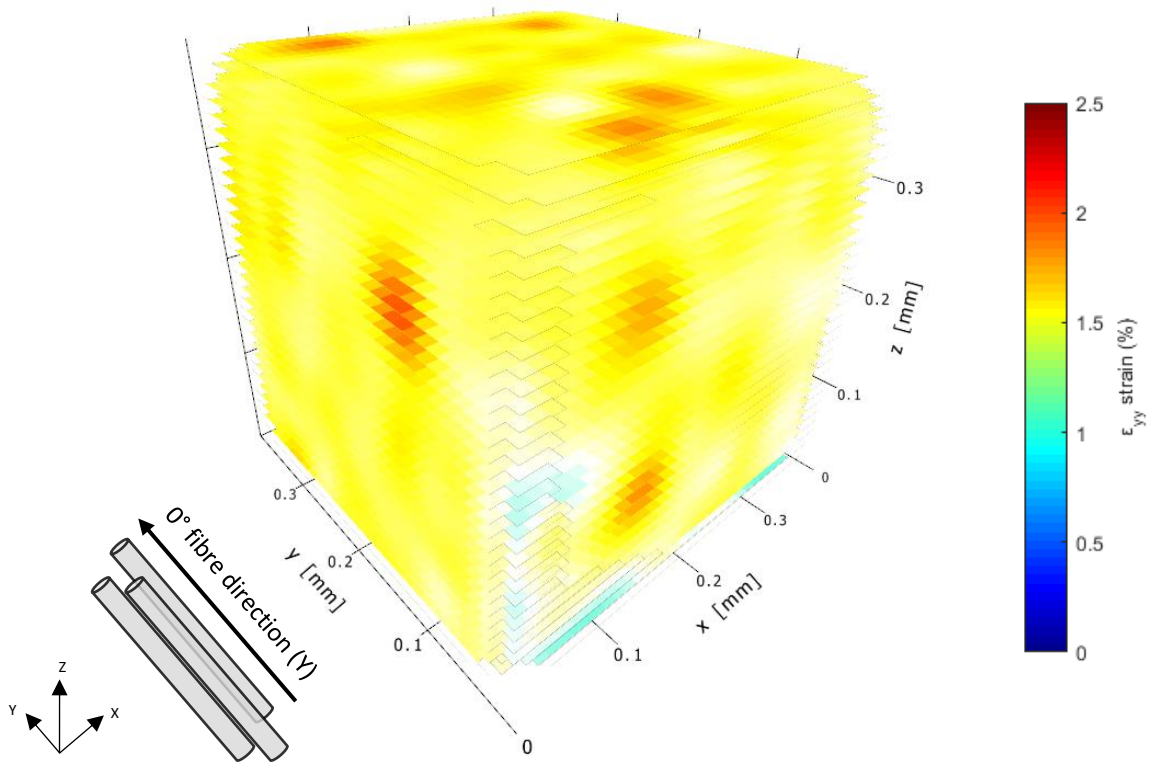

Figure 6-2 – Example stack comprised of 33 DVC slices in the Z-direction ('Z=0' to 'Z=32'), applicable to a sub-set size of 72 voxels with 75 % overlap, loaded to 950 N. In turn, each DVC slice (i.e. plane of sub-sets, one volumetric sub-set thick) is representative for 18 raw CT data slices. Raw data volumes cropped from the 0° plies: 600 × 600 × 600 voxels. Y-axis indicates the fibre direction. X-axis is in-plane orthogonal to the fibre direction, while the Z-axis corresponds to the out-of-plane direction.

A common post-processing aspect of strain computation via DVC (and related DIC algorithms) is the Virtual Strain Gauge (VSG). The VSG defines the local (effective) region of the image that is used for strain calculation at a specific location and is volumetrically analogous to the physical area that a foil strain gauge covers [57]. Additionally, the VSG may also be considered to be a smoothing/noise-removal strategy as it represents a higher-order filtering stage for the computed strains. More details about the application of VSGs can be found in [57].

As noted in **Section 5.2.4**, several key variables affect the VSG size, such as the characteristic length (size) of the: strain window *(L_{SW})*, step *(L_{ST})* and sub-set *(L_{SS})*. As the characteristic length *(L_{VSG})* of the VSG decreases, the noise typically increases, as the amount of global spatial filtering decreases. Similarly, as the size of the VSG decreases, the apparent magnitude of local strain peaks along a line cut (extracted region of highest strain gradient) may be generally expected to increase [57]. In this chapter, a VSG with an L_{SW} of 3 × 3 × 3 neighbouring vectors was used, unless otherwise stated (**Figure 6-3**). The application of a VSG implies that the effective volumetric gauge length over which each strain value is computed is larger than the size of a single sub-set [24], with **Equation 5-1** describing how the characteristic length of the VSG scales with the aforementioned parameters [57].

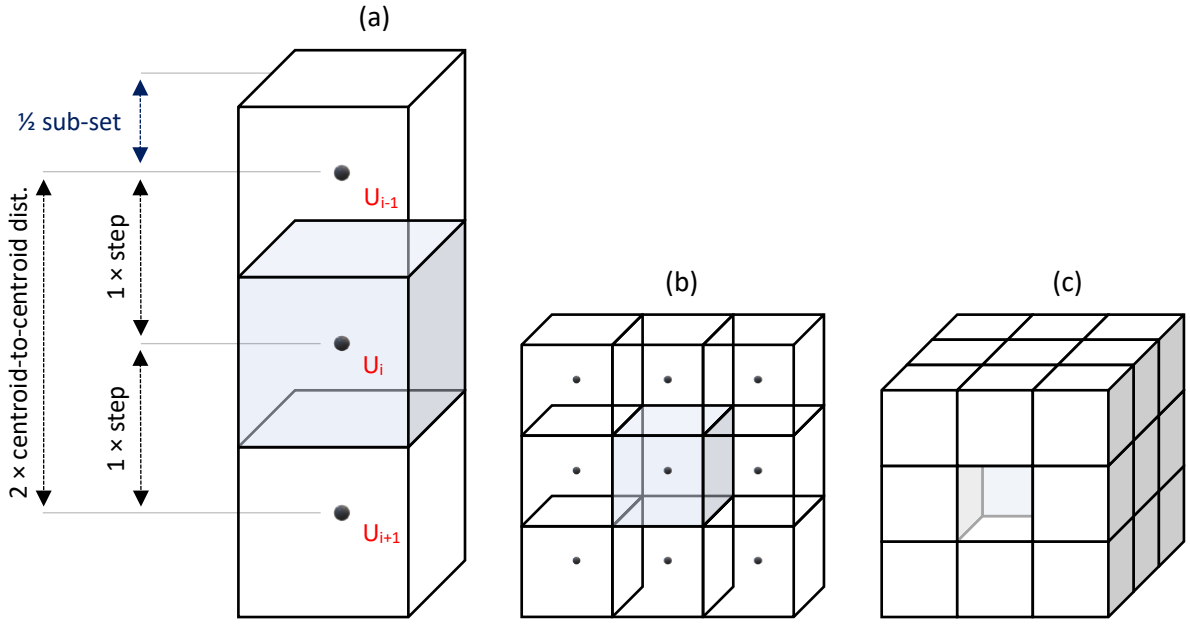

Figure 6-3 – Schematic illustration of different VSGs , depending on the strain window size (L_{SW}) used: (a) anisotropic – L_{SW} of 1 × 3 × 1 vectors, (b) anisotropic – L_{SW} of 3 × 3 × 1 vectors, and (c) isotropic – L_{SW} of 3 × 3 × 3 vectors. Each cube represents a sub-set and its associated centroid, with a grid spacing of one step. Sub-sets are not overlapped here for simplicity reasons. Strain window size of 1 × 3 × 1 emphasises smoothing along the fibre direction, 3 × 3 × 1 in the fibre layup plane, and 3 × 3 × 3 smooths isotopically. Higher-order strain window sizes are possible, but this can lead to an over-smoothing of the strains computed (i.e. reduction in signal-to-noise ratio).

6.3 Results and discussion

6.3.1 Noise and sensitivity

As noted above, to evaluate quantitatively the performance of the DVC technique, noise studies were conducted. The assessment involves two studies, with the approach being similar to that of Schöberl *et al.* [24], Gillard *et al.* [30], Pierron *et al.* [35] and Borstnar *et al.* [40]. The first is a stationary analysis, which involves repeated scanning of the same specimen without any alterations in load (zero displacement, zero strain) or CT parameters (exposure, number of projections, beam energy, current or propagation distance). The purpose of this static noise test is to quantify the intrinsic scanning noise and bias. The second study is a rigid body displacement in which the specimen was moved *in situ* by a predefined displacement, parallel to the fibre direction (Y-axis), using the manipulator stage. CT acquisition was performed between each specimen position to evaluate the magnitude of the displacement vector fields and to assess any interpolation and/or system errors associated with the DVC approach [40]. For a detailed analysis, the reader may consult **Appendix A** to **E**.

6.3.2 Strain field assessment at single fibre breaks

As stated in **Section 6.2.4**, a key aspect of the DVC technique is that the resulting measurements must be regarded as a spatially filtered representation of the real local strains within the material. As such, the deformation captured is affected and/or limited by the volume that is used for strain calculation at a specific location within the material. Since the interest here lies in capturing the strain field longitudinally from a fibre break, a suitable approach is to create a computational domain that isolates the fibre break opening. The rationale is that there can be no strains where there is no material [40] (*e.g.* fibre break openings, cracks). Additionally, no meaningful correlation can be performed between 'non-material' at a break site, and the original material microstructure. An algorithmic mask (proprietary [56]) was thus applied to the cropped data, whereby all voxels with a grey-level below a threshold corresponding to the break opening (50/255) have been excluded from the computational domain. Therefore, the values quoted in this section refer to the average strains derived from the sub-set centroid shifts, where only voxels exceeding the aforementioned grey-levels have been incorporated. The disadvantage of this technique is that voids are also masked, and thus, fail to assist the correlation algorithm. Nonetheless, the impact is considered negligible due to the low content of voids within the manufactured CFRP.

6.3.2.1 Strain transfer lengths

Figure 6-4 presents a representative measured strain map overlaid with the microstructure subjected to *in situ* loading at the 950 N load step. The FOV was centred on a singlet, labelled 'C'. A singlet is defined in this work as a non-interacting break, separated by at least ten fibre diameters longitudinally (Y) and two fibre diameters radially (X & Z), measured from the centre of the nearest neighbouring break.

To make best use of the spatial resolution attainable, correlation was performed with the smallest workable sub-set size of 32 voxels (20.8 µm) and 75 % overlap, yielding a step size of 8 voxels (5.2 µm). Similarly, to limit smoothing in the fibre direction, strain post-processing was performed with a strain window size of 1 × 3 × 1 vectors, resulting in a VSG size of 32 × 48 × 32 voxels. A conversion to physical units and/or equivalent fibre diameters is available in **Appendix C**.

The numerical data, based on centroid-to-centroid measurements, was extracted from the overlapped sub-sets best aligned with the centre of a fractured carbon-fibre. Longitudinally from the break plane, the DVC output yields two near-symmetrical and distinct strain regions – **Figure 6-4**: (1) an 'elevated strain length' measuring ∼16 µm – where the strain drops from the maximum recorded value of ∼4.85 % to ∼zero, and (2) a 'lower strain length' of ∼21 µm – where the strain gradually increases from ∼zero to the far-field measurement of ∼1.5 %. Combined, these strain transfer lengths may be identified with a 'recovery length' from one side of the break, with the 'full-recovery length' being approximatively twice this value.

Figure 6-5 presents a line plot of strain (ε_{yy}) from the bottom side of a break, where half of the 'full-recovery length' is differentiated as described above. The results are expanded in **Figure 6-6**, where a collection of measurements from eight identified singlets ('A' to 'H') is shown, with the strain data extracted from both sides of the break plane (*i.e.* 'full-recovery length'). Good consistency can be observed between the different measurements, where slight deviation from symmetry for some of the gradients may be attributed to measurement noise, microstructural variations, or somewhat different damage evolution mechanisms on opposite sides of the break plane. It is also worth noting that no correlation was found between the broken fibres and high concentration regions of particles.

Given the effective gauge length/volume of strain measurements, it is of course clear that apparent strains will be influenced by crack/break displacements. As such, the 'recovery length' computed via DVC does not follow a typical Cox [59] (shear-lag) profile, which predicts that the strain should fall to zero at the fibre ends. While this may be asserted for measurements that are strictly referred to fibres [10-12], it must be noted that the DVC-estimated strains reflect the spatial filtering associated with the technique. Remote from local discontinuities/cracks, microstructural anomalies and/or other sources of strain gradients, it may be expected that the Voigt [60] isostrain assumption applies to the material and the strains reported by DVC are a good

estimate of both fibre and matrix deformation; with the latter being the dominant contributor, as it contains the fiducial markers used to achieve reliable correlation (**Appendix A**). However, immediately adjacent to fibre breaks, steep strain gradients are expected, and may be influenced by the following mechanisms, or combinations thereof: (1) matrix plastic yielding [21-23], (2) fibre-matrix interfacial debonding (with slippage) [22, 23, 61-64], (3) matrix microcracking [64-67], and (4) fibre unloading and spring-back [3, 68-70]. The relative displacement of the edge-enhanced fibre ends [42] is also expected to contribute to the measured strain field.

Along with the matrix deformation, the local strain profile longitudinal from the broken fibre measured by DVC is, therefore, in fact a superposition of two profiles widely noted in the literature: (1) the 'ineffective length', which is widely defined in the modelling literature as twice the distance from the break plane over which the strain is recovered to a certain percentage in the broken fibre [9-13], and (2) the 'overload length' of the intact fibres associated with the length over which the stresses are increased due to the presence of a fibre break. The DVC-based 'lower strain length' is observed to follow the profile of the former, while the 'elevated strain length' may additionally encompass the 'overload length', or twice the distance between the break plane and the plane at which the intact fibre has an SCF of 0 % [10-13]. Progressing onwards from the 'recovery length', ∼37 µm away from the break plane, the deformations are likely to be entirely elastic.

It is, however, recognized that fibre-matrix interfacial debonding cannot be directly observed in the present experiment, nor in other state-of-the-art *in situ* SRCT works [13-15, 18, 19, 71]. The two debonded surfaces stay in close contact, making it impossible to detect them with CT at voxel resolutions of ∼0.65 µm [1]. Nonetheless, surface experiments (*e.g.* based on Raman spectroscopy [22, 23] and/or photoelasticity [61-64]) report that such damage mechanisms take place under specimen tensile loading, albeit in model microcomposites with a sparse fibre distribution. Whether the knowledge from microcomposites can be reliably transferred to macrocomposites containing bundles of fibres remains unknown [1].

Radially from the centre of the break plane, the strain transfer lengths are observed to fall-off incrementally. **Figure 6-7** presents the strain profile from singlet 'F', whereby the data was collected longitudinally from both sides of the break plane, with the measurements being repeated stepwise in the transverse direction (X). Beyond a radial distance of ∼26 µm or the equivalent of ∼four fibre diameters, it is observed that the strain gradients are significantly reduced, and the far-field strain reading of ∼1.5 % is reached. Although not shown here, owing to the 3D capabilities the data may also be interpreted in the out-of-plane direction (Z), where the strain distributions follow a very similar profile. This implies that the volume of material surrounding a single fibre break measures ∼52 µm × ∼74 µm × ∼52 µm, within which load shedding takes place, increasing the probability of fibre break (or cluster) development. Very similar results are found at each of the eight single fibre break sites investigated.

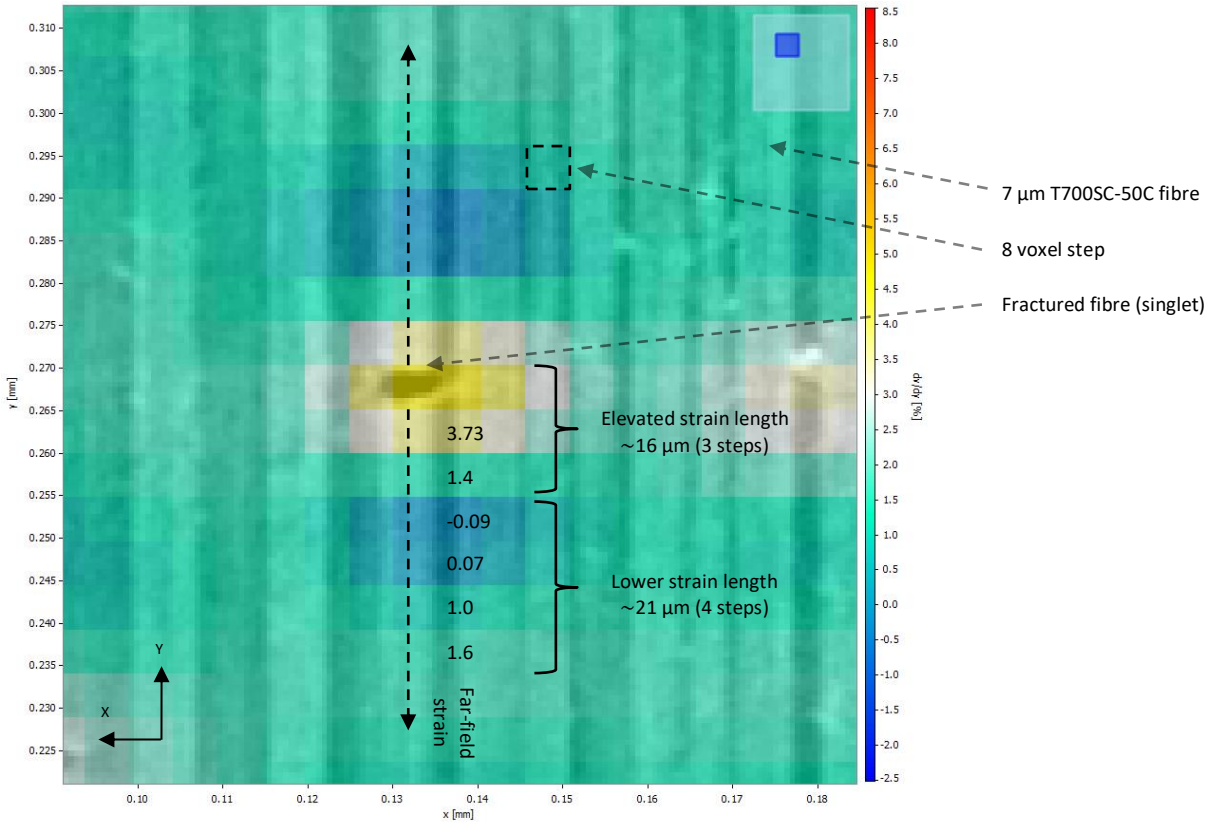

Figure 6-4 – DVC slice 'Z=23' illustrating the 'ε_{yy}' strain field surrounding singlet 'C'. Following correlation with a sub-set size of 32 voxels (75 % overlap) and strain post-processing with a strain window size of 1 × 3 × 1 vectors, the DVC output yields two near-symmetrical and distinct strain regions longitudinally from the break plane: (1) an 'elevated strain length' measuring ~16 µm, and (2) a 'lower strain length' of ~21 µm, after which the far-field strain level of ~1.5 % is attained. Microstructure subjected to in situ tensile loading of 950 N (98 % UTS), with acquisition performed at 855 N. FOV amounts to ~100 µm × ~100 µm. The measurement error corresponds to ~0.093 % (see Appendices).

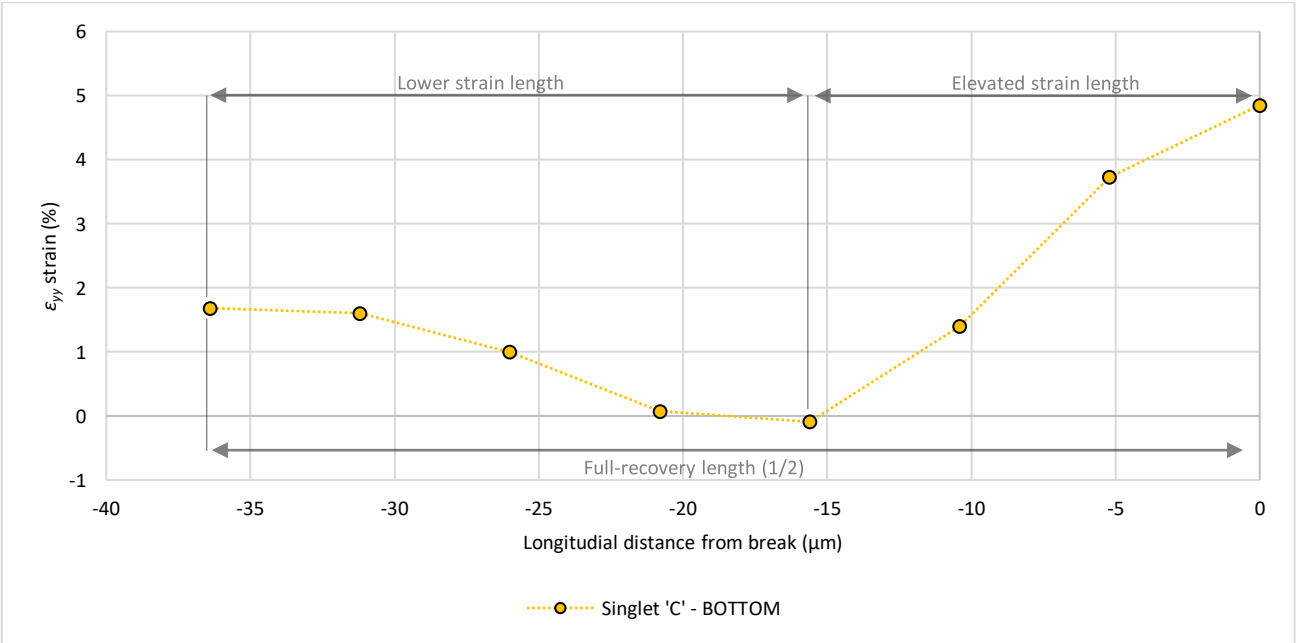

Figure 6-5 – Half of the 'full-recovery length' split into the two distinct strain regions, measured longitudinally from the bottom side of singlet 'C'. The measurement error corresponds to ~0.093 %.

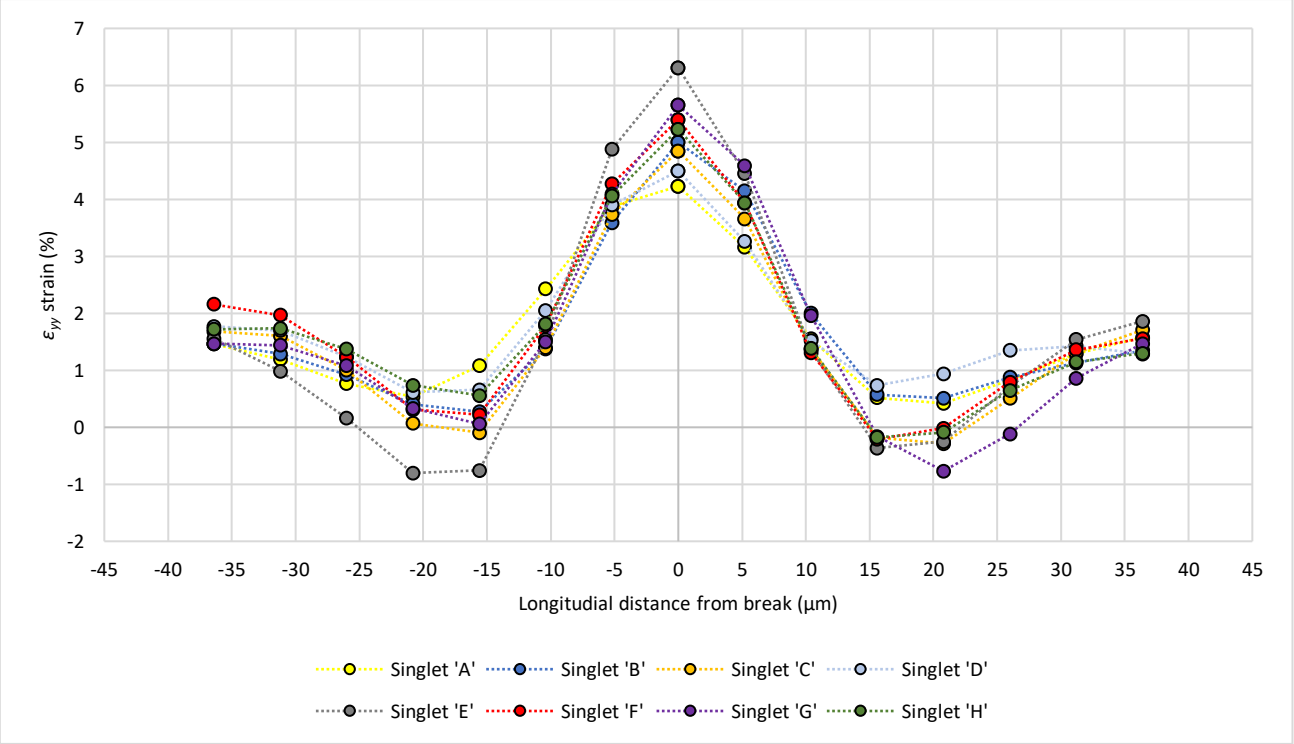

Figure 6-6 – Strain gradients (ε_{yy}) measured longitudinally from eight distinct singlets (both sides of the break plane). Microstructure subjected to in situ tensile loading of 950 N (98 % UTS), with acquisition performed at 855 N. The measurement error corresponds to ~0.093 %.

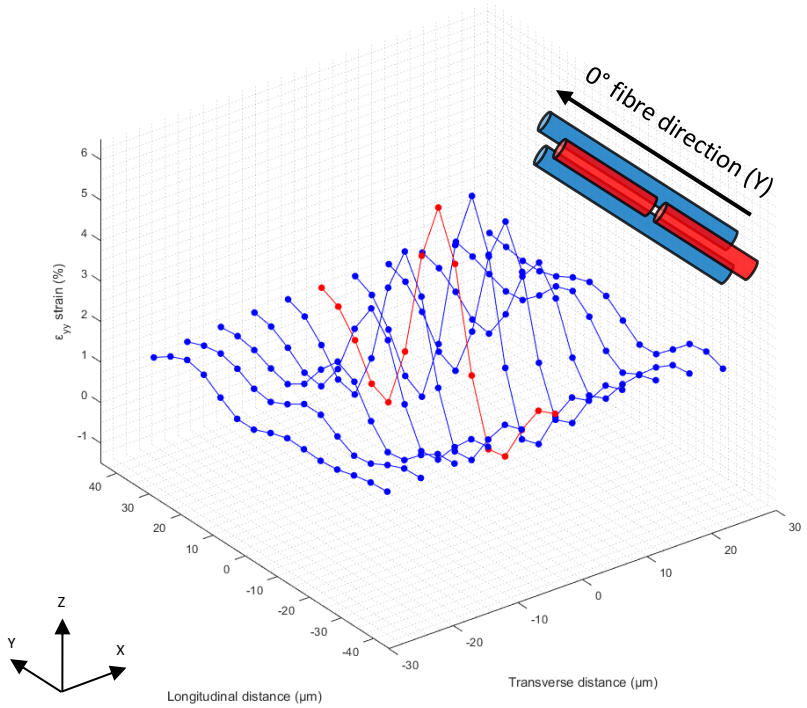

Figure 6-7 – Strain gradient (ε_{yy}) measured longitudinally from singlet 'F' (both sides of the break plane) and repeated stepwise in the transverse direction (X). The far-field strain level of ~1.5 % is attained beyond a radial distance of ~26 µm. Strain distribution indicated in red follows a longitudinal axis from the break plane. Results applicable to DVC slice 'Z=35' Microstructure subjected to in situ tensile loading of 950 N (98 % UTS), with acquisition performed at 855 N. The measurement error corresponds to ~0.093 %.

6.3.2.2 Effect of applied load on strain transfer lengths

Using Rosen's [9] definition of the ineffective length (twice the fibre length over which 90 % of strain recovery occurs), the effect of applied load on the DVC-based 'full-recovery length' is illustrated in **Figure 6-8 (a)**. The strain gradients are compared at the 950 N and 900 N load steps, respectively, with the effect discussed on an average basis. This strategy is employed to resolve the discrepancies from **Figure 6-6**. The eight singlets ('A' to 'H') identified in **Section 6.3.2.1** were used to compute a mean strain distribution at the last loading step, while four singlets could be traced back ('A', 'B', 'D', 'F') to the preceding loading step; with the remaining four singlets spontaneously appearing during specimen loading to the ultimate load step of 950 N. One singlet ('A') could be traced back to two preceding loading steps from 950 N; namely 900 N and 850 N. These results are shown separately in **Figure 6-8 (b)**, noting the quantitative evaluation exceeds that of the measurement noise. Below this load step, the carbon-fibres are predominantly intact, which limits the analysis to a relatively narrow range. As in the previous section, strain gradients at fibre breaks were post-processed with a strain window size of 1 × 3 × 1 vectors, based on a correlation with a sub-set size of 32 voxels and 75 % overlap. At each load step, the far-field strain was computed by taking the mean of all the measured strain components, however, correlated with a coarser sub-set size of 72 voxels (75 % overlap) and post-processed with a higher strain window size of 3 × 3 × 3 vectors. The latter approach, involving considerably lower spatial resolution, was implemented to alleviate the influence of fibre breaks on the far-field strain at high UTS levels, with **Table 6-3** summarizing the details.

From **Figure 6-8 (a)** it can be observed that, at the 950 N load step, the 'full-recovery length' averaged over eight singlets is ∼63 µm. This is consistent with the SRCT estimate of 70 µm made by Scott *et al.* [14], based on the closest separation of fibre breaks along the same fibres in a T700/M21 composite. Additionally, this also matches the order of magnitude of 100 µm reported by various modelling approaches [10-12, 67]; taking into account that the distance is a function of the applied strain, local microstructure variability, fibre-matrix stiffness ratio, debond length, presence of microcracks and elastic properties of the matrix paired with inter-fibre spacing size effects [1, 10, 12, 67, 72]. A slight increase of ∼7 % is observed in the 'full-recovery length' relative to the preceding load step of 900 N, with the effect being more evident on the top side of the break (right-hand side of the graph): ∼1.3 µm and ∼2.8 µm, respectively. These measurements are consistent with those performed on singlet 'A', as illustrated in **Figure 6-8 (b)**. More precisely, a 'full-recovery length' of ∼67 µm is reported, coupled with a small increase from the penultimate load step, although with a reversed prominence: ∼0.4 µm and ∼3.3 µm on the top and bottom side of the break plane, respectively. The increase in 'full-recovery length' is more obvious if the comparison is performed between the 950 N and 850 N load step: ∼1.65 µm and ∼4 µm on the top and bottom side of the break, respectively. Based on singlet 'A', the maximum increase in 'full-recovery length' as returned by the DVC in the present study is ∼9 %. While the

increase is not substantial, it must be viewed in the context of a strain increment of only ~0.23 % – **Table 6-3**. Unpublished data based on a revised version of Swolfs' [10] model (transverse-isotropic fibre, perfectly-plastic matrix, random packing, *'V_f'* of ~55 %) indicates that this relative increase in 'full-recovery length' agrees reasonably well with the relative increase in FE-predicted ineffective length between similar macro-strain levels.

In terms of the underlying micromechanics, two factors are identified as potential contributors to growth in the strain transfer length with increasing applied load: (1) plastic yielding of the matrix, and (2) progressive propagation of fibre-matrix interface debonding, which both exert similar effects on the strain transfer [1, 21-23, 61-64]. This is supported by the sharper gradients at the break plane associated with a higher load, which suggests that local damage is evolving. In turn, debonding is controlled by parameters such as the interfacial shear strength and/or the interface toughness, the fibre-matrix friction, the matrix yield strength and the fibre stiffness [1]. Ongoing work will aim to establish a comparison between the DVC and model predictions, highlighting the effect of various local damage modes.

Although a consistent effect is discerned, indicating that that the 'full-recovery length' increases with the applied load, the relatively small changes combined with the spatial resolution limitations and the small number of fibres investigated imply that the results should be viewed as indicative at present, rather than statistically significant. More measurements, with more broken fibres and over a wider range of load levels and a detailed comparison with micromechanical models will help clarify this matter. In contrast, the general magnitude of the 'full-recovery length' measurement is less affected by these limitations, and thus, may be viewed as being a reliable conclusion.

Reference load applied (N)	Specimen UTS at applied load (%)	Load at CT acquisition (N)	DVC-based far-field strain (%) *
850	88	765	~1.25
900	93	810	~1.37
950	98	855	~1.50

*Table 6-3 – Far-field and recovery strain as a function of different load levels. *Strains computed at acquisition load and not compensated for existing preload in the specimen.*

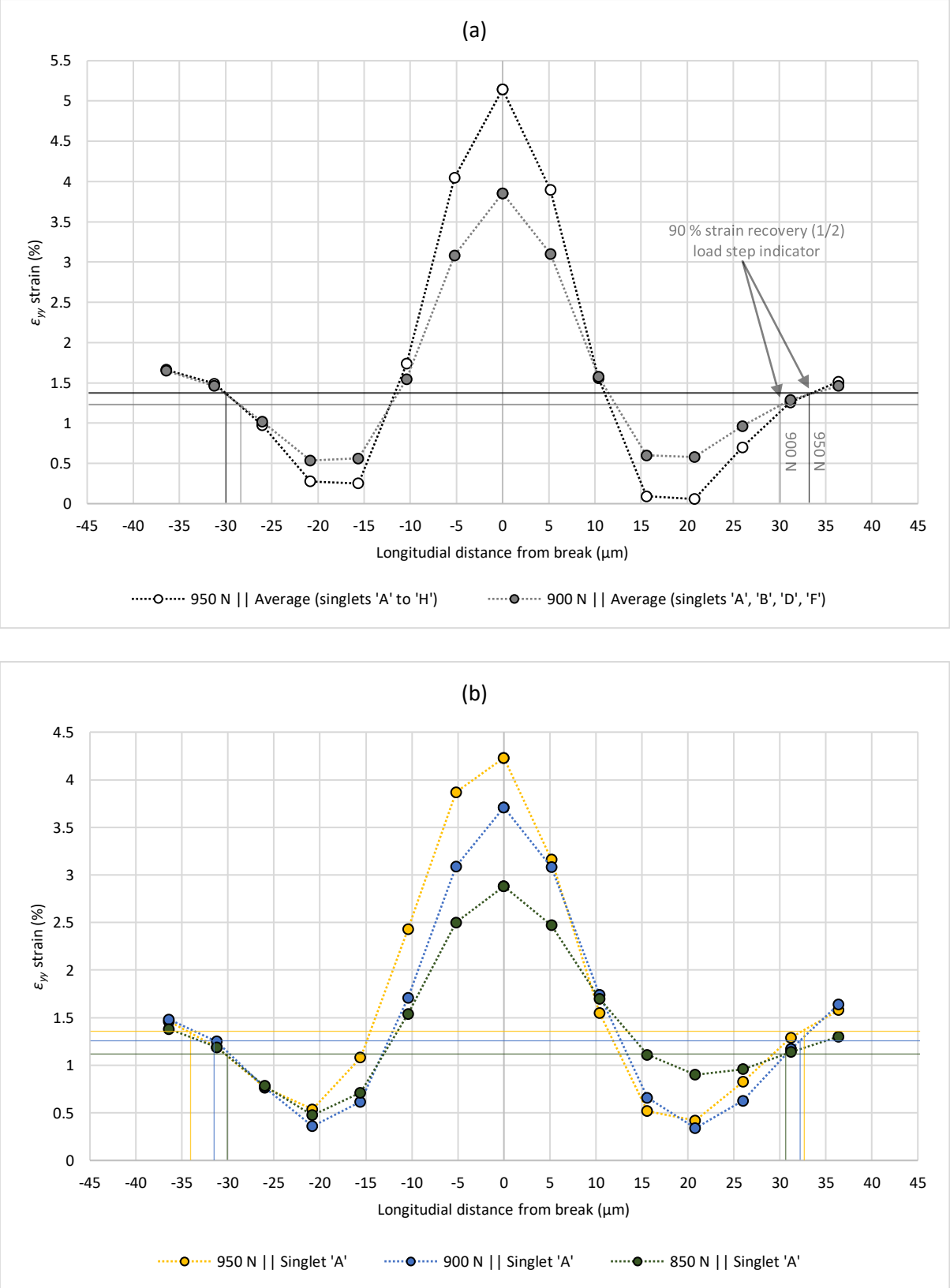

Figure 6-8 – Strain gradients (ε_{yy}) indicating 90 % strain recovery for the different applied load steps: (a) average of eight distinct singlets ('A' to 'H'), and (b) singlet ('A'). Measurements performed on both sides of the break plane. The measurement error corresponds to ~0.093 %.

6.3.3 Strain field assessment at clusters of breaks

The strain field assessment at a cluster of breaks is particularly challenging due to the 3D interaction of strain fields associated with each break (*i.e.* intersection of ineffective and overload length, respectively [73]). Thus, information with minimal spatial resolution artefacts can only be retrieved from fibre breaks that form close-cluster configurations. One such example is the case of co-planar duplets, defined here as two interacting breaks with a separation of less than one fibre diameter longitudinally and two fibre diameters radially. Furthermore, given that the matrix deformation dominates the DVC output, it is not possible to reliably quantify the SCFs for the intact fibres. For consistency, correlation and post-processing parameters were retained as in the assessment of single fibre breaks (*i.e.* sub-set size of 32 voxels and 75 % overlap, with a strain window size of 1 × 3 × 1 vectors).

6.3.3.1 Evolution of clusters of breaks

The evolution of a 'proto-break' site into a singlet, and later into a cluster of breaks, is shown in **Figure 6-9**. The initial fractured fibre 'I' in DVC slice 'Z=36' formed in the penultimate load step of 900 N, with fibre break 'J' forming in a neighbouring fibre in the final load step at 950 N, forming duplet 'IJ'. Based on the previous work of Swolfs *et al.* [13] and Scott *et al.* [14], this incremental formation of a cluster is noted to be unusual, with break clusters much more commonly forming in a 'burst' as a singular event. This may be attributed to the somewhat smaller load increments being applied closer to failure (**Section 6.2.2**) than in [13] and [14], allowing for a more progressive formation of clusters to be captured.

It would appear that the initial break may be triggered by a region of higher strain compared to the immediate surroundings – **Figures 6-9 (a)** and **(b)**. However, it is beyond the scope of the present work to evaluate whether this state of strain is responsible (even in part) for initiating breaks. As such, considering that the carbon-fibre tensile strength distributions follow a Weibull probabilistic model, it may be assumed for the time being that singlet 'I' is simply a stochastic event within the material bulk. In contrast, the second fibre break 'J' appears to form as the result of the increased strain in the fibres surrounding the existing break. Following the development of duplet 'IJ' at the ultimate load step of 950 N, the local strain concentration intensifies. This increases the strain in the surrounding intact fibres, with two additional fibres of interest 'K' and 'L' failing in the same load increment – forming a second duplet 'KL'. The residual strain from the new duplet can be visualised in **Figure 6-9 (c)**, with its corresponding DVC slice 'Z=38' being detailed in the following section, as part of **Figure 6-9 (d)**.

Including both duplets within a single 'full-recovery length', following the approach described in **Section 6.3.3.2**, the formation of a singlet (at 900 N) in this specific cluster configuration (at 950 N) results in a recovery distance increase of ∼11 % for an incremental strain of ∼0.12 % – **Table 6-3**. This growth in 'full-recovery

length' is greater than the ~7 % average for the eight singlets evaluated between the same load steps – **Figure 6-8 (a)**.

These observations suggest that the formation of this cluster is affected by the interaction with the existing break, and its strain field. A further redistribution of strain occurs, causing a further reduction in load carrying capacity at the cluster site. In turn, the additional volume of affected material around the two breaks causes an increase in the full-recovery length when compared to single fibre fractures.

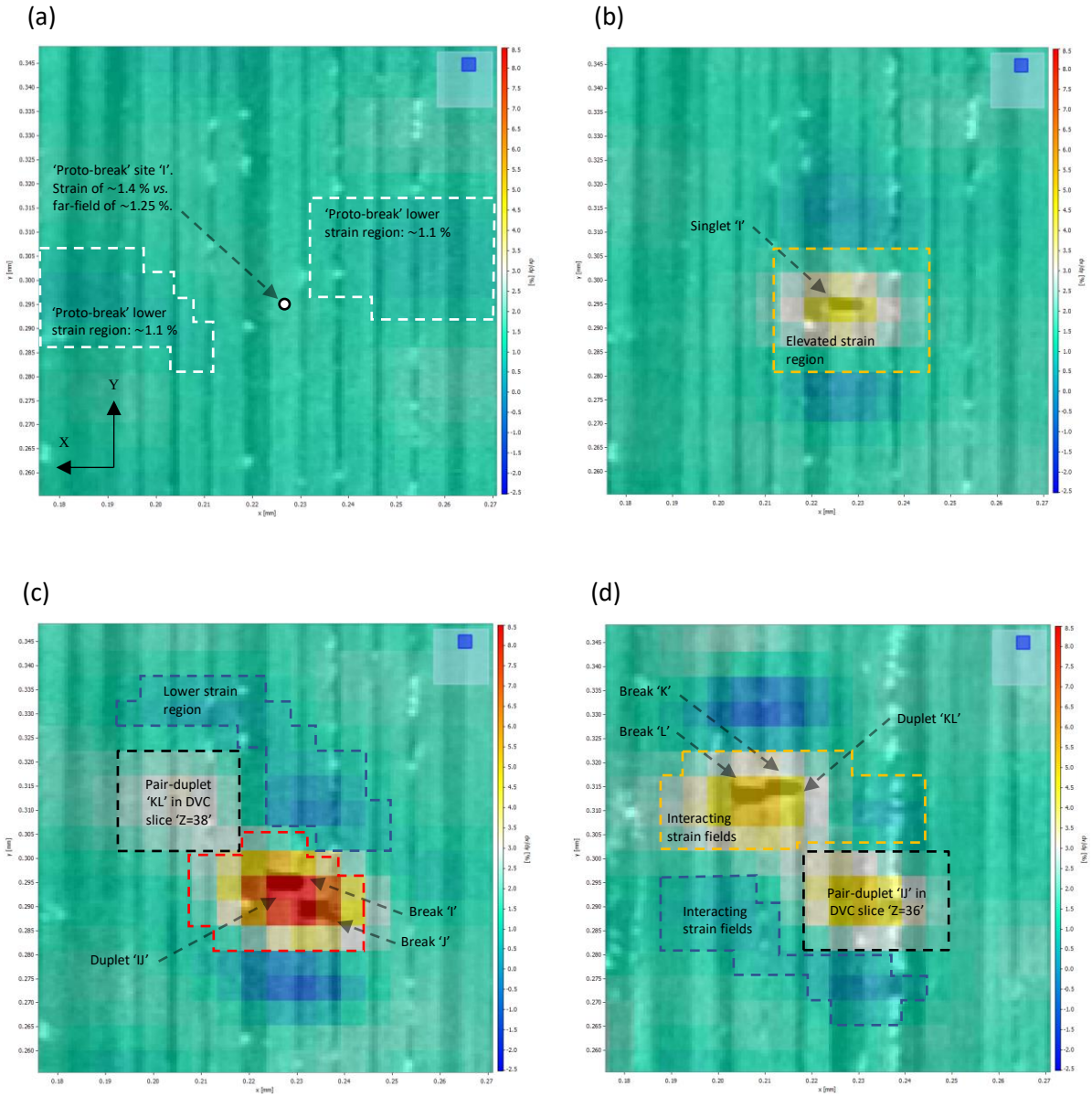

Figure 6-9 – Illustrating the evolution of a cluster of breaks: (a) 'proto-break' site at the 850 N load step – DVC slice 'Z=36', (b) one singe break at the 900 N load step – DVC slice 'Z=36', (c) duplet 'IJ' at the 950 N load step – DVC slice 'Z=36', (d) duplet 'KL' at the 950 load step – DVC slice 'Z=38'. Note the interacting 'ε_{yy}' strain fields surrounding duplets 'IJ' and 'KL', respectively. Correlation performed with a sub-set size of 32 voxels (75 % overlap), while strains were post-processed with a strain window size of 1 × 3 × 1 vectors. FOV amounts to ~100 µm × ~100 µm. The measurement error corresponds to ~0.093 %.

6.3.3.2 Effect of clusters of breaks on strain transfer lengths

Figures 6-9 (c) and **(d)** highlight a sequence of DVC slices centred on two co-planar duplets ('IJ' and 'KL') at the 950 N load step. The first cluster is observable in slice 'Z=36', while the second in 'Z=38'. The corresponding longitudinal (Y), transverse (X) and out-of-plane (Z) separation distances between the two clusters are ∼21 µm, ∼16 µm and ∼10 µm, respectively. An additional fibre break exists ∼36 µm below duplet 'IJ' in slice 'Z=35', however, it is disregarded from the following analysis given its greater separation from the pair of duplets.

As in the case of single fibre breaks, the DVC output yields two near-symmetrical and distinct strain regions – an 'elevated' and 'lower strain length', respectively, on each side of the corresponding duplets. However, due to the spatial proximity of the two duplets, interaction between the strain fields now takes place, with two separate effects observable in **Figures 6-9 (c)** and **(d)**: (1) a merging of the 'lower strain lengths', and (2) a coupling of the 'elevated strain length' with the 'lower strain length'. At the presently attainable spatial resolutions, the former effect leads to an extension of the 'full-recovery length', while the latter promotes a dampening of the strain gradients. More precisely, these redistribution effects are a consequence of the relatively small axial separation of the duplets, with the two breaks associated with duplet 'IJ' being located marginally within the 'recovery length' of 'KL', and *vice versa*. This effect is consistent with that observed numerically in [73], whereby fibre breaks have been shown to trigger an SCF peak within the recovery region of other broken fibres, ultimately resulting in shorter ineffective lengths.

Figure 6-10 presents the strain distributions relative to breaks 'I' and 'K', which yields two longitudinal axes from the peak strains. To account for the interaction of the strain fields, 'IJ' was taken as the datum. First it can be observed that the maximum strain of ∼8.8 % recorded at duplet 'IJ' is higher by a factor of ∼1.6 with respect to duplet 'KL', where a peak value of ∼5.4 % is measured. Given that the 'KL' strain profile is significantly dampened, the discrepancy at the fracture planes may be attributed to different damage mechanisms at the two clusters. In the absence of dissimilar damage scenarios at the fracture plane, similar peak levels would be expected within the 'elevated strain lengths', owing to similar cluster configurations and redistribution effects. For example, at the bottom of break 'J' a small feature which resembles a crack tip, or tear, is visible in between it and the neighbouring intact fibre. Although not observable here, a similar feature exists at top of break 'J' in an adjacent slice. Neither feature is traceable in the previous load steps. The presence of a microcrack would explain the higher strain and strain gradient captured at duplet 'IJ'. Likewise, Swolfs *et al.* [13], predict very high strains and gradients originating at the tip of microcracks in the matrix. Secondly, the peak strain recorded at duplet 'KL' is not substantially higher than the average value of ∼5.15 % at the eight singlets at the equivalent load step – **Figure 6-8 (a)**. This suggests that this cluster is somehow associated with less local damage at the fracture plane, making the relationship between the number of broken fibres and local microstructural damage less straightforward.

The distance over which the far-field strain is recovered from the two duplets is more difficult to interpret due to the interacting strain fields; an effect also visible through the intersecting gradients in **Figure 6-10**. As such it is not possible to completely decouple the 'full-recovery lengths' associated with the two duplets, even more so for the four component fibre breaks. Therefore, the 'full-recovery length' is given by the maximum distance of ∼78 µm which encompasses both clusters. Compared to the average length of ∼63 µm recorded from **Figure 6-8 (a)** at the 950 N load step, this is ∼24 % higher. Interestingly, the 'full-recovery length' does not appear to increase proportionally with the effective diameter of the cluster. For example, it might be expected that if there was scaling with the linear dimensions, a doubling in the number of fibres involved in a cluster, representing a doubling in the cross-sectional area, would represent a √2 (41 %) increase in effective cluster diameter, and a similar increase in the dimensions of all associated damage and strain fields (*e.g.* the Kelly-Tyson perfect-plasticity model [74]). Clearly such an increase is not observed in the present DVC study, which could either be due to a limitation of the technique or indicate a more complex states of damage and strain (*e.g.* as in [73]).

The DVC measured strain field at a cluster of breaks, therefore, indicates a state whereby the full-recovery length near fibre-breaks grows not only with the applied load, but also with cluster size. Compared to single fibre fractures, an additional layer of strain redistribution complexity is detected, and in certain cases links with higher local damage can be made. These findings can also be used to arbitrate between different modelling approaches, as for example, the model proposed by Pimenta and Pinho [75, 76] is the only one in the recent benchmarking exercise [77] that considers a growing ineffective length with applied stress and number of fibres broken in a cluster (also noted in [78]).

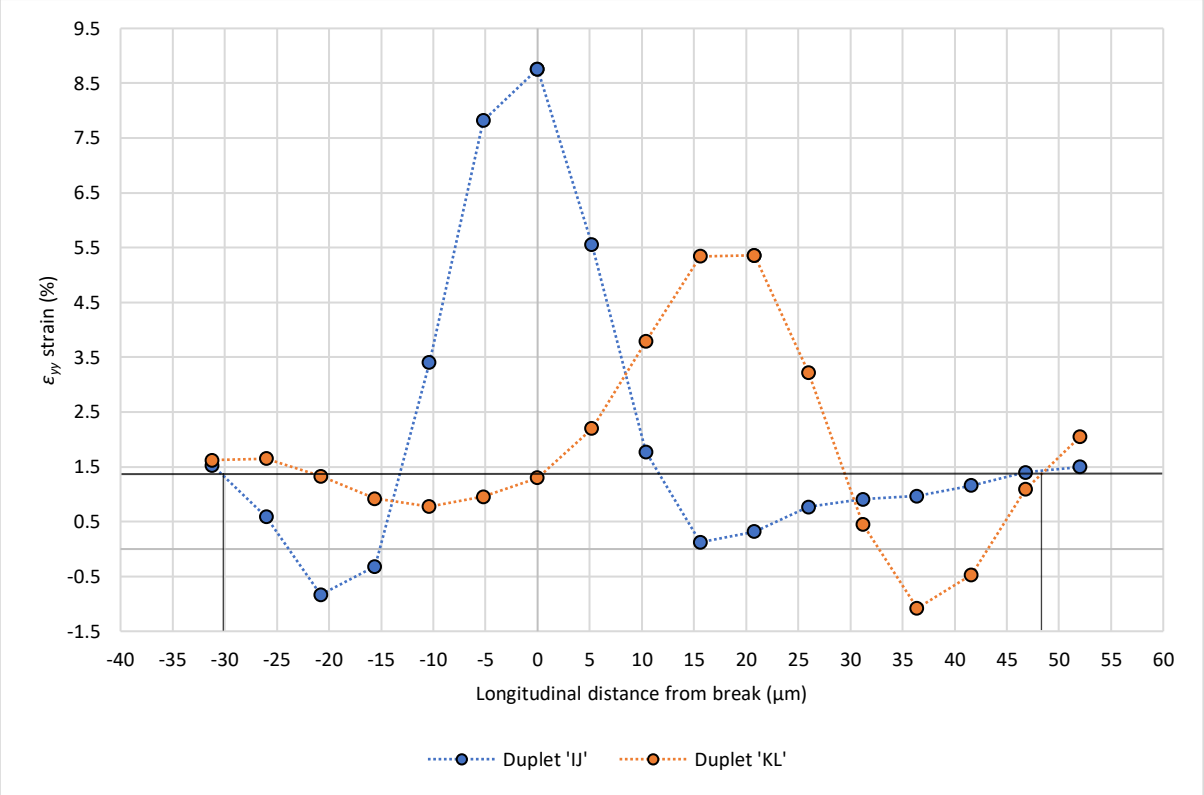

Figure 6-10 – Strain gradients (ε_{yy}) measured longitudinally from breaks 'I' and 'K' of the two duplets (both sides of the break plane). Note the longitudinal (visible), transverse and out-of-plane separation distances of ~21 µm, ~16 µm and ~10 µm, respectively. Microstructure subjected to in situ tensile loading of 950 N (98 % UTS), with acquisition performed at 855 N. The measurement error corresponds to ~0.093 %.

6.4 Summary and conclusions

Digital Volume Correlation was applied in conjunction with *in situ* Synchrotron Radiation Computed Tomography to investigate the strain fields at fibre breaks in unidirectional Carbon-Fibre Reinforced Polymers subjected to quasi-static tensile loading. For the material systems utilized, measurement sensitivity and noise were considered, along with the spatial filtering intrinsic to DVC strain measurements. Correlation between breaks and corresponding strain regions have been established at a level well above the measured noise. To the best of the authors' knowledge, this is the first time that 3D strain measurements have been made within the bulk of representative CFRP materials under applied tensile load.

To eliminate the issue associated with poor correlation along the fibre direction, the matrix was doped with a sparse population of highly contrasted sub-micrometre particles. These acted as fiducial markers, and significantly lowered the measurement uncertainty, allowing for strains to be interpreted at fibre-level. Rigid body displacement tests also confirmed that specimen translation parallel to the fibre direction is in line with the applied displacements, obviating a key problem in applying DVC to such uniformly aligned microstructures.

Compared to volume images acquired through Micro-focus Computed Tomography, the metrological performance of the DVC technique was demonstrated to be superior. Furthermore, hold-at-load artefacts were mitigated due to scan times on the order of seconds as opposed to hours.

The strain field assessment at single fibre breaks resulted in 'full-recovery lengths' consistent with values reported in the modelling literature, ~50-100 μm. However, due to the spatial resolution limitations and associated DVC averaging effects, the deformation at a constituent level could not be separated (*i.e.* between fibre and matrix). Consequently, each of the 'recovery length' profiles encompassed an 'elevated strain length' associated primarily with the matrix deformation at the crack plane, followed by a 'lower strain length' where the DVC is expected to be a good estimate of both fibre and matrix deformation. Additionally, the 'full-recovery lengths' were observed to increase with the applied load, consistent with micromechanical modelling predictions in the literature, indicating that the level of microstructural damage (matrix yielding or debonding) advances with increasing load. The changes are, however, small and must be viewed in the context of a small stress range over which observations can be made, owing to the fact that fibre breaks develop exponentially with stress, with the majority of breaks occurring immediately prior to failure.

The evolution of single fibre breaks into duplets resulted in a considerably larger 'full-recovery length', together with an increased growth compared to single fibre breaks. To determine the relationship more accurately between the number of breaks in a cluster, and the surrounding microstructural damage, acquisition methods capable of substantially higher voxel resolution levels would have to be utilized.

The materials and methods are now developed, and with a high level of confidence in the basic measurements, other application areas can be envisaged where microstructural influence may be important: influences of porosity or ply drops on local load paths/partitioning, compression/microbuckling, and materials with multiaxial or discontinuous reinforcement.

6.5 Appendix A – Static noise test

Under ideal conditions, the obtained displacement vector data and the resulting calculated strains, should be equal to zero. Noise arising from the imaging system (*e.g.* photon counting statistics, electrical noise, scattered radiation) and the surrounding environment (*e.g.* induced vibrations, thermal changes) represents the most significant non-ideality, and consequently erroneous sub-set displacements will generate false strains within the results [30, 35, 40]. However, due to the novelty of the DVC technique, as yet there is no agreed standard for the assessment of the strain error (usually referred to as the strain resolution) [24, 36, 40]. For example, one approach reports the maximum standard deviation of a given strain map (plane of sub-sets) [30, 35], while a second returns the standard deviation of the measured strain components within the volume [24, 40]. Following the first approach, however, can result in overestimating the error, as results can be affected by unrepresentative localised scanning artefacts (*e.g.* rings, detector 'zingers'). In this work, the latter approach is taken for which the error is seen to form a normal distribution with a mean of ∼zero. The advantage of this approach is that both the stochastic noise in the imaging system and any biases in the correlation algorithm are captured and accounted for [24, 40].

A typical effect of the sub-set size on the strain resolution is presented in **Figure 6-11**. As previously reported in the literature, a compromise can be achieved between strain and spatial resolution [24, 29, 30, 32, 37, 40]. As in **Chapter 5**, of particular interest is the normal strain *'ε_{yy}'*, parallel to the fibre direction. Considering the normal components of the strain tensor, it can be observed that the lowest error is generally achieved in the fibre direction (Y), despite the fact that correlation along the fibres themselves has the lowest values, particularly in particle-free CFRPs [40]. This may be rationalised, as the deposition of $BaTiO_3$ during the drum winding process occurred parallel to the fibre direction as the tow was drawn through the die; essentially creating longitudinal bands of fiducial markers in the Y-direction which assists the correlation process significantly, eliminating the self-similar microstructure. Albeit for reduced spatial resolutions, a similar effect is also observed by using μCT on the particle-adapted material in [24], demonstrating reasonable consistency between the different imaging methods.

The compromise between strain and spatial resolution is a critical decision; a smaller sub-set size will contain too few unique features, in this case, the $BaTiO_3$ particles. In contrast, a larger sub-set will compromise spatial resolution [79], as the underlying deformation is representative of the average displacement of all the voxels contained within the sub-set [24, 40]. A larger sub-set size also implies a larger characteristic length for the VSG, which in turn has a negative impact on the global length-scale over which the strains are computed. As the fiducial markers are the main features used for correlating sub-sets between the different deformation states it may be assumed that matrix deformation dominates the DVC output [24].

A trade-off is identifiable in **Figure 6-11** at an isotropic sub-set size of 72 voxels, where the corresponding length of the VSG measures 108 voxels. In contrast, a 32 voxel sub-set size was considered the smallest sub-set size achievable at present for reliable measurements using this material, with the lower limit being a consequence of insufficient $BaTiO_3$ particles captured by smaller sub-sets; containing less than ~10 particles per sub-set. The equivalent VSGs (for different sub-set sizes applied) are shown in **Figure 6-12**, alongside the strain resolution *(ε_{yy})* related to the static noise test. From **Equation 5-1**, it can be observed that for the particular case of a 75 % sub-set overlap, the characteristic length of the VSG measures the constituent sub-set dimension plus one half.

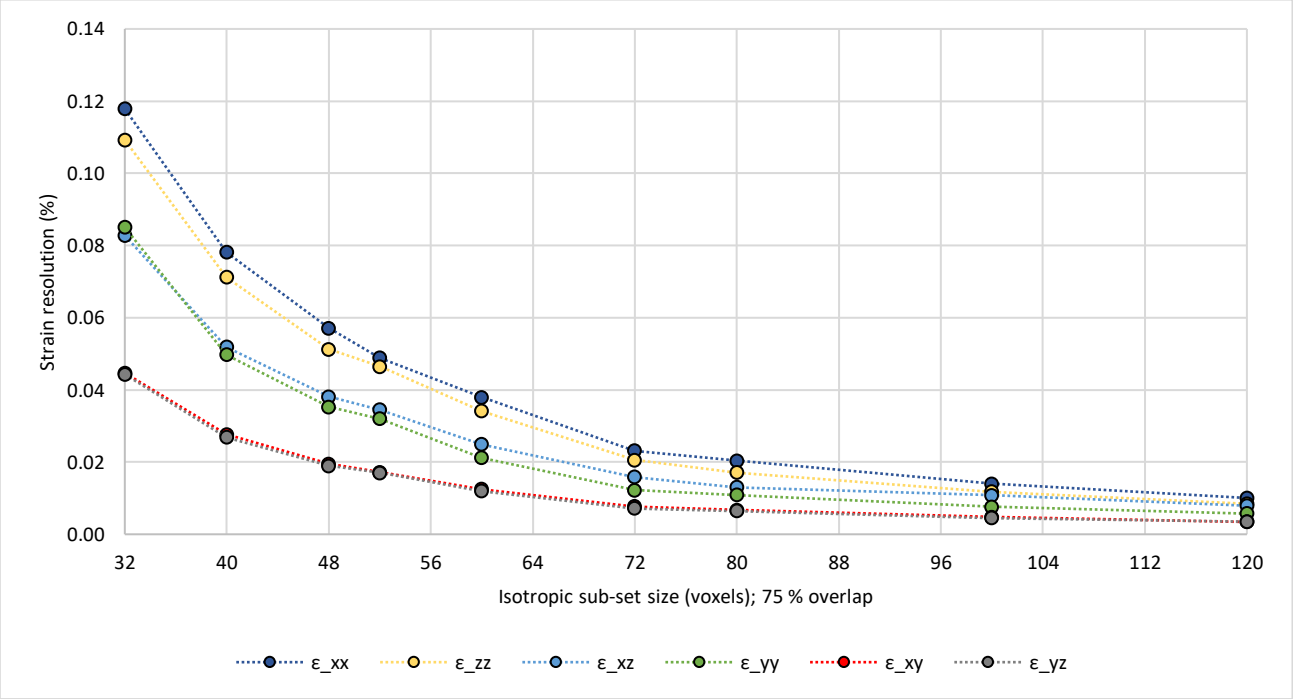

Figure 6-11 – The influence of sub-set size on the strain resolution during SNT scanning (expressed as the standard deviation of the measured strain values), illustrating the compromise between strain and spatial resolution. The 'ε_{yy}' component of the strain tensor denotes the longitudinal (fibre) strain, 'ε_{xx}' the in-plane transverse strain, while the out-of-plane strain component is given by 'ε_{zz}'.

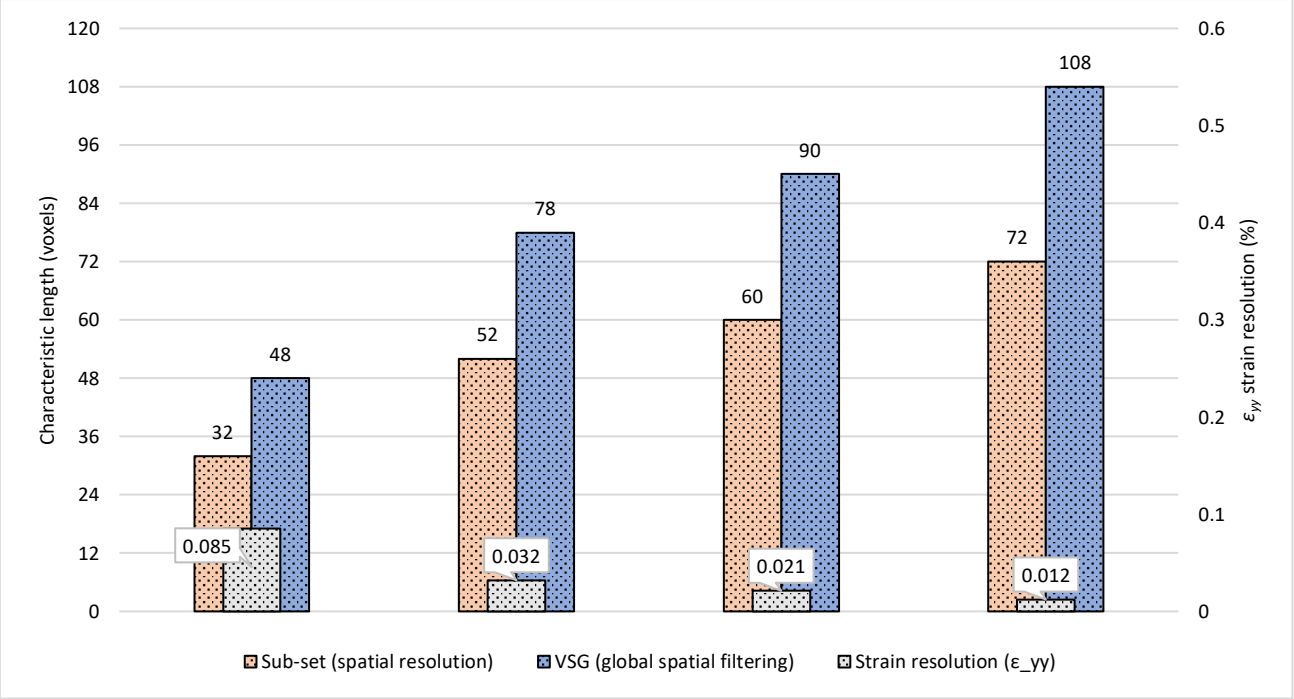

Figure 6-12 – Illustration of VSG and sub-set size, in conjunction with spatial resolution vs. strain resolution (ε_{yy}). Voxel size corresponds to 0.65 µm.

6.6 Appendix B – Rigid body displacement

The displacement field following a movement parallel to the fibre direction was initially computed at a sub-set size of 72 voxels (75 % overlap). The measured variation in displacement via DVC is relatively small, with an average displacement reading of 4.828 µm and a standard deviation of 0.009 µm. The induced Y-displacement was manually confirmed to the nearest pixel in Fiji ImageJ [80]; multiple measurements were taken by determining the distance between a unique feature (*e.g.* a void or $BaTiO_3$ particle) and a reference point. The manual (average) measurement indicates a displacement of ~4.55 ± 0.65 µm, which is within the accuracy of the DVC. As the present work is exclusively focused on fibre direction strain measurements, rigid body displacement analyses were only carried out in the longitudinal direction. Although not an objective here, it is acknowledged that in order to perform reliable transverse (X-direction), and out-of-plane (Z-direction) strain measurements additional noise assessment studies would be required (*e.g.* as in [40]).

A strain map indicating the rigid body correction is shown in **Figure 6-13**, where the magnitude of the longitudinal strain noise is shown on a map overlapped with the microstructure. For smaller sub-sets, the SNT and RBD corrected errors *(ε_{yy})* are collectively summarized in **Figure 6-14**. Edge-artefacts arising from volume displacements were geometrically masked prior to initiating the correlation process, measuring 600 × 8 invalid voxels (rounded to the closest integer), across each of the 600 raw data slices.

Figure 6-14 (a) shows a general trend, where the RBD corrected error tends to be slightly higher than that of the SNT. This is consistent with previous studies which have shown that rigid body displacements can induce higher errors, particularly in the translation direction, due to additional errors from the interpolation biases arising from the specimen movement [24, 30, 35, 40]. Given the single-actuator configuration of the present *in situ* experiment as well as possible compliances within the loading rig, the RBD strain resolution is considered as the relevant representation of the strain error.

Despite a different DVC framework and superior SRCT voxels resolution levels (resulting in non-identical spatial filtering), the magnitude of the RBD corrected strain resolutions are reasonably consistent with those reported in [40] using particle toughened interlayer materials.

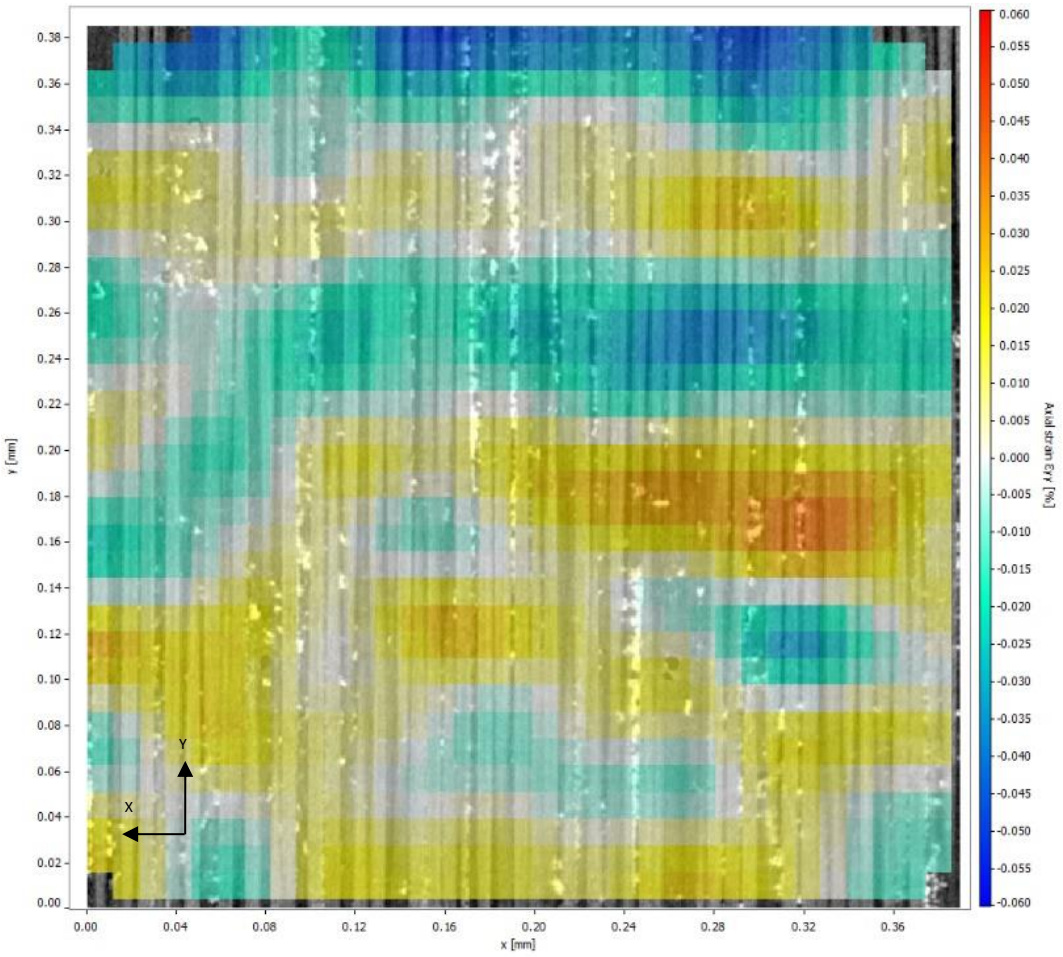

Figure 6-13 – DVC slice 'Z=16' illustrating the 'ε_{yy}' strain map (noise) overlaid with the microstructure following RBD correction. Masking applied (600 × 8 × 600 voxels) to remove edge artefacts for the Y-displaced scans. Map range: -0.060 to 0.060 %. Applicable for a correlation performed with a sub-set size of 72 voxels and 75 % overlap.

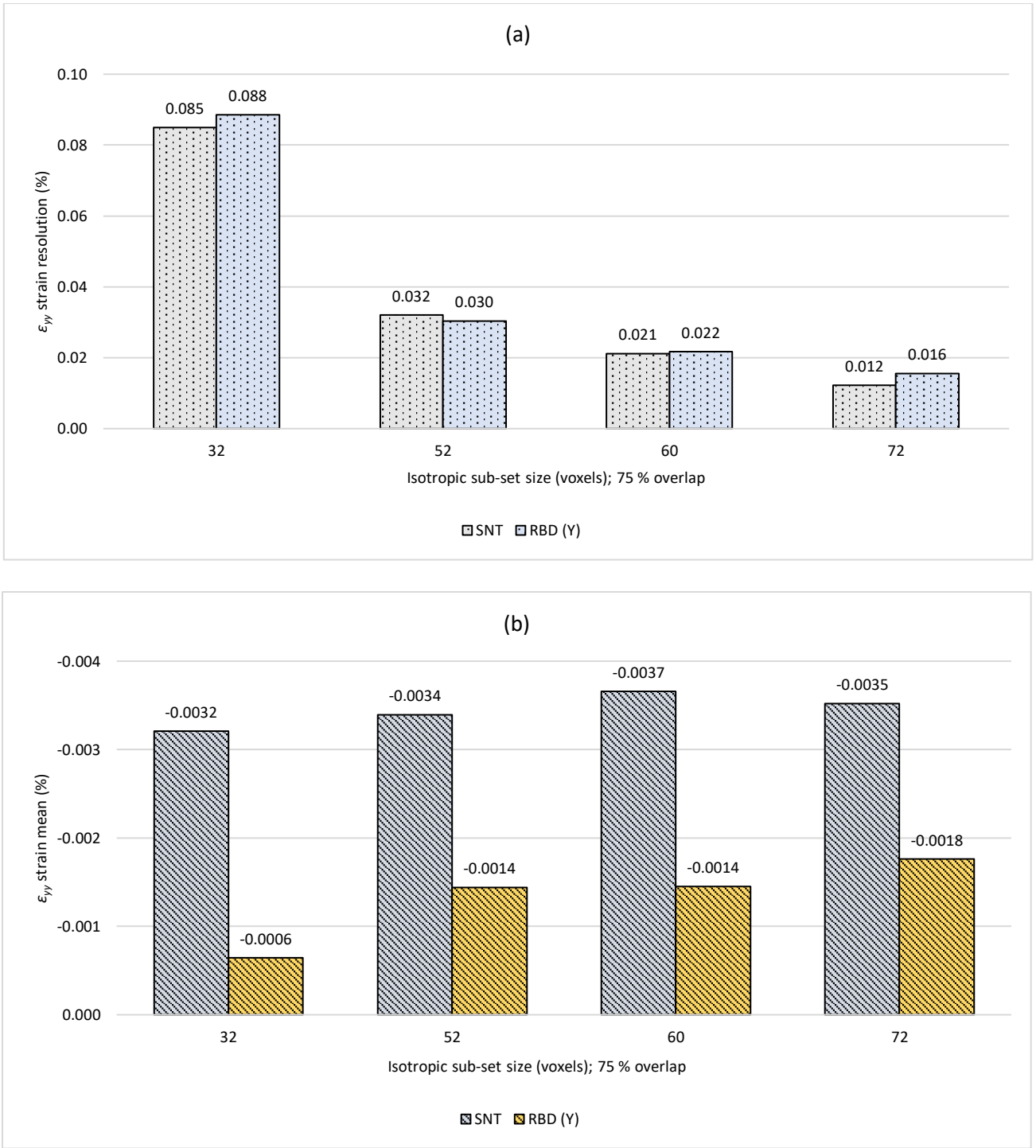

Figure 6-14 – (a) Strain resolution (ε_{yy}), and (b) strain mean (ε_{yy}) for the SNT and RBD corrected scans for various sub-set sizes with 75 % overlap. Masking applied (600 × 8 × 600 voxels) to remove edge artefacts for the Y-displaced scans.

6.7 Appendix C – Effect of strain window size

The effect of strain window size on the SNT and RBD corrected scans is visible in **Figure 6-15**, where the strain resolution associated with the normal strain component 'ε_{yy}' were reprocessed using 1 × 3 × 1 vectors and 5 × 5 × 5 vectors, respectively. Correlation with a sub-set size of 32 voxels and 75 % overlap was maintained throughout. The results are compared against the default strain window size of 3 × 3 × 3 vectors. **Table 6-4** presents the equivalent VSGs in physical units and fibre diameters, respectively, based on the number of neighbouring vectors enclosed.

The strain window limited to smoothing in the fibre direction (*i.e.* 1 × 3 × 1 vectors) leads to the highest measurement uncertainty. This is expected, as a strain window size of 3 × 3 × 3 vectors or 5 × 5 × 5 vectors will reduce the available signal-to-noise ratio by averaging the results over a larger effective volume (smoothing in the fibre direction *vs.* isotopically in the material bulk).

For real deformation tests (**Section 6.3.2** and **Section 6.3.3**) the size of the VSG (a function of: strain window, sub-set size and overlap) should be, however, small enough so that the real amplitude of the fluctuations is fully restored. While beyond the scope of this work, a detailed analysis has shown that an excessively large VSG is susceptible to over-smoothing of the strain data, and implicit loss in information regarding the material deformation. Nonetheless, achievement of strain measurements with very fine spatial resolution is limited in practice, as reported in [24], due to experimental constraints (*e.g.* uniqueness of the material pattern at a microstructural level). Additionally, such an implementation may cause the noise floor to exceed the signal level. Therefore, a balanced signal-to-noise ratio (SNR) must be considered independently for a given sub-set size, which is in turn linked to the materials and imaging methods used.

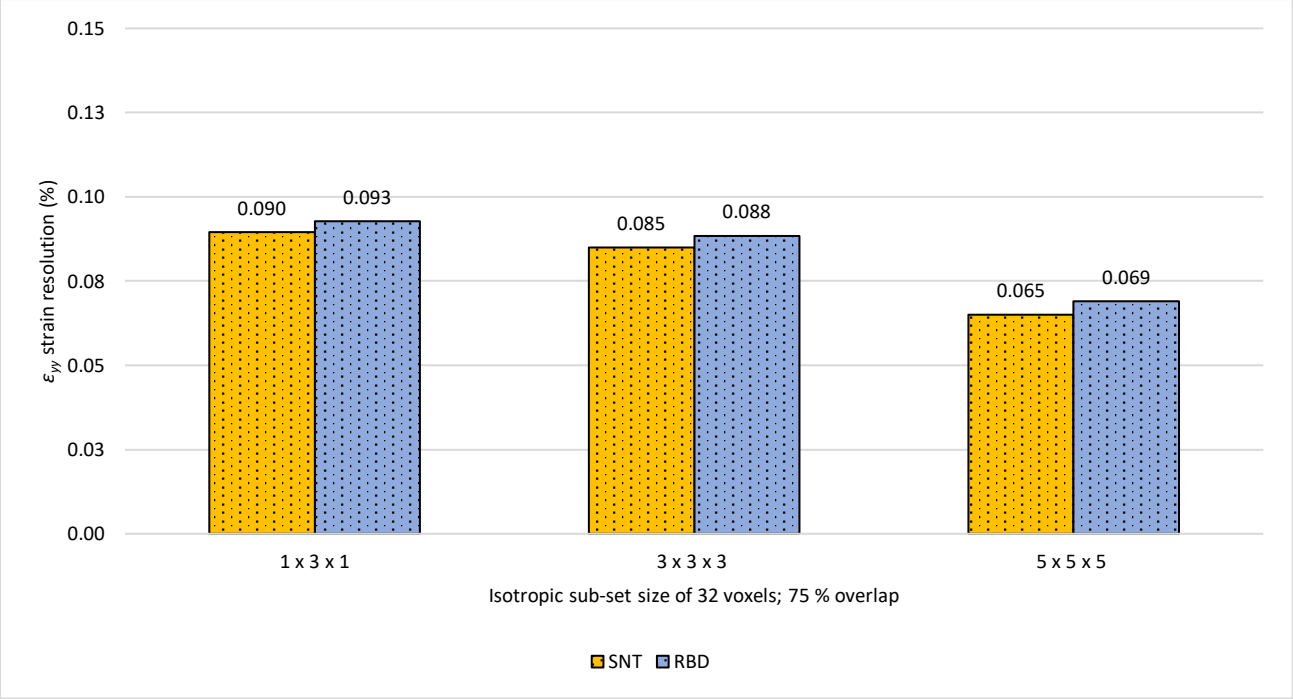

Figure 6-15 – Strain resolution (ε_{yy}) for the SNT and RBD corrected scans for various strain window sizes (L_{sw}), computed with a sub-set size of 32 voxels and 75 % overlap.

Strain window size (vectors)	VSG size (voxels)	VSG size (µm)	VSG size Equivalent fibre Ø
1 × 3 × 1	32 × 48 × 32	20.8 × 31.2 × 20.8	~3 × ~4.5 × ~3
3 × 3 × 3	48 × 48 × 48	31.2 × 31.2 × 31.2	~4.5 × ~4.5 × ~4.5
5 × 5 × 5	64 × 64 × 64	41.6 × 41.6 × 41.6	~6 × ~6 × ~6

Table 6-4 – Equivalent VSG sizes in physical units (1 voxel = 0.65 µm) and fibre diameters (1 fibre diameter = 7 µm), respectively, based on different strain window sizes, applicable to a sub-set size of 32 voxels with 75 % overlap.

6.8 Appendix D – Assessment against conventional microstructures

The difference between the measured uncertainty *(ε_{yy})* for the 'doped material' and 'undoped material' based on a static noise test is shown in **Figure 6-16**. 'DC' was used to perform the correlation, in conjunction with SRCT methods for both material types. As previously illustrated in **Figure 6-11**, a compromise exists between strain and spatial resolution, with the particle-adapted and conventional microstructure exhibiting a similar trendline. The vertical axis in **Figure 6-16** is shown in logarithmic form to compensate for the higher order of magnitude associated with the standard deviation of the measured strain within the volume cropped from the 'undoped material'.

From a sub-set size of 120 voxels up to and including a sub-set size of 80 voxels, the measured uncertainty in the conventional CFRP is greater than in the particle containing material by an average factor of ∼24. At a sub-set size of 72 voxels, the offset increases to a factor of ∼36, while from a sub-set size of 60 voxels onwards, the 'doped material' exhibits a standard deviation of the longitudinal strain greater by an average factor of ∼58. It is likely that for sub-set sizes in excess of 120 voxels enough microstructure variability is captured (*e.g.* fibre misalignment, variations in fibre-matrix volume fraction) to assist the correlation process, and thus, a lower discrepancy between the 'doped material' and 'undoped material' with increasing sub-set size. Relying only on the present SNT results, the technique would, therefore, appear to work at significantly larger length scales (*i.e.* tow-level, exceeding the equivalent of ten fibre diameters) on conventional UD materials; given that the noise level is only a fraction of the expected failure strain. Nonetheless, this interpretation is in absence of RBD tests, where an accurate reading of the displacement is not expected, as reported in [40].

The higher measured uncertainty in the 'undoped material' is also associated with lower correlation values, as shown by the two DVC slices based on the SNT computed with a sub-set size of 32 voxels (75 % overlap) – **Figure 6-17**. However, given the nature of the reduced scale range, whereby coefficients between ∼0.995 and 1.0 are displayed, the differences in correlation values between the particle-adapted and conventional microstructure may be regarded as negligible. As correlation coefficients above 0.8 are generally acceptable [40], it would be straightforward to conclude that fibre-level studies are possible in the 'undoped material'. This is however incorrect, as most of the correlation peaks may be expected to be false due to the self-similar microstructure, as indicated by the elevated standard deviation of the measured strain component *'ε_{yy}'*. It also follows that correlation coefficients should not be considered as standalone results, but rather linked to additional tests as conducted in the present study.

Provided that the typical failure strain of a T700/M21 composite with a V_f of 0.55 is ∼2 % [13], it is evident that for a correlation carried out with a sub-set of 32 voxels (∼21 μm or the equivalent of ∼three fibre diameters), the noise floor in the 'undoped material' is too high to perform any local strain measurements

with satisfactory accuracy: ~2 % ± ~4.5 %. Taken together, further studies such as RBD tests have not been performed on the 'undoped material', where the measurement uncertainty is only expected to increase with a greater test complexity. For the purposes of this work, *in situ* tensile DVC analyses were thus limited to the 'doped material'.

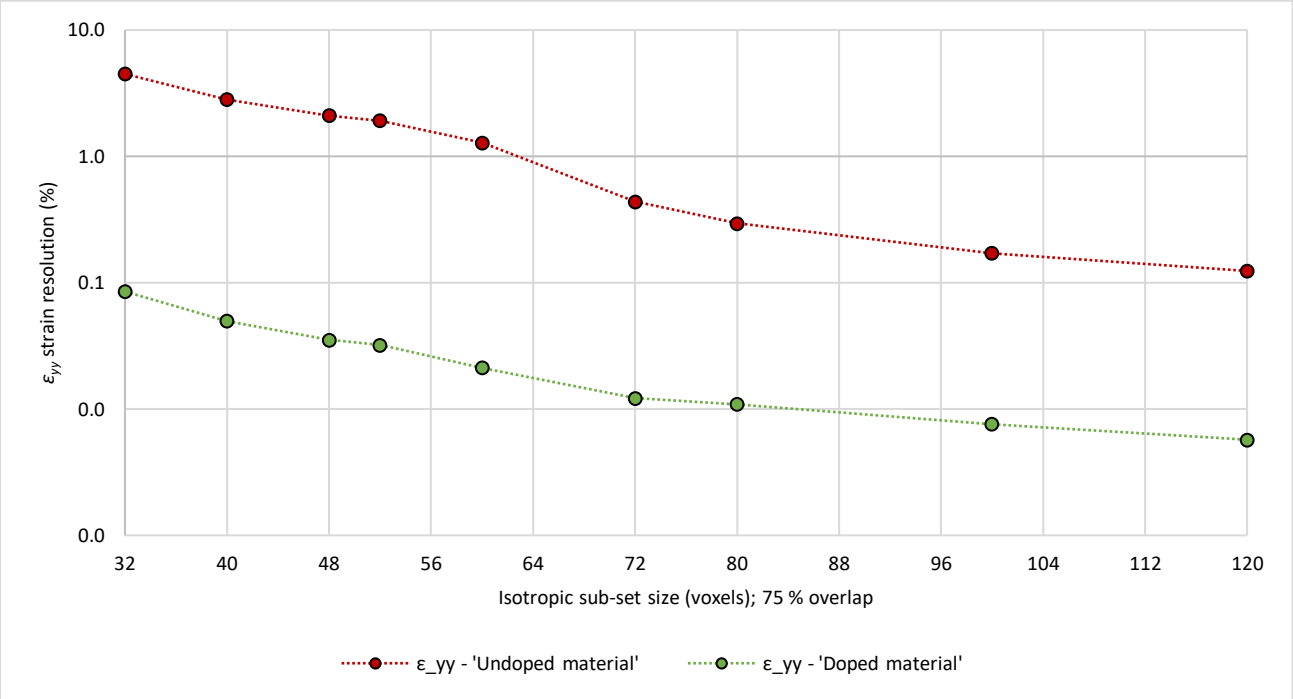

Figure 6-16 – Influence of sub-set size on the strain resolution during SNT scanning, illustrating the compromise between strain and spatial resolution using the different materials (i.e. 'undoped material' vs. 'doped material' with 400 nm, 7.5 wt. % $BaTiO_3$). Results presented for the 'ε_{yy}' component of the strain tensor and applicable to SRCT data. Computed via 'DC'.

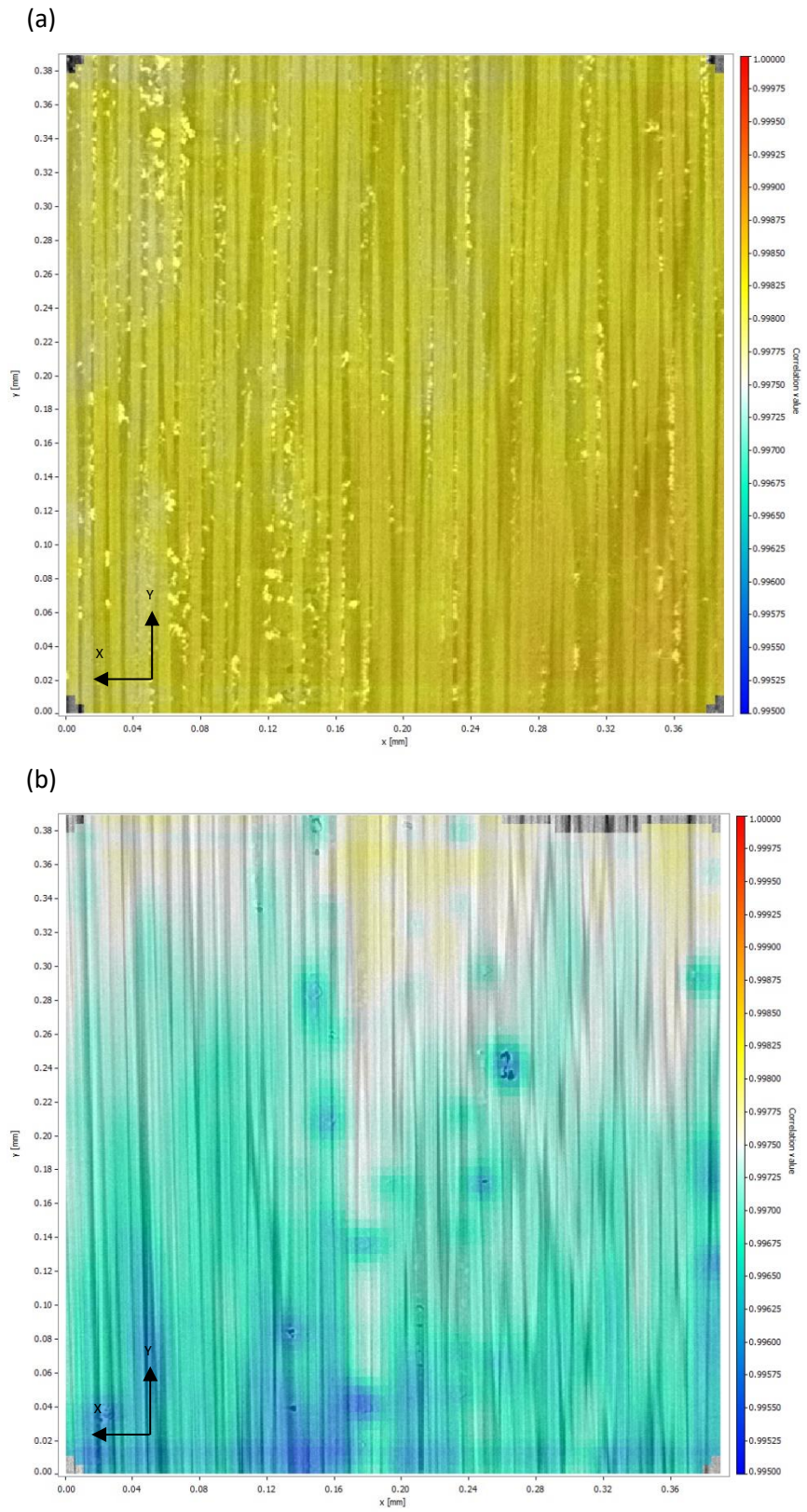

Figure 6-17 – DVC slice 'Z=40' illustrating correlation maps overlaid with the microstructure following SNT scanning: (a) 'doped material' and (b) 'undoped material'. Both materials exhibit very similar correlation coefficients, indicating the need for SNT and RBD tests. Map range: 0.995 to 1.0. Correlation performed with a sub-set size of 32 voxels and 75 % overlap via 'DC'.

6.9 Appendix E – Assessment against Micro-focus Computed Tomography

Figure 6-18 presents the metrological performance of the two different acquisition methods under static noise test conditions, while **Figure 6-19** summarizes the µCT-related SNT and RBD corrected errors. For the Micro-focus CT analysis, imaging data from **Chapter 5** was used (or [24]). Correlation was performed via 'DC' on the 'doped material' for both imaging techniques, with emphasis on normal strain *'ε_{yy}'*. Under SNT conditions, the results yield a similar trendline, illustrating a compromise between strain and spatial resolution, however with an evident offset between the two imaging techniques. More precisely, the µCT-related measured uncertainty is higher by an average factor of ~1.8 across the equivalent range of sub-set sizes investigated.

Progressing onto the µCT-based RBD test, it can be observed that standard deviation of the measured strain component is significantly higher than that of the SNT by an average factor of ~5, across the four different sub-set sizes in **Figure 6-19 (a)**. This contrasts with the RBD corrected error based on the SRCT data, where the DVC output obtained is more consistent between the two zero-strain pair analyses (SNT *vs.* RBD) – **Figure 6-14 (a)**. When the RBD corrected error is compared directly between the different imaging techniques, an average factor of ~8.7 can be discerned, in favour of SRCT. Similarly, a superior DVC metrological performance is also reported by Wang *et al.* [37], in conjunction with SRCT, as opposed with µCT imaging.

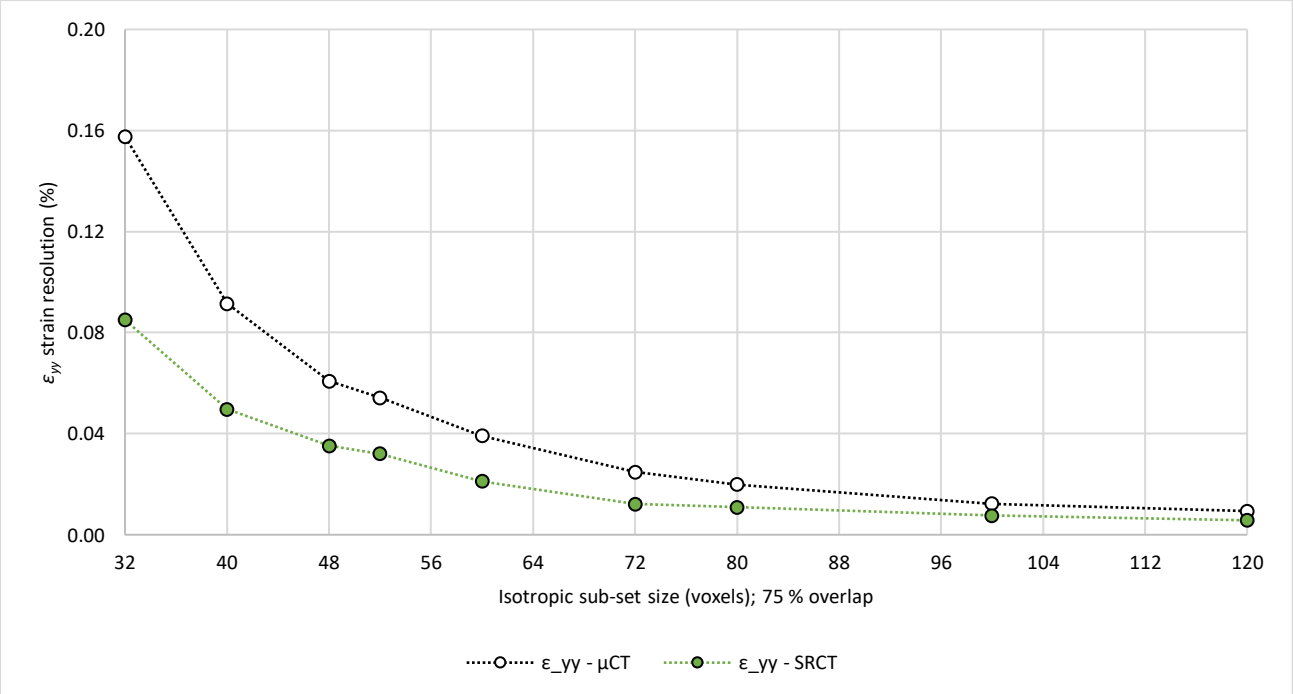

Figure 6-18 – The influence of sub-set size on the strain resolution during SNT scanning, illustrating the compromise between strain and spatial resolution using different imaging acquisition methods (µCT vs. SRCT). Results presented for the 'ε_{yy}' component of the strain tensor.

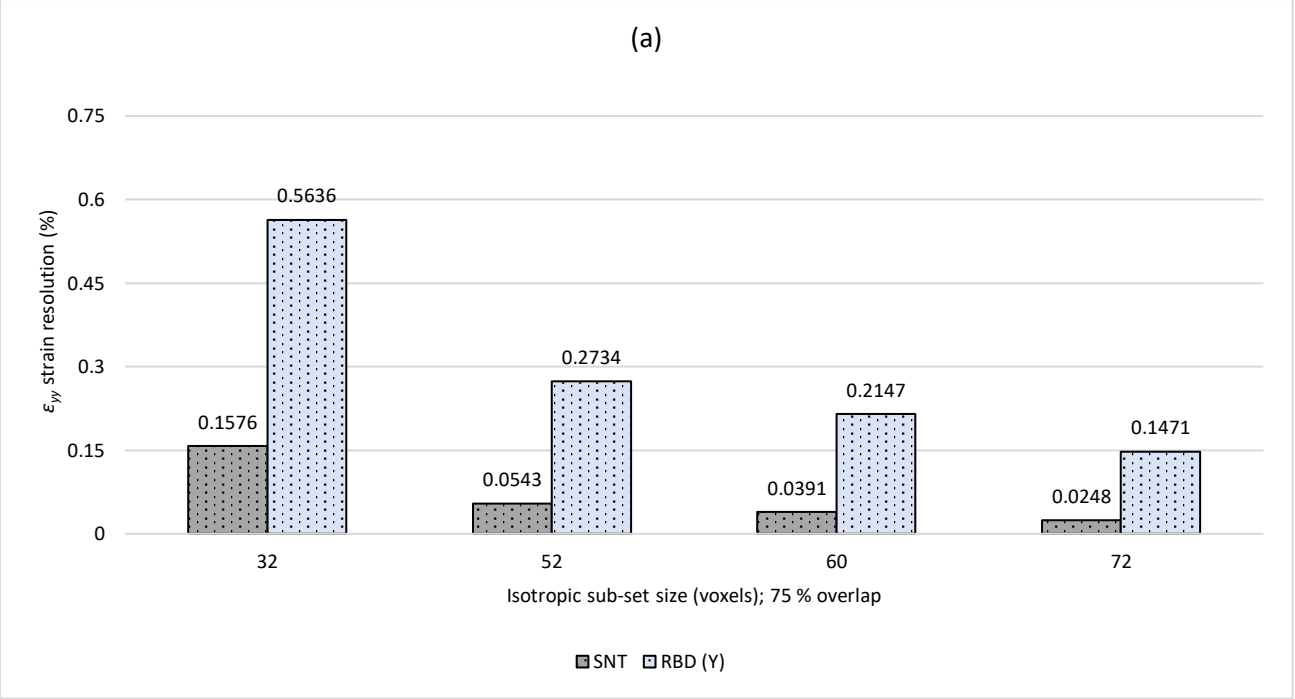

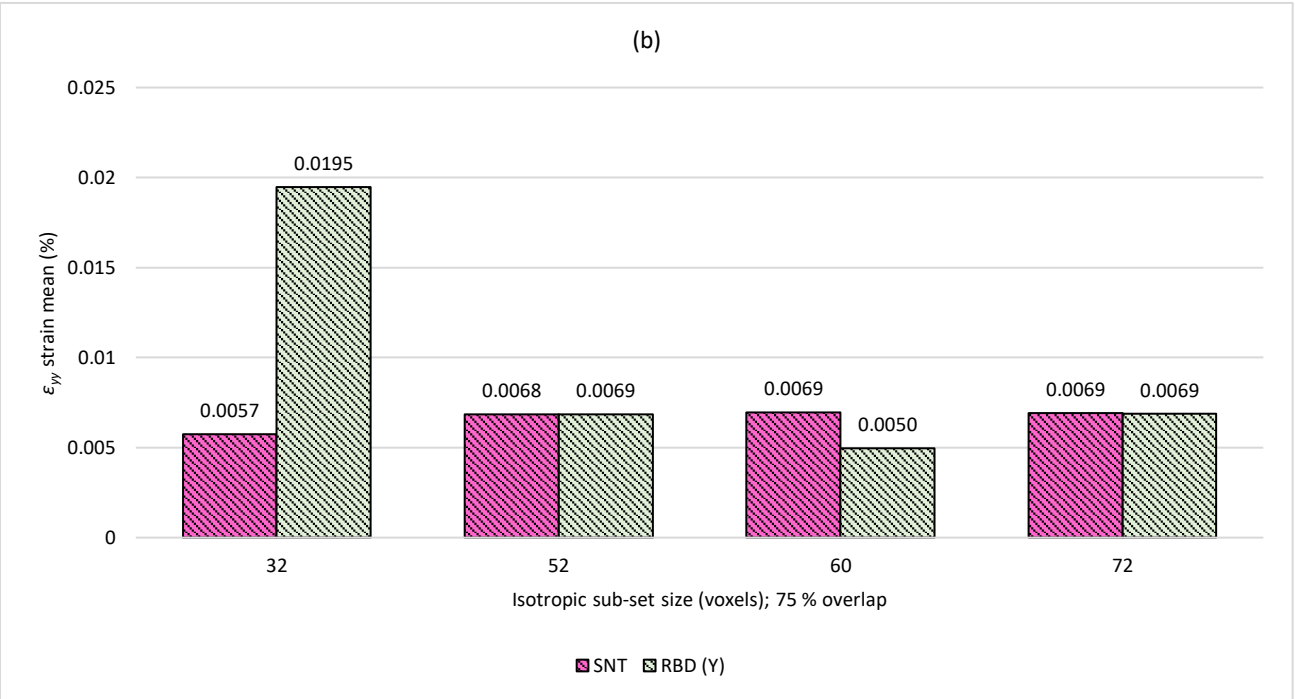

Figure 6-19 – (a) Strain resolution (ε_{yy}), and (b) strain mean (ε_{yy}) for the SNT and RBD corrected scans for various sub-set sizes with 75 % overlap. Masking applied (795 × 16 × 230 voxels) to remove edge artefacts for the Y-displaced scans. Applicable to µCT data (voxel size corresponds to ~0.64 µm).

6.10 References

[1] Y. Swolfs, I. Verpoest and L. Gorbatikh, "A review of input data and modelling assumptions in longitudinal strength models for unidirectional fibre-reinforced composites," *Composite Structures,* vol. 150, pp. 153-172, 2016.

[2] J. Watanabe, F. Tanaka, H. Okuda and T. Okabe, "Tensile strength distribution of carbon fibers at short gauge lengths," *Advanced Composite Materials,* vol. 23, no. 5-6, pp. 535-550, 2014.

[3] J. M. Hedgepeth, "Stress concentrations in filamentary structures (NASA-TN-D-882, L-1502)," NASA Langley Research Center, Hampton, VA, USA, 1961.

[4] J. M. Hedgepeth and P. Van Dyke, "Local stress concentrations in imperfect filamentary composite materials," *Journal of Composite Materials,* vol. 1, no. 3, pp. 294-309, 1967.

[5] C. Zweben, "Tensile failure of fiber composites," *AIAA Journal,* vol. 6, no. 12, pp. 2325-2331, 1968.

[6] H. Fukuda, "Stress concentration factors in unidirectional composites with random fiber spacing," *Composites Science and Technology,* vol. 22, no. 2, pp. 153-163, 1985.

[7] Z. Xia, W. A. Curtin and T. Okabe, "Green's function vs. shear-lag models of damage and failure in fiber composites," *Composites Science and Technology,* vol. 62, no. 10-11, pp. 1279-1288, 2002.

[8] Z. Xia, T. Okabe and W. A. Curtin, "Shear-lag versus finite element models for stress transfer in fiber-reinforced composites," *Composites Science and Technology,* vol. 62, no. 9, pp. 1141-1149, 2002.

[9] B. W. Rosen, "Tensile failure of fibrous composites," *AIAA Journal,* vol. 2, no. 11, pp. 1985-1991, 1964.

[10] Y. Swolfs, L. Gorbatikh, V. Romanov, S. Orlova, S. V. Lomov and I. Verpoest, "Stress concentrations in an impregnated fibre bundle with random fibre packing," *Composites Science and Technology,* vol. 74, pp. 113-120, 2013.

[11] M. R. Nedele and M. R. Wisnom, "Three-dimensional finite element analysis of the stress concentration at a single fibre break," *Composites Science and Technology,* vol. 51, no. 4, pp. 517-524, 1994.

[12] M. R. Nedele and M. R. Wisnom, "Stress concentration factors around a broken fibre in a unidirectional carbon fibre-reinforced epoxy," *Composites,* vol. 25, no. 7, pp. 549-557, 1994.

[13] Y. Swolfs, H. Morton, A. E. Scott, L. Gorbatikh, P. A. S. Reed, I. Sinclair, S. M. Spearing and I. Verpoest, "Synchrotron radiation computed tomography for experimental validation of a tensile strength model for unidirectional fibre-reinforced composites," *Composites Part A,* vol. 77, pp. 106-113, 2015.

[14] A. E. Scott, M. N. Mavrogordato, P. Wright, I. Sinclair and S. M. Spearing, "In situ fibre fracture measurement in carbon-epoxy laminates using high resolution computed tomography," *Composites Science and Technology,* vol. 71, no. 12, pp. 1471-1477, 2011.

[15] A. E. Scott, I. Sinclair, S. M. Spearing, A. Thionnet and A. R. Bunsell, "Damage accumulation in a carbon/epoxy composite: Comparison between a multiscale model and computed tomography experimental results," *Composites Part A,* vol. 43, no. 9, pp. 1514-1522, 2012.

[16] A. Thionnet, H. Y. Chou and A. R. Bunsell, "Fibre break processes in unidirectional composites," *Composites Part A,* vol. 65, pp. 148-160, 2014.

[17] Y. Swolfs, I. Verpoest and L. Gorbatikh, "Issues in strength models for unidirectional fibre-reinforced composites related to Weibull distributions, fibre packings and boundary effects," *Composites Science and Technology,* vol. 114, pp. 42-49, 2015.

[18] S. C. Garcea, I. Sinclair, S. M. Spearing and P. J. Withers, "Mapping fibre failure in situ in carbon fibre reinforced polymers by fast synchrotron X-ray computed tomography," *Composites Science and Technology,* vol. 149, pp. 81-89, 2017.

[19] S. Rosini, M. N. Mavrogordato, O. Egorova, E. S. Matthews, S. E. Jackson, S. M. Spearing and I. Sinclair, "In situ statistical measurement of local morphology in carbon-epoxy composites using synchrotron X-ray computed tomography," *Composites Part A,* vol. 125, pp. 1-14, 2019.

[20] P. W. J. van den Heuvel, T. Peijs and R. J. Young, "Analysis of stress concentrations in multi-fibre microcomposites by means of Raman spectroscopy," *Journal of Materials Science Letters,* vol. 15, no. 21, pp. 1908-1911, 1996.

[21] P. W. J. van den Heuvel, T. Peijs and R. J. Young, "Failure phenomena in two-dimensional multi-fibre microcomposites. Part 4 – A Raman spectroscopic study on the influence of the matrix yield stress on stress concentrations," *Composites Part A,* vol. 31, no. 2, pp. 165-171, 2000.

[22] Y. Huang and R. J. Young, “Analysis of the fragmentation test for carbon-fibre/epoxy model composites by means of Raman spectroscopy,” *Composites Science and Technology,* vol. 52, no. 4, pp. 505-517, 1994.

[23] Y. Huang and R. J. Young, “Interfacial behaviour in high temperature cured carbon fibre/epoxy resin model composite,” *Composites,* vol. 26, no. 8, pp. 541-550, 1995.

[24] E. Schöberl, M. N. Mavrogordato, I. Sinclair and S. M. Spearing, “Fibre-direction strain measurement in a composite ply under pure bending using digital volume correlation and micro-focus computed tomography,” *Journal of Composite Materials,* vol. 54, no. 14, pp. 1889-1911, 2020.

[25] A. J. Moffat, P. Wright, J.-Y. Buffiere, I. Sinclair and S. M. Spearing, “Micromechanisms of damage in 0° splits in a [90/0]s composite material using synchrotron radiation computed tomography,” *Scripta Materialia,* vol. 59, no. 10, pp. 1043-1046, 2008.

[26] P. Wright, A. J. Moffat, I. Sinclair and S. M. Spearing, “High resolution tomographic imaging and modelling of notch tip damage in a laminated composite,” *Composites Science and Technology,* vol. 70, no. 10, pp. 1444-1452, 2010.

[27] B. Pan, K. Qian, H. Xie and A. Asundi, “Two-dimensional digital image correlation for in-plane displacement and strain measurement: A review,” *Measurement Science and Technology,* vol. 20, no. 6, pp. 1-17, 2009.

[28] F. Xu, “Quantitative characterization of deformation and damage process by digital volume correlation: A review,” *Theoretical & Applied Mechanics Letters,* vol. 8, no. 2, pp. 83-96, 2018.

[29] M. Palanca, L. Cristofolini, E. Dall’Ara, M. Curto, F. Innocente, V. Danesi and G. Tozzi, “Digital volume correlation can be used to estimate local strains in natural and augmented vertebrae: An organ-level study,” *Journal of Biomechanics,* vol. 49, no. 16, pp. 3882-3890, 2016.

[30] F. Gillard, R. P. Boardman, M. N. Mavrogordato, D. Hollis, I. Sinclair, F. Pierron and M. Browne, “The application of Digital Volume Correlation (DVC) to study the microstructural behaviour of trabecular bone during compression,” *Journal of the Mechanical Behavior of Biomedical Materials,* vol. 29, pp. 480-499, 2014.

[31] S. P. Timoshenko, Strength of materials. Part 1 – Elementary theory and problems, 2nd ed., New York City, NY, USA: David Van Nostrand Company Inc., 1940, pp. 88-97.

[32] L. Liu and E. F. Morgan, “Accuracy and precision of digital volume correlation in quantifying displacements and strains in trabecular bone,” *Journal of Biomechanics,* vol. 40, no. 15, pp. 3516-3520, 2007.

[33] K. Madi, G. Tozzi, Q. H. Zhang, J. Tong, A. Cossey, A. Au, D. Hollis and F. Hild, “Computation of full-field displacements in a scaffold implant using digital volume correlation and finite element analysis,” *Medical Engineering & Physics,* vol. 35, no. 9, pp. 1298-1312, 2013.

[34] R. Brault, A. Germaneau, J. C. Dupré, P. Doumalin, S. Mistou and M. Fazzini, “In-situ analysis of laminated composite materials by X-ray micro-computed tomography and digital volume correlation,” *Experimental Mechanics,* vol. 53, pp. 1143-1151, 2013.

[35] F. Pierron, S. A. McDonald, D. Hollis, J. Fu, P. J. Withers and A. Alderson, “Comparison of the mechanical behaviour of standard and auxetic foams by X-ray computed tomography and digital volume correlation,” *Strain,* vol. 49, no. 6, pp. 467-482, 2013.

[36] M. Palanca, G. Tozzi, L. Cristofolini, M. Viceconti and E. Dall'Ara, “Three-dimensional local measurements of bone strain and displacement: Comparison of three digital volume correlation approaches,” *Journal of Biomedical Engineering,* vol. 137, no. 7, pp. 1-14, 2015.

[37] L. Wang, N. Limodin, A. El Bartali, J.-F. Witz, R. Seghir, J.-Y. Buffiere and E. Charkaluk, “Influence of pores on crack initiation in monotonic tensile and cyclic loadings in lost foam casting A319 alloy by using 3D in-situ analysis,” *Materials Science & Engineering A,* vol. 673, pp. 362-372, 2016.

[38] D. Kytýř, P. Zlámal, P. Koudelka, T. Fíla, N. Krčmářová, I. Kumpová, D. Vavřík, A. Gantar and S. Novak, “Deformation analysis of gellan-gum based bone scaffold using on-the-fly tomography,” *Materials & Design,* vol. 134, pp. 400-417, 2017.

[39] B. Wang, B. Pan and G. Lubineau, “Morphological evolution and internal strain mapping of pomelo peel using X-ray computed tomography and digital volume correlation,” *Materials & Design,* vol. 137, pp. 305-315, 2018.

[40] G. Borstnar, F. Gillard, M. N. Mavrogordato, I. Sinclair and S. M. Spearing, “Three-dimensional deformation mapping of Mode I interlaminar crack extension in particle-toughened interlayers,” *Acta Materialia,* vol. 103, pp. 63-70, 2015.

[41] M. P. Fernández, A. H. Barber, G. W. Blunn and G. Tozzi, “Optimization of digital volume correlation computation in SR-microCT images of trabecular bone and bone-biomaterial systems,” *Journal of Microscopy,* vol. 272, no. 3, pp. 213-228, 2018.

[42] S. C. Garcea, Y. Wang and P. J. Withers, “X-ray computed tomography of polymer composites,” *Composites Science and Technology,* vol. 156, pp. 305-319, 2018.

[43] J. M. Lifshitz and A. Rotem, “Time-dependent longitudinal strength of unidirectional fibrous composites,” *Fibre Science and Technology,* vol. 3, no. 1, pp. 1-20, 1970.

[44] S. Blassiau, A. R. Bunsell and A. Thionnet, “Damage accumulation processes and life prediction in unidirectional composites,” *Proceedings of the Royal Society A,* vol. 463, no. 2080, pp. 1135-1152, 2007.

[45] A. R. Bunsell and A. Thionnet, “Life prediction for carbon fibre filament wound composite structures,” *Philosophical Magazine,* vol. 90, no. 31-32, pp. 4129-4146, 2010.

[46] A. R. Bunsell and A. Thionnet, “Failure processes governing long term reliability of carbon fibre composites structures,” *Composites and Nanostructures,* vol. 7, no. 4, pp. 216-224, 2015.

[47] L. M. McGrath, R. S. Parnas, S. H. King, J. L. Schroeder, D. A. Fischer and J. L. Lenhart, “Investigation of the thermal, mechanical, and fracture properties of alumina-epoxy composites,” *Polymer,* vol. 49, no. 4, pp. 999-1014, 2008.

[48] C. Chen, R. S. Justice, D. W. Schaefer and J. W. Baur, “Highly dispersed nanosilica-epoxy resins with enhanced mechanical properties,” *Polymer,* vol. 49, no. 17, pp. 3805-3815, 2008.

[49] E. Schöberl, C. Breite, S. Rosini, Y. Swolfs, M. N. Mavrogordato, I. Sinclair and S. M. Spearing, “A novel particle-filled carbon-fibre reinforced polymer model composite tailored for the application of digital volume correlation and computed tomography,” *Journal of Composite Materials,* in press, 2020.

[50] Toray Industries Inc., *Toray Composite Materials,* Tokyo, Japan, 2019.

[51] US Research Nanomaterials Inc., *Micron Powders,* Houston, TX, USA, 2019.

[52] Sicomin, *Epoxy Systems,* Châteauneuf-les-Martigues, France, 2018.

[53] Ultrawave Ltd., *U100/U100H Ultrasonic Cleaning Bath,* Cardiff, UK, 2017.

[54] 3M Company, *Epoxy Adhesive,* Maplewood, MN, USA, 2019.

[55] Deben Ltd., *CT5000 5kN in-situ tensile stage for µXCT applications,* Woolpit, Suffolk, UK, 2019.

[56] LaVision GmbH, *DaVis v10 StrainMaster (Digital Volume Correlation),* Göttingen, Germany, 2018.

[57] E. M. C. Jones and M. A. Iadicola, "A good practices guide for digital image correlation," International Digital Image Correlation Society (iDICs), 2018.

[58] A. Buljac, T. Taillandier-Thomas, L. Helfen, T. F. Morgeneyer and F. Hild, "Evaluation of measurement uncertainties of digital volume correlation applied to laminography data," *The Journal of Strain Analysis,* vol. 53, no. 2, pp. 49-65, 2018.

[59] H. L. Cox, "The elasticity and strength of paper and other fibrous materials," *British Journal of Applied Physics,* vol. 3, no. 3, pp. 72-79, 1952.

[60] W. Voigt, "Ueber die Beziehung zwischen den beiden Elasticitätsconstanten isotroper Körper," *Annalen der Physik,* vol. 274, no. 12, pp. 573-587, 1889.

[61] B. W. Kim and J. A. Nairn, "Observations of fiber fracture and interfacial debonding phenomena using the fragmentation test in single fiber composites," *Journal of Composite Materials,* vol. 36, no. 5, pp. 1825-1858, 2002.

[62] B. W. Kim and J. A. Nairn, "Experimental verification of the effects of friction and residual stress on the analysis of interfacial debonding and toughness in single fiber composites," *Journal of Materials Science,* vol. 37, no. 18, pp. 3965-3972, 2002.

[63] Z. Yang, B. Zhang, L. Zhao and X. Sun, "Stress transfer around a broken fiber in unidirectional fiber-reinforced composites considering matrix damage evolution and interface slipping," *Science China Physics, Mechanics and Astronomy,* vol. 54, no. 2, pp. 296-302, 2011.

[64] A. N. Netravali, R. B. Henstenburg, S. L. Phoenix and P. Schwartz, "Interfacial shear strength studies using the single-filament-composite test. I: Experiments on graphite fibers in epoxy," *Polymer Composites,* vol. 10, no. 4, pp. 226-241, 1989.

[65] A. Pegoretti, M. L. Accorsi and A. T. Dibenedetto, "Fracture toughness of the fibre-matrix interface in glass-epoxy composites," *Journal of Materials Science,* vol. 31, no. 23, pp. 6145-6153, 1996.

[66] F. M. Zhao and N. Takeda, “Effect of interfacial adhesion and statistical fiber strength on tensile strength of unidirectional glass fiber/epoxy composites. Part I: Experiment results,” *Composites Part A,* vol. 31, no. 11, pp. 1203-1214, 2000.

[67] Y. Swolfs, R. M. McMeeking, I. Verpoest and L. Gorbatikh, “Matrix cracks around fibre breaks and their effect on stress redistribution and failure development in unidirectional composites,” *Composites Science and Technology,* vol. 108, pp. 16-22, 2015.

[68] X. Ji, X. R. Liu and T. W. Chou, “Dynamic stress concentration factors in unidirectional composites,” *Journal of Composite Materials,* vol. 19, no. 3, pp. 269-275, 1985.

[69] S. L. Phoenix and I. J. Beyerlein, Comprehensive composite materials. Chapter 1.19 – Statistical strength theory for fibrous composite materials, 1st ed., vol. 1, A. Kelly and C. Zweben, Eds., Oxford, UK: Pergamon Press, 2000, pp. 559-639.

[70] R. P. Tavares, F. Otero, J. Baiges, A. Turon and P. P. Camanho, “A dynamic spring element model for the prediction of longitudinal failure of polymer composites,” *Computational Materials Science,* vol. 160, pp. 42-52, 2019.

[71] A. E. Scott, I. Sinclair, S. M. Spearing, M. N. Mavrogordato and W. Hepples, “Influence of voids on damage mechanisms in carbon/epoxy composites determined via high resolution computed tomography,” *Composites Science and Technology,* vol. 90, pp. 147-153, 2014.

[72] T. Hobbiebrunken, B. Fiedler, M. Hojo and M. Tanaka, “Experimental determination of the true epoxy resin strength using micro-scaled specimens,” *Composites Part A,* vol. 38, no. 3, pp. 814-818, 2007.

[73] Y. Swolfs, C. Breite, S. V. Lomov and L. Gorbatikh, “Fibre break interactions in unidirectional composites under longitudinal tensile loading,” in *The 7th European Community on Computational Methods in Applied Sciences*, Girona, Spain, 2019.

[74] A. Kelly and W. R. Tyson, “Tensile properties of fibre-reinforced metals: Copper/tungsten and copper/molybdenum,” *Journal of the Mechanics and Physics of Solids,* vol. 13, no. 6, pp. 329-350, 1965.

[75] S. Pimenta and S. T. Pinho, “Hierarchical scaling law for the strength of composite fibre bundles,” *Journal of the Mechanics and Physics of Solids,* vol. 61, no. 6, pp. 1337-1356, 2013.

[76] S. Pimenta, “A computationally-efficient hierarchical scaling law to predict damage accumulation in composite fibre-bundles,” *Composites Science and Technology,* vol. 146, pp. 210-225, 2017.

[77] A. Bunsell, L. Gorbatikh, H. Morton, S. Pimenta, I. Sinclair, S. M. Spearing, Y. Swolfs and A. Thionnet, “Benchmarking of strength models for unidirectional composites under longitudinal tension,” *Composites Part A,* vol. 111, pp. 138-150, 2018.

[78] M. R. Wisnom and D. Green, “Tensile failure due to interaction between fibre breaks,” *Composites,* vol. 26, no. 7, pp. 499-508, 1995.

[79] S. Yaofeng and J. H. L. Pang, “Study of optimal subset size in digital image correlation of speckle pattern images,” *Optics and Lasers in Engineering,* vol. 45, no. 9, pp. 967-974, 2007.

[80] J. Schindelin, I. Arganda-Carreras, E. Frise, V. Kaynig, M. Longair, T. Pietzsch, S. Preibisch, C. Rueden, S. Saalfeld, B. Schmid, J.-Y. Tinevez, D. J. White, V. Hartenstein, K. Eliceiri, P. Tomancak and A. Cardona, “Fiji: An open-source platform for biological-image analysis,” *Nature Methods,* vol. 9, pp. 676-682, 2012.

Chapter 7 Summary, conclusions and further work

7.1 Summary

Chapter 4 presented the foundations of the work conducted here, which in turn supported the subsequent analyses. More specifically, the development of a novel particle-filled Carbon-Fibre Reinforced Polymer model composite was described, tailored for the application of Digital Volume Correlation and Computed Tomography. To permit the application of DVC to displacement and/or strain measurements parallel to the fibre orientation, the matrix was doped with a sparse population of sub-micrometre particles to act as displacement trackers (*i.e.* fiducial markers). This was required because the highly anisotropic and somewhat regular/self-similar microstructures found in well-aligned unidirectional materials at high fibre volume fractions are intrinsically challenging for DVC, especially along the fibre direction at microstructural length-scales on the order of a few fibre diameters. In this context, 38 different cross-ply laminates with a $[90/0]_s$ layup were manufactured, forming an extensive test matrix with a range of possible particle compositions, mean sizes and concentrations. To preserve the tensile behaviour of a commercially representative material, whilst still allowing the application of DVC parallel to the fibre direction, a series of considerations were established, and subsequently assessed qualitatively in detail, through the use of Micro-focus Computed Tomography. In this context, the use of barium titanate particles permitted a volume fraction low enough to minimize any substantial disruption in the separation and packing of fibres at tow-level within the 0° plies, while at the same time satisfying the imaging requirements.

Subsequently, double-edge notched specimens were machined, and subjected to in *situ* Synchrotron Radiation Computed Tomography at a sub-micrometre resolution of 0.65 µm. The use of SRCT permitted scan times on the order of seconds as opposed to hours, noting that this strategy was used to help mitigate undesirable hold-at-load artefacts. In conjunction with image analysis, it was shown that the macro- and micromechanical responses of the doped material were mechanistically representative of undoped materials made by the same manufacturing route, and was consistent with other materials made by other processes. Within the current sample gauge volumes, which encompassed a region of interest from the 0° plies in the vicinity of the notch, there was no appreciable difference in the total number of fibre breaks between the specimens loaded to failure, particularly considering the statistical nature of fibre strength. Likewise, within the statistical power of the sample gauge volumes analysed, the behaviour of clusters also appeared to be stochastic. However, by decoupling the total number of fibre breaks into singlets and cluster of breaks it was possible to observe the existence of distinct damage variability, even in the absence of barium titanate. Correspondingly, some variability in mechanical behaviour was discerned between individual specimens, and material types (doped

and undoped), which was attributed to both manufacturing inconsistencies (such as distinct differences in fibre volume fraction) and a potential contribution of the doping particles. Notwithstanding these effects, doped carbon-fibre reinforced epoxy materials were identified as a suitable model system for validating the DVC methodology, and subsequent mechanistic investigations.

Chapter 5 presented an experimental demonstration and validation of high-resolution three-dimensional experimental strain measurement using Digital Volume Correlation, via through-thickness strain analysis under a state of pure bending. In this context, high-resolution *ex situ* µCT measurements were performed using a simple standard specimen subjected to a four-point flexural test, which resulted in a linear strain distribution through the beam thickness. As a result of the narrow field of view available, and thus the small specimen dimensions required, a rig was specifically designed for this study, whereby its main component (*i.e.* the reaction tube) was constructed from a polymer-based material to minimize X-ray absorption.

A series of noise tests were performed to determine the experimental error. These included a static repeat scan and a rigid body displacement assessment, respectively. The static repeat scan demonstrated a key aspect for DVC analyses, whereby a compromise was achieved between strain and spatial resolution. This occurred as a smaller sub-set size contained too few unique features, in this case, the barium titanate particles. In contrast, a larger sub-set compromised spatial resolution, as the underlying deformation was representative of the average displacement of all the voxels contained within a given sub-set. The rigid body displacement assessment also confirmed that that specimen translation parallel to the fibre direction was in line with the applied displacements, obviating a key problem in applying DVC to such uniformly aligned microstructures. Subsequently, this demonstrated that the selection of barium titanate, as a fiducial marker system, was an adequate choice from an imaging perspective.

Classical beam theory was used to compare the DVC results extracted from the 0° plies in incrementally decreasing averaging schemes, and at various spatial resolutions: 120 voxels, 100 voxels and 80 voxels sub-set size, with 50 % overlap applied between adjacent sub-sets. Good agreement was found between the Euler-Bernoulli beam theory and DVC output providing that the mean of three or more standalone sub-sets was taken, demonstrating the effectiveness of DVC in measuring local strains parallel to the fibre direction in UD laminae. Edge-artefacts were shown to introduce subtle nonlinearities in the measurements, which in turn illustrated that any DVC results located at the edge of the cropped/masked volume image must be treated with caution. Deviations from the classical beam theory, exceeding that of the experimental error, were observed when sampling was performed with single 120 voxel size sub-sets. This was judged as a practical lower limit for the spatial resolution using the technique employed in this thesis, notwithstanding that this may also be attributed to variations in the material microstructure.

The methodology provided a framework for accessing unprecedented opportunities to identify the local strain distributions before and after damage formation in composite materials, in 3D, at relatively high spatial resolutions. In this context, and in line with the objectives of the project, DVC measurements in relation to local fibre failure events, such as strain transfer lengths (ineffective length), were performed. To eliminate some of the present caveats, in particular related to temporal, spatial and strain resolutions achievable, these analyses were performed on the SRCT specimen data from **Chapter 4**.

Chapter 6 focused on fibre-direction strain measurements in a composite ply under quasi-static tensile loading using Digital Volume Correlation and *in situ* Synchrotron Radiation Computed Tomography. Similar to the four-point bending study detailed in **Chapter 5**, measurement sensitivity and noise were considered, along with the spatial filtering intrinsic to DVC strain measurements. Compared to volume images acquired through µCT, the metrological performance of the DVC technique was demonstrated to be superior. Subsequently, correlation between breaks and corresponding strain regions have been established at a level well above the measured noise, despite the fact that significantly smaller sub-set size/higher spatial resolution (*i.e.* 32 voxels sub-set, with 75 % overlap applied between adjacent sub-sets) was used compared to **Chapter 5**.

The strain field assessment at single fibre breaks resulted in 'full-recovery lengths' consistent with values reported in the modelling literature, on the order of 50-100 µm. However, due to the spatial resolution limitations and associated DVC averaging effects, a key aspect highlighted was that the deformation at a constituent level could not be separated (*i.e.* between fibre and matrix). In this context, each of the 'recovery length' profiles encompassed an 'elevated strain length', which was associated primarily with the matrix deformation at the crack plane. This was followed by a 'lower strain length', where the DVC data was considered to be a good estimate of both fibre and matrix deformation. Additionally, the 'full-recovery lengths' were observed to increase with the applied load, consistent with micromechanical modelling predictions in the literature. Subsequently, this was considered a potential indicator that the level of microstructural damage (matrix yielding or debonding) increased with increasing load. The changes reported were, however, small and must be viewed in the context of the small stress range over which observations could be made, owing to the fact that fibre breaks develop exponentially with stress, with the majority of breaks occurring immediately prior to failure.

Lastly, the evolution of single fibre breaks into duplets resulted in a considerably larger 'full-recovery length', together with an increased growth compared to single fibre breaks. The study, therefore, demonstrated that such previously unavailable, mechanistically-consistent 3D strain measurements may be made in relation to fibre failure events, delineating aspects of the load shedding phenomenon. However, as detailed in **Section 7.3**, to determine the relationship more accurately between the number of breaks in a cluster, and the

surrounding microstructural damage, acquisition methods capable of achieving improved voxel resolution levels would have to be utilized.

7.2 Conclusions

The conclusions of the thesis can be summarized through the following key points:

- Barium titanate particles, with a mean particle size of 400 nm and concentration of ∼1.44 vol. %, were found to offer the most favourable compromise between contrast in CT images and the ability to obtain a homogeneous distribution over useful imaging volumes with sufficient particle compactness for local DVC analyses.
- Within the statistical power of the sample gauge volumes investigated (∼0.34 mm^3), the presence of barium titanate particles did not appear to have had an exceptional effect on the total number of breaks at fracture. More specifically, 913 and 873 breaks were reported for the different materials (doped and undoped), resulting in a difference of less than ∼5 % – notwithstanding the slightly different fraction of UTS achieved in each case (98 % and 95 %, respectively).
- Likewise, the behaviour of clusters was found to be stochastic, whereby the largest clusters found in this work were: a 19-plet and two 9-plets in the doped and undoped specimen, respectively, loaded to failure.
- Ultimately, the response of the doped material was shown to be mechanistically representative of undoped materials, whereby specimen failure was likely to be determined by intrinsic stochastic factors, such as fibre strength and local microstructure, rather than particularly the inclusion of fiducial markers.
- A practical lower limit for the spatial resolution was discerned, below which DVC measurements were no longer considered reliable. For underlying volume images obtained via μCT this corresponded to an isotropic sub-set size of 120 voxels (with 50 % overlap), while for SRCT, a significantly smaller isotropic sub-set of 32 voxels could reliably be used (with 75 % overlap). This highlighted a crucial aspect, whereby to avoid over-smoothing of the displacement/strain data, a balanced signal-to-noise ratio must be considered independently for a given sub-set size, which is in turn linked to the materials and imaging methods used.
- At a maximum applied load of 950 N (equivalent to 98 % UTS or a stress of ∼2300 MPa in the 0° plies) the ‘full-recovery length’ averaged over eight single fibre breaks was ∼63 μm. Relative to the preceding load step of 900 N (corresponding to an incremental strain of ∼0.12 %), a slight increase of ∼7 % was reported in the ‘full-recovery length’.

- Based on a single representative fibre break, the maximum increase in 'full-recovery length' between the 950 N and 850 N load step as returned by the DVC was ~9 %. While this increase is not substantial, it must be viewed in the context of a strain increment of only ~0.23 % (*i.e.* between 98 % UTS or a stress of ~2300 MPa and 88 % UTS or a stress of ~2000 MPa, respectively).
- The evolution of a single fibre break (at 900 N) into a cluster encompassing two breaks (at 950 N) resulted in a recovery distance increase of ~11 %. While somewhat subtle, this growth in 'full-recovery length' was greater than the ~7 % average for the eight singlets evaluated between the same load steps.
- The 'full-recovery length' of two duplets was given by the maximum distance of ~78 μm which encompasses both clusters. Compared to the average length of ~63 μm recorded at the 950 N load step, *i.e.* ~24 % higher.

To sum up, the 'full-recovery lengths' were observed to increase with the applied load, providing an indication that the level of microstructural damage advances with increasing load, recognising that confirming such small changes is difficult to achieve in practice. Likewise, the additional volume of affected material around a cluster caused an increase in the 'full-recovery length', noting that this was considerably higher compared to single fibre fractures. This work represents the first successful attempt to estimate *via* experiments the three-dimensional stress redistribution around broken fibres in representative carbon fibre polymer matrix composites. These experimental measurements have significance for the development, calibration and validation of models for *in situ* fibre failure, and thus tensile strength. Prediction of these phenomena is of scientific and technological importance.

7.3 Further work

7.3.1 Experimental

- It was acknowledged in **Chapter 4**, that the micromechanical analysis (*i.e.* fibre break and cluster behaviour) relied on two undoped and one doped specimen, respectively. To improve the statistical power of the results, a larger number of specimens would need to be examined. This would help in establishing a more refined conclusion regarding the relative contribution of the fiducial markers compared to the intrinsic variability of the material (*i.e.* stochastic factors, such as fibre strength and local microstructure). However, as previously noted, a large experimental trial is not trivial to achieve in practice, primarily due to the limited availability of the SRCT beam time required to achieve such results. While, *in situ* tensile tests could be performed using conventional μCT to alleviate some of the

aforementioned experimental constraints, it is important to highlight that, hold-at-load artefacts may be introduced. This, in turn, would make discerning any potential effects (or lack thereof) of the fiducial markers compared to the intrinsic variability of the material even more challenging.

- In the context noted above, efforts should be made to manufacture specimens with the same fibre volume fraction. This is, however, challenging particularly for the doped materials, whereby the inclusion of fiducial markers is expected to increase the viscosity of the resin, and reduce subsequent bleed-out during the autoclave process.
- Recognizing that the principle of embedding ceramic particles as fiducial markers was demonstrated successfully in CFRPs for the purpose of three-dimensional microscopic strain mapping along the fibre direction, it would be interesting to exploit the use of alternative phases, such as thermoplastics or carbon black. While, due to the low attenuation of carbon, this undoubtedly represents a challenge from an imaging perspective, such markers may be engineered to reduce any potential micromechanical influence of the markers on failure; notwithstanding, that for the specimens tested in tension, the response of the material doped with barium titanate was shown to be mechanistically representative of undoped materials.
- DVC studies at fibre break sites focused on the effect of fibre-matrix interface sliding, debonding, matrix deformation and microcracking on the strain transfer lengths. However, this would require significantly finer spatial resolutions, which would in turn necessitate obtaining superior underlying scans, at 'true' nanometre voxel resolutions levels (see **Section 7.3.2**), and secondly, a potentially improved spatial distribution of the fiducial markers.
- Given that the materials and methods are now developed, and with a high level of confidence in the basic measurements, other application areas can be envisaged within the 0° plies. For example, this may include studies to probe the understanding of: fibre misalignment, porosity or ply drops on local load paths/partitioning, different reinforcements types (*e.g.* glass-fibre), in addition to different loading conditions (*e.g.* compression, torsion, time-varying, fatigue). Likewise, the methodology can be adapted for off-axis ply orientations, providing the opportunity to study the initiation and growth of transverse ply cracks in the 90° plies. Furthermore, analyses at larger length-scales would be valuable in the future (*e.g.* up to the structural level) and in the context of multiaxial or discontinuous reinforcements.

7.3.2 Imaging

- To determine the relationship more accurately between the number of breaks in a cluster, and the surrounding microstructural damage, acquisition methods capable of achieving improved voxel resolution levels would have to be utilized. Likewise, despite the fact that strain mapping at fibre break

sites was performed at superior voxel resolutions levels (~0.65 μm) than previously reported in the literature, this was insufficient to confirm/inform the presence of fibre-matrix interface debonding. Given that fibre-matrix interface debonding directly affects the length over which stress/strain is recovered in a broken fibre (and subsequently the gauge volume over which SCFs are significant), it would be valuable to discern such damage mechanisms in future studies.

- This would, however, require voxel resolution levels approximatively one order of magnitude higher and in turn, limit the sample size achievable by the imaging – which is an unavoidable trade-off. This is because, a larger sample size than that of the field of view, would introduce imaging artefacts. Subsequently, specimens with significantly smaller cross-sections than those used in the present work would be required, notwithstanding that this would be challenging to achieve in practice from both a manufacturing and a mechanical testing perspective.
- Performing *in situ* mechanical tests at higher acquisition speeds, or preferably via continuous imaging, would be desirable to further alleviate hold-at-load artefacts. However, achieving a good balance between the imaging quality required for DVC and the acquisition speed is difficult to achieve in practice, in addition to the fact performing such scans are currently feasible using synchrotron sources only.

7.3.3 Digital Volume Correlation

- Acknowledging that the work in this thesis relied on investigating the displacements, and implicit strain fields parallel to the fibre direction, future studies could focus on the remaining strain components, depending on the loading scenario and the researcher's interest. This is possible due to the fact that through DVC, full-field displacement and strain maps can be obtained. However, this would require, detailed noise studies (*i.e.* rigid body displacements) in all directions (*cf.* a single direction of interest), which is not trivial to achieve in practice, particularly using μCT methods.
- In conjunction with very much higher voxel resolutions levels and a potentially improved spatial distribution of the fiducial markers, it would be interesting to utilize a more refined DVC grid (*i.e.* smaller sub-sets) in future studies. This would help alleviate the practical lower limit for the spatial resolution using the technique employed in this thesis.
- The DVC work is consistent with the philosophy of 'data rich mechanics', whereby very high levels of utilisation of data obtained from individual, state-of-the-art, experiments can be used to inform model development and validation. As such, it would be valuable to consider a comparison between numerical and analytical model predictions. Nonetheless, the approach is not simple or direct. That is because any comparison/validation of corresponding modelling must include spatial filtering (*e.g.* sub-set grid spacing) to match the experimental constraint.

(End of document)